ENVIRONMENTAL AND HOST FACTORS THAT INFLUENCE RESPIRATORY VIRUS PATHOGENESIS AND TRANSMISSION USING *IN VITRO* AND *IN VIVO* MODEL SYSTEMS

by

BRITTANY SEIBERT

(Under the Direction of Daniel R. Perez)

ABSTRACT

Viral infections can have detrimental effects worldwide, leading to declining economies, loss of school days, workdays, numerous physician visits, hospitalizations, and death. Concerning respiratory viral infections, viruses belonging to the families *Orthomyxoviridae* (influenza virus) and *Coronaviridae* (severe acute respiratory syndrome coronavirus 2 (SARS-CoV-2)) have been prominent causes of morbidity and mortality worldwide, resulting in previous and current epidemics and pandemics. Multiple biological and environmental factors such as sex, age, nutrition, disease status, and the host residential microbiome can affect the pathogenesis and transmission of respiratory viruses.

The studies presented here aimed to investigate environmental and host factors influencing respiratory virus pathogenesis and transmission *in vitro* and *in vivo* using two primary pathogens, influenza A virus (FLUAV) and SARS-CoV-2. I used molecular virology techniques and bioinformatic tools to analyze virus infection and transmission using *in vitro* systems. I also assessed pathogenesis and changes within the respiratory and intestinal tract in two animal models post-respiratory virus infection. I designed a model system to study FLUAV transmission *in vitro*. The results showed successful aerosol inoculation of three subtypes of FLUAV (H1N1, H3N2, and H9N2) in a common cell line, Madin-Darby canine kidney (MDCK) cells. Further, I was able to infect differentiated human airway epithelial cells with the H1N1 and H3N2 FLUAV utilized within these studies. Assessing aerosol inoculation in an *in vitro* system can be valuable in testing molecular markers associated with increased respiratory transmission. My advances a technique that can be utilized to assess molecular markers involved in FLUAV transmission prior to *in vivo* testing.

In addition to understanding aerosol transmission, I analyzed the effect of various biological and environmental factors on the pathogenesis of FLUAV and SARS-CoV-2 *in vivo*. First, I tested the effect of antibiotic growth promoter administration on FLUAV infection in broiler chickens, including the impact of virus shedding and dysbiosis of the respiratory and intestinal microbiome. In addition to analyzing environmental factors, I examined the effect of FLUAV exposure prior to SARS-CoV-2 infection on viral titers, disease pathology, and the respiratory and intestinal microbiome in aged Golden Syrian hamsters. Both studies showed changes within the respiratory and intestinal microbial community, notably the enrichment of opportunistic pathogens and microbes associated with inflammation. The relationship between the residential microbiome and other confounding factors such as respiratory virus infection, age, and antibiotic growth promoter administration contributes to a better understanding of the complexities associated with the host responses during viral infections.

INDEX WORDS: Avian influenza, Influenza A virus, SARS-CoV-2, Antibiotic growth promoters, Microbiome, Transmission

ENVIRONMENTAL AND HOST FACTORS THAT INFLUENCE RESPIRATORY VIRUS PATHOGENESIS AND TRANSMISSION USING *IN VITRO* AND *IN VIVO* MODEL SYSTEMS

by

BRITTANY SEIBERT

B.S., University of California, Davis, 2015

M.Sc., University of California, Davis, 2017

A Dissertation Submitted to the Graduate Faculty of The University of Georgia in Partial

Fulfillment of the Requirements for the Degree

DOCTOR OF PHILOSOPHY

ATHENS, GEORGIA

2022

ENVIRONMENTAL AND HOST FACTORS THAT INFLUENCE RESPIRATORY VIRUS PATHOGENESIS AND TRANSMISSION USING *IN VITRO* AND *IN VIVO* MODEL SYSTEMS

by

BRITTANY SEIBERT

Major Professor:	Daniel R. Perez
Committee:	Daniela Rajao Elizabeth Ottesen Amanda Frossard Andrew Park

Electronic Version Approved:

Ron Walcott
Vice Provost for Graduate Education and Dean of the Graduate School
The University of Georgia
December 2022

DEDICATION

This dissertation is dedicated to my father, mother, brother, and fiancé for their unconditional support.

ACKNOWLEDGEMENTS

I would like to acknowledge my graduate advisor, Dr. Daniel R. Perez, for allowing me to join his laboratory and pursue my interests in understanding bacterial-viral interactions. I really appreciate all the advice and support from Dr. Perez and his wife, Andrea, and Dr. Daniela Rajao throughout my years as a student. I would also like to acknowledge all members of my dissertation committee, Dr. Daniela Rajao, Dr. Elizabeth Ottesen, Dr. Amanda Frossard, and Dr. Andrew Park, for their advice and time spent helping me improve project designs and analysis. I am also very appreciative to have had the opportunity to learn diverse skills from all members of my dissertation committee.

I would like to recognize all the former members of the CRP-FLU lab, including Stivalis, Lucas, John, Jeff, Ade, Zhimin, Pilar, and Ruby, and current members including, Silvia, Joaquin, Lucia, Claire, Flavio, Matias, Brianna, Lisa, Giulia, and Ginger for all the constant support and close friendship. I would also like to thank the friends I made at UGA including, Anna, Christina, and Sydney, and those in California including, Ashley, Sara, Jess, and Tatyana. All these individuals have been so important in helping me in and outside the lab, and I am eternally grateful for their constant care and support in everything I do.

I would also like to thank my family, my father, Ralph, my mother, Terrie, my brother, Steven, and my future husband, Stuart, for always motivating me and showing their endless support in my academic career. My parents taught me to have a strong work

ethic and pursue a career that I truly enjoy. Their support has been instrumental throughout my years at the University of Georgia graduate school program.

TABLE OF CONTENTS

Page

CHAPTER

Influenza virus

SARS-CoV-2

APPENDIX

LIST OF TABLES

Page

LIST OF FIGURES

CHAPTER 1

INTRODUCTION

Viral infections can have detrimental effects worldwide, leading to declining economies, loss of school days, workdays, numerous physician visits, hospitalizations, and death. Viral pathogens can infect an array of tissues, including the upper respiratory tract and lungs (influenza virus and coronavirus), intestine (rotavirus and norovirus), spinal cord (poliovirus), and more (1). In recent years, two prominent respiratory viruses belonging to the families *Orthomyxoviridae* (influenza virus) and *Coronaviridae* (severe acute respiratory syndrome coronavirus 2 (SARS-CoV-2)) have caused considerable morbidity and mortality worldwide, resulting in previous and current epidemics and pandemics.

There are four types of influenza viruses: A, B, C, and D. Influenza A (FLUAV) and B (FLUBV) viruses are responsible for yearly epidemics in humans, requiring annual changes to the vaccine to protect against current circulating strains. FLUAV infects a broad host range of avian and mammalian species, while FLUBV is primarily confined and adapted to humans (2, 3). FLUAVs and FLUBVs contain two major surface glycoproteins, hemagglutinin (HA) and neuraminidase (NA), which are the main antigenic determinants that elicit neutralizing antibodies (4-6). FLUAVs are classified into subtypes based on a combination of the surface proteins; currently, 18 HA and 11 NA subtypes have been described (4-8). Most FLUAV epidemics in humans are caused by subtypes H1N1 and H3N2, as well as FLUBVs (9). However, most FLUAV subtypes are described in wild aquatic birds, principally *Anseriformes* and *Charadriiformes*, considered natural hosts (10, 11). Avian-origin FLUAVs are grouped as low pathogenicity avian influenza viruses (LPAIVs) and high pathogenicity avian influenza viruses (HPAIVs) based on the pathogenesis in chickens and/or the presence of a polybasic amino acid cleavage site in the HA containing Arginine or Lysine (10, 12). The polybasic cleavage site in HPAIV enables the HA to be processed by endogenous cellular furin-like proteases promoting systemic infection; meanwhile, LPAIV typically contains a monobasic cleavage site limiting the HA processing to extracellular trypsin-like proteases, thus restraining the infection to specific sites (10, 12). Viruses with the H5 and H7 subtypes have been associated with HPAIV, while H9N2 is the most prevalent LPAIV subtype (10, 13). H9N2 LPAIV infections can be mild in poultry but can lead to significant economic loss because of lower egg production and delayed growth (10). Aside from having an impact on the poultry industry, H9N2 LPAIV is considered zoonotic and has been reported in humans, swine, dogs, horses, and minks; in addition, H9N2 LPAIV has previously contributed to internal gene segments of other FLUAV subtypes such as H5N1, H5N6, H7N9, H10N8, and H10N3 resulting in human infections (10, 14-21). Spillover events between wild birds and domestic poultry have also been reported for H5, H7, and H9N2 FLUAV subtypes (10, 13, 22-24). Therefore, understanding host factors that can affect the spread and infectivity of H9N2 LPAIV in poultry is essential for limiting economic loss and zoonotic potential.

Influenza viruses continuously evolve within animal and human hosts, partially due to low-fidelity RNA polymerase proofreading, leading to antigenic drift in both FLUAVs. Cumulative changes, particularly in the surface proteins, can enhance immune evasion and viral fitness (ex. transmission or replication) (9, 25). Current literature indicates that transmission of FLUAVs occurs through direct and indirect contact, respiratory droplets (particle size > 5 µm), and aerosol or droplet nuclei particles (particle size < 5 µm) (26, 27). Larger respiratory droplets settle on surfaces such as floors, walls, beds, etc., after droplet release because of gravity (28). Conversely, respiratory droplets evaporate to form droplet nuclei in which the virus can be independently suspended or attached to the particles (28). Initially, the virus aerosols diffuse and remain suspended indoors because they are too small to settle because of gravity (28). Over time, virus aerosols will gradually deposit on environmental surfaces; however, the aerosols can be resuspended by human movement and continue to spread until the virus particles become inactive (28). Aerosols can also travel considerable distances from the infectious source (up to 3.7 m away) and can result from respiratory droplet desiccation called droplet nuclei (28, 29). Previous studies reported infectious virions and vRNA in respiratory droplets and aerosol particles; however, aerosol particles are primarily expelled and contain more viral copies than respiratory droplets (30-33). While direct inoculation is the most common route of infection within a laboratory environment, multiple studies reported that the inoculation route (direct inoculation versus aerosol inoculation) can significantly influence resulting morbidity and mortality following infection, particularly in HPAIV (34-37). Further, various viral, host, and environmental factors can influence successful FLUAV transmission (28, 38).

The emergence of SARS-CoV-2 in humans has led to the current COVID-19 pandemic resulting in millions of deaths and declining economies worldwide. SARS-CoV-2 is an enveloped positive-sense single-stranded RNA virus belonging to the genus

Betacoronavirus within the family *Coronaviridae* (39). Previous studies reported susceptibility to SARS-CoV-2 infection in an array of mammalian species, including dogs, cats, ferrets, minks, hamsters, rhesus macaques, cynomolgus macaques, African green monkeys, common marmosets, rabbits, and fruit bats (40). Proposed methods of SARS-CoV-2 transmission include respiratory droplet transmission, aerosol transmission, surface contamination, and the fecal-oral route; however, respiratory droplet transmission is the most notable route reported throughout the pandemic, along with direct contact spread (41). While some patients can present as asymptomatic, common symptoms associated with SARS-CoV-2 infection include fever, cough, dyspnea, and occasional gastrointestinal symptoms, which can progress to acute respiratory distress, pneumonia, renal failure, and death, particularly in older adults (41-44). Previous studies reported high pathogenesis in aged individuals during infections is predominantly associated with the immune response after viral infection (reviewed in (42)). Notably, aging can lead to pro-inflammatory cytokine production, reduced and delayed type I interferon responses, and impaired antigen presentation and T cell priming (reviewed in (42)).

Recently, multiple reports suggested that the respiratory and intestinal microbiome can directly impact host cells or indirectly impact the immune system during viral infections (45, 46). The human microbiome consists of more than a trillion microorganisms interacting in a complex ecosystem throughout the human body, including the intestine, skin, mucosal surfaces, lungs, and many more (47, 48). The bacterial, viral, and fungal residential microbes play an essential role in various host functions, including metabolism, development, and regulation of the immune response and physical defenses against invading pathogens (47). In addition, the intestinal microbiota interacts with the respiratory tract forming the gut-lung axis; however, multiple factors can induce changes within the residential population affecting intestinal and respiratory immune responses (49, 50). Biological and environmental factors such as sex, age, nutrition, and disease status can affect the diversity and abundance of bacteria associated with good health leading to dysbiosis (48, 51, 52). Further, multiple studies showed that the host residential microbiome plays an essential role in respiratory viral infections by promoting viral infections, such as poliovirus, reovirus, and certain retroviruses or having a protective role, such as FLUAV and rotavirus (53-55).

Research objectives and aims

The main purpose of this project was to investigate environmental and host factors that influence respiratory virus pathogenesis and transmission *in vitro* and *in vivo* using two primary pathogens, FLUAV and SARS-CoV-2. We will use molecular virology techniques to analyze virus infection and transmission using an *in vitro* system and bioinformatic tools to examine microbiome changes within the respiratory and intestinal tract using two animal models. The main research objectives are specified below.

Specific aim 1: *To establish and characterize an in vitro model system to study influenza A virus aerosol transmission*.

i. Establish an *in vitro* model system to infect cell culture with aerosolized FLUAV.

ii. Compare aerosol and direct inoculation methods of three FLUAV subtypes, including H1N1, H3N2, and H9N2 in Madin-Darby Canine Kidney (MDCK) cells.

iii. Compare aerosol and direct inoculation methods of three FLUAV subtypes, including H1N1, H3N2, and H9N2 in a more relevant cell line including differentiated human airway epithelial cells.

Specific aim 2: *To analyze the effect of antibiotic growth promoter (AGP) administration on virus shedding and the intestinal microbiota post avian influenza virus (AIV) infection in broiler chickens.*

i. Evaluate the effect of in-feed AGP-induced changes on growth performance after AIV infection.

ii. Evaluate the indirect effect of in-feed AGP administration on susceptibility to AIV shedding.

iii. Analyze microbiome changes within the oropharynx and cloaca post-AIV infection with and without AGP use.

Specific aim 3: *To analyze the pathobiology and dysbiosis of the respiratory and intestinal microbiota in aged 14-month-old Golden Syrian hamsters infected with SARS-CoV-2.*

i. Assess viral loads and disease pathology at 3- and 6-days post-challenge.

ii. Analyze microbiome changes within the lungs and intestinal tract post-SARS-CoV-2 infection.

CHAPTER 2

LITERATURE REVIEW

Influenza virus

Classification

FLUAV *Alphainfluenzavirus* (type A influenza virus) belongs to the family *Orthomyxoviridae* (Order: Articulavirales, Class: Insthoviricetes, Subphylum: Polyploviricotina, Phylum: Negarnaviricota) along with seven other genera, including, *Betainfluenzavirus* (type B influenza virus, FLUBV), *Gammainfluenzavirus* (type C influenza virus, FLUCV), *Deltainfluenzavirus* (type D influenza virus), *Isavirus, Quaranjavirus, Sardinovirus,* and *Thogotovirus* (56). Two new genera, *Sardinovirus* and *Mykissvirus*, were ratified in March 2022 by the International Committee on Taxonomy of Viruses (56). FLUAV, FLUBV, and FLUCV can infect an array of vertebrates, including horses, swine, birds, dogs, seals, and humans (57). FLUAVs and FLUBVs contain two major surface glycoproteins, HA and NA, which are the main antigenic determinants that elicit neutralizing antibodies (4-6). FLUAVs are classified into subtypes based on a combination of the surface proteins; currently, 18 HA and 11 NA subtypes have been described (4-8). Influenza viruses are further classified using standard nomenclature, including virus type, species from which it was isolated, location of isolation, isolate number, isolate year, and then HA and NA subtype (for FLUAV viruses) (58). Most FLUAV subtypes have been described in wild aquatic birds, principally *Anseriformes* and

Charadriiformes, considered natural hosts (10, 11). Sixteen HA and nine NA subtypes have been isolated from birds (H1 to H16 and N1 to N9), while RNA from two additional HA and NA subtypes have been isolated in bats (H17 and H18, and N10 and N11) (59). However, spillover events between wild birds and domestic poultry have been reported for H5, H7, and H9N2 IAV subtypes (10, 22-24). Meanwhile, most influenza epidemics in humans are caused by subtypes H1N1 and H3N2, as well as FLUBVs (9).

Virion structure

The shape of FLUAV virus particles can be pleomorphic, forming both spherical (about 100 nm in diameter) or filamentous (can reach up to 30 µm in size) virions of various lengths (60, 61). Filamentous particles are generally observed in low-passage-number isolates, while laboratory-adapted strains are almost exclusively spherical particles (60, 61). Previous research suggests that the filamentous shape confers a selective advantage *in vivo*, while spherical shapes have a fitness advantage in embryonated eggs (61). On the outer surface, the FLUAV particle contains HA and NA glycoproteins projecting from a host cell-derived lipid membrane, referred to as the envelope, in a ratio of approximately four to one (62). In a lower abundance, an additional surface protein called the matrix 2 (M2) protein is present at a ratio of one M2 channel to 10^1 to 10^2 HA molecules (62). The envelope is supported by the matrix 1 (M1) protein, which contains the nuclear export protein (NEP/NS2) and eight viral ribonucleoprotein (vRNP) complexes, typically aligned in a 1 + 7 configuration (62, 63). Each vRNP consists of a viral RNA (vRNA) segment wrapped around multiple copies of the viral nucleoprotein (NP) in a rod-like structure (62, 64). The ends of the vRNA segments form a helical hairpin bound by a single copy of the viral RNA-dependent RNA polymerase (RdRp) (62, 64). The heterotrimeric RdRp consists of three subunits: polymerase basic 1 (PB1), polymerase basic 2 (PB2), and polymerase acidic (PA) (62-64).

The FLUAV genome contains eight single-stranded, negative-sense vRNAs encoding for at least 12 viral proteins (6, 62, 64, 65). Each segment contains a partially complementary conserved 5’ and 3’ termini, segment-specific untranslated regions (UTRs), and at least one open reading frame (ORF) (63). The eight segments of FLUAV are numbered by decreasing length (62). Segment 1 is 2,341 nucleotides in length and encodes for the PB2 protein, which forms part of the RdRp and plays a role in gathering 5’ capped RNA fragments from host cellular mRNA molecules used for viral transcription (63). Recently, a new viral protein, PB2-S1, encoded by a spliced mRNA, has also been identified to inhibit the host RIG-I-dependent interferon signaling pathway (66). Segment 2 is also 2,341 nucleotides in length and encodes for the PB1 protein, which is involved in RNA elongation and endonuclease activity (62). An additional accessory protein may be encoded called PB1-F2, resulting from an alternate open reading frame (+1) and plays a role in the pathogenesis and virus clearance in mice (67). Segment 3 is 2,233 nucleotides in length and encodes for PA (62). The viral protein PA-X is generated through ribosomal frameshifting and plays a role in virus replication and inhibition of the host antiviral response (62, 68). Segment 4 is ~1,780 nucleotides in length (depending on subtype) and encodes for the surface glycoprotein HA, which plays a key role in receptor recognition, virus attachment, membrane fusion, and virus entry (62, 69). Segment 5 is 1,565 nucleotides in length and encodes for the NP, which is involved in nuclear import (62). Segment 6 is ~1,413 nucleotides in length (depending on subtype) and encodes for the second surface glycoprotein NA (62). Segment 7 is 1,027 nucleotides in length and encodes for the M1 matrix protein and, through RNA splicing, the M2 ion channel (62). Segment 8 is 890 nucleotides in length and encodes for NS1, an essential protein involved in combatting host innate immunity, and NEP/NS2 through RNA splicing (62, 70).

Replication cycle

Virus attachment: FLUAV infection initiates with virus recognition and attachment to N-acetylneuraminic acid (also referred to as sialic acids (SA)) on the surface of host cells, which are commonly located at the termini of numerous glycoconjugates (62, 64). The carbon-2 of the terminal SA can bind to the carbon-3 or carbon-6 of galactose forming two different linkages: α-2,3 or α-2,6-linkage (62). The globular head on the HA1 portion of the homotrimeric class I fusion glycoprotein HA contains the receptor-binding site (RBS), which recognizes the receptor on a target cell (71). It is well known that amino acid changes in the RBS and type of SA linkage can significantly influence host restriction and tissue tropism of FLUAVs (69, 72-74). SA with α-2,6-linkage predominates in the upper respiratory tract of humans, while α-2,3-linkage are commonly expressed on respiratory and intestinal epithelial cells of birds (72-74). Generally, HAs from avian FLUAVs possess a higher binding specificity to α-2,3-linked SA, while HAs from human FLUAVs prefer α-2,6-linked SA (73, 74).

Virus entry: HA-mediated binding to the host receptor initiates endocytosis in a clathrin-dependent manner or by macropinocytosis (64, 75). The FLUAV is then trafficked to the endosome (62, 64). The low pH activates the M2 ion channel and triggers a conformational change in the HA, allowing for the fusion of the viral envelope and the endosomal membrane (62, 64). The activation of the M2 ion channel leads to an increase of hydrogen ions within the virus particle, which then disrupts the protein-protein interactions leading to the release of vRNPs from M1 into the host cytoplasm (62). The vRNPs are then trafficked into the nucleus using viral proteins' nuclear localization signals and host cell machinery (62, 64, 76). Numerous studies showed that it takes approximately 10 min for virus entry and fusion but about 1 hour for FLUAV vRNPs to enter the nucleus from the cell surface (64, 77).

Transcription and replication of the viral genome: Synthesis of capped, polyadenylated messenger RNA (mRNA) and the vRNA segments used for progeny virus occurs within the nucleus (62). The viral RdRp uses the negative sense vRNA as a template to synthesize two types of positive sense RNAs: (1) mRNA copies used as a template for viral protein synthesis and (2) complementary RNA (cRNA) intermediates used as a template to transcribe additional negative-sense vRNA for progeny virus (62). Capping of the mRNA copies occurs through a process called "cap snatching"; the viral RdRp employs the PB2 subunit to bind to 5' capped primers (~12 nucleotides) from host pre-mRNA transcripts while the PA subunit endonuclease domain cleaves 10-13 nucleotides downstream (64). Meanwhile, polyadenylation of the viral mRNAs occurs through reiterative stuttering when the viral RdRp reads five to seven uracil residues encoded in the 5’ end of the negative-sense vRNA (62, 64). Once capped and polyadenylated, the viral mRNA is exported out of the nucleus and translated by host machinery within the cytoplasm (62, 64). Translation of the viral mRNAs for PB1, PB2, PA, NP, NS1, NS2, and M1 occurs by cytosolic ribosomes, while membrane proteins such as HA, NA, and M2 are translated by endoplasmic reticulum (ER)-associated ribosomes (64). Multiple proteins, including PB2, PB1, PA, and NP, are imported back into the nucleus to assist in additional viral mRNA transcription and vRNA replication; M1, NS1 (to inhibit host interferon signaling), and NS2 are also imported back into the nucleus, but the role for M1 and NS2 are unclear (64). Regarding replication of the FLUAV genome, the viral RdRp initiates the synthesis of the positive sense cRNA after complimentary base pairing in the 3’ end of the vRNA requiring no priming (64). As the cRNA exits the polymerase, NP molecules and a single copy of the viral polymerase will bind to the cRNA resulting in cRNP assembly (64). The cRNPs are then used as a template for synthesizing new negative-sense vRNAs, which bind to NPs, and a viral polymerase to produce new vRNPs for budding viruses (64).

Assembly and release. Localization of the vRNPs within the cytoplasm to the plasma membrane for viral assembly has been previously demonstrated to involve microtubules (78). It has been hypothesized that efficient vRNP transport consists of the movement of RNPs by the Rab11-dependent vesicular transport pathway because of interactions between PB2 and Rab11 (78). Additional studies suggest efficient virion packaging follows a mechanistic model in which specific recognition of vRNA segments is linked to efficient virion formation, contradicting the random-incorporation model (79). After assembly, FLUAV budding occurs at the plasma membrane and consequently binds to SA on the cell surface via HA activity (62). However, the NA protein cleaves terminal SA residues from glycoproteins and gangliosides on the cell surface to release virus progeny and limit aggregation of virus particles leading to an overall increase in virus replication and infectivity (62).

Respiratory Transmission

Transmission of respiratory viruses among humans occurs via two main mechanisms: contact between an infected and a susceptible individual or airborne transmission (29, 38). Contact transmission can be direct via physical contact or indirect contact with contaminated surfaces or objects (fomites) (26, 29, 38). Meanwhile, airborne transmission refers to when an infected individual expels infectious viral particles into the air, which then settle on the mucosa of a susceptible person (29). There are two main mechanisms of airborne transmission: respiratory droplets or small aerosol/droplet nuclei particles (26, 29). However, there is a lack of standardization in the terminology used to differentiate between respiratory droplets and aerosols, but it is generally based upon particle size (38). Particle size depends on the site of aerosol formation; the smaller the size, the deeper the respiratory tract the aerosols originate (80). Generally, respiratory droplet transmission, or droplet spray, is defined as having an aerodynamic diameter greater than 5 µm that is propelled at less than a meter distance to reach the mucosa directly (28, 29). Respiratory droplets are aerodynamically different from small aerosols and often emitted during coughing, sneezing, and talking (28, 29). Contrastingly, aerosols are defined as having an aerodynamic diameter smaller than 5 µm and can remain suspended in the air for longer periods due to the slow settling velocity (28, 29). Respiratory aerosols from healthy and infected individuals are generally expelled during breathing, talking, singing, shouting, coughing, sneezing, and feces (ex. toilet flushing) (29, 31, 38, 80-82). Aerosols can travel considerable distances from the infectious source (up to 3.7 m away), accumulate in poorly ventilated spaces, and be inhaled at short and long distances (28, 29, 80). While larger respiratory droplets settle on surfaces such as floors, walls, beds, etc., after droplet release because of gravity, aerosols diffuse and remain suspended indoors because they are too small to settle (28). Over time, virus aerosols will gradually deposit on environmental surfaces; however, the aerosols can be resuspended by human movement and continue to spread until the virus particles become inactive increasing infection risk (28). While the difference between respiratory droplets and aerosols has been historically based on a size distinction of 5 µm, it has recently been suggested that the size cutoff should be updated to 100 µm (80). At this size, the droplets and aerosols possess different aerodynamic behavior as 100 µm is the largest size in which a particle can remain suspended in the air for more than 5 seconds from a height of 1.5 meters, travel more than 1 meter from an infectious person, and be inhaled (80). When analyzing FLUAV spread, previous studies suggest that aerosol transmission is responsible for half of all FLUAV transmission events within a household setting, suggesting that aerosol transmission is an essential route for FLUAV spread (26).

While respiratory droplets and aerosols differ in aerodynamic properties, there are also multiple differences when analyzing viral loads and infectivity. Aerosols produced by numerous activities such as breathing and coughing have different aerosol size distributions and airflow velocities, which can impact the viral load, suspension time, distance traveled, and deposition location in the contact person (80, 83). For instance, viral load within aerosols expelled through speaking and other activities is much higher than respiratory droplets produced through coughing and sneezing (80). Aerosol size is a critical factor affecting survival and infectivity due to aerodynamic characteristic differences and variation of deposition site, which determines the site of infection (80). Aerosols up to 100 µm can be inhaled; particles with a diameter of 10-100µm are primarily deposited in the oropharynx, while particles 5-10 µm are deposited in the central airway (80, 84, 85). In comparison, aerosol particles < 5 µm can reach the lower respiratory tract, such as alveoli within the lungs (84, 85).

Other factors can affect deposition, including anatomical and physiological barriers, anatomical structure, breathing patterns, and respiratory mucus (80, 86). Within the respiratory tract, heavily glycosylated and sialylated mucins can form a barrier against glycan-receptor-binding viruses such as FLUAV (86). A balanced receptor-binding protein HA and receptor-cleaving protein NA are essential in virus motility in host mucus (87, 88). FLUAV binds dynamically to receptor-coated surfaces via HA, but NA activity drives directional rolling-type motility over the receptor surface (86, 88-90). Regarding deposition sites, the human respiratory tract can be broadly divided into three anatomical regions according to previous research:

1) Extrathoracic region (ET), 2) Tracheo-bronchial region (TB), and 3) Pulmonary region (P) (91). The ET is the respiratory tract entry site exposed to an array of aerosols and includes the naso-oro-pharyngo-laryngeal region (91). The TB consists of the trachea and the branching airways. The P region is the location of gas exchange consisting of alveolar ducts and sacs (91). The general population breathes through the nares at rest but switches to oral/nares breathing during heavy exercise (91). Therefore, aerosol particles can be inhaled through the nasal or oral passages (91). The inhalation ability decreases as the particle size increases (91). Experimental data showed that nearly 100% of particles smaller than 5 µm while only 50% of particles greater than 50µm could enter an individual through the nares and mouth (91). After airborne particles enter the respiratory tract through the nose or mouth, they can be deposited in different locations due to airflow and respiratory impediments such as bifurcations (91). Respiratory droplets may deposit in the upper respiratory system because of impaction, particularly in the oropharyngeal region, while deposition in the lower respiratory system is because of sedimentation (91). Meanwhile, aerosol particles may be deposited in the upper and lower respiratory tract areas by diffusion (91). Further, numerous studies have reported higher FLUAV vRNA loads in smaller aerosols of less than 5 µm compared to larger respiratory droplets (32, 33, 81, 92-94). While infectious FLUAV has been isolated from aerosols in symptomatic individuals, sampling and detecting viruses can be difficult because of the low concentration and destruction by aerosol samplers (28, 38, 80, 92, 95-97). Additional physicochemical properties, including pH, electrostatic charge, and other chemical components such as

electrolytes, proteins, and surfactants, can also influence the durability and outcome of the infectious aerosol (80).

Virus, host, and environmental factors can influence successful transmission because the air environment does not contain ideal conditions for FLUAV survival (28, 38). Previous literature has described aerosol virus decay in two stages: the first stage suggests about half of the virus is inactivated in the first few seconds after aerosol formation, and the second stage suggests that slower virus inactivation is affected by viral characteristics, host responses, and environmental factors such as temperature, relative humidity, and ultraviolet rays (28). The transmission efficiency is affected by virus stability under environmental stress, which is partially influenced by the structure and composition of the virus (38). FLUAV vRNAs have high mutation rates that contribute to viral infections with diverse genomic variants termed quasispecies, leading to faster adaptation for efficient aerosol transmission (98). However, not all FLUAV strains can efficiently infect mammalian hosts via aerosol. For example, a previous study suggested that an optimal ratio of HA to NA is needed for efficient respiratory droplet transmission and that loss of glycosylation at specific HA amino acid positions increases the transmissibility of avian FLUAV in mammalian species (99, 100). In addition, amino acid substitutions E627K and D701N in the PB2 enhanced polymerase activity and replication at 33°C (temperature in the human upper respiratory tract); these residues are commonly found in isolates that support aerosol transmission (101-103). The matrix gene has also been previously determined to be an essential factor in pH1N1 transmission in guinea pigs (104). In addition to virus particle characteristics, host determinants such as tissue and cellular tropism can also influence efficient transmission. Tissue-specific expression of receptors and glycosylation along the respiratory tract can affect the deposition and preferential route of infection (38). Studies analyzing pandemic FLUAV demonstrated that α 2,6- linked sialic acids (SA) preference was also a determinant of host adaptation and airborne transmission (105-107). α2,6-SA are prevalent on the surface of ciliated and goblet cells in the upper respiratory tract, while α2,3-SA are more abundant on the surface of non-ciliated bronchoepithileum cells and type II pneumocytes in the lower respiratory tract (107). Since HA from human influenza viruses preferentially bind to α2,6-SA while avian influenza virus HA preferentially binds to α2,3-SA, receptor distribution and compatibility is a critical determinant for transmissibility (108). In addition to host determinants, environmental factors such as temperature, relative humidity, UV radiation, materials of environmental objects, and airflow can also affect the efficacy of viral aerosol transmission. Temperature plays a crucial role in the survival and transmission of viruses in aerosols by potentially affecting protein, lipid, and vRNA stability (80). Previous reports showed that high temperatures can be detrimental to aerosol transmission and that the decay of aerosolized FLUAV increases with relative humidity (109-112). However, a study using a physiologically more relevant medium, such as material from the apical surface of differentiated human airway epithelial cells, remained highly stable in aerosols across multiple relative humidities ranging from 20% to 100% (113). UV radiation has been demonstrated to inactivate numerous airborne viruses, including FLUAV, by damaging genetic material; therefore, FLUAV would likely not be able to survive within the sunlight over long distances (114, 115). Indoor ventilation and directional airflow can also influence the transport of aerosols and contribute to greater dispersion distances; however, the airflow is constrained indoors by walls and ceilings (80). The indoor airflow depends on multiple factors, including the type of ventilation system, airflow patterns, change rate, and other air filtration systems (80). Additional research is needed to establish ventilation rates based on ventilation type to help mitigate the risk of FLUAV transmission.

Host factors

Human FLUAV infections present a wide range of clinical disease severity ranging from asymptomatic infection to death (9). Symptoms begin to increase as early as 1-day post inoculation and peak by day 2 or 3 post-infection (9). Symptoms are generally not observed by 8-9 days after infection (9). The most common symptoms include tracheobronchitis and pharyngitis within the upper respiratory tract, along with fever, malaise, and myalgia (9). On the other hand, severe symptoms include hospitalization with pneumonia, acute respiratory distress syndrome (ARDS), and death (9). Children, the elderly, pregnant women, and individuals with immunosuppression or chronic medical conditions are at higher risk of developing more severe diseases (116). Previous reports using murine models suggest that sex hormones may contribute to the disease severity of FLUAV in female mice compared with male mice (117, 118). In most mouse models, young adult female mice demonstrate more severe outcomes and increased pulmonary inflammatory response compared with male mice (117, 118). In addition to sex, previous mouse studies have shown that genetically obese mouse strains and diet-induced obese mice present with increased morbidity and mortality, including increased viral spread, decreased pulmonary function, severe pathology, and defective viral clearance during FLUAV infection; these results are consistent with clinical observations in humans as obese individuals account for most FLUAV-related hospitalizations (119, 120). On the other hand, malnourishment, particularly vitamin A, C, and D deficiency, and inadequate amounts of protein led to decreased mucosal antibody response in respiratory tissues and increased disease severity, respectively (119, 121, 122). Pregnancy has also been shown to be a risk factor in animal models as pregnant mice infected with FLUAV during mid-gestation present with higher viral loads, increased lung pathology, severe pneumonitis, lung edema, cytokine storm and reduced regeneration of epithelial cells within the lung (123-125). In addition, age groups such as the very young and the elderly, are at the highest risk for severe disease (119). The higher risk in children has been hypothesized to be caused by having no pre-existing immunity and a lack of sex hormones (126). Alternately, the positive correlation between morbidity and age is likely because of immunosenescence and increased incidence of other comorbidities (127). In addition to enhanced disease severity, comorbidities, sex, age, and pregnancy have also been associated with increased single nucleotide polymorphisms (SNPs) in the FLUAV genome because of a less stringent selective environment promoting variants with increased pathogenicity (119, 124). Influenza pathogenesis severity involves the complex relationship between host and viral factors, notably the immune response.

Role of the microbiome in FLUAV infections

The respiratory and intestinal microbiota can directly impact host cells or indirectly impact the immune system during viral infections (45, 46). The human microbiome consists of more than a trillion microorganisms interacting in a complex ecosystem throughout the human body, including the intestine, skin, mucosal surfaces, lungs, and many more (47, 48). The bacterial, viral, and fungal residential microbes play an essential role in various host functions, including metabolism, development, regulation of the immune response, and physical defenses against invading pathogens (47). Generally, the microbiome can present antiviral activity through four main mechanisms: 1) Enhanced mucosal barriers, 2) production of antimicrobial compounds, 3) inhibit virus attachment, and 4) modulation of the immune response (1). Multiple biological and environmental factors such as sex, age, nutrition, and disease status can affect the diversity and abundance of bacteria associated with good health leading to dysbiosis (48, 51, 52).

Respiratory microbiome alterations during FLUAV infections

The respiratory microbiome has been previously understudied compared to the intestine, mainly because of the previous dogma of lung sterility. Historical understanding considered healthy lungs to be sterile or free from bacteria; however, reports from 2010 showed evidence of bacteria within the lungs using culture-independent techniques (128-130). While earlier studies debated if the detected bacterial DNA was real or contaminated, there is a current consensus that the lungs are not sterile and harbor microorganisms that exist in healthy individuals and those suffering from respiratory disease (128, 130, 131). Compared to the lower intestine, which averages 10^{11} to 10^{12} bacteria per gram of tissue, the lung averages 10^3 to 10^5 bacteria per gram of tissue (132, 133). The epithelial surfaces of the trachea and bronchi are lined with mucus, while the alveoli of the lungs are lined with a surfactant that has been previously demonstrated to inhibit the growth of gram-negative bacteria (134). Due to the mucosal immunity within the respiratory tract, a constant balance of tolerance for commensal microbes and immune response toward pathogens is needed (135). In healthy individuals, bacteria migrate into the lungs by mucosal dispersion and micro-aspiration from the upper respiratory tract, further supported by recent culture-independent studies (136-138). Multiple reports suggest minimal spatial microbial diversity in the lungs compared to the upper respiratory tract by showing that the lung microbiome primarily resembles the oropharynx in adults and the nasopharynx and oropharynx in children (137, 138). The data support the hypothesis that the healthy lung microbiota is composed of transient microorganisms derived from the upper respiratory tract instead of containing a residential community like what is observed in chronic respiratory diseases (139). Further, a recently proposed ecological model, “the adapted island model,” suggests that the lung microbiome in healthy individuals is more influenced by immigration and elimination than by local ecological conditions on bacterial reproduction, which are more influential in lung disease (140). The origin and function of the lung microbiome are unclear; however, multiple studies have used gnotobiotic animal models to investigate direct correlations and various contributions of the lung microbiome in protecting from invading pathogens, shaping and modulating the immune system, and nutrient uptake

(133, 141, 142). In healthy adults, common microbes within the nasal cavity include Actinobacteria, such as *Corynebacterium* spp., *Propionibacterium* spp., Firmicutes, such as *Staphylococcus* spp., and Proteobacteria (135). The oropharynx consists of Firmicutes, Proteobacteria, and Bacteroidetes, such as *Streptococcus, Neisseria, Haemophilus,* and *Lachnospira* spp. while *Streptococcus, Staphylococcus, Corynebacterium*, and *Prevotella* are within the nasopharynx (135). Meanwhile, the lung microbiome is characterized by a diverse bacterial community present in low abundance, with the most prominent phyla as Bacteroidetes and Firmicutes and predominant genera including *Prevotella, Veillonella,* and *Streptococcus* within humans (130, 131, 143). When in a healthy state, the microbial richness is reduced in the lower respiratory tract compared to the upper respiratory tract; however, individuals with respiratory infections or diseases such as chronic obstructive pulmonary disease (COPD) have increased bacteria within the lungs and differences within the relative abundance of notable species (135). The relationship between respiratory viral infections and changes within the residential microbial communities is currently being investigated further.

FLUAV infection in humans – Numerous recent studies observed differences in the respiratory microbiota among healthy and chronic pulmonary disease patients suggesting that residential pulmonary microbes may play a role in the pathogenesis of viral respiratory infections (144). Within children infected with FLUAV, the diversity of the nasopharyngeal microbiota increased along with a reduction of commensal microbes such as *Moraxella, Staphylococcus, Corynebacterium,* and *Dolosigranulum,* while *Streptococcus* was increased (145, 146). Further, *Prophyromonas* spp., *Fusobacterium* spp., *Lachnospiracea* spp., *Veillonella* spp., *Prevotella* spp., *Granulicatella* spp, *Streptobacillus* spp., and *Haemophilus* spp. were associated with severe FLUAV infection in children (147). In a different study, FLUAV and FLUBV infections were also associated with significantly different nasopharynx microbial compositions in adults compared to healthy controls, including enrichment of *Dolosigranulum*, *Staphylococcus,* and *Moraxella* spp. (148). Further, the administration of a live-attenuated influenza virus (LAIV) vaccine led to significant changes within the nasal microbial structure, diversity, and taxonomy with an increase in *Staphylococcus* and *Bacteroides* genera (149). However, another study showed that experimental H3N2 challenge of healthy adult volunteers led to no significant differences over time; this was potentially explained because of the observed mild disease within the healthy individuals (150). Utilizing data from a household transmission study, the naso/oropharyngeal microbiota composition was associated with decreased susceptibility to FLUAV infection, particularly with relative abundances of *Alloprevotella*, *Prevotella,* and *Bacteroides* (151). Moreover, higher bacterial diversity within the nose/throat was associated with longer shedding duration and earlier time of infection, specifically the relative abundance of *Neisseria* (152). While human clinical samples are very informative, the human microbiome is highly variable and impacted by diverse environmental conditions. This complicates analysis and contributes to inter-individual variation of human population studies (153). Therefore, analyzing the respiratory microbiome of an animal model in a controlled environment is beneficial in understanding the relationship between FLUAV and the host microbiome.

FLUAV infection in animal models – Multiple animal models have been used to investigate the role of the respiratory microbiome and FLUAV infection, including mice, ferrets, chickens, and pigs. In mice, respiratory microbiome changes during FLUAV infection displayed reduced abundances of *Alphaproteobacteria* and increased abundances of *Gammaproteobacteria*, *Actinobacteria*, and facultative anaerobes such as *Streptococcus* and *Staphylococcus* (154). Due to the similar physiology between the upper respiratory tract of humans and ferrets, ferrets are an ideal model for studying FLUAV infection (155). A previous study analyzed the similarities between a human cohort and ferrets experimentally infected with FLUAV (155). The study showed a robust microbial consistency among the two hosts suggesting that ferrets are a representative model for studying microbiome changes during FLUAV infection (155). In addition to ferrets, a positive correlation between FLUAV H3N2 viral load and enrichment of Neisseriaceae was observed within the nasal microbiota of pigs; however, the bacterial richness remained stable after infection (156). While the upper respiratory tract has been more extensively studied, especially in humans, the microbiome changes within the lower respiratory tract, particularly the lungs, have been investigated in mice. Significant changes within the lung and BALF were observed in the acute (7 days post-infection (dpi)), convalescent (14 dpi), and recovery (28 dpi) stages post-FLUAV H1N1 inoculation. This included shifts from Alphaproteobacteria to Gammaproteobacteria and Actinobacteria and an increase of anaerobes and facultative anaerobes, including *Streptococcus* and *Staphylococcus* in infected mice (154). It has also been shown that *Staphylococcus epidermidis*, a common gram-positive commensal bacterium, can suppress FLUAV infectivity partially by using a giant extracellular matrix-binding protein *in vitro* and *in vivo* in chickens through stimulating interferon-related innate immune responses (157). Further, *S. epidermidis* has been shown to prevent FLUAV replication in the nasal mucosa and lungs by decreasing the expression of serine proteases by inducing Serpine1 in mice (158). Priming with *Staphylococcus aureus* has also been shown to attenuate FLUAV-mediated immune pathogenesis within the lungs by recruiting peripheral CCR2+CD11b+ monocytes that polarize M2 alveolar macrophages (159). In addition to the direct effects of commensal bacteria, activation of type III interferon in response to FLUAV infection has been shown to have a major impact on the upper respiratory microbiome and thus increasing susceptibility to secondary bacterial infections within the lower respiratory tract in mice (160).

Intestinal microbiota influences host responses to FLUAV infections

While the potential for respiratory diseases to impact the residential microbiome is clear, many studies have also observed impacts on the intestinal microbiome during respiratory infections. The intestine is the most colonized bacterial organ, with a bacterium-to-host cell ratio of 1:1 (48, 161). While both the intestinal tissues and the lungs are luminal organs with a mucosa lining, microbes in the intestine must survive acidic pH in the stomach and alkaline pH in the duodenum (162). The intestine remains at a consistent internal body temperature of 37°C in a primarily anaerobic state (163, 164). Previous studies described that a healthy adult intestinal microbiota consists mainly of *Roseburia*, *Enterococcus*, and *Faecalibacterium* belonging to the phyla Firmicutes, and *Bacteroides* and *Prevotella* belonging to the phyla

Bacteroidetes (165, 166). The gut microbiota has been shown to affect the immune system within the lungs through the gut-lung axis. Previous studies have demonstrated the essential role of commensal gut microbes in antiviral responses within the lungs, such as type I interferon receptors in respiratory epithelial cells (47). Type I interferon receptors respond to viral infections via IFN-α and IFN-β production resulting in restricted viral replication (167). Proposed mechanisms on how the intestinal microbiota impact respiratory mucosal immunity include: 1) mucosal tissue from the gastrointestinal tract can influence distant mucosal sites such as the lungs, 2) cytokines and other by-products such as growth factors secreted within the intestinal tract in response to commensal microbes can enter circulation and act on the respiratory mucosal tissues, 3) microbial-associated molecular patterns (MAMPs) can be absorbed in other intestinal tissues and activate pattern recognition receptors thus influencing innate immune response, 4) microbiota metabolites such as short-chain fatty acids, can be absorbed in the intestinal mucosa and can then modulate innate immune responses (47). Viral pathogens that infect or replicate in mucosal tissues most likely encounter commensal microbiota inhabiting the mucosal surfaces. Therefore, the intestinal microbiota can either promote viral infections, such as poliovirus, reovirus, and certain retroviruses, or have a protective role, such as with FLUAV and rotavirus (53, 54).

FLUAV infection in humans – Fecal microbial changes within human patients after FLUAV infection showed a significant decrease in diversity compared to healthy controls that were disease-specific shifts compared to Coronavirus disease 19 (COVID-19) infection (168). Taxonomic changes within this cohort included a reduction in bacteria belonging to anaerobic butyrate-producing bacteria from families Lachnospiraceae and Ruminococcaceae, specifically *Blautia*, *Agathobacter*, *Anaerostipes*, *Fusicatenibacter*, *Eubacterium hallii* group, unclassified Lachnospiraceae, *Dorea*, *Faecalibacterium* and *Ruminococcus-2* (168). On the other hand, the fecal microbiome of FLUAV patients was dominated by *Enterococcus, Prevotella, Finegoldia,* and *Peptoniphilus,* while six biomarkers, including *Fusicatenibacter*, *Romboutsia, Anaerostipes, E. hallii group, Ruminococccus torques* group, and *Blautia* were identified as selective differentials for FLUAV H1N1 patients (168). Further, differential abundance testing in a different cohort suggested that fecal microbiota changes differed among FLUAV and FLUBV and that relative abundances of *Bacteroides fragilis* were significantly higher in individuals that shed virus compared to non-shedders (169).

FLUAV infection in Animal Models- Like the respiratory tract, an array of animal models has been used to investigate the role of the intestinal microbiome during FLUAV infection, including mice, chickens, and pigs. Within the murine model, FLUAV H1N1, H3N2, and H5N1 FLUAV infections have been associated with dysbiosis in the gut microbiota (52, 170-173). A previous study also showed that pulmonary-induced IFN-Is led to the enrichment of Proteobacteria and depletion of obligate anaerobic bacteria, inhibiting antimicrobial and inflammatory responses and further enhancing secondary *Salmonella* intestinal colonization and systemic spread (170). Additionally, intestinal commensal microbes, specifically neomycin-sensitive bacteria, regulate the generation of virus-specific CD4 and CD8 T cells and antibody responses within the lung post-FLUAV infection in mice (174). FLUAV infection also induces bacterial depletion, disruption of mucus integrity, and promotes higher levels of antimicrobial peptides produced in Paneth cells within the small intestine of mice (172). FLUAV-mediated intestinal depletion led to increased susceptibility to secondary bacterial invasions such as *Salmonella enterica* serovar Typhimurium (172). Mechanistically, a recent study showed that sublethal infection of H1N1 and H3N2 FLUAV was associated with cecal and intestinal dysbiosis with reduced production of short-chain fatty acids (SCFA) (173). The alterations to the microbiota compromised the pulmonary immune response against a secondary *Streptococcus pneumoniae* infection, which was directly demonstrated by a fecal microbial transplant (173). The effect on the immune response was due to the decreased production of acetate, which further altered the bactericidal activity of alveolar macrophages (173). SCFA supplementation during FLUAV infection further reduced the translocation of *Salmonella* and reduced the mortality of mice infected with both pathogens (173, 175). It was further demonstrated that TLR5 sensing of flagellated microbes in the intestine increased antibody responses post-influenza virus vaccination, and oral administration of gut microbe *Akkermansia muciniphila* reduced weight loss and mortality during HPAIV in mice (176, 177). It was also reported in antibiotic-treated mice that the intestinal microbiota regulates local and systemic IFN-I response via IFN-β secretion of colonic immune cells (178). In addition to mice, previous studies examined the importance of the microbiome in response to LPAIV infection in chickens. Chickens infected with LPAIV showed an intestinal microbiome population shift, including increased *Escherichia coli* and decreased probiotic organisms like *Lactobacillus* or *Enterococcus* (179, 180). Further, similar studies reported that the absence of commensal gut microbes in chickens increased virus shedding and compromised immune responses such as down-regulation of type I interferon responses toward LPAIV infection, suggesting the importance of the intestinal microbiome in battling influenza infection (181). Further, chickens treated with probiotics or received a fecal microbial transplant after antibiotic depletion of the intestinal microbiome had significantly higher virus-specific IgM and IgG titers compared to antibiotic-depleted chickens, suggesting that the composition of the gut microbiota in chickens may result in antibody immune response changes to FLUAV (182). Similar results were observed in pigs as FLUAV infection led to altered microbial richness and diversity with increased abundances of Prevotellaceae while Clostridiaceae and Lachnospiraceae were decreased (51). Conclusively, multiple studies suggest the role of the commensal intestinal microbiome during FLUAV infection by altering the host immune response within humans and multiple animal models.

SARS-CoV-2

Classification

Severe acute respiratory syndrome 2 virus (SARS-CoV-2) is an enveloped positive-sense single-stranded RNA virus belonging to the subfamily *Coronavirinae* within the family Coronaviridae in the order Nidovirales (183). Coronavirinae is further divided into four genera: *Alphacoronavirus*, *Betacoronavirus*, *Gammacoronavirus*, and *Deltacoronavirus* (183). Alphacoronaviruses and betacoronaviruses infect mammals, while the gammacoronaviruses and deltacoronaviruses infect primarily birds but can also infect mammals (183). Seven coronaviruses have been associated with human coronaviruses (HCoV) (9). Four coronaviruses, including HCoV-229E, HCoV-OC43, HCoV-NL63, and HCoV-HKU1, cause seasonal and predominantly mild respiratory symptoms, often associated with symptoms of the "common cold" and thus go under-reported (39). However, severe acute respiratory syndrome (SARS-CoV), Middle East respiratory syndrome coronavirus (MERS-CoV), and SARS-CoV-2 are highly pathogenic that can develop into severe respiratory disease (39). Bioinformatic analyses showed that SARS-CoV-2 belongs to betacoronavirus 2B lineage and shares 79.5% sequence identity with SARS-CoV; however, the closest relationship of SARS-CoV-2 at 96% identity was to a bat SARS-like coronavirus strain BatCov RaTG13 (184).

Virion structure

Coronaviruses have the largest genome among RNA viruses, flanked by 5’ and 3’ untranslated regions containing cis-acting RNA structures utilized for RNA synthesis (9, 39). The genome of SARS-CoV-2 consists of ~30 kb encoding 14 open reading frames (ORF); two-thirds correspond to 16 nonstructural proteins (nsp1-16), while one-third contain nine accessory proteins and four structural proteins (41). Fifteen nonstructural proteins generate the viral replication and transcription complex, including the RNA-processing and RNA-modifying enzymes and RNA proofreading function (39). Meanwhile, the function of the accessory proteins is largely unknown (39). The four structural proteins include spike, envelope, membrane, and nucleocapsid (41). The RNA genome is encapsulated by the nucleocapsid and then surrounded by the membrane and envelope (39). Similar to HA in FLUAV, homotrimeric class I fusion protein spike extends from the host-derived viral envelope for cellular entry (41). Spike encodes a receptor-binding domain that interacts with the host angiotensin-converting enzyme 2 (ACE2) receptor for cellular entry (41). Spike is divided into two distinct parts: S1 contains the receptor binding domain that binds to the host cell receptor, while the transmembrane S2 domain contains heptad repeat regions and mediates the fusion of viral and cellular membranes (39). An S1/S2 polybasic cleavage site is then proteolytically cleaved for entry at the plasma membrane surface by transmembrane protease serine 2 (TMPRSS2) or in the endosome by cathepsin L (41).

Replication cycle

Replication of SARS-CoV-2 initiates through the binding of spike to the host receptor ACE2 (41). The S1/S2 site is cleaved by surface TMPRSS2 and/or endolysosomal cathepsin L, enabling membrane fusion of the virus and cell at the surface or endosomal compartment (41). The RNA genome is then released into the cytosol and uncoated for immediate translation of the ORF1a and ORF1b, resulting in the polyproteins pp1a and pp1b (39, 41). These proteins are co-translationally and post-translationally processed into sixteen nonstructural proteins (nsp1-11 from pp1a and nsp1-10, nsp12-16 from pp1b) post-proteolytic cleavage by proteases located within nsp3 and nsp5 (39, 41). Proteolytic cleavage of nsp1 leads to the utilization of host translational machinery, while nsp2-16 makes up the viral replication and transcription complex (39). Virus replication occurs in virus-induced perinuclear double-membrane vesicles (DMVs) created from the endoplasmic reticulum (ER), convoluted membranes (CMs), and small open double-membrane spherules (DMSs) (39, 41). These provide a protective micro-environment for viral genomic RNA replication and transcription of subgenomic mRNAs (sg mRNA) (39, 41). The positive-stranded genome serves as a template for full-length negative-strand RNA and sgRNAs (39, 41). The translation of the sg mRNAs results in structural and accessory proteins, which are then translocated into the ER membrane and inserted into the ER-Golgi intermediate compartment (ERGIC) (39, 41). Within the ERGIC, the proteins interact with the nucleocapsid and newly produced genomic RNA for virion assembly and budding into the lumen of secretory vesicular compartments (39, 41). The virions are then secreted from the plasma membrane by exocytosis (39, 41).

Pathogenesis and host factors

SARS-CoV-2 infection causes coronavirus disease 2019 (COVID-19), which can present a wide range of disease severity from asymptomatic to death (9). Symptoms are generally observed 4.8 days after exposure, and 95% of symptomatic patients will present with symptoms by 14 days after exposure (9). The most common symptoms include cough, fever, myalgia, shortness of breath, and headache (9, 185). Less frequent symptoms include sore throat, diarrhea, nausea, chest pain, chills, and loss of smell and taste (9, 185). Severe symptoms can include dyspnea, ARDS, acute cardiac injury, and multi-organ failure (185). Pathogenesis of severe disease includes diffuse alveolar damage, deposition of proteinaceous alveolar fluid compromising gas exchange with increased type II pneumocytes, and interstitial oedema within the lungs (9). Inflammation and neutrophil infiltration within the lower respiratory tract are also commonly observed in severe infections (9). Immunohistochemistry staining of SARS-CoV-2 is observed within alveolar pneumocytes, ciliated epithelial cells within the lungs, and epithelial cells within the kidney (9). SARS-CoV-2 particles have also been observed in enterocytes within the intestine by electron microscopy, and viral RNA has been detected within the lung, kidney, large intestine, blood, spleen, heart, and pulmonary tissues (9). Several risk factors for severe disease have been observed in genome-wide association and epidemiological studies. Metabolic disorders such as diabetes, obesity, and kidney disease have been associated with increased disease severity along with cardiovascular conditions, including hypertension, congenital heart disease, and coronary artery disease (9). Sex has also been shown to be a risk factor for severe disease. A recent study showed within the US that males were more likely to test positive for COVID-19, have more complications, require ICU admission and mechanical ventilation, and have higher mortality than females (186). While all ages are susceptible to infection, elderly individuals (above 60 years of age) are more likely to develop severe respiratory disease, including ARDS leading to prolonged hospitalization (9, 185).

Microbiome changes during SARS-CoV-2 infections

While multiple studies examined residential microbiome changes in response to FLUAV, recent literature has focused on the effect of SARS-CoV-2 on the microbiome in nasopharyngeal and fecal samples, mainly because numerous studies have observed vRNA in the feces of infected individuals and occasional gastrointestinal upset during infection (187, 188). Further, patients with gastrointestinal symptoms are likely to be more susceptible to symptoms including fever, fatigue, shortness of breath, and headache (168). Numerous studies have shown that the host respiratory and intestinal microbiome is disturbed during SARS-CoV-2 infection. It has also been suggested that the intestinal microbiome may be closely related to ACE2 expression (189). A previous study showed that colonic ACE2 expression was significantly decreased in the presence of established intestinal microbiota in a humanized mouse model and rats compared to animals with depleted intestinal microbes (190, 191). While specific interactions between specific bacterial species and SARS-CoV-2 pathogenesis is lacking, there is indirect evidence that the respiratory and intestinal microbiota may have a role in the overall severity of COVID-19.

Respiratory microbiota and SARS-CoV-2 infections

SARS-CoV-2 infection in humans – Within the upper respiratory tract, a study analyzing mild COVID-19 patients showed no significant difference in richness and diversity compared to uninfected controls (192). However, another cohort showed that older patients displayed decreased microbial diversity, suggesting an age-dependent dysbiosis in the pharyngeal microbiome (193). Meanwhile, *Acinetobacter, Brevundimonas, Burkholderia, Chryseobacterium, Sphingobium* species, and Enterobacteriaceae were the most prevalent within the lung of 20 fatal COVID-19 patients (194). A study analyzing bronchioalveolar lavage fluid (BALF) from patients with COVID-19, community-acquired pneumonia, and healthy individuals showed that the microbial composition of patients with COVID-19 was comparable to those with pneumonia (195). Multiple co-bacterial-infections in COVID-19 patients have also been observed, including *Streptococcus pneumoniae, Staphylococcus aureus, Klebsiella pneumoniae, Haemophilus influenzae, Mycoplasma pneumoniae, Acinetobacter baumanni, Legionella pneumophila* and *Chlamydia pneumoniae* (196). Viral co-infections include influenza, coronavirus, rhinovirus/enterovirus, parainfluenza, metapneumovirus, and human immunodeficiency virus (196). Secondary bacterial infections have been understood to be caused by the outgrowth of opportunistic bacterial pathogens already residing within the host (196); therefore, understanding the possible mechanisms of bacterial co-infections and COVID-19 may contribute to potential preventative measures for SARS-CoV-2 patients during the pandemic.

SARS-CoV-2 infection in animal models – While numerous studies analyzed the relationship between SARS-CoV-2 and the respiratory microbiome in humans, limited research has been conducted in animal models. A previous study from our group examined the diversity and taxonomic classification of the lungs in K18-hACE2 mice, a transgenic mouse model expressing human ACE2 under the control of the epithelial cell cytokeratin-18 promoter, challenged with SARS-CoV-2 (197). Limited alpha and beta diversity differences were observed when comparing control mice to mice challenged with a low or high dose of SARS-CoV-2, which resembles observations of FLUAV infection in mice (197). However, within-group variance increased in an infectious-dose-dependent manner, consistent with the Anna-Karenina model of disease-induced dysbiosis (197). Firmicutes and Proteobacteria were enriched in the high-and low-virus-dose SARS-CoV-2 mice compared to that in the mock controls, consistent with previous reports of patients infected with influenza virus (197). An additional study showed that alveolar microbes could increase translation and reduce amino acid metabolism of a compound RS5645, which was shown to attenuate the pulmonary hyper-inflammatory response induced by SARS-CoV-2 spike protein (198). Further, supplementation of cultured oral bacteria from a healthy volunteer administered with an intranasal SARS-CoV-2 spike protein vaccine significantly increased the production of vaccine-specific nasal IgA and serum IgG response and resulted in reduced viral titers within the lungs of SARS-CoV-2 challenged hamsters (199); these results were also demonstrated when testing a quadrivalent HA vaccine in mice (199).

Intestinal microbiota and effects on SARS-CoV-2 infection

SARS-CoV-2 infection in humans – Overall, fecal microbiome studies reported a decrease in the intestinal microbiota diversity and abundance in SARS-CoV-2 patients compared to controls (168, 200, 201). Further, prolonged gastrointestinal symptoms such as diarrhea were inversely correlated with decreased intestinal richness and diversity and associated with delayed SARS-CoV-2 clearance and immune dysregulation (47, 168). Multiple bacterial genera associated with opportunistic pathogens such as *Streptococcus*, *Rothia, Veillonella, Erysipelatoclostridium, Actinomyces, Collinsella,* and *Morganella* had increased relative abundance in fecal samples collected from SARS-CoV-2 patients compared to controls within a cohort in China (168, 200). Patients also showed a decrease in the relative abundance of *Faecalibacterium prausnitzii* and *Bifidobacterium bifidum*, which produce butyrate, an SCFA that influences the proliferation and differentiation of intestinal epithelial cells (200). In a group of hospitalized patients, the relative abundance of *Coprobacillus, Clostridium ramosum,* and *Clostridium hathewayi* positively correlated with COVID-19 severity, while *Faecalibacterium prausnitzii* was inversely correlated with severity (200). Further, intestinal dysbiosis was observed post-symptoms and SARS-CoV-2 detection (200). In another study, patients with elevated SARS-CoV-2 vRNA demonstrated increased relative abundance of *Collinsella aerofaciens, C. tanakaei, Morganella morganii*, and *Streptococcus infantis*; on the other hand, *Slistipes onderdonkii, Bacteroides stercoris, Lachnospiraceae bacterium*, and *Parabacteroides merdae* were enriched in patients with decreased SARS-CoV-2 vRNA (201). A recent study also showed that fecal microbial differences depended on the severity of the COVID-19 disease (202). Severe COVID-19 patients displayed a greater abundance of opportunistic pathogens, while butyrate-producing groups of bacteria were depleted compared with mild and moderate cases (202). Further, dysbiosis of the intestinal microbiome was associated with pro-inflammatory cytokines, including an increase in *Bacteroides* and Enterobacteriaceae and decreased *Bifidobacterium, Streptococcus*, and *Collinsella* (203). Interestingly, individuals with mild disease mount an immune response characterized by CD8+ T cells and Th1 cells, while severe/critical patients display a dysregulated hyperinflammatory response (203).

SARS-CoV-2 infection in animal models – The intestinal and fecal microbiota of numerous animal models, including mice, hamsters, and nonhuman primates, have been investigated in relation to SARS-CoV-2 infection. Our group previously reported that K18-hACE2 mice challenged with low and high doses of SARS-CoV-2 showed decreased alpha diversity and dissimilar beta diversity measurements compared to the control mice (197). Phyla, including Firmicutes, specifically Lachnospiraceae and Oscillospiraceae, were significantly less abundant, while Verrucomicrobia, particularly Akkermansiaceae, were more prevalent during peak infection in mice challenged with a high dose of SARS-CoV-2 (197). Another study showed alpha and beta diversity differences between vaccinated and infected K18-hACE2 mice, which was also observed in humans (202). Notably, unvaccinated mice displayed a significant increase in abundance of *Odoribacter* and *Akkermansia muciniphia* and depletion of *Lactobacillus reuteri* and *Bacteroides uniformis* (202). A study using germ-free, conventional pathogen-free, and gnotobiotic mice showed the intestinal microbiome is associated with ACE2 expression within the respiratory and digestive tract; in particular, respiratory and intestinal ACE2 expression was significantly increased in germ-free mice and gnotobiotic mice (204). Intestinal microbiota differences have also been studied in golden Syrian hamsters, which were previously described to mirror human clinical symptoms and pathogenesis of COVID-19 (205). Fecal samples from male Syrian hamsters challenged with SARS-CoV-2 displayed progressive alterations of the bacterial composition, including reduction of bacteria associated with SCFA production, including Ruminocacaceae and Lachnospiraceae, while harmful bacteria such as Enterobacteriaceae and Desulfovibrionaceae were enriched (206). These results were further related to an overall decrease in SCFA levels in the blood during infection (206). These effects were also examined within an obese hamster model with nonalcoholic steatohepatitis due to the increased risk of developing more severe symptoms of COVID-19 (207). Lean hamsters showed more prominent changes with the fecal microbiota at 4 days post-infection, while dysbiosis persisted until day 10 within obese hamsters (207). Pathological differences, including more severe lung and liver inflammation, were also observed within the obese hamster compared to the lean (207). Taxa such as *Blautia* and *Peptococcus* were associated with pro-inflammatory markers within the lungs and liver in obese hamsters infected with SARS-CoV-2 (207). In addition to hamsters, significant changes in the fecal microbiota composition 10-13 days post-SARS-CoV-2 infection were observed in nonhuman primates (208). Specifically, several bacteria part of the Proteobacteria phylum, such as those within the genus Acinetobacter, were abundant early in infection (208). Meanwhile, Gammaproteobacteria, Betaproteobacteria, and Deltaproteobacteria were more abundant later (10-13 dpi) in infection (208). Several bacteria also correlated with SARS-CoV-2, particularly Acinetobacter and Peptostreptococcaceae (208). Comprehensively, the residential microbiota, along with the immune system within humans and animal models, plays an important role when combatting respiratory viral infections, notably FLUAV and SARS-CoV-2.

CHAPTER 3

CHARACTERIZATION OF AN IN VITRO MODEL SYSTEM TO STUDY AEROSOL TRANSMISSION OF INFLUENZA VIRUS

Brittany Seibert, C. Joaquin Caceres, Matias Cardenas, L. Claire Gay, Brianna Cowen, Stivalis Cardenas-Garcia, Flavio Cargnin Faccin, Ginger Geiger, Jong Suk Mo, Lisa Stabler, Silvia Carnaccini, Daniela Rajao, and Daniel R. Perez.

To be submitted to *Plos One.*

Abstract

Aerosol transmission of influenza A viruses (FLUAV) is an essential mode of FLUAV spread among humans; however, numerous *in vitro* and *in vivo* studies use a liquid inoculum for virus infection. To better replicate natural infections *in vitro*, we generated a calm-aerosol settling chamber system that is easy to assemble, cost-effective, and designed to examine the aerosol infectivity of FLUAV viruses in different cell types. Aerosol infection and calculation of the aerosol infectious dose 50 were characterized for a pandemic H1N1, seasonal swine H3N2, and avian H9N2 FLUAV using this exposure system. While all three viruses displayed high replication within MDCK cells via liquid inoculation, differences in infectivity were observed via aerosol inoculation. This was further observed in differentiated human airway epithelial cells (BCi-NS1.1) cultured in an air-liquid interface. These results suggest that this system can be utilized to expand the current knowledge on molecular virological markers that influence FLUAV respiratory transmission in conjunction with *in vivo* studies for pandemic risk assessment of circulating FLUAV strains.

Introduction

Various respiratory viruses have been identified to infect humans. Notably, viruses within *Orthomyxoviridae, Coronaviridae,* and *Paramyxoviridae* can cause recurrent epidemics associated with severe disease and zoonotic transmission from animals to humans (29). Influenza A viruses (FLUAV), classified within the *Orthomyxoviridae* family, results in seasonal epidemics in the global population that is controlled by annual vaccination; however, occasional zoonotic transmission of FLUAV can potentially lead to a pandemic outbreak affecting millions of individuals worldwide. Generally, zoonotic events are restricted to sporadic primary individual cases; however, influenza viruses from other species can acquire the ability to transmit between humans and lead to the start of a pandemic (29). Four major pandemics have been documented in the past century, including the 1918 H1N1 Spanish Influenza pandemic, the 1957 H2N2 Asian Influenza pandemic, the 1968 H3N2 Hong Kong Influenza pandemic, and the 2009 H1N1 pandemic (pH1N1) in which animal-origin viruses became transmissible among humans (29). Only H1-H3 FLUAV subtypes have obtained efficient human-to-human transmission and become endemic; however, sporadic human infections with H5, H7, and H9 avian influenza viruses (AIV) have been reported (209). Understanding the processes involved in FLUAV transmission between hosts, particularly aerosol transmission, can aid in performing studies analyzing pandemic risk assessment to help direct public health preparedness.

Current literature indicates two primary modes of FLUAV transmission, including contact between an infected and a susceptible individual or airborne transmission (29, 38). Contact transmission can be direct, by transferring infectious particles via physical contact, or indirect, by contaminated surfaces or objects (fomites) (26, 29, 38). Meanwhile, airborne transmission refers to when an infected individual expels infectious viral particles into the air, which then settle on the mucosa of a susceptible person (29). Two main mechanisms of airborne transmission are respiratory droplets or small aerosol/droplet nuclei particles (26, 29). The differentiation between the two mechanisms is generally based on particle sizes; however, standardization of the terminology is lacking (38). Generally, respiratory droplet transmission, or droplet spray, is defined as having an aerodynamic diameter greater than 5µm that is propelled at less than a meter distance to reach the mucosa directly (28, 29). Respiratory droplets are aerodynamically different from small aerosols and often emitted during coughing, sneezing, and talking (28, 29). Divergently, aerosols are defined as having an aerodynamic diameter smaller than 5 µm and can remain suspended in the air for more extended periods due to the slow settling velocity (28, 29). Respiratory aerosols from healthy and infected individuals are generally expelled during breathing, talking, singing, shouting, coughing, sneezing, and feces (ex. toilet flushing) (29, 31, 38, 80-82). While larger respiratory droplets settle on surfaces such as floors or walls after droplet release because of gravity, aerosols diffuse and remain suspended indoors and travel considerable distances from the infectious source (up to 3.7 m away), accumulate in poorly ventilated spaces and can be inhaled at short and long distances (28, 29, 80).

While respiratory droplets and aerosols differ in aerodynamic properties, there are also multiple differences when analyzing viral loads and infectivity. Aerosols produced by numerous activities such as breathing and coughing have different aerosol size distributions and airflow velocities, which can impact the viral load, suspension time, distance traveled, and deposition location in the contact person (80, 83). Aerosols up to 100 µm can be inhaled; particles with a diameter of 10-100 µm are primarily deposited in the oropharynx, while particles 5-10 µm are deposited in the central airway (80, 84, 85). In comparison, aerosol particles < 5 µm can reach the lower respiratory tract, such as alveoli within the lungs (84, 85). Numerous other factors, including anatomical and physiological barriers, anatomical structure, breathing patterns, and respiratory mucus, can also affect virus-laden aerosol deposition (80, 86). Further, numerous studies have reported higher FLUAV vRNA loads in smaller aerosols of less than 5 µm compared to larger respiratory droplets (32, 33, 81, 92-94).

While aerosol transmission is a standard route of FLUAV infection in humans, many *in vivo* studies inoculate animal models via direct contact (intranasal). Therefore, multiple groups have examined differences in pathogenesis when inoculating via intranasal or aerosol (34-36, 210-212). Within ferrets, a more considerable amount of FLUAV delivered via intranasal inoculation was observed in the lower lobes of the lungs (49% in peripheral lung tissue, 2% in the nasal turbinates, 26% in the upper trachea, 17% in the esophagus, and 6% in the bronchi), while FLUAV delivered via aerosol was deposited primarily in the upper respiratory tract (70% in the upper trachea, 1% in the nasal turbinates, 4% esophagus, 5% bronchi, and 14% in peripheral lung tissue); however, a greater amount of virus was re-directed to the digestive tract in ferrets inoculated via the intranasal route (210). Ferrets inoculated via aerosol also exhibited a gradual progression of clinical signs, while ferrets inoculated via the intranasal route exhibited a sudden onset of severe disease (210). Nevertheless, both inoculation routes resulted in similar lethality (210). Another study analyzing different inoculation methods in non-human primates showed that challenge with a pH1N1 (A/California/04/2009) FLUAV via aerosol resulted in upper and lower respiratory tract virus distribution while intranasal infection had confined distribution in the upper respiratory tract (213).

Animal models such as ferrets and guinea pigs are frequently utilized to understand the aerosol transmission of numerous FLUAV subtypes, including H1N1, H3N2, H5N1, H9N2, and H10N7 (214-218) (27, 219-222). While the ferret model recapitulates human disease regarding susceptibility, pathogenesis, and transmission, ferrets are expensive and potentially difficult to work with in high numbers (214, 223, 224). Therefore, assessing aerosol transmission in an *in vitro* system can be valuable for screening viruses for potentially enhanced human-to-human transmission prior to or in conjunction with *in vivo* studies. Infection of adherent cell monolayers with a liquid inoculum to study virus replication is an established method, which is relatively inexpensive, allowing for testing of multiple experimental conditions and cell lines of different origins with considerable reproducibility. However, traditional liquid infection for *in vitro* replication poorly represents natural exposure and infection of cells within the respiratory tract (225).

A previous study adapted an aerosolized system that had the ability to inoculate epithelial cell monolayers with high pathogenicity avian influenza (HPAI) H5N1, a low pathogenicity avian influenza (LPAI) H7N9, and a seasonal H3N2 FLUAV (225). While the authors were able to infect cell culture monolayer and primary human alveolar epithelial cells, the system reported had numerous components to manipulate multiple environmental factors. Therefore, we aimed to develop a simple *in vitro* model system to infect adherent cell monolayers and differentiated human airway epithelial (HAE) cells cultured in air-liquid interface (ALI) conditions via aerosol inoculation. We calculated the relative infectious dose 50 for aerosol inoculation for three FLUAV subtypes: a pH1N1, swine-origin H3N2, and avian-origin H9N2. We show that all three viruses were able to infect a commonly utilized cell line, Madin-Darby canine kidney (MDCK) cells, and a recently developed immortalized differentiated human airway epithelial cell line (BCi-NS1.1) (225, 226). Further, we demonstrate higher aerosol infection efficiency in the pH1N1 strain compared to the swine-origin H3N2 and avian-origin H9N2 in MDCK cells and differentiated human cells. Due to its simplistic setup, this *in vitro* system can screen numerous FLUAV viruses for aerosol infection efficiency before or in conjunction with *in vivo* studies analyzing pandemic risk assessment to help direct public health preparedness.

Materials and Methods

Cells

MDCK cells were a kind gift from Robert Webster (St Jude Children's Research Hospital, Memphis, TN, USA). Cells were maintained in Dulbecco's Modified Eagles Medium (DMEM, Sigma-Aldrich, St Louis, MO, USA) containing 10% fetal bovine serum (FBS, Sigma-Aldrich, St. Louis, MO, USA), 1% antibiotic/antimycotic (AB, VWR, Radnor, PA, USA) and 1% L-Glutamine (Sigma-Aldrich, St Louis, MO, USA). Cells were cultured at 37°C under 5% CO2.

Human airway epithelial cells BCi-NS1.1 were obtained from Dr. Ronald Crystal (Weill Cornell Medicine, NY, USA). Cells were maintained in 1X Basal Media containing PneumaCult-Ex Plus Basal Medium (490mL) (STEMCELL Technologies, Vancouver, Canada), PneumaCult-Ex Plus 50X Supplement (STEMCELL Technologies, Vancouver, Canada), 0.1% Hydrocortisone (STEMCELL Technologies, Vancouver, Canada), 1% Penicillin-Streptomycin (5000 U/mL; ThermoFisher Scientific, MA, USA), 0.5% Amphotericin B (ThermoFisher Scientific, MA, USA), and 0.5% Gentamycin (50 mg/mL; Sigma-Aldrich, St Louis, MO, USA). Cells were cultured at 37°C under 5% CO2. Trypsin-EDTA (Sigma-Aldrich, ST Louis, MO, USA) followed by a solution of 85% HEPES Buffered Saline (Lonza, Basel, Switzerland) with 15% FBS (Sigma-Aldrich, St. Louis, MO, USA) were used for passaging the cells. The BCi-NS1.1 were not used after 25 passages.

Differentiation of the BCi-NS1.1 was performed in 12 mm transwell plates with 0.4 um pore polyester membrane inserts (Corning Inc., NY, USA). Prior to plating, transwell membranes were coated with human type IV collagen (Sigma-Aldrich, St. Louis, MO, USA) and then rinsed with 1X phosphate-buffered saline (PBS; ThermoFisher Scientific, MA, USA). Once the membrane was dry, 300,000 BCi-NS1.1 cells/well were plated into the transwell membrane insert with 1X Basal Media and cultured at 37°C under 8% CO2. After reaching 100% confluency, the cells were changed to ALI conditions by removing the apical media and then changing the basal media for 1X ALI media. ALI media contained PneumaCult ALI Base Medium (450mL) (STEMCELL Technologies, Vancouver, Canada), 10X PneumaCult ALI Supplement (50mL) (STEMCELL Technologies, Vancouver, Canada), 1% Penicillin-Streptomycin (5000 U/mL; ThermoFisher Scientific, MA, USA), 0.5% Amphotericin B (ThermoFisher Scientific, MA, USA), 0.5% Gentamycin (50 mg/mL; Sigma-Aldrich, St Louis, MO, USA), 1% PneumaCult ALI Maintenance Supplement (STEMCELL Technologies, Vancouver, Canada), 0.2% Heparin solution (STEMCELL Technologies, Vancouver, Canada), and 0.5% Hydrocortisone Stock solution (STEMCELL Technologies, Vancouver, Canada). Cells were cultured in ALI conditions at 37°C under 8% CO2 for 5 days. The cells were incubated at 37°C under 5% CO2 until they reached 17 days in ALI conditions.

Viruses

Virus stocks of the mouse-adapted pH1N1 A/California/04/2009 (Ca04; H1N1), swine-origin A/turkey/Ohio/313053/04 (Oh/04; H3N2), and avian-origin A/Guinea Fowl/Hong Kong/WF10/99 (WF10; H9N2) were generated in 10-day old specific pathogen-free (SPF) embryonated chicken eggs. These viruses were chosen because of their relevance in FLUAV transmission, infection in humans or potential for zoonosis. MDCK cells were used for FLUAV infection and titration of virus stocks. Virus stocks were titrated by tissue culture infectious dose 50 (TCID50), and virus titers were established by the Reed and Muench method (227).

Liquid inoculation

Confluent monolayers of MDCK cells were inoculated with 500 µL of ten-fold dilutions of a multiplicity of infection (MOI) starting at 0.01 until 10^{-6} for each virus. Numerous MOIs were tested to follow similar experimental setup as the aerosol inoculation below. Negative controls included inoculation of 500 µL of Opti-MEM 1 (Life Technologies, CA, USA), containing antibiotic-antimycotic solution (Opti-AB). Plates were incubated for 1 hour and rocked every 15 min at 37°C under 5% CO2. The virus inoculum was removed, and the cells were washed twice with 1 mL of PBS. Subsequently, 2 mL of Opti-AB containing 1 μg/mL N-p-tosyl-ʟ-phenylalanine chloromethyl ketone (TPCK)-treated trypsin (Worthington Biochemicals, NJ, USA) was added to each well. At 0, 12-, 24-, 48-, and 72-hours post-inoculation (hpi), 200 µL of tissue culture supernatant from inoculated cells were collected and then replaced. One-fourth of the volume collected was used for a hemagglutination assay titration, and the rest of the volume was stored at -80°C. Each virus contained 6 wells per dilution and each experiment was performed a total of 2 times.

Differentiated HAE cells incubated in ALI conditions for 17 days were washed 3 times with PBS before inoculation to remove accumulated mucus. Cells were then inoculated with 500 µL of the ten-fold dilution of an MOI starting at 1 until 0.01 for each virus. Negative controls included inoculation of 500 µL Opti-AB. Plates were incubated for 1 hour at 37°C under 5% CO2. The virus inoculum was removed, and the cells were washed with 1 mL of PBS three times. Following, 1.5 mL of new ALI media was added to the basal compartment. At the indicated time points, 200 µL of Opti-AB was added to the apical part of the well and then incubated for 10 min at 37°C under 5% CO2. The media was then collected and used for hemagglutination (HA) assay titration while the rest of the volume was stored at -80°C. Each virus contained 6 wells per dilution and was repeated twice.

In order to examine initial virus replication of the three different subtypes in differentiated BCi-NS1.1 cells, cells were inoculated with 1 MOI for each virus. Negative controls included inoculation of 500 µL Opti-AB. Infection and sample collection were performed as stated above. Titration of collected samples was achieved by TCID50, and virus titers were established by the Reed and Muench method (227).

Aerosol inoculation

The bioaerosol system used for all experiments was adapted from previously published designs (210, 225, 228). Included within the aerosol chamber setup are a pump (flow rate 13.3 L/min), Buxco Mass dosing controller (Data Sciences International, MN, USA), Aeroneb lab control module (Kent Scientific, CT, USA), Aeroneb Lab Nebulizer unit (Small VMD; Kent Scientific, CT, USA), Mass dosing chamber (Data Sciences International, MN, USA), SKC BioSampler (SKC, PA, USA), BioLite+ High-volume sample pump (SKC, PA, USA), NIOSH Bioaerosol sampler, liquid traps (Fisher Scientific, NH, USA), HEPA-CAP filters (VWR, PA, USA) and multiples sizes of plastic tubing and tubing adapters (Fig 3.1A). Regarding airflow, 6 mL of virus dilution or Opti-AB (negative control) was aerosolized using the Aeroneb Lab Nebulizer with an expected particle size of 2.5 - 4 µm at a rate of 0.1 mL/min. For MDCK cell exposures, ten-fold dilutions of a MOI starting at 0.01 until 10^{-6} was used for each virus. For differentiated HAE cells, ten-fold dilution of an MOI starting at 1 until 0.01 was used for each virus. Multiple MOI dilutions were used to calculate the aerosol infectious dose 50 (AID50) discussed below. The nebulizer was connected to the Aeroneb lab control module, which was then connected to the Buxco Mass dosing controller. An input of HEPA-filtered air into the mass dosing chamber was provided by pooled air from the air pump and Buxco mass dosing controller at a rate of 16 L/min. The flow rate for each pump was measured at the start of each experimental exposure. Relative humidity was reduced using silicone desiccating beads placed within two containers in the exposure chamber. Cells were placed inside the exposure chamber in the same position for each run. MDCK cells contained 500 µL of Opti-AB to prevent the cells from drying while differentiated HAE cells were under ALI conditions. Aerosol exposures were conducted at room temperature (20-22°C) and 40-60% relative humidity for 15 min followed by a 5 min purge to enable clearing of the aerosolized virus from the chamber. Subsequently, cells were removed from the chamber, incubated for 1 hour, and rocked every 15 min at 37°C under 5% CO2. Washing of the cells and sample collection at indicated time points followed the previous protocol discussed above. Each virus contained 6 wells per dilution and was repeated twice.

To examine the amount of virus-laden aerosols generated, two biosamplers were included within the chamber setup: the SKC Biosampler and the NIOSH biosampler. In different experiments, 6 ml of 1 x 10^6 TCID50/ml of each virus was aerosolized using the Aeroneb Lab Nebulizer as previously described. The Biosampler collection was conducted for 15 min. The SKC Biosampler contained 10 mL of Opti-AB and ran at a rate of 12.5 L/min while the NIOSH composed of a 15 mL conical tube, 1.5 mL screw-cap tube, and PTFE filter (0.3 µm) and ran at a rate of 3.5 L/min. After collection, an aliquot of the SKC Biosampler was stored at -80°C for future titration. For the NIOSH biosampler, 4 mL of Opti-AB for the first stage tube, 1.5mL of Opti-AB for the second stage, and 4mL of Opti-AB for the filter were used to wash the walls of the tubes/filter after aerosol collection. Samples were stored at -80°C for future titration. SKC Biosampler and NIOSH biosampler collections were titrated by one-step real-time quantitative PCR (RT-qPCR). RNA was extracted from the biosampler collection using the MagMax-96 AI/ND viral RNA isolation kit (ThermoFisher Scientific, MA, USA) following the manufacturer's protocol. Primers M+25 (AGATGAGTCTTCTAACCGAGGTCG) and M-124 (TGCAAAAACATCTTCAAGTCTCTG) were used for titrating samples inoculated with WF10. Primer M-124_Ca/04_CJC (TGCAAAGACACTTTCCAGTCTCTG) and M-124_Ty/04_CJC (TGCAAAAACGTCTTCGAGTCTCTG) were used in replacement of M-124 for Ca04 and Oh/04 titration, respectively. A probe with FAM as a reporter and TAMRA as a quencher was used (56-FAM/TCA GGC CCC CTC AAA GCC GA/36-TAMSp). The RT-qPCR was performed using a Quantabio qScript XLT One-Step RT-qPCR ToughMix kit (Quantabio, MA, USA) in a 20 µL final reaction volume on the QuantStudio 3 Real-Time PCR System (ThermoFisher Scientific, MA, USA). Each reaction contained 1X master mix, 0.5 µM of each primer, 0.3 µM probe, and 5 µL of RNA. The qPCR cycling conditions were 50°C, 20 min; 95°C, 1 min, 40 cycles at 95°C, 1 min; 60°C, 1 min; and 72°C 1s; with a final cooling step at 4°C. A standard curve was generated using 10-fold serial dilutions of the virus stock of known titer to correlate RT-qPCR crossing point (Cp) values with the viral load. RNA virus loads were calculated as $\log_{10}$ TCID50 equivalents/mL. Infectious virus was determined byTCID50 using the Reed and Muench method (227). The SKC Biosampler collections were also titrated by TCID50 and virus titers were established by the Reed and Muench method (227).

Hemagglutination (HA) Assay

Hemagglutination titers were calculated as previously described (229). Turkey (used for Ca04 and Oh/04) and chicken (WF10) red blood cells (RBCs) were separated from whole blood, isolated, and diluted to 0.5% in PBS. Diluted RBCs were incubated with two-fold serial dilutions of cell culture supernatant. For MDCK experiments, hemagglutination units (HAU) were determined after 45 min incubation at room temperature. For differentiated HAE cells, HAU were determined after overnight incubation at 4°C as previously described for differentiated nasal epithelial cells (229).

Histology and Immunofluorescence of differentiated HAE cells

Differentiation of HAE cells in ALI culture were confirmed using immunofluorescent staining of paraffin-embedded cross-sections or by top-staining of the transwell membrane. Briefly, transwell membranes were cut out of the well, rolled into a cassette, and fixed in 10% neutral-buffered formalin (NBF) for at least 72 hours. The cells were then embedded in paraffin and processed for routine histopathology with hematoxylin and eosin staining (HE). Non-stained slides were also used for immunofluorescent staining. Slides were de-paraffinized in xylene and ethanol as previously described (230). Heat antigen retrieval was performed by steaming the slides for 45 min with citrate buffer solution followed by PBS washing. For top staining, the transwells were fixed directly with 4% paraformaldehyde in PBS for 30 min and then washed 2X with PBS. Samples were then permeabilized with 0.3% triton X-100 in PBS, followed by blocking with 5% bovine serum albumin in PBS for 1 hour at room temperature. The samples were then stained with the following primary antibodies: KRT5 (basal cell; 2 µg/ml; HPA059479; Millipore Sigma, MA, USA), beta-tubulin I and II (cilia; 1/800; T8535, Sigma-Aldrich, MO, USA), CC16 (Club cell; 2 µg/ml; RD181022220-01; BioVendor, NC, USA), MUC5AC (M1 mucin; 2 µg/ml; MA5-12178, ThermoFisher, MA, USA), and TFF3 (goblet cell; 2 µg/ml; HPA035464; Millipore Sigma, MA, USA) for 1 hr at room temperature. To visualize the staining, samples were incubated with Alexa Fluor 488 Goat Anti-Mouse IgG (1/1000; A-11032, ThermoFisher, MA, USA) or Alexa Fluor 594 Donkey Anti-Rabbit IgG (1/1000; A-21207; ThermoFisher, MA, USA) as secondary antibodies with DAPI to identify cell nuclei for 1 hour at room temperature. Actin staining was performed by incubating samples with ActinGreen 488 ReadyProbes (R37110, ThermoFisher, MA, USA) for 5 min. Subsequently, membranes were mounted using Vectashield plus antifade mounting medium (Vector laboratories, CA, USA). Immunofluorescent microscope images were collected using a Nikon confocal microscope with a 60x lens. Images were captured and adjusted using Nikon NIS-Elements software (v 4.60.00).

For α2,3 and α2,6 receptor staining, samples were not permeabilized until after the secondary antibody incubation. Further, the samples were stained with the following primary antibodies: Maackia Amurensis Lectin II (α2,3, Biotinylated, 15 µg/ml; B-1265-1; Vector laboratories, CA, USA) and Sambucus Nigra Lectin (α2,6, Fluorescein, 15 µg/ml; F13012; Vector Laboratories, CA, USA) for 30 min at room temperature. The samples were then incubated with 1 secondary Streptavidin Alexa Fluor 594 conjugate (1/1000; S32356; ThermoFisher, MA, USA) for 30 min at room temperature. Cells were then permeabilized for 10 min as previously described and stained for DAPI to visualize the cell nuclei for 10 min. The membranes were mounted using Vectashield plus antifade mounting medium and imaged as previously described.

Virus Binding

MDCK cells were plated on coverslips in a 12-well plate to analyze virus binding and HAE were differentiated as described above. Prior to inoculation, differentiated HAE cells were washed 3X with PBS to remove mucus, and both cell lines were incubated at 4°C for 10 min. MDCK cells and differentiated HAE cells were then inoculated with Ca04 or WF10 at an MOI of 100 on ice and then incubated at 4°C for 30 min. The samples were washed 3X with PBS and then fixed with 4% paraformaldehyde in PBS for 30 min at room temperature. The cells were then stained for receptors following the protocol described previously with the addition of primary antibodies anti-hemagglutinin Ca04 H1N1 antibody (1/500; VWR, PA, USA) or anti-hemagglutinin H9 antibody for 1 hour at room temperature. The secondary antibody used for the additional primary antibody was Alexa Fluor 647 Goat Anti Mouse (1/1000; A2137, Invitrogen, MA, USA). Cells were then permeabilized for 10 min as previously described and stained for DAPI for 10 min to visualize the cell nuclei. The membranes were mounted using Vectashield plus antifade mounting medium and imaged as previously described.

Exposure dose and infectious dose 50 calculations

The concentration of infectious virus in an aerosol (C_{aer}) was calculated by integrating the media volume (V_{samp}), the concentration of virus (C_{samp}), and the flow rate (Q_{samp}) as previously described (225):

$$C_{aer} = \frac{(C_{samp})(V_{samp})}{(Q_{samp})(t)}$$

Further, the total number of infectious virions moving through the exposure chamber during the 15 min exposure (N_{cham}) was calculated as previously described (225):

$$N_{cham} = \frac{(C_{samp})(V_{samp})(Q_{cham})}{Q_{samp}}$$

The equation considers the concentration of the virus (C_{samp}), the volume of media (V_{samp}), the flow rate of the chamber (Q_{cham}), and the flow rate of the sampler (Q_{samp}). Following Creager et al., the N_{cham} was multiplied by the ratio of the surface area of each 6-well ($9.6cm^2$) or 12-well transwells ($1.1cm^2$; diameter = 12mm) to the cross-sectional area of the chamber ($1,670cm^2$; l (19.2 in) x w (13.5 in)) to calculate the exposure dose (ED) (225). The AID50 was calculated by graphing a non-linear regression model and determining the half maximal effective concentration (EC50) of the ED.

Graphs/Statistical Analyses

Data analyses and graphs were performed using GraphPad Prism software version 9.4 (GraphPad Software Inc., CA, USA). A P value below 0.05 was considered significant.

Results

Aerosol exposure chamber system setup

Previous studies have reported an exposure system used to aerosolize FLUAV in an *in vitro* and *in vivo* setting; however, these systems generally contain multiple components to control environmental factors along with the high cost of implementation and assembly. Therefore, we generated a calm-aerosol settling chamber system that is easy to assemble with less equipment and more cost-effective for analyzing aerosol infection efficiency of different FLUAV viruses (Fig 3.1A). This system contains a large exposure chamber, which can be used to expose several plates of cells or utilized for *in vivo* studies. It also includes two biosamplers, in which the SKC Biosampler has been commonly used in aerosol chamber experiments to collect infectious FLUAV, while the NIOSH biosampler can compartmentalize aerosols of different sizes (>4 µm, 1-4 µm, <1 µm) (Fig 3.1B). Therefore, this system can be utilized for preliminary assessment of aerosol transmission efficiency of different FLUAV strains complementary with *in vivo* data. Aerosol inoculation of cell culture plates was conducted in the following manner. MDCK and differentiated HAE cells were exposed to ten-fold serial dilutions of aerosolized FLUAV of three different subtypes for 15 min followed by a 5 min purge. The cells were then incubated at 37°C for 1 hour, washed with PBS to remove leftover inoculum and unbound FLUAV, and then incubated for 3 days. Mock infections led to no visible decrease in cell viability, suggesting that the cells remained viable during the exposure time. As a control, cells were inoculated via liquid with 500 µL of the same MOI dilutions for each virus that were aerosolized because of the low-dose inoculums tested.

Liquid and aerosol infection of an H1N1, H3N2, and H9N2 in MDCK cells

Initial aerosol exposure studies were conducted in MDCK cells to validate the aerosol chamber study design. This cell line is commonly utilized in FLUAV research and has been previously shown to support the replication of numerous FLUAV subtypes.

Three FLUAV of different subtypes (A/California/04/2009 (Ca04; H1N1), A/turkey/Ohio/313053/04 (Oh/04; H3N2), and A/Guinea Fowl/Hong Kong/WF10/99 (WF10; H9N2)) that have been previously shown to replicate with high efficiency in MDCK cells were serially diluted and used to inoculate six wells via aerosol or liquid inoculation at different MOIs. Cell culture supernatant was collected at 0, 12-, 24-, 48-, and 72 hpi and used for initial titration by HA assay. HAU below the limit of detection ($\leq$ 2 HAU) was observed at 0 and 12 hpi for all three viruses in aerosol and liquid inoculation (data not shown). At 24 hpi, 10/12 wells exposed to aerosolized Ca04 at an MOI of 0.01 had HAU above the limit of detection, while Oh/04 and WF10 contained no wells positive by HAU (Fig. 3.2). Within liquid inoculation, Ca04 and Oh/04 both had wells positive at MOI of 1 x 10^{-5} while WF10 had wells positive by HA in MOI of 1 x 10^{-2}. At 48 hpi, 4/12 wells exposed to aerosolized Ca04 had detectable HAU at an MOI of 1 x 10^{-4}, while Oh/04 had 2/12 wells positive at the same dilution; however, 1/12 wells had detectable HAU at an MOI of 1 x 10^{-3} when exposed to aerosolized WF10 (Fig 3.2). Among the liquid inoculation, 7/12 wells were positive at MOI of 1 x10^{-6} for Ca04 and Oh/04, while 5/12 wells were positive at MOI of 1 x 10^{-5} for WF10 at 48 hpi. Similar results to 48 hpi were observed at 72 hpi for wells infected with aerosolized Ca04 and Oh/04, while more wells exposed to aerosolized WF10 (8/12) were positive at an MOI of 1 x 10^{-3} and 1/12 wells were positive at MOI of 1 x 10^{-4} (Fig 3.2). At 72 hpi, more wells were positive via liquid inoculation of WF10, while the number of wells considered positive via Ca04 and Oh/04 stayed the same. As expected, no HAU above the detection limit was observed among the negative controls at all sample collections. Overall, differences among the number of positive wells via aerosol infection were observed when comparing a pH1N1, swine-origin H3N2, and avian-origin H9N2 FLUAV.

Considering we were able to infect MDCK cells at different MOI dilutions via aerosol, we next investigated the ability to calculate the AID50 for each virus in MDCK cells. Since the liquid inoculation of WF10 was lower at 48 hpi but similar at 72 hpi compared to Ca04 and Oh/04, the results from the 72 hpi collection were used for calculating the AID50. To determine the AID50, the proportion of wells with HAU greater than 2 and their respective dilution factor were used in a non-linear regression model to calculate the EC50 (Fig 3.3A). Results showed that Ca04 had the lowest EC50 with an MOI of $1 \times 10^{-3.7}$, followed by WF10 with an MOI of $1 \times 10^{-3.2}$ and Oh/04 with an MOI of $1 \times 10^{-2.6}$ (Fig 3.3A). EC50 values of the liquid inoculated viruses were similar for Ca04 and WF10 but lower for Oh/04. To further visualize the results, we examined the area under the curve (AUC) from the non-linear regression (Fig 3.3B). Similar to the EC50 values, results showed that Ca04 (1.74) had the largest AUC followed by WF10 (1.24) and then Oh/04 (0.82) when cells were inoculated via aerosol (Fig 3.3B). Contrastingly, Oh/04 (3.79), followed by WF10 (3.08) and Ca04 (3.08), had the largest AUC when cells were inoculated via liquid (Fig 3.3B). Utilizing different parameters within the aerosol exposure chamber design (Table 3.1), we calculated the total concentration of infectious virus in an aerosol (C_{aer}), the total number of aerosolized particles passing through the chamber during an exposure (N_{cham}), and the exposure dose per well (ED) using the surface area of a 6-well plate, as previously described (Table 3.2) (225). Subsequently, we calculated the EC50 based on the ED for each run to determine the AID50. The AID50s for each run were averaged to give the final AID50 calculated for each virus. The lowest AID50 among the three viruses was Ca04 at 88.1 TCID50/well, followed by WF10 with an average of 308.3 TCID50/well and Oh/04 at 942.3 TCID50/well. Conclusively, the AID50 results demonstrate different aerosol infection efficiencies among the three viruses, specifically Ca04 and Oh/04, in MDCK cells within this aerosol chamber system.

Since differences in AID50 were observed among the three FLUAV subtypes, we analyzed the amount of infectious virus and viral RNA (vRNA) collected from two different biosamplers when 1×10^6 TCID50/mL of each virus was aerosolized within the exposure chamber. For the SKC Biosampler, collected inoculum and samples were titrated for infectious virus by TCID50 and vRNA loads by RT-qPCR (Fig 3.3C). The SKC Biosampler titers were normalized using the equation to calculate the C_{aer} as previously described (225). Briefly, the calculated titers were multiplied by the volume within the sampler and then divided by the sampler's flow rate multiplied by the exposure time. Parameters used in calculating the titers obtained from SKC Biosampler are displayed in Table 3.1. Results showed lower titers of infectious virus and vRNA loads from the SKC Biosampler compared to the inoculum (Fig 3.3C). Further, infectious virus titers and vRNA loads were similar among all three viruses collected in the SKC Biosampler. Concurrently, we sampled aerosolized virus using the NIOSH biosampler, which can compartmentalize aerosols of different sizes (>4 µm, 1-4 µm, <1 µm). Similar to the SKC Biosampler, calculated titers were multiplied by the volume within the sampler and then divided by the flow rate of the sampler multiplied by the exposure time. Results showed lower vRNA loads in Ca04 compared to the other two viruses in all stages of the NIOSH, particularly within the filter (Fig 3.3D). Overall, similar amounts of aerosolized infectious virus and vRNA were collected within the SKC Biosampler and NIOSH biosampler among the three viruses.

Characterization and FLUAV infection of differentiated human airway epithelial cells BCi-NS1.1

Since we were able to infect MDCK via aerosol with all three FLUAV subtypes, we next investigated the ability to infect more relevant cells, differentiated HAE cells, via liquid and aerosol inoculation. Previously, Walters et al. immortalized HAE (BCi-NS1.1) by infecting the human airway basal cell line obtained from brushings of the airway epithelium of a healthy nonsmoker with a retrovirus expressing human telomerase (226). Differentiation of BCi-NS1.1 under ALI conditions showed multipotent differentiation capacity for over 40 passages (226). Here, we utilized differentiated BCi-NS1.1 cells to investigate the ability to infect differentiated HAE cells via aerosol using the aerosol exposure system established here and further analyze the aerosol inoculation efficiency of FLUAV of different subtypes. However, prior to testing the ability to infect the differentiated BCi-NS1.1 cells with FLUAV, we confirmed the differentiation of the HAE cells by analyzing cross-sections of BCi-NS1.1 cells cultured in ALI conditions. H&E staining of the cross sections of non-differentiated BCi-NS1.1 cells showed a limited number of cell layers resembling more of a monolayer phenotype (Fig 3.4A left). Contrastingly, BCi-NS1.1 cells cultured in ALI conditions for 17 days displayed characteristics of pseudostratified ciliated epithelium with visible cilia toward the top of the cells and intermittent presence of goblet cells (Fig 3.4A right). Immunofluorescent staining for KRT5 (basal cell marker) and β-tubulin I and II (ciliated cell marker) showed positive staining for basal cells closer to the membrane and ciliated cells toward the top of the epithelium with DAPI (cell nuclei marker) in between (Fig 3.4B). Further, top immunofluorescent staining of CC16 (club cell marker), MUC5AC (mucin marker), and TFF3 (goblet cell marker) displayed positivity for all these cell types in BCi-NS1.1 cells cultured in ALI conditions for 17 days (Fig 3.4C). Notably, the cells contained a high prevalence of ciliated cells, correlating with what was observed in the cross-section histology images. In conclusion, we confirmed that the culture of BCi-NS1.1 cells for 17 days in ALI conditions resulted in phenotypes resembling a pseudostratified ciliated human airway epithelium.

While BCi-NS1.1 cells have been used in a previous study to examine the role of IRF7 during H1N1 FLUAV infection, the distribution of FLUAV cell receptors within the differentiated BCi-NS1.1 cell line has not been reported. Therefore, we stained via immunofluorescence for the distribution of α 2,3- and α 2,6- sialic acids (SA) in 17-day ALI cultures (Fig 3.5A). Numerous studies have previously demonstrated that the hemagglutinin (HA) from human-origin FLUAV preferentially binds α2,6-SA while HA from avian-origin FLUAV preferentially binds to α2,3-SA (108). Immunofluorescence showed positivity for both α 2,3 and α 2,6 on the differentiated BCi-NS1.1 cells; however, the cells had more staining of α 2,6 receptor positivity compared to α 2,3-SA (Fig 3.5A). Since we confirmed the presence of both SA receptor confirmations, we examined the replication of Ca04 H1N1, Oh/04 H3N2, and WF10 H9N2 in differentiated BCi-NS1.1 cells at an MOI 1 via liquid inoculation (Fig 3.5B). Results showed similar virus replication kinetics between Ca04 and Oh/04, with the largest amount of virus replication occurring between 0 and 24 hpi (Fig 3.5B). However, WF10 displayed a slight increase in virus titer at 24 hpi but then decreased until 72 hpi suggesting restrictive replication within the differentiated BCi-NS1.1 cells (Fig 3.5B). Virus titers were below the limit of detection in the negative control. Because we saw limited replication of WF10 in the differentiated BCi-NS1.1 cells, we further examined virus binding of Ca04 and WF10 in this cell line with co-staining of the α 2,3- and α 2,6-SA. MDCK cells were used as a control. Virus binding of Ca04 and WF10 was present in MDCK cells, while the negative control had no positive virus HA staining (purple) (Fig 3.5C). Ca04 virus positivity predominantly overlapped with α 2,6-SA staining, while WF10 virus positivity largely overlapped with α 2,3-SA staining. While less binding was observed, both Ca04 and WF10 HA staining were observed within the differentiated BCi-NS1.1 cells, suggesting that restrictive replication of WF10 is not exclusively the result of reduced virus binding.

Liquid and aerosol infection of an H1N1 and H3N2 in differentiated human airway epithelial cells BCi-NS1.1

Since we were able to infect differentiated BCi-NS1.1 cells with the H1N1 and H3N2 FLUAV strains, we investigated the ability to infect differentiated HAE cells via aerosol using this exposure system. WF10 was not evaluated for aerosol infection since liquid inoculation at 1 MOI resulted in limited replication. Similar to the experiments performed in MDCK cells, cell culture supernatant was collected at 0, 12-, 24-, 48-, and 72 hpi and used for initial titration by HA. HAU below the limit of detection ($\leq$ 2 HAU) were observed at 0, 12, and 24 hpi for both viruses in aerosol and liquid inoculation (data not shown). At 48 hpi, 6/12 transwells exposed to aerosolized Ca04 at an MOI of 0.1 had

HAU above the detection limit, while 4/12 wells exposed to Oh/04 at an MOI of 1 were positive. When analyzing positivity in liquid inoculated transwells, a similar number of transwells were positive for Ca04 and Oh/04 (Fig 3.6). When inoculated via liquid with Ca04, 6/12 transwells were positive at an MOI 0.1 and 1/12 transwells at MOI 0.01, while liquid inoculation with Oh/04 resulted in 8/12 positive transwells at an MOI 0.1 (Fig 3.6). Compared to 48 hpi, an increased number of transwells were positive via aerosol and liquid inoculation for both viruses at 72 hpi (Fig 3.6). When exposed to aerosolized Ca04, 7/12 transwells were considered positive at an MOI of 0.01, while 6/12 transwells exposed to aerosolized Oh/04 at an MOI of 0.1 were considered positive (Fig 3.6). While the number of wells infected via aerosol differed among the two viruses, a similar number of wells were positive via liquid inoculation (Fig 3.6). Overall, differences among the number of positive wells via aerosol infection were observed when comparing a pandemic H1N1 and a seasonal swine H3N2 in differentiated HAE cells.

Similar to the experiments performed in MDCK cells, we examined the AID50 for Ca04 and Oh/04 in differentiated BCi-NS1.1 cells. At 48 hpi, we calculated the proportion of wells with HAU greater than 2, and their respective dilution factor was used in a non-linear regression model to calculate the EC50 value (Fig 3.7A). Results showed that Ca04 had the lowest EC50 with an 0.20 MOI compared to Oh/04 with an MOI of 2.11 when cells were infected via aerosol (Fig 3.7A). When examining liquid inoculation, Oh/04 had an EC50 of 0.064 MOI, while Ca04 had an EC50 of 0.092 MOI (Fig 3.7A). We examined the AUC from the non-linear regression to further visualize the results. Similar to the EC50 values, Ca04 (0.51) had the largest AUC value, followed by Oh/04 (0.14) when cells were inoculated via aerosol (Fig 3.7B). Meanwhile, similar AUC values were observed for Oh/04 (0.78) and Ca04 (0.70) when cells were inoculated via liquid (Fig 3.7B). A similar difference between the two viruses was observed at 72 hpi. Ca04 had an EC50 of 0.0068 MOI, while Oh/04 had an EC50 of 0.10 MOI at 72 hpi. EC50 values from liquid inoculation of Ca04 (EC50 = 0.0034 MOI) and Oh/04 (EC50 = 0.0020 MOI) were also similar at 72 hpi. Compared to the EC50 values, Ca04 (Aerosol = 1.74; Liquid = 1.79) had a higher AUC value than Oh/04 (Aerosol = 1.00; Liquid = 1.91) when cells were inoculated via aerosol, while AUC values were similar among liquid inoculated cells. Utilizing different parameters within the aerosol exposure chamber design (Table 3.1), we calculated the C_{aer}, N_{cham}, and ED using the surface area of the transwells membranes as previously described (Table 3.2) (225). We then calculated the EC50 based on the ED for each run to determine the AID50. The AID50s for each run were averaged to give the final AID50 calculated for each virus. Results from 72 hpi sample collection were used to determine the AID50 since additional wells were positive at this time point when compared to 48 hpi. The exposure dose was similar among the two viruses; however, differences within the AID50 were observed (Table 3.3). The lowest AID50 among the two viruses was Ca04 with 1,037.1 TCID50/well, followed by Oh/04 at 15,085.5 TCID50/well (Table 3.3). Overall, the results demonstrate different aerosol infection efficiencies similar to those observed in MDCK cells between Ca04 and Oh/04 in differentiated BCi-NS1.1 cells.

Discussion

Within this study, we generated a calm-aerosol settling chamber system that is easy to assemble and cost-effective to infect a standard cell line utilized in influenza research, MDCK cells, and a more relevant cell line, immortalized differentiated HAE cells. We demonstrate that MDCK cell monolayers and differentiated HAE cells can be infected via aerosol by three different subtypes of FLUAV using this exposure system. Similar to what was performed in a previous study by Creager et al., we measured viral infectivity at various MOIs at different time points. We further showed that the HA assay could be used as a readout for analyzing aerosol infectivity. Compared to traditional methods for virus titration, such as plaque assay or RT-qPCR, results of an HA assay can be recorded in a shorter time and are more affordable. The results from this study demonstrated differences among three FLUAVs, including a pH1N1, H3N2, and H9N2 in both cell lines, suggesting that understanding aerosol infectivity *in vitro* in conjunction with *in vivo* studies can be used for pandemic risk assessment of influenza viruses and to assess the role of molecular markers involved in transmission efficiency (225).

While a previous study described the use of an exposure chamber to examine the effects of a high pathogenicity avian influenza virus (HPAIV) H5N1 and a low pathogenicity avian influenza virus (LPAIV) H7N9, we utilized this system to examine the aerosol infectivity of a human pandemic H1N1 (Ca04), a swine-origin H3N2 (Oh/04), and avian-origin H9N2 (WF10). These viruses were chosen because of their relevance in FLUAV transmission, human infection, or potential for zoonosis. Ca04 H1N1 is a prototypical strain isolated from a pediatric patient and has been previously shown to transmit via respiratory droplets in ferrets (231). Within this study, the mouse-adapted Ca04 strain previously described to carry five amino acid substitutions was used for the intent of performing future *in vivo* exposure studies in mice (232). Oh/04 H3N2 is most closely related to the isolate A/Swine/WI/14094/99 (H3N2) that has been circulating in pigs since 1998 and is a triple reassortment virus containing the triple-reassortant internal gene (TRIG) cassette (233, 234). The TRIG cassette includes a human-origin PB1, avian-origin PA, and PB2, and a swine-origin M, NP, and NS gene segments (233, 234). The TRIG cassette is stable but can support different HA and neuraminidase (NA) combinations of viruses circulating in pigs within North America (235). Further, Oh/04 has been previously shown to have the capability to transmit both ways between swine and turkeys (236). H9N2 avian influenza viruses (AIV) are zoonotic agents and gene donors to other influenza virus subtypes, such as H5N1/N6, H7N9, and H10N8/N3, resulting in human infections (13-17, 19, 20, 80, 237, 238). More specifically, a previous study showed efficient replication and transmission by direct contact and aerosol of viruses carrying the surface proteins of WF10 but the internal constellation of a pH1N1 in ferrets (239). Further, all three viruses replicate with high efficiency in MDCK cells. MDCK cells were utilized for initial testing of the aerosol exposure system because they are commonly used in FLUAV research and have been previously shown to support the replication of numerous FLUAV subtypes of different host-origins. Therefore, the exposure system utilized within this study can be used with MDCK cells to analyze the aerosol infectivity of various FLUAVs of different host-origin.

While MDCK cells have been previously shown to support replication of Ca04, Oh/04, and WF10, differences in the number of positive wells via aerosol exposure and the AID50 were observed here. Results showed that Ca04 had the lowest AID50, followed by WF10 and then Oh/04. Since all three viruses replicated at the same efficiency via liquid inoculation, the differences in AID50 are most likely due to variations in aerosol infectivity; therefore, the results suggest that the aerosol exposure system described within this study can be utilized to screen FLUAV strains for enhanced or reduced aerosol infectivity. While differences in aerosol infectivity were observed among the different viruses, similar viral titers and vRNA loads were collected by the SKC Biosampler and NIOSH biosampler. Equivalently, a previous study showed similar virus titers from samples collected from the NIOSH filter during aerosol exposure to H1N1 and H3N2 FLUAV (240). These results suggest that the generation of virus-laden aerosols and the stability of those aerosols during the 15 min of exposure within this exposure system were similar and most likely not contributing to the differences observed in aerosol infectivity.

In addition to examining the aerosol infectivity within MDCK cells, we analyzed aerosol and liquid inoculation of Ca04, Oh/04, and WF10 in a differentiated HAE cell line (BCi-NS1.1) immortalized by Walters and colleagues (226). It was previously demonstrated that BCi-NS1.1 retained characteristics of primary cells for over 40 passages and demonstrated differentiation into secretory (MUC5AC, MUC5B), goblet (TFF3), Clara (CC10), and ciliated (DNAI1, FOXJ1) cells when cultured in ALI conditions (226). Further, the differentiated HAE cells can respond to external stimuli such as IL-13, which alters the normal differentiation process (226). Considering the cells can be passaged and maintained within the laboratory for more extended periods compared to primary cell lines, utilization of the differentiated BCi-NS1.1 cells could be advantageous because of the ability to plate more cells for additional replicates within an experiment and potentially increase homogeneity across replicate experiments by decreasing the variability of having primary cells from different donors. While Walters and colleagues cultured BCi-NS1.1 cells for 28 days, BCi-NS1.1 cells cultured in ALI conditions for 17 days within this study displayed characteristics of pseudostratified ciliated epithelium with the presence of multiple cell types, including secretory and ciliated cells (226). Due to the limited information on FLUAV infection within these cells, we examined the distribution of both α 2,3 and α 2,6-SA receptors. Numerous studies have previously demonstrated that the HA from human-origin FLUAV preferentially binds α2,6-SA while HA from avian-origin FLUAV preferentially binds to α2,3-SA (108). Further, α2,6-SA are prevalent on the surface of ciliated and goblet cells in the upper respiratory tract, while α2,3-SA are more abundant on the surface of non-ciliated bronchoepithileum cells and type II pneumocytes in the lower respiratory tract (107). Immunofluorescence staining of the differentiated BCi-NS1.1 cells showed positivity for both receptor linkages with visually more staining of α 2,6-SA; however, additional quantitative analysis is needed for confirmation. Since we confirmed the presence of both SA receptors on the surface of the differentiated BCi-NS1.1 cells, we analyzed the replication kinetics of Ca04, Oh/04, and WF10 via liquid inoculation at a high MOI. While Ca04 and Oh/04 showed similar replication kinetics, WF10 displayed reduced virus replication after 24 hpi. While WF10 could bind to the differentiated BCi-NS1.1 cells, multiple other factors, such as the polymerase complex, could contribute to the observed restrictive replication; however, this was not within the scope of the study.

Since liquid inoculation of Ca04 and Oh/04 in differentiated BCi-NS1.1 cells led to similar virus replication kinetics, we analyzed these two viruses via aerosol inoculation within the BCi-NS1.1 cells. We demonstrated that aerosol inoculation of differentiated HAE cells in ALI conditions was successful when using the aerosol exposure system described within this study. Interestingly, similar differences within the AID50 between

Ca04 and Oh/04 observed in MDCK cells were also detected in differentiated BCi-NS1.1 cells. These results suggest that these differences are most likely not because of the cell type or inherent replication within the specific cell line but because of the disparity within the aerosol infectivity efficiency among the two viruses; however, additional experiments are needed to determine the molecular mechanism influencing the aerosol infection differences between the two strains observed within this study.

Numerous groups have reported differences in pathogenesis and virus deposition when inoculating animal models via aerosol versus intranasal inoculation (34-36, 210, 212, 241). Therefore, aerosol inoculation of *in vitro* cell culture can be valuable in studying molecular markers that influence the transmission efficiency of FLUAV and virus-cell interactions resembling natural infection in the human respiratory tract. Not only can this system be used to analyze infection, but it can be utilized for various other experiments, such as examining aerosol exposure of FLUAV vaccine strains in animal models to develop a vaccine with intranasal delivery. This vaccine delivery method is of higher interest due to the increasing fear of needles. While the aerosol exposure system presented within this study successfully infects different subtypes of FLUAV in two cell lines, it does not control for numerous environmental factors affecting aerosol viability and stability, which is needed for efficient aerosol transmission. Environmental factors such as temperature, relative humidity, and UV radiation play a crucial role in the survival and transmission of FLUAV aerosols by potentially affecting protein, lipid, and vRNA stability (80). Since the system's primary objective was to examine the aerosol infectivity of different viruses, direct manipulation of environmental factors was not needed since environmental conditions were relatively similar across experiments. In addition to examining FLUAV, this system can be utilized to study other respiratory viruses such as SARS-CoV-2. Using an *in vitro* aerosol exposure system, in conjunction with *in vivo* studies, can aid in expanding the current knowledge on molecular virological markers that influence respiratory virus transmission that can help direct public health preparedness and pandemic risk assessment of circulating FLUAV strains.

Figure 3.1. Graphic representation of aerosol exposure system. A schematic representation of the aerosol exposure system. The airflow is represented by arrows starting with HEPA-filtered air (blue arrow) that is provided by a pump and Buxco Mass dosing controller. Virus (red arrow) was aerosolized directly into the exposure chamber using the Aeroneb nebulizer. To aid in controlling the relative humidity, silicone desiccating beads were placed in two containers within the exposure chamber. Two samplers were used in the design including the SKC Biosampler and the NIOSH biosampler. Virus laden aerosols were collected from one output port into the SKC Biosampler, followed by a liquid trap and then HEPA filter before entering the SKC pump. In a second output port, tubes connected to the NIOSH are connected to a liquid trap and then HEPA filter before entering the SKC pump. Each experiment consisted of a 15 min of exposure followed by a 5 min purge prior to removing the cells from the exposure chamber. Cells were placed in the same orientation and location for each exposure. **(B)** Setup of the NIOSH sampler inside the exposure chamber and silica beads used for minimal control of relative humidity.


A
B
Nebulizer
SKC Pump
SKC Pump
Liquid Trap
SKC
HEPA
Exposure Chamber
HEPA
Buxco
Pump

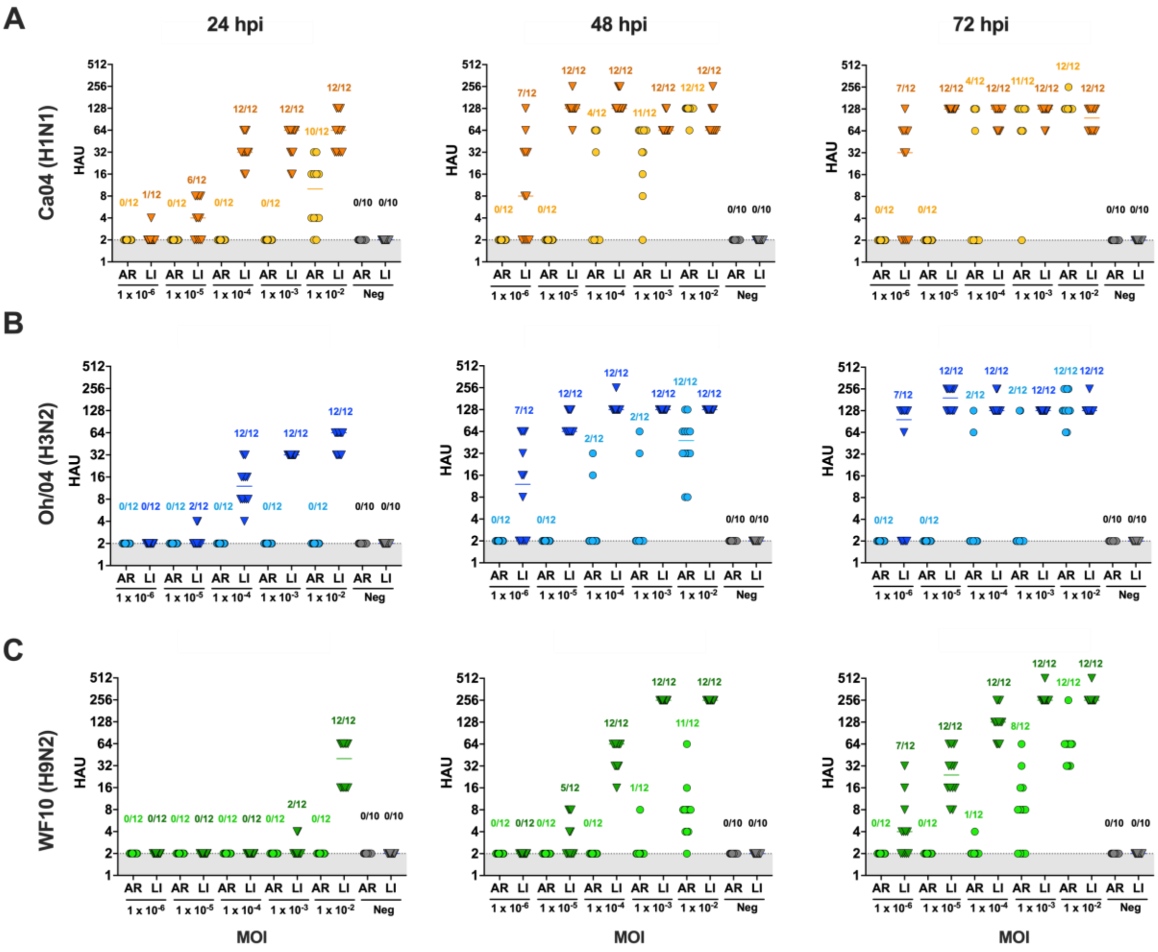

Figure 3.2. Hemagglutination (HA) assay titration of Ca04, Oh/04, and WF10 FLUAV post aerosol and liquid inoculation in MDCK cells. MDCK cells were inoculated via aerosol (AR; circles) or liquid (LI; triangles) of ten-fold dilutions from 1 MOI of **(A)** Ca04 (H1N1), **(B)** Oh/04 (H3N2), and **(C)** WF10 (H9N2). Cell culture supernatant was collected at 0-, 12-, 24- , 48-, and 72-hours post inoculation. The first two time points (0 and 12 hpi) resulted in HAU below the limit of detection and are therefore not shown. Each point represents that HAU from 1 well. Numbers above the points represent the number of wells considered positive / total number of wells. Wells with HAU > 2 were considered positive. Viruses are distinguished by difference in color (Ca04: orange, Oh/04: blue, WF10: green).

Figure 3.3. Graphical representation of the non-linear regression model from FLUAV exposure in MDCK cells and viral titers collected from biosamplers implemented with the aerosol exposure system. (A) The proportion of wells with HAU greater than 2 and their respective dilution factor were graphed in a non-linear regression model to calculate the half maximal effective concentration (EC50). The EC50 are displayed in text. Solid lines indicate aerosol exposure while dashed lines represent liquid inoculation. Viruses are distinguished by difference in color (Ca04: orange, Oh/04: blue, WF10: green). **(B)** The area under the curve (AUC) from the non-linear regression displayed in A is represented in a bar graph. **(C)** Infectious virus (bars; left axis) titration by TCID50 and vRNA loads (points; right axis) quantification by RT-qPCR was performed on the inoculum and samples collected from the SKC Biosampler. vRNA loads are conveyed as log10 TCID50 equivalent (TCID50eq) per mL. (D) vRNA load quantification from samples collected from each stage of the NIOSH biosampler displayed as as log10 TCID50 equivalent per mL. Viruses are distinguished by difference in color (Ca04: orange, Oh/04: blue, WF10: green). AR = aerosol; LI = liquid. Statistical analysis was performed using a two-way ANOVA with Tukey correction.

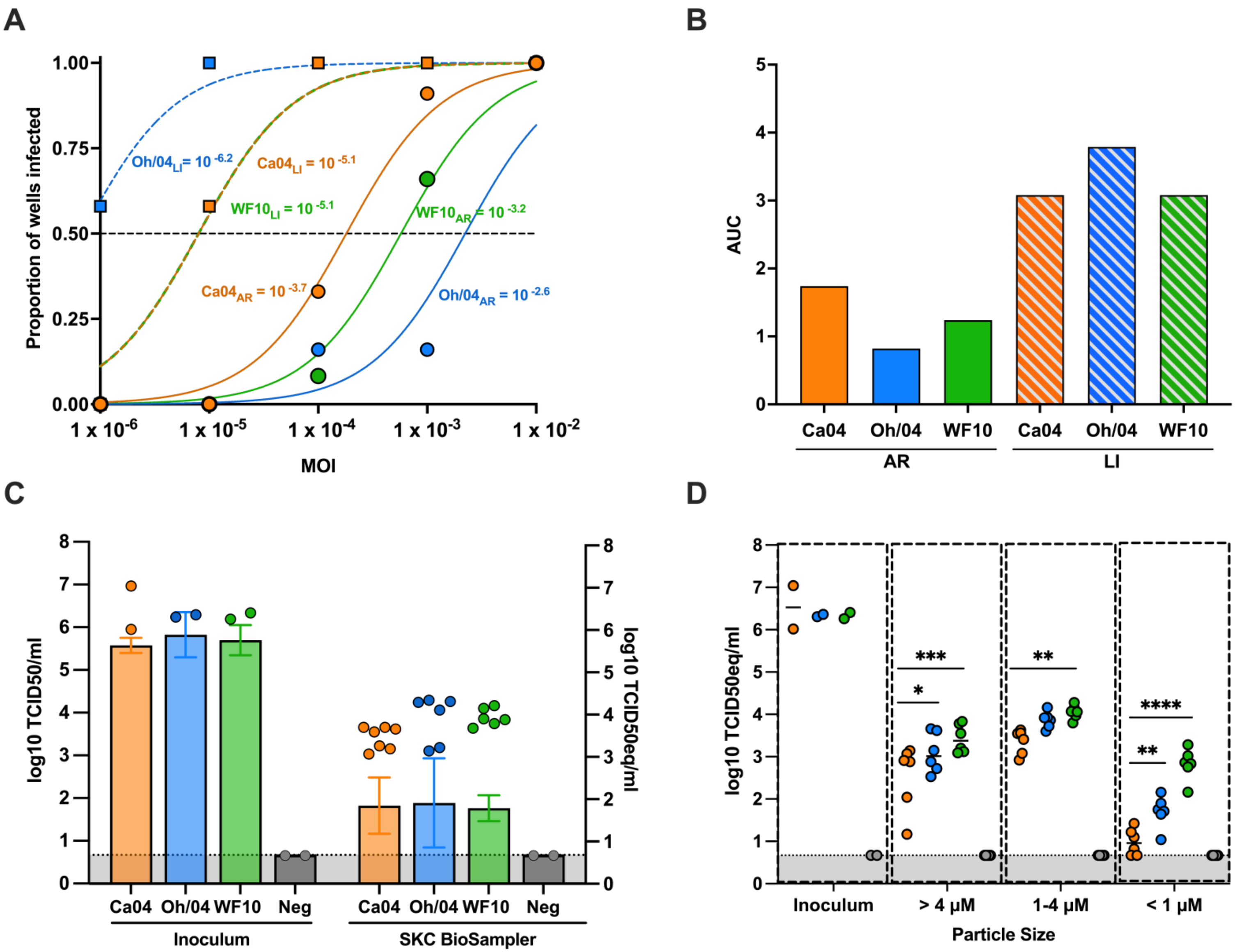
A
Proportion of wells infected
1.00
0.75
0.50
0.25
0.00
1 x 10-6
1 x 10-5
1 x 10-4
1 x 10-3
1 x 10-2
MOI
Oh/04LI = 10 -6.2
Ca04LI = 10 -5.1
WF10LI = 10 -5.1
WF10AR = 10 -3.2
Ca04AR = 10 -3.7
Oh/04AR = 10 -2.6
B
AUC
0
1
2
3
4
5
Ca04
Oh/04
WF10
Ca04
Oh/04
WF10
AR
LI
C
log10 TCID50/ml
log10 TCID50eq/ml
0
1
2
3
4
5
6
7
8
Ca04
Oh/04
WF10
Neg
Ca04
Oh/04
WF10
Neg
Inoculum
SKC BioSampler
D
log10 TCID50eq/ml
0
1
2
3
4
5
6
7
8
***
*
**
****
**
Inoculum
> 4 μM
1-4 μM
< 1 μM
Particle Size

Figure 3.4. Characterization of differentiated BCi-NS1.1 cells. BCi-NS1.1 cells were cultured under air-liquid interface (ALI) conditions for 17 days. **(A)** Paraffin-embedded cross sections embedded in paraffin of BCi-NS1.1 cells prior to ALI conditions (left) and after 17 days in ALI (right) with H&E staining. Images were captured at 40X magnification. **(B)** Paraffin-embedded cross sections of ALI cultured BCi-NS1.1 cells stained by immunofluorescence with KRT5 (basal cell marker; green), DAPI (cell nuceli; blue), and β-tubulin I and II (ciliated cell marker; red). Images were captured using Nikon confocal microscope with NIS Elements software at 40X (left) and 60X (right). **(C)** ALI cultured BCi-NS1.1 cells were fixed with 4% paraformaldehyde and stained for β-tubulin I and II (ciliated cell marker; red), CC16 (club cell marker; red), MUC5AC (mucin makrer), TFF3 (goblet cell marker), actin (green), and DAPI (cell nuclei; blue). Each panel with separate staining from the same column was merged in the last row. Images were captured using Nikon confocal microscope with NIS Elements software at 60X.

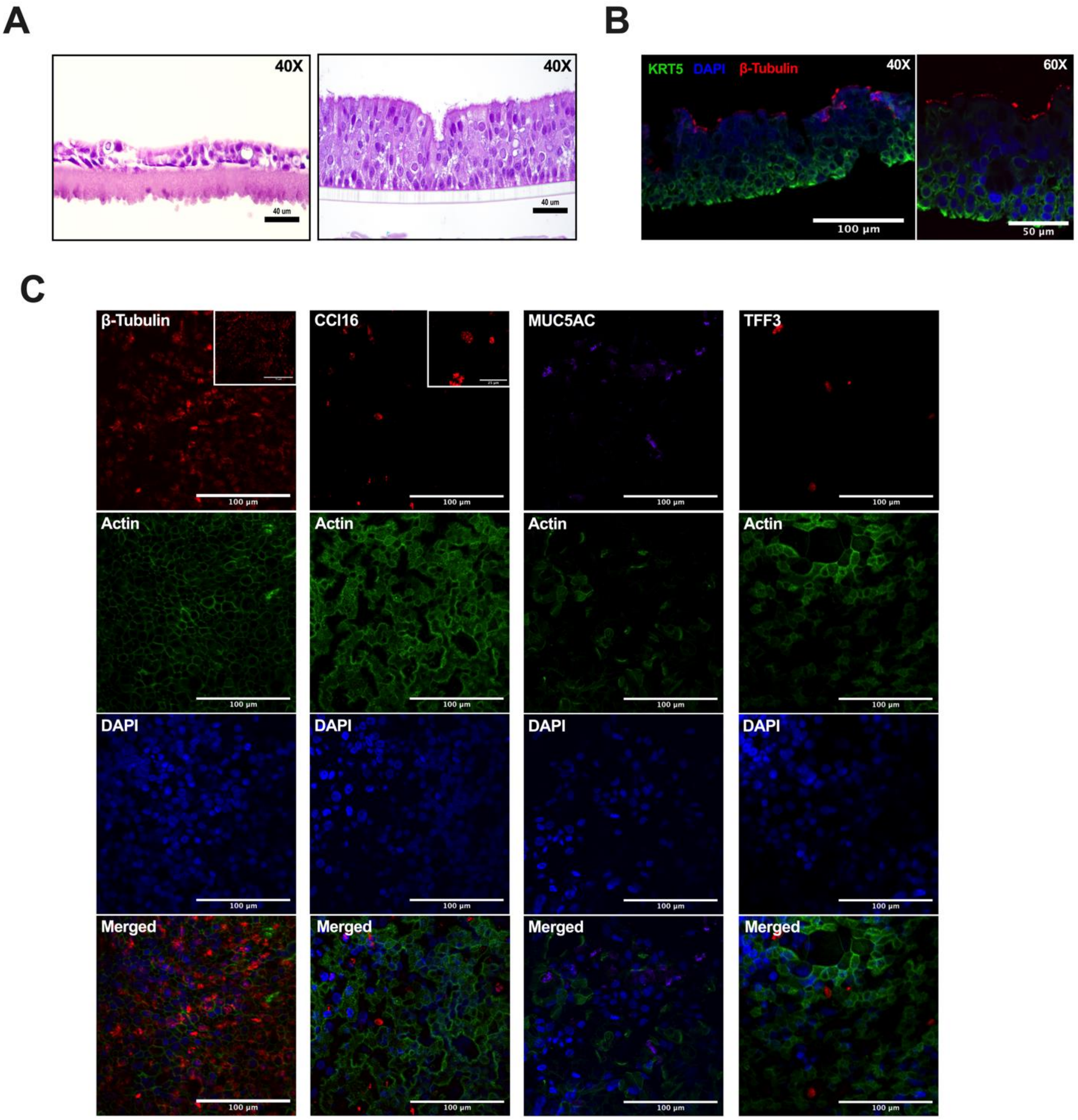
A
40X
40 um
40X
40 um
B
KRT5 DAPI β-Tubulin
40X
100 µm
60X
50 µm
C
β-Tubulin
CCl16
MUC5AC
TFF3
Actin
Actin
Actin
Actin
DAPI
DAPI
DAPI
DAPI
Merged
Merged
Merged
Merged
100 µm

Figure 3.5. Characterization of FLUAV cell receptors, replication and and binding in differentiated BCi-NS1.1 cells. (A) ALI cultured BCi-NS1.1 cells were fixed with 4% paraformaldehyde and stained for α 2,3- (red) and α 2,6- (green) sialic acids (SA) distribution. Images were captured using Nikon confocal microscope with NIS Elements software at 60X. A 3D construction of the cell distribution with DAPI (cell nuclei; blue) staining was generated using NIS Elements software. **(B)** ALI cultured BCi-NS1.1 cells were infected with 1 MOI of each virus. Samples were collected from the apical part of the tranwell at 0-, 12-, 24-, 48-, and 72 hours post inoculation. The samples were then titrated by TCID50. Viruses are distinguished by difference in color (Ca04: orange, Oh/04: blue, WF10: green). **(C)** Virus binding of Ca04 and WF10 was assessed in MDCK and differentiated BCi-NS1.1 cells. Binding was performed by inoculating each cell line with 100 MOI of virus followed by an incubation at 4C for 30 min. Cells were then washed and fixed in 4% paraformaldehyde. Cells were stained via immunofluorescence for α 2,3-SA (red), α 2,6-SA (green), DAPI, and virus HA (purple).

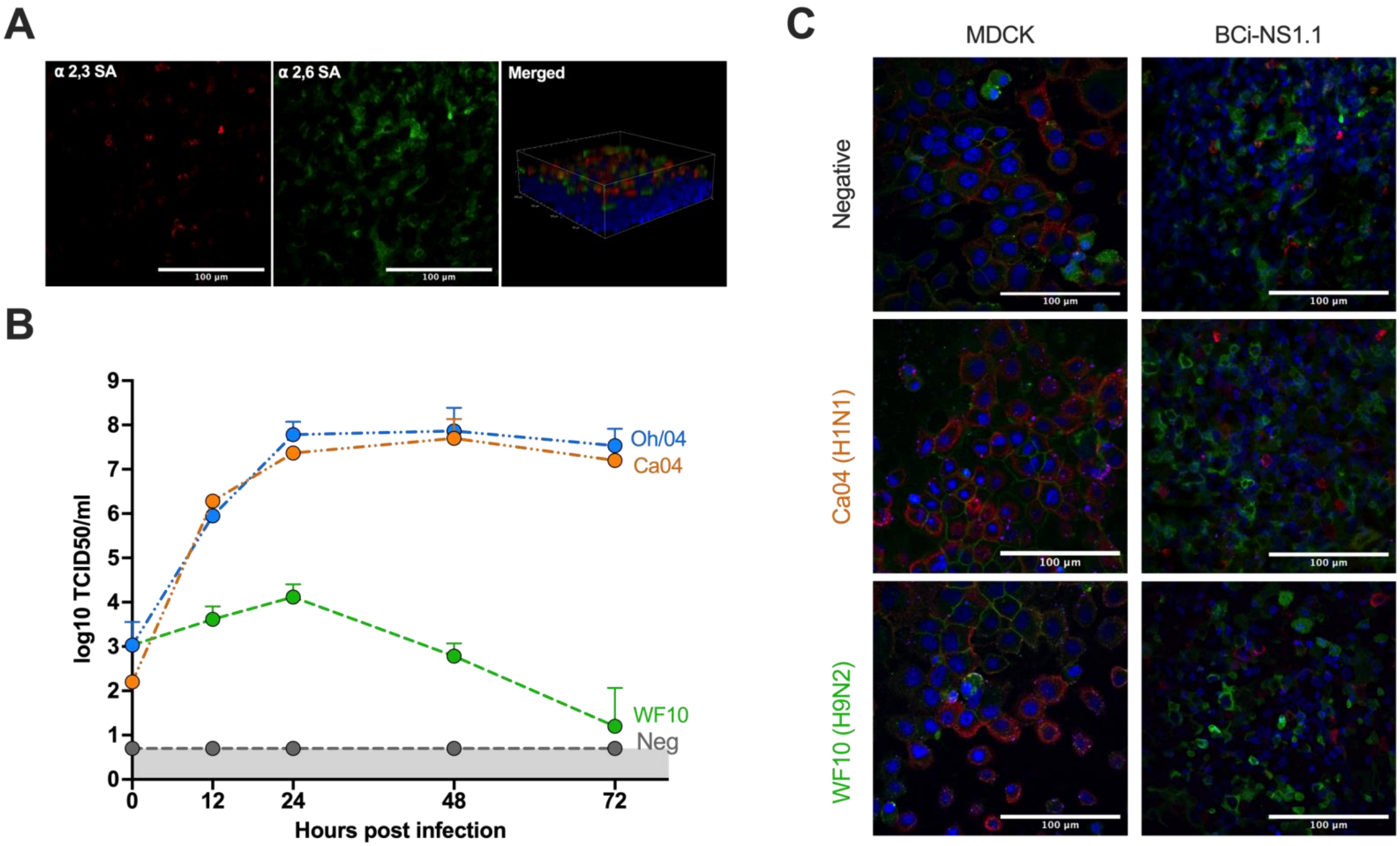
A
α 2,3 SA
α 2,6 SA
Merged
100 µm
100 µm
B
log10 TCID50/ml
9
8
7
6
5
4
3
2
1
0
0
12
24
48
72
Hours post infection
Oh/04
Ca04
WF10
Neg
C
MDCK
BCi-NS1.1
Negative
Ca04 (H1N1)
WF10 (H9N2)
100 µm

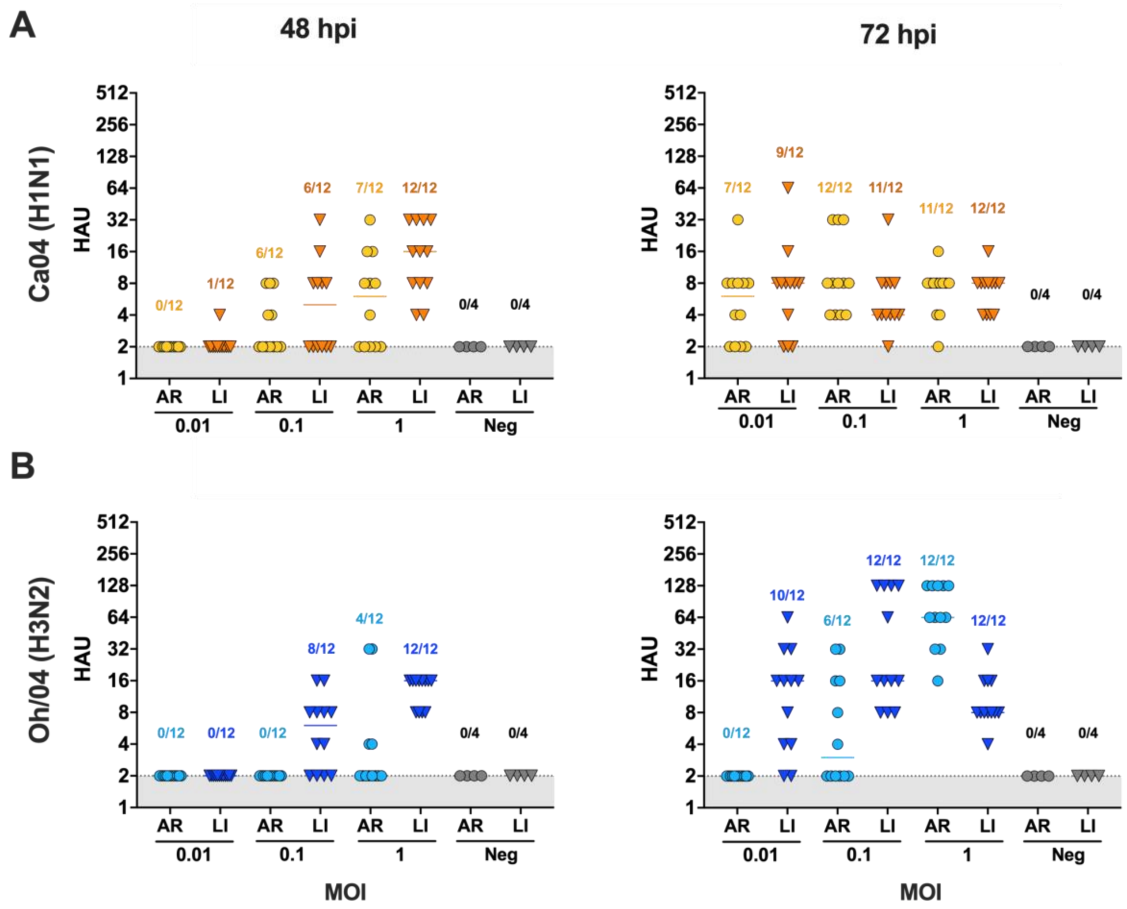

Figure 3.6. Hemagglutination (HA) assay titration of Ca04, and Oh/04 FLUAV post aerosol and liquid inoculation in differentiated BCi-NS1.1 cells. Differentiated BCi-NS1.1 cells were inoculated via aerosol (AR; circles) or liquid (LI; triangles) of ten-fold dilutions from 1 MOI of **(A)** Ca04 (H1N1) or **(B)** Oh/04 (H3N2). Cell culture supernatant was collected at 0-, 12-, 24- , 48-, and 72-hours post inoculation. The first two three points (0-, 12-, and 24-hpi) resulted in HAU below the limit of detection and are therefore not shown. Each point represents that HAU from 1 well. Numbers above the points represent the number of wells considered positive / total number of wells. Wells with HAU > 2 were considered positive. Viruses are distinguished by difference in color (Ca04: orange and Oh/04: blue). AR = aerosol; LI = liquid.

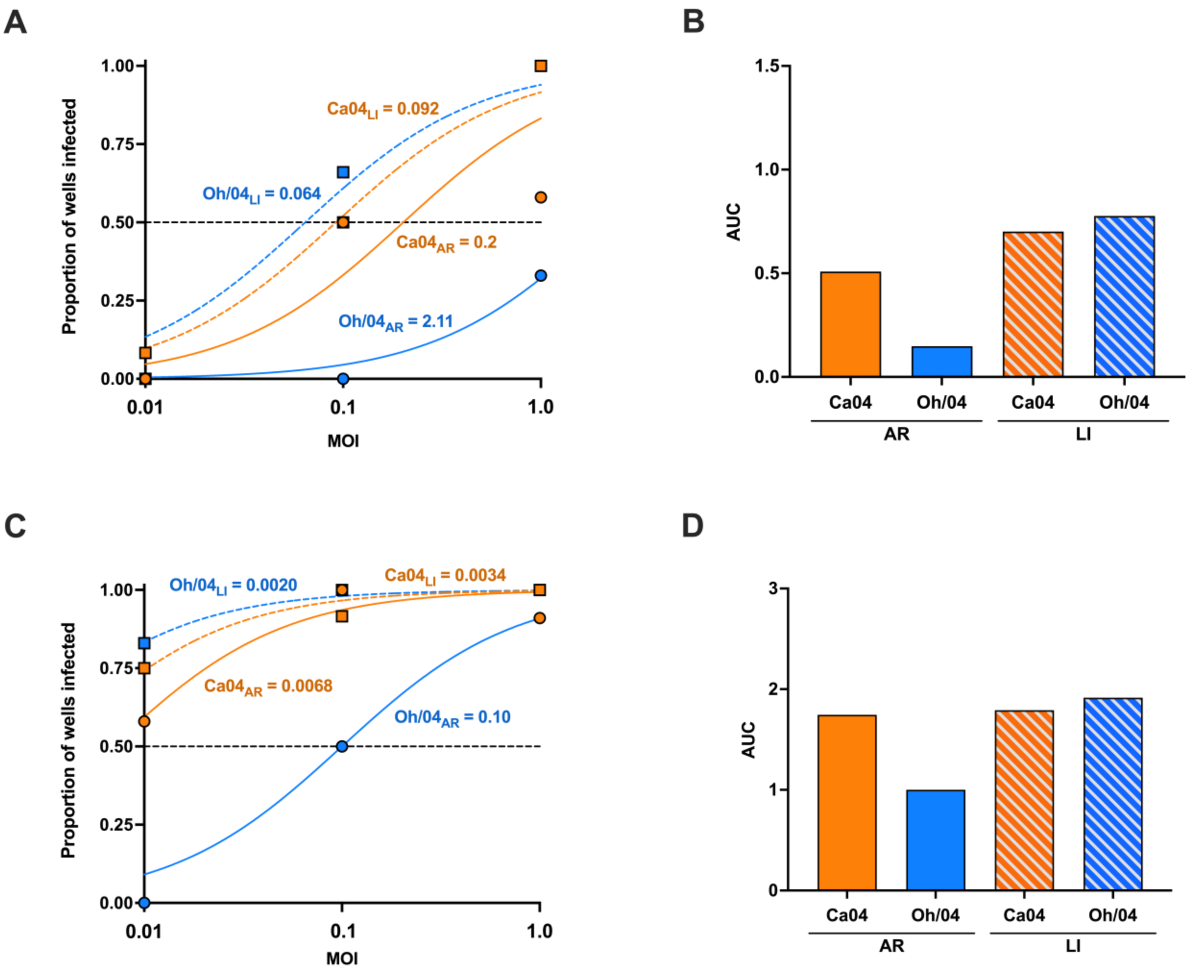

Figure 3.7. Graphical representation of the non-linear regression model from differentiated BCi-NS1.1 cells infected with liquid or aerosolized FLUAV. At **(A)** 48 hours post inoculation (hpi) or **(C)** 72 hpi, the proportion of wells with HAU greater than 2 and their respective dilution factor were graphed in a non-linear regression model to calculate the half maximal effective concentration (EC50). The EC50 are displayed in text. Solid lines indicate aerosol exposure while dashed lines represent liquid inoculation. Viruses are distinguished by difference in color (Ca04: orange and Oh/04: blue). The area under the curve (AUC) from the non-linear regression for **(A)** 48 hpi or **(B)** 72 hpi is represented in a bar graph. AR = aerosol; LI = liquid.

Table 3.1. Aerosol exposure system parameters used for the calculation of different of total virus in aerosol (C_{aer}), total virus passing through the chamber during an exposure (N_{cham}), and the exposure dose per well (ED). The flow rate of HEPA filtered air entering the exposure chamber was a total of 16 L/min while the flow rate for the SKC Biosampler was 12.5 L/min and the NIOSH biosampler was 3.5 L/min adding to a total 16 L/min. Since the input and output were the same, this coefficient was not used in the calculations.

Parameters	**Coefficient**	**Units**
Determining Exposure Dose		
Inoculum Volume (V_{samp})	6	mL
Flow rate of nebulizer (Q_{samp})	0.1	mL/min
Time (t)	15	min
Flow rate of chamber (input = output so this coefficient was not used)*		
Surface area of well in 6 well plate (SA_{6well})	9.6	cm^2
Surface area of 1 transwell (12 well plate) ($SA_{Transwell}$)	1.1	cm^2
Cross sectional area of exposure chamber (XA)	16,710.4	cm^2
Normalizing SKC BioSampler Concentrations		
Sampler Volume (V_{samp})	10	mL
Flow rate of Sampler (Q_{samp})	12.5	L/min
Time (t)	15	min
Normalizing NIOSH (> 4 µM)		
Sampler Volume (V_{samp})	4	mL
Flow rate of Sampler (Q_{samp})	3.5	L/min
Time (t)	15	min
Normalizing NIOSH (1-4 µM)		
Sampler Volume (V_{samp})	1.5	mL
Flow rate of Sampler (Q_{samp})	3.5	L/min
Time (t)	15	min
Normalizing NIOSH (< 1 µM)		
Sampler Volume (V_{samp})	4	mL
Flow rate of Sampler (Q_{samp})	3.5	L/min
Time (t)	15	min

Table 3.2. Total virus in aerosol, total virus passing through the chamber during an exposure, exposure dose per well, and aerosol infectious dose 50 calculation for each virus exposed via aerosol in MDCK cells.

		Dilution from MOI 1				
		10^{-2}	**10^{-3}**	**10^{-4}**	**10^{-5}**	**10^{-6}**
Ca04 (H1N1)	Inoc ^{1} (TCID50/mL)	11,000.0	1,100.0	110.0	11.0	1.1
	# of positive wells / total wells ^{1}	6/6	6/6	3/6	0/6	0/6
	Total virus in aerosol (C_{aer}^{1})	44,000.0	4,400.0	440.0	44.0	4.4
	Total virus through chamber (N_{cham} ^{1})	660,000.0	66,000.0	6,600.0	660.0	66.0
	Exposure dose (ED ^{1})	3,793.1	379.3	37.9	3.8	0.4
	AID_{50} = 37.9 TCID50/well					
	Inoc ^{2} (TCID50/mL)	12,400.0	1,240.0	124.0	12.4	1.2
	# of positive wells / total wells ^{2}	6/6	5/6	1/6	0/6	0/6
	Total virus in aerosol (C_{aer} ^{2})	49,600.0	4,960.0	496.0	49.6	5.0
	Total virus through chamber (N_{cham} ^{2})	744,000.0	74,400.0	7,440.0	744.0	74.4
	Exposure dose (ED ^{2})	4,275.9	427.6	42.8	4.3	0.4
	*AID_{50} = 138.3 TCID50/well - **Average AID50 = 88.1 TCID50/well***					
Oh/04 (H3N2)	Inoc ^{1} (TCID50/mL)	12,200.0	1,220.0	122.0	12.2	1.2
	# of positive wells / total wells ^{1}	6/6	1/6	2/6	0/6	0/6
	Total virus in aerosol (C_{aer}^{1})	48,800.0	4,880.0	488.0	48.8	4.9
	Total virus through chamber (N_{cham} ^{1})	732,000.0	73,200.0	7,320.0	732.0	73.2
	Exposure dose (ED ^{1})	4,206.9	420.7	42.1	4.2	0.4
	AID_{50} = 866.6 TCID50/well					
	Inoc ^{2} (TCID50/mL)	12,400.0	1,240.0	124.0	12.4	1.2
	# of positive wells / total wells ^{2}	6/6	1/6	0/6	0/6	0/6
	Total virus in aerosol (C_{aer} ^{2})	49,600.0	4,960.0	496.0	49.6	5.0
	Total virus through chamber (N_{cham} ^{2})	744,000.0	74,400.0	7,440.0	744.0	74.4
	Exposure dose (ED ^{2})	4,275.9	427.6	42.8	4.3	0.4
	*AID_{50} = 1,018.0 TCID50/well - **Average = 942.3 TCID50/well***					
WF10 (H9N2)	Inoc ^{1} (TCID50/mL)	12,400.0	1,240.0	124.0	12.4	1.2
	# of positive wells / total wells ^{1}	6/6	4/6	0/6	0/6	0/6
	Total virus in aerosol (C_{aer}^{1})	49,600.0	4,960.0	496.0	49.6	5.0
	Total virus through chamber (N_{cham} ^{1})	744,000.0	74,400.0	7,440.0	744.0	74.4
	Exposure dose (ED ^{1})	4,275.9	427.6	42.8	4.3	0.4
	AID_{50} = 275.8 TCID50/well					
	Inoc ^{2} (TCID50/mL)	19,600.0	1,960.0	196.0	19.6	2.0
	# of positive wells / total wells ^{2}	6/6	4/6	1/6	0/6	0/6
	Total virus in aerosol (C_{aer} ^{2})	78,400	7,840.0	784.0	78.4	7.8
	Total virus through chamber (N_{cham} ^{2})	1,176,000.0	117,600.0	11,760.0	1,176.0	117.6
	Exposure dose (ED ^{2})	6,758.6	675.9	67.6	6.8	0.7
	*AID_{50} = 340.9 TCID50/well - **Average = 308.3 TCID50/well***					

Table 3.3. Total virus in aerosol, total virus passing through the chamber during an exposure, exposure dose per well, and aerosol infectious dose 50 calculation for each virus exposed via aerosol in differentiated BCi-NS1.1 cells

		MOI		
		1	**0.1**	**0.01**
Ca04 (H1N1)	Inoc ^{1} (TCID50/mL)	3,710,000.0	371,000.0	37,100.0
	# of positive wells / total wells ^{1}	6/6	6/6	4/6
	Total virus in aerosol (C_{aer}^1)	14,840,000.0	1,484,000.0	148,400.0
	Total virus through chamber ($N_{cham}{}^1$)	222,600,000.0	22,260,000.0	2,226,000.0
	Exposure dose (ED ^{1})	146,587.6	14,658.8	1,465.9
	AID_{50} = 723.2 TCID50/well			
	Inoc ^{2} (TCID50/mL)	3,710,000.0	371,000.0	37,100.0
	# of positive wells / total wells ^{2}	5/6	6/6	3/6
	Total virus in aerosol ($C_{aer}{}^2$)	14,840,000.0	1,484,000.0	148,400.0
	Total virus through chamber ($N_{cham}{}^2$)	222,600,000.0	22,260,000.0	2,226,000.0
	Exposure dose (ED ^{2})	146,587.6	14,658.8	1,465.9
	AID_{50} = 1,351.0 TCID50/well - ***Average AID50 = 1,037.1 TCID50/well***			
Oh/04 (H3N2)	Inoc ^{1} (TCID50/mL)	3,410,000.0	341,000.0	34,100.0
	# of positive wells / total wells ^{1}	6/6	2/6	0/6
	Total virus in aerosol (C_{aer}^1)	13,640,000.0	1,364,000.0	136,400.0
	Total virus through chamber ($N_{cham}{}^1$)	204,600,000.0	20,460,000.0	2,046,000.0
	Exposure dose (ED ^{1})	134,734.2	13,473.4	1,347.3
	AID_{50} = 21,506 TCID50/well			
	Inoc ^{2} (TCID50/mL)	3,410,000.0	341,000.0	34,100.0
	# of positive wells / total wells ^{2}	6/6	4/6	0/6
	Total virus in aerosol ($C_{aer}{}^2$)	13,640,000.0	1,364,000.0	136,400.0
	Total virus through chamber ($N_{cham}{}^2$)	204,600,000.0	20,460,000.0	2,046,000.0
	Exposure dose (ED ^{2})	134,734.2	13,473.4	1,347.3
	AID_{50} = 8,665 TCID50/well - ***Average AID50 = 15,085.5 TCID50/well***			

Acknowledgements

This study was supported by was supported by a subcontract from the Center for Research on Influenza Pathogenesis (CRIP) to DRP under contract HHSN272201400008C from the National Institute of Allergy and Infectious Diseases (NIAID) Centers for Influenza Research and Surveillance (CEIRS) and the Caswell S. Edison endowment fund, University of Georgia.

CHAPTER 4

THE EFFECT OF BACITRACIN METHYLENE DISALICYLATE-SUPPLEMENTED FEED ON AVIAN INFLUENZA VIRUS SHEDDING, BODY WEIGHT GAIN, AND THE OROPHARYNGEAL AND CLOACAL MICROBIOME IN BROILER CHICKENS

Brittany Seibert, C. Joaquin Caceres, Stivalis Cardenas Garcia, Silvia Carnaccini, Ginger Geiger, Lucia Ortiz, Jong Suk Mo, L. Claire Gay, Flavio Cargnin Faccin, Jo Anne Crum-Bradley, Daniela Rajao, Elizabeth Ottesen, and Daniel R. Perez.

To be submitted to *Poultry Science*.

Abstract

Outbreaks of avian influenza virus (AIV) can have detrimental effects on poultry flocks resulting in mortality and indirect costs because of eradication efforts, control, and loss of markets. The role of the microbiota in essential physiological processes and disease progression has expanded recently. While it has been shown that the intestinal microbiota affects AIV infection, it is not well-known how altering the intestinal microbiota will affect AIV replication and shedding. Extensive literature reports indicated that various antibiotic growth promoters (AGPs) change the composition and diversity of the microbiota at different parts of the avian intestinal tract. While the literature is rich in the relationship between AGPs and the intestinal microbiota, little is known about the effect of AGP-induced microbiota changes on AIV shedding. Therefore, we explored the potential impact of a widely used AGP (Bacitracin methylene disalicylate (BMD)) on AIV shedding and weight gain in broiler chickens. Results showed limited differences in virus shedding among the groups with and without BMD supplementation. Further, changes within the taxonomic abundance in the oropharyngeal and cloacal microbiota were observed. Understanding the relationship between AGP-induced microbiota changes and AIV infection will further increase our comprehension of the microbiota's impact on AIV infection in poultry.

Introduction

Outbreaks of avian influenza virus (AIV) can have extensive detrimental effects on poultry flocks resulting in direct costs due to mortality and indirect costs because of eradication efforts, control, and loss of markets (3). The natural hosts of influenza A viruses (FLUAV) are wild aquatic birds; however, sporadic spillover into domestic poultry species may cause severe disease (10). Spillover has been previously reported for some H5Nx, H7Nx, and H9N2 AIV viruses (10, 22-24). While the pathotype of AIV of the H5 and H7 subtypes have been associated with high pathogenicity avian influenza viruses (HPAIV), H9N2 AIV is the most prevalent low pathogenicity avian influenza viruses (LPAIVs) and is widespread around the world in waterfowl, shorebirds, and numerous species of domestic poultry (10, 13, 242). Although infection with H9N2 AIV can be mild, clinical signs in chickens are associated with a drop in water and food intake, lower egg production, reduced eggshell quality, and deterioration of the eggshell leading to significant economic losses (10, 13, 243, 244). Further, H9N2 infections in chickens can increase susceptibility to secondary infections such as *Salmonella enteritidis* and *Chlamydia psittaci* (245, 246). Common respiratory signs associated with mild cases of H9N2 infections in chickens include swelling of the sinuses and discharge of the eyes, nares, and mouth; conversely, birds with severe cases develop dyspnea and have difficulty breathing (13, 243). H9N2 AIV is prevalent in poultry throughout Asia, the Middle East, and North Africa but is also a cause of concern to human health as H9N2 AIV are zoonotic agents and gene donors to other influenza virus subtypes (238, 247, 248). H9N2 AIV has contributed internal gene segments to zoonotic strains such as H5N1/N6, H7N9, and H10N8/N3, which resulted in human infections (16, 17). Further, H9N2 AIV has been reported in multiple mammalian species, such as dogs, mink, swine, and horses (10, 14, 15, 19, 249). Generally, H9N2 AIV infections in humans present mild influenza-like symptoms such as coughing, fever, nasal discharge, sore throat, and headache (13, 14). Recently, a 30-year-old female was found positive for H9N2 AIV in China, potentially caused by the transfer of fomites from a nearby live poultry market (250). Therefore, investigating different host factors that affect AIV H9N2 shedding in domestic poultry is paramount in AIV disease control.

Multiple factors have been shown to affect the spread and infectivity of FLUAV, including the host residential microbiome. As the availability of non-culture techniques to study microbiome interactions increase, knowledge on the role of the microbiota in essential physiological processes and disease progression has significantly expanded. Multiple studies in human and animal models, including mice, ferrets, and pigs, have reported that the respiratory and intestinal microbiome changes during FLUAV infection, most notably enrichment of opportunistic pathogens such as *Staphylococcus* (144, 145, 148, 154). Changes in the intestinal microbial composition were also shown to affect the host interaction with FLUAV; for example, studies in mice demonstrated that antibiotic-induced depletion of the gut microbiota composition resulted in increased susceptibility to FLUAV infection and mortality (174, 251). A shift in the fecal microbiome has also been observed in chickens infected with H9N2 AIV, particularly an increase in Proteobacteria phylum and genera V*ampirovibrio, Pseudoflavonifractor, Ruminococcus, Clostridium cluster XIVb* and *Isobaculum* (180). The notable role of the intestinal microbiota during AIV infection in chickens has been further demonstrated in a previous study that showed increased virus shedding and compromised immune responses in chickens administered antibiotics for microbiome depletion compared to non-depleted controls; additionally, the adverse effects of AIV infection in antibiotic-treated chickens were reversed by treatment with probiotics (*Lactobacillus spp*.) or a fecal microbial transplant (FMT), restoring immune responses during AIV infection (180, 252). Chickens with a depleted microbiome also had significantly down-regulated type I interferon responses in the respiratory and intestinal tissues but significantly higher antibody titers and IgG levels in the serum (180). In a follow-up study, chickens that received antibiotics for 16 days for microbial depletion had higher cloacal virus shedding and reduced type I interferon and IL-22 expression, while antibiotic-depleted chickens with probiotics or fecal microbial transplant showed reduced virus shedding and restored IL-22 expression (181). Altogether, the residential gut microbes can modulate the innate and adaptive immune response and affect virus shedding during H9N2 AIV infection in chickens.

While previous studies showed that the intestinal microbiota affects FLUAV infection, it is not understood how altering the intestinal microbiota before infection will affect viral replication and shedding. Multiple environmental factors can induce changes in the intestinal microbiome, such as diet, which can also be manipulated to induce these changes. Antibiotic growth promoters (AGPs) are antimicrobials administered at low, sub-therapeutic doses in animal feed to increase production in agricultural species, primarily in poultry (211, 253). Various AGPs change the composition and diversity of the microbiota in different parts of the avian intestinal tract, leading to an increase or decrease in specific bacterial species (211, 253-260). Crisol-Martinez et al. showed that zinc bacitracin increased the microbial diversity in the cecum with large shifts, primarily in *Lactobacillus* species (257). Alternately, enramycin was associated with decreased diversity, and Virginiamycin was associated with the enrichment of Faecalibacterium and *Lactobacillus* spp. (253). While the mechanisms of AGPs are not fully understood, they have been used for several decades to promote faster growth and feed conversion rates, increase disease resistance, and reduce mortality (211, 257). However, there has been recent pressure to discontinue AGPs because of the concern for the emergence of antimicrobial resistance (261). The European Union prohibited antibiotics for growth in 2006, and the FDA implemented a program to eliminate the use of all medically important antimicrobials for production purposes since 2017 (http://eur-lex.europa.eu/en/index.htm) (262). However, AGPs are continuously used in other countries because they provide the greatest feed conversion ratio and contain preventative properties against specific poultry diseases (253, 257).

Although AGP-induced changes in the intestinal microbiome have been previously associated with growth and protection against enteric pathogens, it is currently unknown if these changes could affect the susceptibility to a respiratory pathogen, such as AIV. Therefore, we used Bacitracin methylene disalicylate (BMD) to analyze the effect of AGP administration on virus shedding, growth performance, and the respiratory and intestinal microbiome composition post H9N2 AIV infection in broiler chickens. The results show limited differences in virus shedding among the groups with and without BMD supplementation. Analysis of residential microbiota showed the most notable changes within the oropharyngeal (OP) microbiota compared to the cloaca (CL) and feces. Within the OP, AIV infection with BMD supplementation more heavily impacted the microbial diversity than without BMD supplementation; however, AIV infection was the primary factor influencing OP microbial dysbiosis. Meanwhile, taxonomic differences were observed among the different groups within the CL during peak virus infection. On the other hand, limited differences were observed with the fecal microbiota compared to the OP and CL microbial diversity and composition.

Materials and Methods

Ethics Statement

Animal studies were conducted and approved by the Institutional Animal Care and Use Committee (IACUC) at the University of Georgia (Protocol A2019 03-032-Y2-A9). The infection study was conducted under animal biosafety level (ABSL) 2 conditions at the Poultry Diagnostic and Research Center (PDRC).

Cells and virus

Virus stocks of A/Guinea fowl/Hong Kong/WF10/99 (WF10, H9N2) were generated in 10-day-old specific pathogen-free (SPF) embryonated chicken eggs. Madin-Darby canine kidney (MDCK) cells, a kind gift from Robert Webster (St. Jude Children's Research Hospital, Memphis, TN, USA), were used for AIV titration. Virus stocks were titrated by tissue culture infectious dose 50 ($TCID_{50}$), and virus titers were established by the Reed and Muench method (227). Cells were maintained in Dulbecco’s Modified Eagles Medium (DMEM, Sigma-Aldrich, St Louis, MO, USA) containing 10% fetal bovine serum (FBS), Sigma-Aldrich, St. Louis, MO, USA), 1% antibiotic/antimycotic (AB, Sigma-Aldrich, ST Louis, MO, USA) and 1% L-Glutamine (Sigma-Aldrich, St Louis, MO, USA). Cells were cultured at 37°C under 5% CO2.

Chickens

One-day-old Ross/Ross 708 broiler chickens were allocated into isolators (n = 6 chicks/isolator). Isolators were randomly assigned into two groups with four repetitions per treatment: control (no AGP) and Bacitracin Methylene Disalicylate (BMD, 50g/ton, Zoetis, NJ, USA). All animals received a standard all-grain diet (Start N-Grow (FB), Southern States, GA, USA) from 1 to 26 days of age with or without supplemented BMD. Antibiotic growth promoters were given to the chickens throughout the study starting at 1 day of age. Weight gain was recorded at 1, 5, 8, 12, 15, 19, 22, and 26 days of age. At 5 days of age, serum samples from sixteen chicks were collected to determine if the chicks had previous exposure to FLUAV by ELISA against the nucleoprotein (NP) (IDEXX, Westbrook, ME, USA). At 8 days of age, chicks from the control (no BMD) isolators were inoculated with 500 µL (100 µL in each eye, 2 drops in each nare, 2 drops in the trachea, and orally) of phosphate buffer solution (PBS) (n = 12 chicks/isolators, 2 isolators total, Mock group) or 1 x 10^6 $TCID_{50}$ of WF10 (n = 12 chicks/isolators, 2 isolators total, AIV group). Similar to the control group, isolators given BMD were also inoculated with PBS (n = 12 chicks/isolators, 2 isolators total, Mock-BMD group) or 1 x 10^6 $TCID_{50}$ of WF10 (n = 12 chicks/isolators, 2 isolators total, AIV-BMD group). Chickens were monitored daily for 21 days post-infection (dpi). Oropharyngeal (OP) and cloacal (CL) swabs were collected at 1, 3, 5, 7, 14, and 21 dpi to analyze virus shedding and the residential microbiome composition. Swabs collected for virus shedding were collected in 1 mL of Brain heart infusion (BHI) broth containing Gentamicin solution (50mg/mL, Sigma-Aldrich, MO, USA) and frozen immediately at -80°C. Swabs collected for microbiome analysis were frozen immediately at -80°C. Terminal bleeding was performed at the end of the experimental study at 21 dpi, and sera were analyzed for antibody titers by hemagglutination inhibition (HI) assay as described below.

Virus Shedding

RNA was extracted from the swabs and virus stock using the MagMax-96 AI/ND viral RNA isolation kit (ThermoFisher Scientific, MA, USA) following the manufacturer's protocol. The amount of virus RNA was determined by one-step real-time quantitative PCR (RT-qPCR) using primers M+25 (AGATGAGTCTTCTAACCGAGGTCG) and M-124 (TGCAAAAACATCTTCAAGTCTCTG) targeting the Nucleoprotein. A probe with FAM as a reporter and TAMRA as a quencher was used (56-FAM/TCA GGC CCC CTC AAA GCC GA/36-TAMSp). The RT-qPCR was performed using a Quantabio qScript XLT One-Step RT-qPCR ToughMix kit (Quantabio, MA, USA) in a 20 µL final reaction volume on the QuantStudio 3 Real-Time PCR System (ThermoFisher Scientific, MA, USA). Each reaction contained 1X master mix, 0.5 µM of each primer, 0.3 µM probe, and 5 µL of RNA. The qPCR cycling conditions were 50°C, 20 min; 95°C, 1 min, 40 cycles at 95°C, 1 min; 60°C, 1 min; and 72°C 1s; with a final cooling step at 4°C. A standard curve was generated using a 10-fold serial dilution of the WF10 virus stock of known titer to correlate RT-qPCR crossing point (Cp) values with the viral load from the swabs. RNA virus loads were calculated as Log_{10} TCID50 equivalents/mL (263). Infectious virus shedding was determined by tissue culture infectious dose 50 (TCID_{50}) using the Reed and Muench method (227). Infectious virus shedding and viral RNA loads were plotted using Prism v9.4.1 (GraphPad Software, CA, USA).

Hemagglutination Inhibition (HI) Assay

Whole blood was collected and then centrifuged at 1000 x g for 15 min at room temperature. Sera was then collected and stored at -80°C until further processing. Sera was pre-absorbed with a 10% suspension of chicken red blood cells (chRBC), specifically 50 µL of serum was mixed with 100 µL of 1X PBS and 50 µL of 10% chRBC and incubated at room temperature for 30 min. During the incubation, the samples were mixed every 10 min. Following, erythrocytes were allowed to settle down at 4°C for 2 h. The treated sera were then collected and brought to a final dilution of 1:10. The HI assay was performed using four hemagglutination units (HAU) of viral antigen per 25 µL as previously described (264). Succinctly, two-fold serial dilutions were prepared by mixing 25 µL of the 10-fold diluted sera with 25 µL of 1X PBS in a V-bottomed microtiter plate. Following, 4 HAU (in 25 µL) of WF10 was added to each sera dilution and incubated for 15 min at room temperature. Next, 50 µL of 0.5% suspension of chRBC was added to the mix and incubated for 45 min at room temperature. The HI titer for each sample was interpreted as the highest dilution that showed complete hemagglutination inhibition. The HI titers were expressed as dilution values and plotted using Prism v9.4.1.

DNA extraction

DNA was extracted from the OP and CL swabs by using the MoBio Power Soil kit (Qiagen, Gaithersburg, MD) with minor changes according to the earth microbiome protocol as follows: additional incubation at 65 °C for 10 min after the addition of solution C1, beads were shaken at 20Hz for 20 min instead of 10 min, and samples were incubated at 4°C for 10 min instead of 5 min and then stored at -80°C until further processing.

Amplicon library preparation and sequencing

The V4 hypervariable region of the 16S rRNA gene was amplified using Phusion Hot Start 2 DNA polymerase (Thermo Fisher, Waltham, MA) using primers 515F (59-GTGCCAGCMGCCGCGGTAA-39) and 806R (59-GGACTACHVGGGTWTCTAAT-39) in 20 µl PCR reaction (8.9 µl of molecular-grade water, 4 µl of 5X HF buffer, 0.4 µl of 10mM deoxynucleoside triphosphates [dNTPs], 1.25 µl of 10 mM 515F, 1.25 µl of 10 mM 806R, 4 µl of DNA, and 0.2 µl of polymerase) under the following conditions: 98°C (30 s), followed by 25 cycles of 98°C (10 s), 52°C (30 s), and 72°C (30 s), a final elongation step at 72°C (5 min), and held at 4°C. The PCRs were performed in duplicates and then visualized on a 1% agarose gel. Duplicate PCR products of the same sample were pooled in equal volumes, cleaned by 0.45X Agencourt AMPure XP magnetic beads (Beckman Coulter, CA, USA) according to the manufacturer's protocol, and eluted in molecular biology grade water (Genesee Scientific, CA, USA). Amplicon concentration was measured using the Qubit dsDNA HS assay kit (Thermo Fisher) on a Qubit 3.0 fluorometer (Thermo Fisher). DNA concentrations were normalized to 1.0 ng/ml. Subsequently, amplified DNA was used in a secondary amplification/dual barcode annealing reaction. Forward and reverse dual barcode primers (primers and barcodes with different reference indexes) were designed based on primers by Caporaso et al. (265). Secondary amplification reactions were performed using NEBNext high-fidelity 2X PCR master mix (NEB) in 50 µl reactions (26 µl of 2X mix, 20.5 µl of water, 2.5 µl of barcoded forward and reverse primers [10mM], 1 µl of DNA) under the following conditions: 98°C (30 s), followed by four cycles of 98°C (10 s), 52°C (10 s), and 72°C (10 s), followed by 6 cycles of 98°C (10 s) and 72°C (1 min), followed by a final extension of 72°C (2 min) and then held at 4°C. According to the manufacturer's protocol, samples were subsequently cleaned by 0.45X of Agencourt AMPure XP magnetic beads and eluted in molecular biology-grade water. Fragment size distribution was analyzed on a subset of samples using the Agilent Bioanalyzer 2100 DNA-HS assay (Agilent, Santa Clara, CA, USA). Sample libraries were then normalized and pooled to a concentration of 2 nM based on a predicted total product size of 420 base pair (bp) using the Qubit dsDNA HS assay kit on the Qubit 3.0 fluorometer. The loading concentration of the pooled libraries was 8 pM. Libraries were sequenced using Illumina MiSeq V2 chemistry (Illumina, San Diego, CA), 2 by 250 paired-end. Negative controls, including DNA extraction and PCR blank, were included in each sequencing run (7 runs total).

Data analysis

Primer removal and demultiplexing were performed using Illumina BaseSpace using default settings. Initial sequencing analysis was performed using open-source software QIIME 2 (v.2020.11) (223). Each sequencing batch was processed separately until chimera removal. For each batch, the quality of the raw paired-end reads was visualized and then used to determine the appropriate truncation of read 1 (R1) by 14 bp (left) and 188 bp (right) while read 2 (R2) by 40 bp (left) and 129 (right). Trimming, denoising, merging, and chimera removal were performed using Dada2 with the function *dada2 denoise-paired* (266). Taxonomy was assigned using the function *feature-*

classifier classify-sklearn in Qiime2 using a pre-trained classifier from the Silva v.38 database specific for the 515F/806R region (267, 268). A count table and taxonomy file used for downstream analysis were created from .qza files using RStudio (version 2022.07.2) package ‘qiime2R’ (269, 270). The OP swabs generated 9,829,906 reads, averaging 58,862 reads / sample. For the CL swabs, a total of 10,111,040 reads with an average of 60,545 reads / sample, while for feces, a total of 2,039,360 reads with an average of 36,417 reads / sample were generated. Samples were then filtered to remove amplicon sequence variants (ASV) with non-classified phylum or classified as Chloroplast or Mitochondria using the package ‘phyloseq’ (version 1.38.0) (271). Further, ASV found in less than 1% of samples were removed to avoid potential contaminants in diversity estimates. Post-filtering, an average of 43,715 reads/sample were generated for OP swab samples, 59,248 reads/sample for CL samples, and 33,882 reads/sample for fecal samples (Fig 4.1A).

Bioinformatic Analysis

Alpha diversity, examined by the observed number of ASV and Shannon diversity, was calculated using rarified counts using phyloseq. Briefly, all samples were rarified to 19,111 reads using the command *rrarefy* in the vegan package (version 2.6.4) (272). Rarefaction plots were generated using phyloseq.extended package (version 0.1.1.6) and edited using ggplot2 package (version 3.3.6) and edited using ggplot2 package (version 3.3.5) (273). Rarefaction curves showed a similar number of observed species among the reads, suggesting adequate coverage (Figs 4.1B-D). The rarified counts were imported into phyloseq, and diversity indexes were calculated using command *estimate richness*. Results were graphed using the ggpubr package (version 0.4.0) (274). Statistical comparison across groups was performed using the Kruskal-Wallis, while the Wilcox rank test with Bonferroni correction was used for pair-wise comparisons.

Regarding beta diversity, a non-metric multidimensional scaling (NMDS) plot showing unweighted Jaccard and weighted Bray-Curtis dissimilarity metrics were calculated with 3 dimensions, a maximum of 500 random starts, and 999 maximum iterations using the rarified count data. NMDS plots and ellipses based upon the standard deviation were illustrated using *ordiellipse* from the vegan package. Multivariate statistics analysis, permutational multivariate analysis of variance (PERMANOVA), was calculated using beta diversity distances with 999 permutations using vegan *adonis2* assessing the marginal effects of the terms.

Relative abundances at the phylum and lowest classified level were generated using package phyloseq. For the phylum taxonomic barplot, ASVs were agglomerated to the phylum level and then transformed into relative abundances using phyloseq. Taxa with an overall prevalence of less than 1% were grouped. For the taxonomic barplot incorporating the lowest classification, relative abundances were calculated using phyloseq, and taxa with an overall prevalence of less than 1% were grouped. The final plots were combined using Prism (v 9.1.0).

Differential analysis among groups of taxa at the genus level was performed using linear discriminant analysis effect size (LEfSe) (275). ASVs in less than 20% of samples with a total abundance of fewer than 10 reads were removed for all differential analyses. Rarified counts were inputted, and a p-value < 0.05 was considered significant.

Graphs/Statistical analyses

Statistical analysis, including two-way ANOVA and generation of graphs/figures, was performed using GraphPad Prism software version 9.3 (GraphPad Software Inc., San Diego, CA). A p-value < 0.05 was considered significant. Graphs were also edited using PDF Expert (Readdle Inc, Odesa, Ukraine) and Affinity Photo (Serif, West Bridgford, United Kingdom).

Results

The administration of BMD post-AIV H9N2 infection led to increased weight gain

At the start of the experiment, one-day-old broiler chickens were divided into two groups: 50% of the chickens were fed a recommended standard start-n-grow diet, while the other 50% of chickens were fed the standard diet with supplemented BMD (50 g/ton) (Fig 4.2A). At 8 days of age, the chickens were further divided into four groups: AIV-BMD chickens were infected with 1 x 10^6 $TCID_{50}$/chick of AIV WF10 H9N2 and fed a supplemented BMD diet, while AIV chickens were infected with AIV but fed the standard diet. Mock-BMD chickens were administered 1X PBS and fed a supplemented BMD diet, while the mock was fed a standard diet (Fig 4.2A). Assessment of humoral responses to AIV before infection revealed undetectable antibody responses (enzyme-linked immunosorbent assay (ELISA)), suggesting that the chickens had not been previously exposed to AIV. Prior to AIV infection, individual weights across groups were similar; however, AIV-BMD chickens had significantly higher weight at 19 days of age (11 dpi, $p = 0.04$, 2-way ANOVA), 22 days of age (14 dpi, $p = 0.025$, 2-way ANOVA), and 26 days of age (18 dpi, $p = 0.049$, 2-way ANOVA) compared to the mock controls

(Fig 4.2B). Comprehensively, a significant weight increase was observed starting 11 days post AIV infection when chickens were supplemented with BMD compared to the mock controls.

In addition to weight change, OP and CL swabs were collected to analyze infectious AIV shedding and viral RNA (vRNA) loads. Within the OP swabs, infectious virus was highest at 1 dpi, followed by 3 dpi and then 5 dpi (Fig 4.3A). No statistically significant differences between the two groups were observed. However, one bird from the AIV-BMD group was shedding infectious virus at 5 dpi compared to no birds within the FLUAV group (Fig 4.3A). Similar viral RNA loads in the OP swabs among both groups were detected at 1, 3, 5, and 7 dpi (Fig 4.3A). Conversely, no infectious AIV and vRNA loads were observed at all dpi in CL swabs of the AIV group (Fig 4.3B). Within the AIV-BMD group, one bird shed infectious virus and had detectable vRNA loads at 1 and 3 dpi (Fig 4.3B). When analyzing humoral response at 21 dpi, similar antibody responses (hemagglutination inhibition (HI)) was observed regardless of the diet (Fig 4.3C). Collectively, similar virus titers and vRNA loads were detected among the two groups except for prolonged infectious virus within the OP and shedding in the CL among the birds supplemented with BMD in their diet.

AIV infection in combination with BMD supplementation alters the composition of the oropharyngeal microbiota

To characterize the OP microbiome in chickens, we sequenced the V4 region of 16S rRNA genes amplified from OP swabs collected at -1, 1, 3, 5, 7, 14, and 21 dpi. Alpha diversity (observed number of amplicon sequence variants (ASVs)), Shannon diversity, and Simpson evenness index were calculated across dpi (Fig 4.4A-C). As the chicks' age increased, the number of observed ASVs increased in all groups (Fig 4.4A). Notably, the observed number of ASVs within the AIV-BMD group was higher than the mock, starting at 5 dpi and continuing until 21 dpi; however, the comparison between the two groups was only statistically significant at 14 dpi (p=0.026; Wilcox) (Fig 4.4A). Similar to the observed number of ASVs, Shannon diversity was significantly larger in the AIV-BMD (p=0.026; Wilcox) and AIV (p=0.026; Wilcox) group compared to the mock at 5 dpi and continued until 21 dpi, although not significant (Fig 4.4B). The AIV-BMD (p = 0.026; Wilcox) and AIV (p = 0.026; Wilcox) groups also had significantly larger Simpson indexes at 5 dpi; however, diversity indexes were similar at 7, 14, and 21 dpi (Fig 4.4C). To evaluate changes in the OP microbial composition post-AIV infection, we analyzed beta diversity using unweighted Jaccard and weighted Bray-Curtis's dissimilarity metrics through non-metric multidimensional scaling (NMDS) ordination. Both ordinations showed distinct clustering of the pre-infected samples compared to the other samples (Jaccard: R2 = 0.067, p <0.01; Bray: R2 = 0.10, p < 0.01; PERMANOVA) (Fig 4.4D-E). In addition, separated clustering by group during infection (1, 3, 5, and 7 dpi), particularly the AIV-BMD and AIV chickens, is observed notably in the unweighted dissimilarity metric (Jaccard: R2 = 0.13, p < 0.01; Bray: R2 = 0.17, p <0.01; PERMANOVA) (Fig 4.4F). Days post-infection (Jaccard: R2 = 0.057, p<0.01; Bray: R2 = 0.080, p<0.01: PERMANOVA) was also considered a significant factor affecting ordination clustering along with the interaction between groups and dpi (Jaccard: R2 = 0.054, p<0.05; Bray: R2 = 0.052, p<0.01: PERMANOVA). When analyzed separately, both BMD supplementation (Jaccard: R2= 0.033, p<0.01; Bray: R2 = 0.038, p<0.01;

PERMANOVA) and AIV infection (Jaccard: R2 = 0.077, p<0.01; Bray: R2 = 0.11, p <0.01; PERMANOVA) were considered significant factors in effecting ordination clustering. While the study included both males and females within the population, sex (Jaccard: R2 = 0.014, p=0.11; Bray: R2 = 0.016, p = 0.12; PERMANOVA), and different isolators (cage effect) (Jaccard: AIV-BMD: R2=0.040, p = 0.12; AIV: R2 = 0.038, p = 0.15; Mock-BMD: R2 = 0.039, p = 0.12; Mock: R2 = 0.030, p = 0.40; PERMANOVA) were not considered to have a significant effect on the ordination clustering. Overall, AIV infection with BMD supplementation more heavily impacts the OP microbial diversity than without BMD supplementation; however, AIV infection is the primary factor influencing OP microbial dysbiosis.

At the phylum level, the OP microbiota was primarily classified into Firmicutes (mean (x̄): AIV-BMD: 71.8%, AIV: 70.8%, Mock-BMD: 65.5%, and Mock: 63.9%) and Proteobacteria (x̄: AIV-BMD: 27.3%, AIV: 28.3%, Mock-BMD: 32.9%, and Mock: 33.5%) when all dpc were combined (Fig 4.5A). When examining each dpi separately, all groups had similar relative abundances of the two phyla (Fig 4.5B). However, both AIV-infected groups at 5 dpi, particularly the AIV group compared to the Mock-BMD (p = 0.026; Wilcox), have decreased relative abundances of Proteobacteria compared to the mock controls (x̄: AIV-BMD: 21.3%, AIV: 10.9%, Mock-BMD: 38.0%, Mock: 45.9%) (Fig 4.5B). A difference in relative abundance was also observed at lower taxonomic levels (Fig 4.5C). When all dpi is combined, *Pseudomonas* had the largest relative abundance in both AIV-infected groups (x̄: AIV-BMD: 17.8%, AIV: 21.8%, Mock-BMD: 9.04%, Mock: 7.6%) while *Escherichia-Shigella* was the most prevalent in both mock controls (x̄: AIV-BMD: 8.4%, AIV: 11.2%, Mock-BMD: 18.3%, Mock: 20.07%).

We performed differential abundance testing at the genus level using linear discriminant analysis effect size (LefSE). When comparing the mock controls fed a standard diet to chickens fed a diet supplemented with BMD including all dpi, Firmicutes genera including *Bacillus* (p=0.00031), *Lactobacillus* (p=0.0096), and *Enterococcus* (p=0.033) were enriched within the mock controls while *Lachnospiraceae GCA_900066575* (p=0.045), *Incertae Sedis* (p=0.042), and *Pediococcus* (p=0.0022) were enriched within the group supplemented with BMD. Proteobacteria genera, including *Enydrobacter* (p=0.0090), were enriched within the mock, while *Proteus* (0.014) and *Massilia* (p=0.0020) were enriched in the chickens supplemented with BMD. When comparing the mock controls and the AIV group during peak virus infection (1dpi-7dpi), Firmicutes genera *Chryseobacterium* (also significantly enriched (sigEn) at 14 dpi; p=0.00093), *Lactobacillus* (SigEn at 14 dpi; p=0.00014), *Pediococcus* (SigEn at 1 and 7 dpi, p=0.00048), and *Oscillospiraceae UCG-005* (SigEn at 1 and 3 dpi; p=0.00067) were enriched within the mock controls while Firmicutes genera *Clostridium sensu stricto 5* (SigEn at 1 and 3 dpi; p=0.0087), *Eisenbergiella* (SigEn at 5 and 7 dpi; p=0.00090), *Lachnospiraceae GCA_900066576* (SigEn at 5, 7, 14, and 21 dpi; p=0.0020), *Lachnosclostridium* (SigEn at 5 and 21 dpi; p=0.039), *Lachnospiraceae UCG-004* (SigEn at 5 and 7 dpi; p=0.0088), *Colidextribacter* (SigEn at 5 and 21 dpi; p=0.020), *Flavonifractor* (SigEn at 5 dpi, p=0.033), *Pseudoflavonifractor* (SigEn at 5 and 21 dpi; p=0.0091), *Incerta Sedis* (SigEn at 5 and 21 dpi; p=0.0028), Negativibacillus (p=0.043), and *Acinetobacter* (SigEn at 3 dpi; p=0.0046), were enriched within the AIV group. In between 1 and 7 dpi, the largest number of significant taxa reported when comparing the mock and AIV group was observed at 3 dpi; however, 21 dpi had the greatest number of different significant taxa between the two groups when analyzing all days sampled. Numerous other genera were considered significantly different among the mock and AIV group; however, these genera were also significantly different before infection and were therefore not considered a result of AIV infection (data not shown). Comparison between the AIV group and AIV-BMD groups during infection (1-7 dpi) showed enrichment of Firmicutes genera *Bacillus* (SigEn at 3 and 5 dpi; p=4.87E-6), *Enterococcus* (SigEn at -1, 1 and 3 dpi; p=0.0015), *Lactobacillus* (SigEn at -1, 3, 5, and 14 dpi; p=1.97E-5), *Eisenbergiella* (SigEn at 3 and 5 dpi; p=0.005), and *Flavonifractor* (SigEn at 5 dpi; p=0.0045), and Proteobacteria genus *Dechloromonas* (SigEn at -1, 1, and 3 dpi; p=0.0016) within the AIV group. Meanwhile, *Pediococcus* (SigEn at 3 dpi; p=0.032), *Weisella* (SigEn at -1 and 1 dpi; p = 0.024), *Clostridia UCG-014* (SigEn at 5 and 14 dpi; p=0.019), *Clostridium sensu stricto 1* (SigEn at 3 dpi; p=0.017), *Eubacterium halli group* (SigEn at 3 and 5 dpi; p=0.017), *Blautia* (p=0.0079), *Sellimonas* (p=0.039), UCG-005 (SigEn at 1 dpi; p=0.014), *Caproiciproducens* (SigEn at 3 dpi; p=0.035), *DTU089* (SigEn at 3 dpi; p=0.043), and Proteobacteria genera *Sphingobium* (p=0.021), *Massilia* (SigEn at -1, 3, 5, 21 dpi; 0.0024; p=0.0024), *Pantoeae* (SigEn at -1, 3, 5, and 7 dpi; p=0.0028), *Proteus* (SigEn at 3 and 5 dpi; p=0.0026), and *Enydrobacter* (SigEn at -1, 5, 7, and 14 dpi; p = 7.46E-5) were enriched within the AIV-BMD group. Overall, taxonomic differences were observed among the different groups, including those that differed by BMD supplementation and/or AIV infection within OP swabs collected during peak virus infection.

AIV infection alters the composition of the cloacal microbiota more than supplementation of BMD

The V4 region of 16S rRNA genes amplified from the CL swabs collected at -1, 1, 3, 5, 7, 14, and 21 dpi were sequenced and analyzed to examine changes within the CL microbiota post-AIV infection with BMD supplementation. Similar to the OP swabs, alpha diversity (observed number of ASVs) increased as the chicks' age increased in all groups (Fig 4.6A). There was no significant difference among the groups and observed number of ASVs across all time points (Fig 4.6A). However, the Shannon diversity of the AIV-BMD group was significantly larger than the AIV group 1 day before infection (Fig 4.6B), while it was similar at all other dpi among all groups (Fig 4.6B). The Shannon diversity was higher in the AIV-BMD group at 5 dpi; however, this was not statistically significant ($p > 0.05$; Wilcox) (Fig 4.6B). Contrarily, the AIV-BMD group had a significantly lower Simpson index compared to the mock at 3 dpi ($p = 0.026$; Wilcox), and the Mock-BMD group had a significantly lower Simpson index compared to the mock at 14 dpi ($p = 0.026$; Wilcox) (Fig 4.6C). To investigate changes in the CL microbial composition post-AIV infection, we analyzed beta diversity using unweighted Jaccard and weighted Bray-Curtis’s dissimilarity metrics through NMDS ordination. Similar to the OP swabs, both ordinations showed distinct clustering of the pre-infected samples compared to the other samples (Jaccard: $R2 = 0.036$, $p<0.01$; Bray: $R2 = 0.052$, $p<0.01$: PERMANOVA) (Fig 4.6D-E). When analyzing the groups during infection (dpi 1, 3, 5, and 7), beta diversity using NMDS ordination plots showed limited clustering of groups in unweighted (Jaccard) and weighted (Bray-Curtis) dissimilarity metrics (Fig 4.6F); however, PERMANOVA analysis showed significant differences by group

(Jaccard: R2 = 0.074, p<0.01; Bray: R2 = 0.083, p<0.01: PERMANOVA) and dpi (Jaccard: R2 = 0.037, p<0.05; Bray: R2 = 0.046, p<0.05: PERMANOVA) but not the interaction of both factors (Jaccard: R2 = 0.022, p=0.84; Bray: R2 = 0.018, p=0.84: PERMANOVA). When examined individually, BMD supplementation was considered significant in unweighted distances but not weighted distances (Jaccard: R2 = 0.024, p=0.034; Bray: R2 = 0.025, p=0.055: PERMANOVA), while AIV infection was considered a significant factor in effecting both unweighted and weighted dissimilarity distances (Jaccard: R2 = 0.034, p<0.01; Bray: R2 = 0.042, p<0.01: PERMANOVA). While the study included both males and females within the population, sex (Jaccard: R2 = 0.0040, p=0.84; Bray: R2 = 0.0033, p=0.78: PERMANOVA) and different isolators (cage effect) (Jaccard: Mock: R2 = 0.021, p = 0.40; Mock-BMD: R2 = 0.042, p = 0.13; FLUAV: R2 = 0.043, p = 0.12; AIV-BMD: R2=0.04, p = 0.11; PERMANOVA) were not considered to have a significant effect on the ordination clustering. Conclusively, AIV infection more heavily impacts the CL microbial diversity than BMD supplementation but is less clear than changes observed within the OP.

When analyzing taxonomic differences at the phylum level, the CL microbiota was predominantly classified into Firmicutes (x̄: AIV-BMD: 77.1%, AIV: 72.6%, Mock-BMD: 67.3%, and Mock: 69.5%) and Proteobacteria (x̄: AIV-BMD: 31.6%, AIV: 26.2%, Mock-BMD: 31.6%, and Mock: 28.2%) (Fig 4.7A). When analyzing each dpi separately, the amount of Proteobacteria increased as the dpi increased or as the age of the chicks increased (Fig 4.7B). At 1 and 3 dpi, the relative abundance of Proteobacteria was enriched in the AIV-infected groups compared to the mock controls (x̄ at 1 dpi: AIV-BMD: 93.3%, AIV: 93.5%, Mock-BMD: 72.0%, Mock: 81.4%; x̄ at 3 dpi: AIV-BMD:

88.4%, FLUAV: 91.6%, Mock-BMD: 66.3%, Mock: 84.5%); however, this relationship was also observed 1 day before infection (x̄: AIV-BMD: 81.1%, AIV: 91.6%, Mock-BMD: 62.4%, Mock: 74.9) (Fig 4.7B). Taxonomic differences at the lowest classification were also observed among different groups (Fig 4.7C). When all dpi were combined, *Escherichia-Shigella* (x̄: AIV-BMD: 20.3%, AIV: 29.0%, Mock-BMD: 23.9%, Mock: 20.2%) followed by *Romboutsia* (x̄: AIV-BMD: 16.8%, AIV: 18.9%, Mock-BMD: 21.2%, Mock: 16.6%) were the most prevalent ASVs among all groups. When comparing the mock controls fed a standard diet to chickens fed a diet supplemented with BMD, including each sample collection day, Actinobacteriota genera *Corynebacterium* (p=0.0029) and Firmicutes genera *Lactobacillus* (p=0.019), *Clostridia UCG-014* (p=0.0197), *Eubacterium coprostanoligenes group* (p-0.00096), *Flavonifractor* (p=0.049) and *Pseudoflavonifractor* (p=0.0080) was enriched within the mock group fed a standard diet. Contrastingly, Firmicutes *Staphylococcus* (p=2.73E-07) and *Romboutsia* (p=0.0053) and Proteobacteria genera *Acinetobacter* (p=8.29E-06) and *Pseudomonas* (p=0.019) were enriched with the mock group supplemented with BMD. When comparing the mock controls and the AIV group during infection (1dpi-7dpi), Actinobacteriota genera *Corynebacterium* (SigEn at 7 and 14 dpi; p= 0.00036), and Firmicutes genera Turicibacter (SigEn at 7 and 14 dpi; p=0.17), *Pediococcus* (SigEn at 3 and 14 dpi; p=0.00044), *Clostridia UCG-014* (SigEn at 3 and 5 dpi; p=0.017), *Anaerostipes* (SigEn at 1 dpi; p=0.032), *Sellimonas* (SigEn at 5 dpi; p=0.047), *Shuttleworthia* (SigEn at 3 dpi; p=0.019), *UCG-009* (p=0.040), *UCG-005* (0.0017), *Anaerotruncus* (SigEn at 5 dpi; p=0.018) were enriched within the mock control group compared to AIV infected chickens. In contrast, Firmicutes genera *Enterococcus* (p=0.037) and *Negativibacillus* (p=0.025) and Proteobacteria genus *Pseudomonas* (SigEn at 5 and 14 dpi; p=0.032) were enriched within the AIV infected group. Similar to the OP swabs, numerous other genera were considered significantly different among the mock and AIV group; however, these genera were also significantly different before infection and were therefore not considered a result of AIV infection (data not shown). Comparison between the AIV group and AIV-BMD group during infection (1-7 dpi) showed enrichment of Firmicutes genus *Enterococcus* (SigEn at 5 dpi; p=0.0073) and Lactobacillus (p=0.002) within the AIV group while Firmicutes genera Weisella (SigEn at 1 dpi; p=0.0046), Eubacterium halli group (p=0.045), Anaerostipes (SigEn at 5 dpi; p=0.027), Blautia (SigEn at 5dpi; p=0.034), Sellimonas (SigEn at 5 dpi; p=0.0064), Shuttleworthia (SigEn at 5 dpi; p=0.044), and Proteobacteria genera *Proteus* (SigEn at 7 dpi; p=0.0017) and *Pseudomonas* (p=0.025) was observed in the AIV-BMD group. Conclusively, taxonomic differences were observed among the different groups, including those that differed by BMD supplementation and/or AIV infection within cloacal swabs collected during peak virus infection.

Limited differences within the fecal microbiota post-FLUAV infection and supplementation of BMD

We sequenced the V4 region of 16S rRNA genes amplified from pooled fecal samples collected at -1, 1, 3, 5, 7, 14, and 21 dpi. When all dpi were combined, alpha diversity (observed number of ASVs), Shannon diversity, and Simpson evenness index were not significantly different among groups (Fig 4.8A-C); however, the observed number of ASVs and Shannon diversity were greater in the AIV-BMD group compared to the rest of the groups (Fig 4.8A-B). To examine changes in the fecal microbial composition post-FLUAV infection, we analyzed beta diversity using unweighted Jaccard and weighted Bray-Curtis dissimilarity metrics through NMDS ordination. Dissimilar to the OP and CL swabs, both ordinations showed limited clustering of groups (Fig 4.8D-E); however, PERMANOVA analysis exhibited significant differences by group (Jaccard: R2 = 0.13, p<0.01; Bray: R2 = 0.16, p<0.01; PERMANOVA). In addition, we observed separated clustering by group during infection (1, 3, 5, and 7 dpi), notably in the AIV group in the unweighted Jaccard metric (Fig 4.8F; R2 = 0.16, p=0.018; PERMANOVA) and AIV-BMD in the weighted Bray-Curtis metric (Fig 4.8G; R2 = 0.17, p=0.022; PERMANOVA). Days post-infection (Jaccard: R2 = 0.088, p<0.01; Bray: R2 = 0.11, p<0.01: PERMANOVA) was also considered a significant factor affecting ordination clustering but not the interaction between groups and dpi (Jaccard: R2 = 0.08, p=0.50; Bray: R2 = 0.065, p=0.67: PERMANOVA). When analyzed individually, both BMD supplementation (Jaccard: R2 = 0.051, p=0.11; Bray: R2 = 0.057, p=0.11: PERMANOVA) and infection status (Jaccard: R2 = 0.057, p=0.079; Bray: R2 = 0.058, p=0.096: PERMANOVA) were not considered significant factors in effecting ordination clustering. Different isolators (cage-effect) (Jaccard: Mock: R2 = 0.088, p = 0.39; Mock-BMD: R2 = 0.085, p = 0.41; FLUAV: R2 = 0.081, p = 0.49; AIV-BMD: R2=0.077, p = 0.48; PERMANOVA) was also not considered to have a significant effect on the ordination clustering. Overall, the combination of AIV infection with BMD supplementation more heavily impacts change in the fecal microbial diversity than AIV or BMD factors individually.

Similar to OP and CL swabs, Firmicutes (x̄: AIV-BMD: 86.86%, AIV: 75.47%, Mock-BMD: 62.84%, and Mock: 75.48%) and Proteobacteria (x̄: AIV-BMD: 13.12%, AIV: 24.52%, Mock-BMD: 36.50%, and Mock: 24.12%) were the most common phyla classified when all dpc were combined (Fig 4.9A). Overall, AIV-BMD isolators had a reduced relative abundance of Proteobacteria compared to the Mock-BMD group (p=0.018; Wilcox) (Fig 4.9A). When analyzing dpi individually, the relative abundance of Proteobacteria increases as the dpi or the chicks' age increases (Fig 4.9B). While not statistically significant, both AIV groups had reduced relative abundance of Proteobacteria at 1 (x̄: AIV-BMD: 4.17%, AIV: 0.0072%, Mock-BMD: 31.92%, and Mock: 10.19%), 3 (x̄: AIV-BMD: 0.62%, AIV: 6.42%, Mock-BMD: 21.57%, and Mock: 2.21%), and 5 (x̄: AIV-BMD: 7.12%, AIV: 9.38%, Mock-BMD: 39.57%, and Mock: 34.10%) dpi. Further, the relative abundance of Proteobacteria continued to be less in the AIV-BMD group compared to the other groups at 7 (x̄: AIV-BMD: 10.50%, AIV: 60.50%, Mock-BMD: 35.52%, and Mock: 35.98%) and 14 (x̄: AIV-BMD: 29.75%, AIV: 63.71%, Mock-BMD: 52.57%, and Mock: 36.84%) dpi. Differences in the relative abundance of fecal samples were also observed at the lowest taxonomic classification (Fig 4.9C). When all dpi were combined, *Escherichia-Shigella* had the largest relative abundance in all groups (x̄: AIV-BMD: 23.10%, AIV: 30.23%, Mock-BMD: 30.98%, Mock: 26.63%) followed by *Romboutsia* (x̄: AIV-BMD: 18.76%, AIV: 23.97%, Mock-BMD: 23.96%, Mock: 21.19%). When comparing the mock controls fed a standard diet to chickens fed a diet supplemented with BMD, including each sample collection day, Actinobacteriota genera *Lactobacillus* (p=0.017) was enriched within the mock group fed a standard diet while Colidextribacter (p=0.032) was increased in mock chickens supplemented with BMD. When comparing the mock controls and the AIV group during infection (1dpi-7dpi), Firmicutes genera *Pediococcus* (p=0.011), *Weisella* (p=0.0063), and *Shuttleworthia* (p=0.0061) were enriched within the mock group whereas Firmicutes genus *Lactobacillus* (p=0.045) and Proteobacteria genera *Acinetobacter* (p=0.027) and *Pseudomonas* (0.026) were enriched within the IAV infected chickens. Comparison between the AIV group and AIV-BMD group during infection (1-7 dpi) showed enrichment of Firmicutes genus *Lactobacillus* (p=0.0031) in the AIV group while Firmicutes genera *Pedicoccus* (p=0.015), *Weissella* (p=0.0011), *Clostridia vadin BB60 group* (p=0.015), *Shuttleworthia* (0.025), *Butyricicoccus* (p=0.027), *Oscillibacter* (p=0.016), *Incertae Sedis* (0.046) and *Proteus* (p=0.0077) were enriched within the AIV-BMD. Overall, taxonomic differences were observed among the different groups; however, the differences were more limited in the feces compared to the OP and CL swabs.

Discussion

This study investigates the effect of BMD administration on AIV infection in broiler chickens on virus shedding and its compound effect on the respiratory/intestinal microbiota in anatomical locations with detectable virus shedding. To our knowledge, no previous studies have examined the impact of BMD supplementation on common respiratory virus infections within poultry. Further, previous studies have focused mainly on the effect of BMD on the ceca with only limited analysis on the feces and small intestine (253, 254, 257, 276, 277); however, no studies to our knowledge have analyzed the effect of BMD supplementation on the OP and CL microbiota.

AGPs are hypothesized to enhance growth by modulating the gut microbiome to increase nutrient utilization, reduce inflammation, and limit the colonization of pathogens (276). BMD is commonly used in some countries for growth promotion and to treat and prevent necrotic enteritis caused by *Clostridium perfringens* (254, 278). Low doses of BMD can increase villi height within the small intestine and improve digestion leading to increased body weight and feed conversion ratio (254). BMD primarily targets gram-positive bacteria such as *Streptococci, Staphylococci, Clostridia, Fusobacterium*, and *Actinomyces* (254). It is not well-absorbed in the intestine and can therefore affect residential bacteria inducing bacterial rupture by inhibiting the dephosphorylation of pyrophosphate, which can lead to the prevention of synthesis and transport of peptidoglycan precursors resulting in defects within the cell wall (254, 279, 280). Within this study, we observed limited alpha and beta diversity differences between chickens fed a standard diet compared to those supplemented with BMD in the cloaca and feces. However, a previous study showed increased diversity within young broiler chickens (19 days) fed BMD within the distal colon but fewer changes within the cecum (254). Further, a previous report showed that chicks fed a supplemented BMD diet at 14 days and 28 days had a significantly decreased number of features but similar Shannon and Simpson diversity indexes within the cecum (280). Meanwhile, a study analyzing different anatomical locations in young (24 days) and older broilers (40 days) showed a modest impact of BMD on the community composition in numerous anatomic sites, including the gizzard, duodenum, jejunum, ileum, ceca, and colon (276). Differences in the anatomical location of the various sample sites could explain the disparity among the results. The cloaca contains a more aerobic environment than the colon; it has been reported that the microbial diversity and composition of the cloaca are distinct from the other locations within the intestinal tract, partially because the terminal parts of the urinary, reproductive, and digestive systems of birds connect to the cloaca (281). It has been previously described that the cloaca harbors a different microbiota community than the colon or magnum (281). Therefore, the dichotomy of the observations within this study and previous studies may be explained by the difference in sample type and anatomical location.

Similar to the cloaca and feces, we observed limited alpha and beta diversity differences in the OP samples among chicks fed a standard diet and those provided a BMD-supplemented diet; however, there was an increase in the number of observed ASVs as the chicks increased in age. To our knowledge, no other reports have examined the oropharyngeal microbiome of broiler chickens fed BMD-supplemented diets. The oropharyngeal microbiota primarily consisted of Firmicutes and Proteobacteria with a small relative abundance of Bacteroidota in chicks fed both diets. At lower taxonomic levels, *Escherichia-Shigella,* followed by *Pseudomonas,* were the most prevalent in both groups when all days of sampling were combined. *Escherichia coli* has been previously isolated from the trachea, air sacs, and lungs in 85% of broiler chickens (21 days of age) analyzed within the study in which the chickens showed no clinical signs of disease (282). As previously demonstrated, the buccal microbiota was mainly populated with *Lactobacillus,* while *Staphylococcus* was the most prevalent taxa in the nasal microbiota (283). Interestingly, *Bacillus, Lactobacillus, Enterococcus,* and *Enydrobacter* were enriched in the OP of chicks fed a standard diet, while *Lachnospiraceae GCA_900066575, Incertae Sedis, Pediococcus,* and *Massilia* were increased within the chicks supplemented with BMD suggesting a reduction in more beneficial bacteria such as *Lactobacillus* when BMD is added as a supplement.

Multiple reports have demonstrated that AIV infection in chickens results in a dysbiosis of the fecal microbiota (180, 181, 252). Further, microbiota depletion leads to increase virus shedding in the OP and CL post-H9N2 AIV infection (181). Within this study, the number of observed ASVs and Shannon diversity index in AIV-infected chicks was lower at 5 dpi compared to the mock controls but not significant. These results correlate with what has been observed in the cloacal microbiome of wild mallards positive for influenza virus infection (284). Within the beta diversity analysis, we observed distinct clustering from the pre-infection groups compared to the AIV-infected groups, which was also observed in fecal samples collected from chickens infected with AIV H9N2 in a previous report (180). Interestingly, alpha and beta diversity differences were more pronounced in the OP microbiome than in the CL and fecal microbiome. Shedding of H9N2 AIV occurred primarily via the OP, except for one bird that shed via the CL. Therefore, increased shedding of AIV within the OP may have a larger effect on the OP microbial environment compared to a distal location such as the CL and feces. During virus infection (1– 7 dpi), bacteria known to have beneficial effects, such as *Lactobacillus* and *Oscillospiraceae UCG-005,* were differentially enriched within the mock-infected chickens compared to those that were infected with IAV within the OP. This trend has also been previously reported in the respiratory tract of turkeys infected with AIV (285).

While extensive studies have analyzed the effect of AGPs and AIV infection in the gut microbiome of chickens, it is not well established if AGP administration affects

AIV infection. While AGPs are considered the “gold standard” of growth promoters in agriculture, there is a considerable concern due to the association of sub-therapeutic doses of antibiotics associated with the selection of antibiotic-resistant pathogens (286). However, there is limited information on the effect of low-dosage antibiotics on AIV infection. Notably, results within this study showed increased weight gain among chickens infected with AIV and supplemented with BMD compared to the mock controls. Therefore, the results suggest that AIV infection may not affect the weight gain observed when BMD is administered as an AGP. When analyzing virus shedding, similar OP virus shedding was observed for chicks fed a standard diet and those supplemented with BMD; however, OP infectious virus shedding was prolonged until 5 dpi compared to the chicks fed a standard diet. Further, one chicken fed a supplemented BMD diet shed virus via the cloaca compared to those fed a standard diet. Since BMD supplementation induces changes in specific bacteria at the taxonomic level, it may cause a similar effect to what is observed when the microbiome is depleted increasing virus replication but to a lesser extent. However, further studies are needed to examine the mechanism of the effect of AGP administration and respiratory virus infections.

In summary, we examined the effect of BMD administration on AIV infection in broiler chickens, including virus shedding and the compound effect on the respiratory/intestinal microbiota. However, several limitations of this study must be noted: while we observed differences in virus shedding among the groups with and without BMD supplementation, the study contained a relatively small size. Further, the immune response plays an essential role during early viral infection and the host microbiota; however, this study did not evaluate the immune response. Additional studies are needed to understand if AGP supplementation and its effect on the microbiome alters the host immune response during respiratory virus infection. Yet, the proof-of-principle approach of this study identifies prolonged AIV virus shedding and significant changes in the OP, CL, and fecal microbiomes of young broiler chickens when the diet is supplemented with BMD, warranting more in-depth studies on the effect of AGP administration of respiratory virus infections in agricultural species.

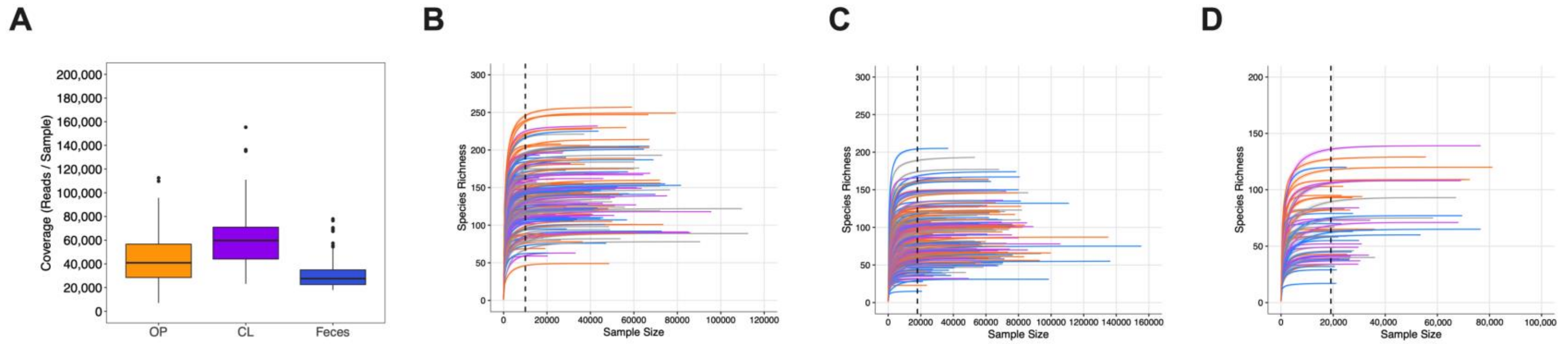

Figure 4.1. Sample Coverage and Rarefaction curves for alpha diversity analysis. (A) Sample coverage measured by the number of reads per sample separated by sample type. The samples are color-coded by sample type (Oropharyngeal: yellow, Cloaca: purple, Feces: blue). (B) Rarefaction curve of the Oropharyngeal (OP) in which samples are colored by group (AIV-BMD: orange, AIV: blue, Mock-BMD: purple, Mock: grey). The dashed line (x = 10,027) represents the number of reads each sample was rarified for downstream diversity analyses. Rarefaction curve of the cloacal (C) and feces (D) in which samples are colored by group (AIV-BMD: orange, AIV: blue, Mock-BMD: purple, Mock: grey). The dashed line (x = 17,935) represents the number of reads each sample was rarified for downstream diversity analyses.

Figure 4.2. Experimental design and body weights of chickens pre- and post-AIV infection with and without BMD supplementation. (A) At 1 day of age, chickens were divided into two groups: 50% of the chickens were fed a recommended standard start-n-grow diet, while the other 50% of chickens were fed the standard diet with supplemented BMD (50g/ton). At 5 days of age, a subset of chickens was bled and humanely euthanized to determine status of previous exposure to AIV. At 8 days of age, chickens were infected with PBS (mock controls) or 1 x 10^6 $TCID_{50}$/chick of AIV WF10 H9N2. Oropharyngeal (OP) and cloacal (CL) swabs and feces were collected at 1, 3, 5, 7, 14 and 21 dpi. At 21 dpi, remaining chickens were bled and humanely euthanized to determine antibody titers post infection. (B) Weight change was calculated for all groups pre- and post-AIV infection. Groups are color coded (AIV-BMD: orange, AIV: blue, Mock-BMD: purple, Mock: grey). Statistical analysis was performed by two-way ANOVA with a Dunnett’s multiple comparisons test, * <0.05.

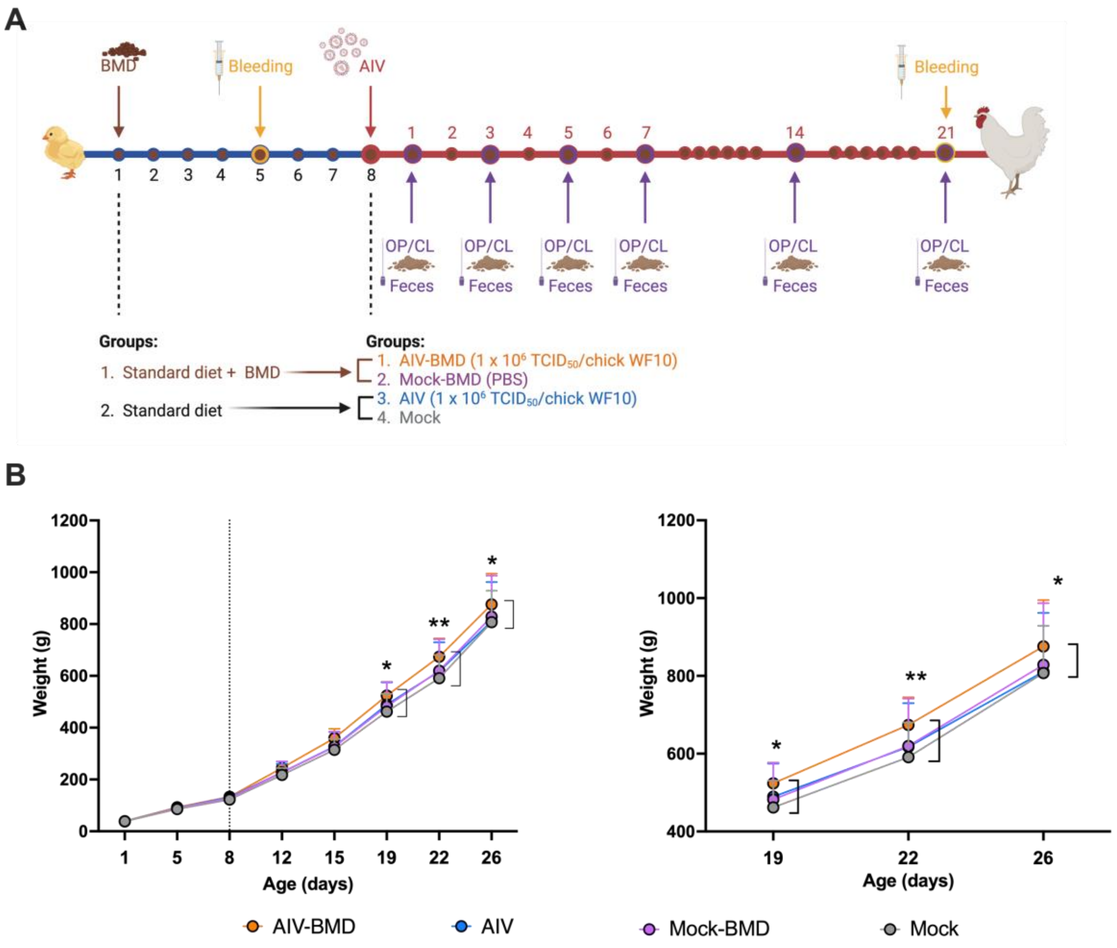
A
BMD
Bleeding
AIV
Bleeding
1 2 3 4 5 6 7 8
1 2 3 4 5 6 7 14 21
OP/CL
Feces
OP/CL
Feces
OP/CL
Feces
OP/CL
Feces
OP/CL
Feces
OP/CL
Feces
Groups:
1. Standard diet + BMD
2. Standard diet
Groups:
1. AIV-BMD (1 x 10⁶ TCID₅₀/chick WF10)
2. Mock-BMD (PBS)
3. AIV (1 x 10⁶ TCID₅₀/chick WF10)
4. Mock
B
Weight (g)
Age (days)
1200
1000
800
600
400
200
0
1 5 8 12 15 19 22 26
*
**
*
Weight (g)
Age (days)
1200
1000
800
600
400
19 22 26
*
**
*
AIV-BMD
AIV
Mock-BMD
Mock

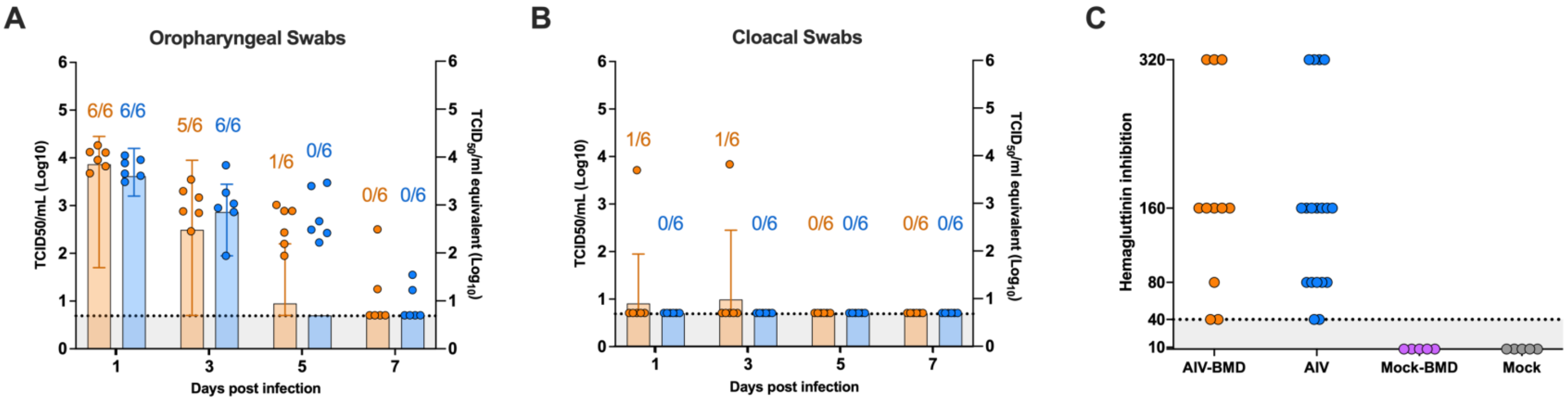

Figure 4.3. Virus shedding and antibody titers in chickens infected with AIV supplemented with and without BMD supplementation. Viral loads of the oropharyngeal (A) and cloacal (B) swabs collected at 1, 3, 5, and 7 dpi. Infectious virus titrated by TCID50 are graphed as the group mean ± standard deviation in a bar graph. Numbers above the bar graph represent the number of birds positive by TCID50. Viral RNA loads, represented by colored points, were determined by RT-qPCR and conveyed as log10 TCID50 equivalent (TCID50eq) per ml. Groups are color coded (AIV-BMD: orange, AIV: blue). (C) Hemagglutinin inhibition titers 21 days post infection.

Figure 4.4. Alpha and beta diversity of the OP in AIV-BMD, AIV, Mock-BMD and Mock chickens. Alpha diversity measure of the (A) observed number of ASVs, (B) Shannon diversity, and (C) Simpson index between AIV-BMD (orange), AIV (blue), Mock-AIV (purple), and Mock (grey) containing all dpi from the rarified ASV count table. Multiple group comparisons were performed using Kruskal-Wallis, while pair-wise comparisons were conducted using the Wilcox test with Bonferroni correction. NMDS plot of (D) unweighted Jaccard dissimilarity distance, and (E) weighted Bray-Curtis dissimilarity distance. (F) NMDS plot of unweighted Jaccard dissimilarity distance only showing 1-7 dpi. The color designates groups (AIV-BMD: orange, AIV:blue, Mock-AIV:purple, and Mock:grey), and dpi is categorized by the shape (-1 dpi: X, 1 dpi: circle, 3 dpi: square, 5 dpi: triangle, 7 dpi: diamond, 14 dpi: *, and 21 dpi: circle with X). Ellipses were constructed using the standard deviation.

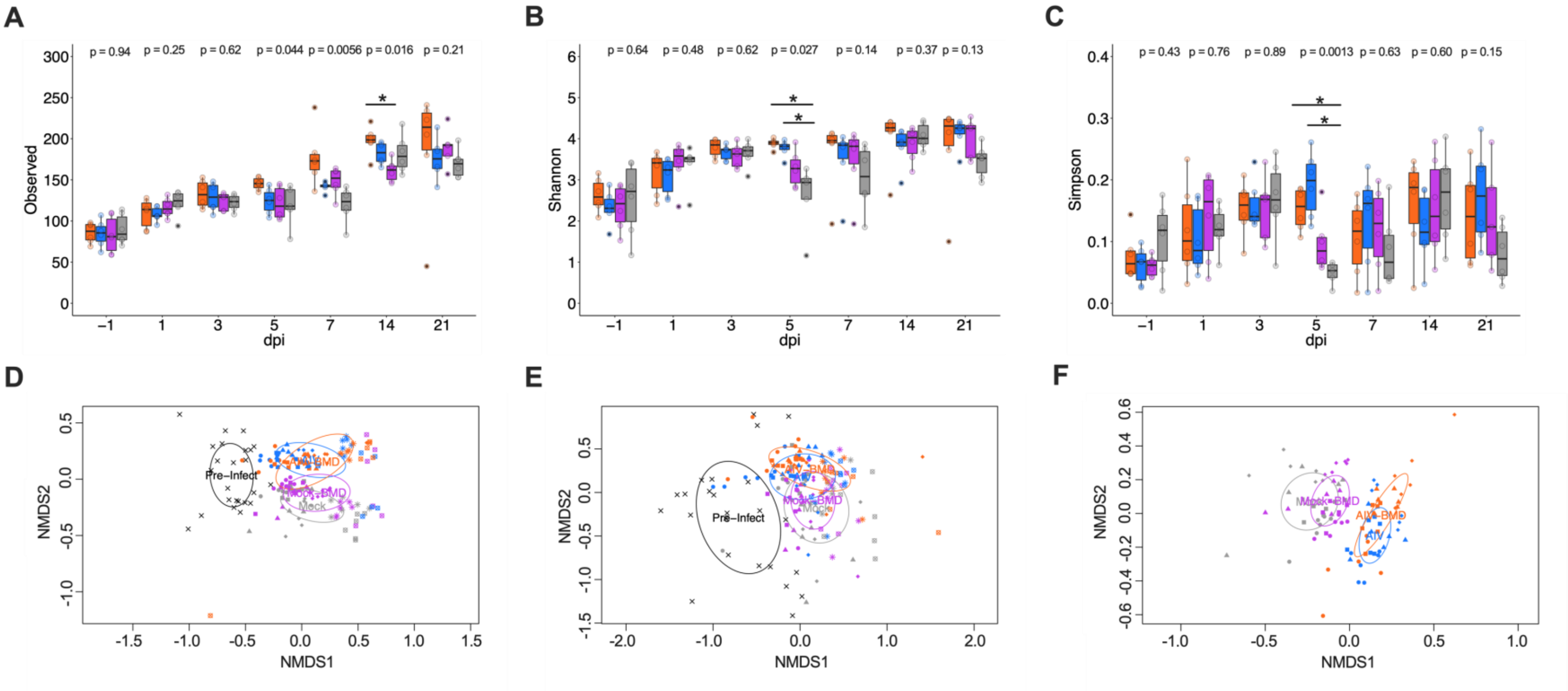
A
B
C
p = 0.94
p = 0.25
p = 0.62
p = 0.044
p = 0.0056
p = 0.016
p = 0.21
Observed
dpi
p = 0.64
p = 0.48
p = 0.62
p = 0.027
p = 0.14
p = 0.37
p = 0.13
Shannon
p = 0.43
p = 0.76
p = 0.89
p = 0.0013
p = 0.63
p = 0.60
p = 0.15
Simpson
*
−1
1
3
5
7
14
21
D
E
F
Pre−Infect
AIV-BMD
AIV
Mock-BMD
Mock
NMDS1
NMDS2

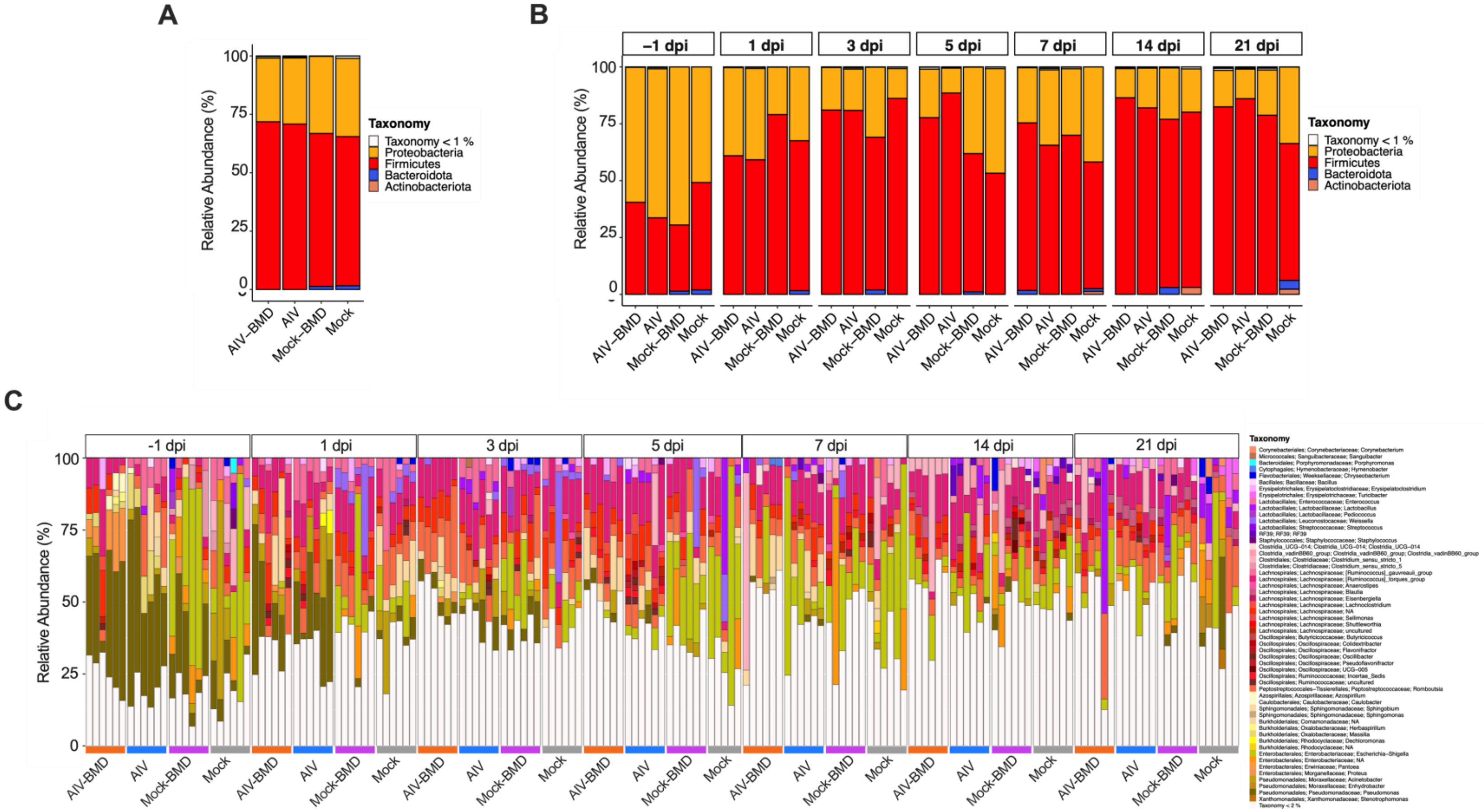

Figure 4.5 Relative abundance (%) of microbial communities of the OP at the phylum and lowest taxonomic classification. (A) Relative abundances agglomerated at the phylum level separated by group when all dpi were combined or (B) separated by dpi. (C) Relative abundances of each chicken at the lowest taxonomic rank identified separated by group and ordered by dpi.

Figure 4.6. Alpha and beta diversity of the CL in AIV-BMD, AIV, Mock-BMD and Mock chickens. Alpha diversity measure of the (A) observed number of ASVs, (B) Shannon diversity, and (C) Simpson index between AIV-BMD (orange), AIV (blue), Mock-AIV (purple), and Mock (grey) containing all dpi from the rarified ASV count table. Multiple group comparisons were performed using Kruskal-Wallis, while pair-wise comparisons were conducted using the Wilcox test with Bonferroni correction. NMDS plot of (D) unweighted Jaccard dissimilarity distance, and (E) weighted Bray-Curtis dissimilarity distance. (F) NMDS plot of unweighted Jaccard dissimilarity distance only showing 1-7 dpi. The color designates groups (AIV-BMD: orange, AIV:blue, Mock-AIV:purple, and Mock:grey), and dpi is categorized by the shape (-1 dpi: X, 1 dpi: circle, 3 dpi: square, 5 dpi: triangle, 7 dpi: diamond, 14 dpi: *, and 21 dpi: circle with X). Ellipses were constructed using the standard deviation.

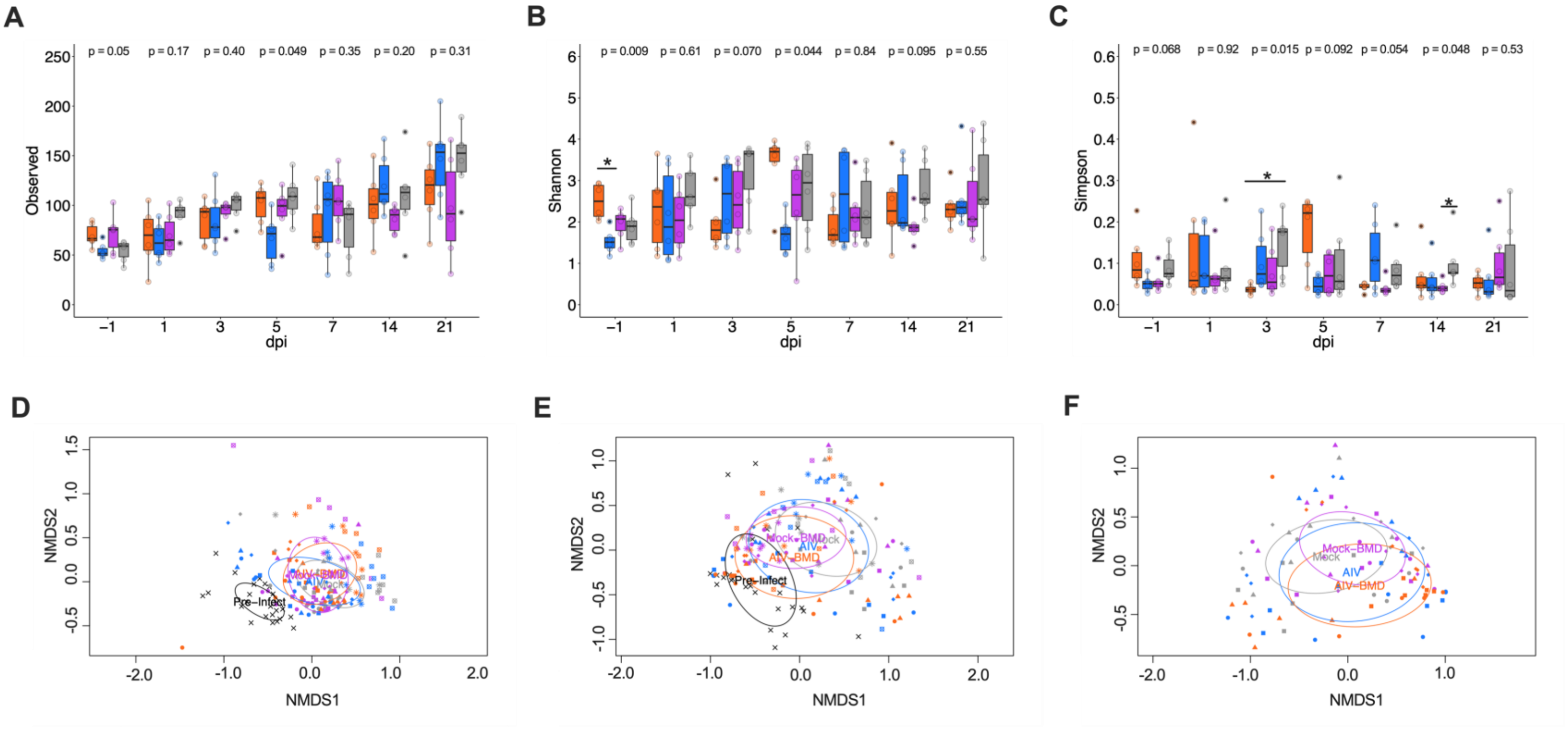
A
p = 0.05
p = 0.17
p = 0.40
p = 0.049
p = 0.35
p = 0.20
p = 0.31
Observed
250
200
150
100
50
0
−1
1
3
5
7
14
21
dpi
B
p = 0.009
p = 0.61
p = 0.070
p = 0.044
p = 0.84
p = 0.095
p = 0.55
Shannon
6
5
4
3
2
1
0
*
−1
1
3
5
7
14
21
dpi
C
p = 0.068
p = 0.92
p = 0.015
p = 0.092
p = 0.054
p = 0.048
p = 0.53
Simpson
0.6
0.5
0.4
0.3
0.2
0.1
0.0
*
*
−1
1
3
5
7
14
21
dpi
D
NMDS2
1.5
1.0
0.5
0.0
-0.5
Pre−Infect
Mock−BMD
AIV
Mock
AIV−BMD
-2.0
-1.0
0.0
1.0
2.0
NMDS1
E
NMDS2
1.0
0.5
0.0
-0.5
-1.0
Mock−BMD
Mock
AIV
AIV−BMD
Pre−Infect
-2.0
-1.0
0.0
1.0
2.0
NMDS1
F
NMDS2
1.0
0.5
0.0
-0.5
Mock−BMD
Mock
AIV
AIV−BMD
-2.0
-1.0
0.0
1.0
NMDS1

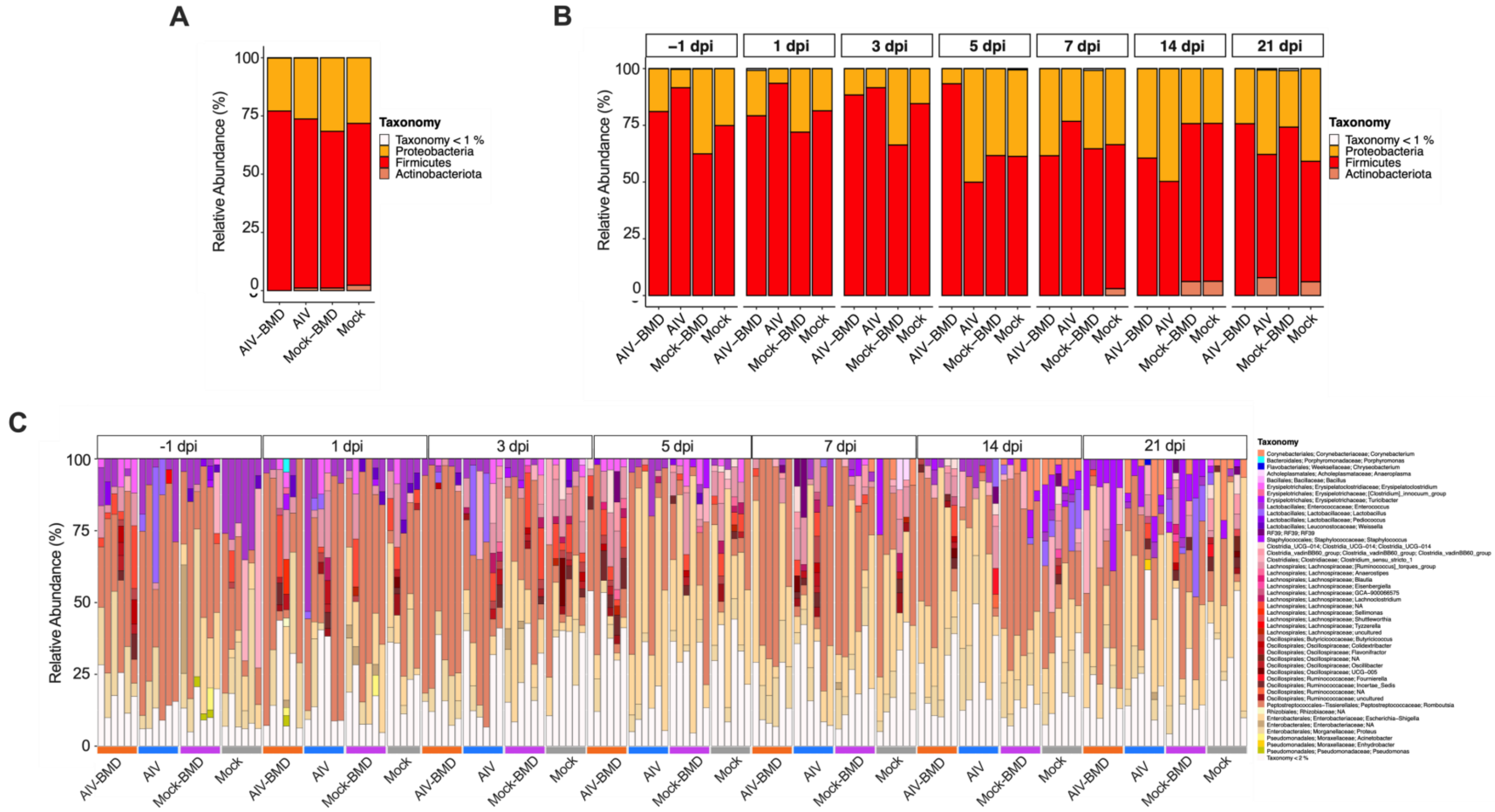

Figure 4.7 Relative abundance (%) of microbial communities of the CL at the phylum and lowest taxonomic classification. (A) Relative abundances agglomerated at the phylum level separated by group when all dpi were combined or (B) separated by dpi. (C) Relative abundances of each chicken at the lowest taxonomic rank identified separated by group and ordered by dpi.

Figure 4.8. Alpha and beta diversity Feces in AIV-BMD, AIV, Mock-BMD and Mock chickens. Alpha diversity measure of the (A) observed number of ASVs, (B) Shannon diversity, and (C) Simpson index between AIV-BMD (orange), AIV (blue), Mock-AIV (purple), and Mock (grey) combining all dpi from the rarified ASV count table. Multiple group comparisons were performed using Kruskal-Wallis, while pair-wise comparisons were conducted using the Wilcox test with Bonferroni correction. NMDS plot of (D) unweighted Jaccard dissimilarity distance and (E) weighted Bray-Curtis dissimilarity distance. NMDS plot of (F) unweighted Jaccard dissimilarity distance and (G) weighted Bray-Curtis dissimilarity distance only showing 1-7 dpi. The color designates groups (AIV-BMD: orange, AIV:blue, Mock-AIV:purple, and Mock:grey), and dpi is categorized by the shape (-1 dpi: X, 1 dpi: circle, 3 dpi: square, 5 dpi: triangle, 7 dpi: diamond, 14 dpi: *, and 21 dpi: circle with X). Ellipses were constructed using the standard deviation.

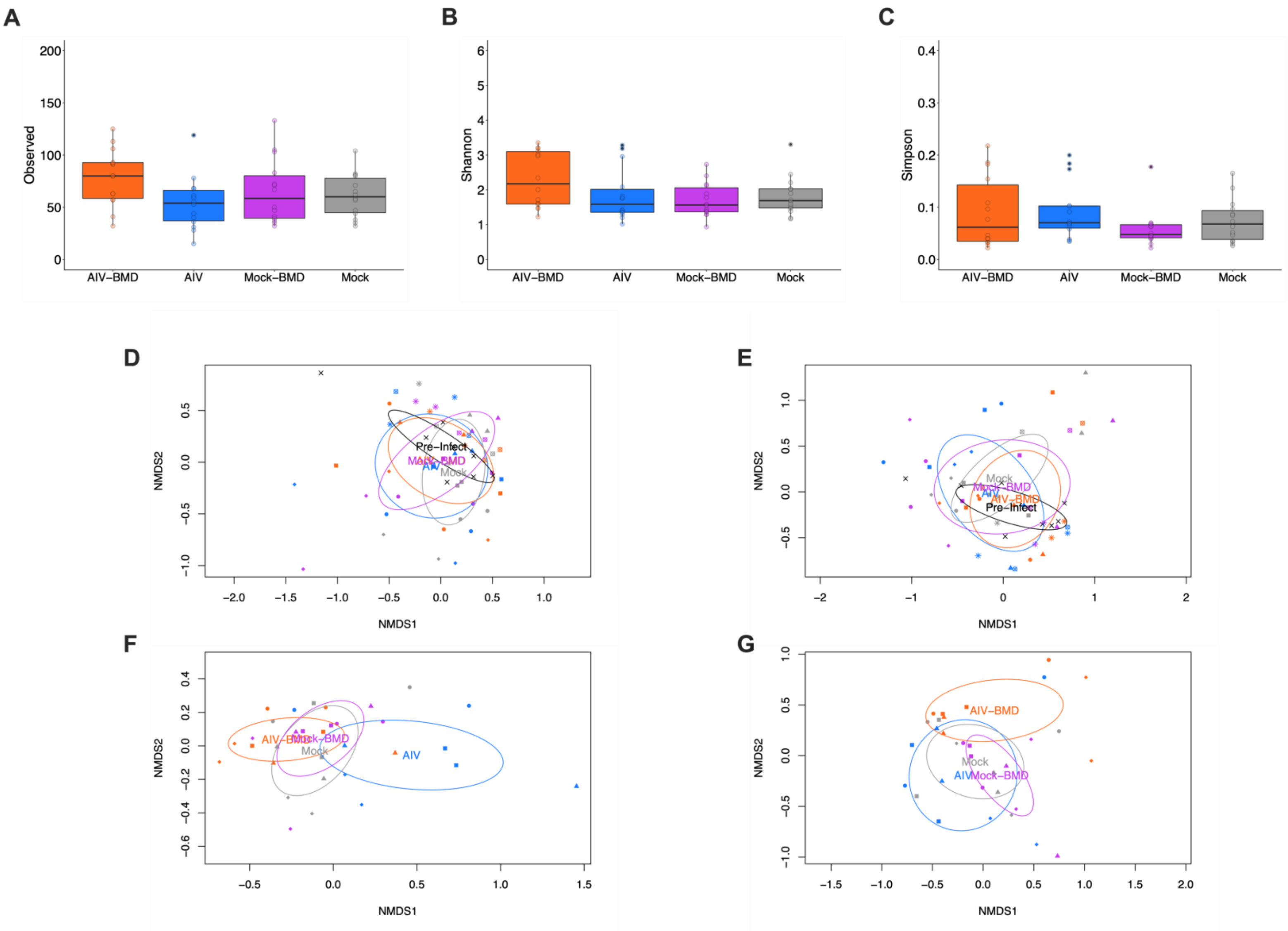
A
B
C
Observed
Shannon
Simpson
AIV−BMD
AIV
Mock−BMD
Mock
D
E
F
G
NMDS1
NMDS2
Pre−Infect
AIV−BMD
AIV
Mock−BMD
Mock

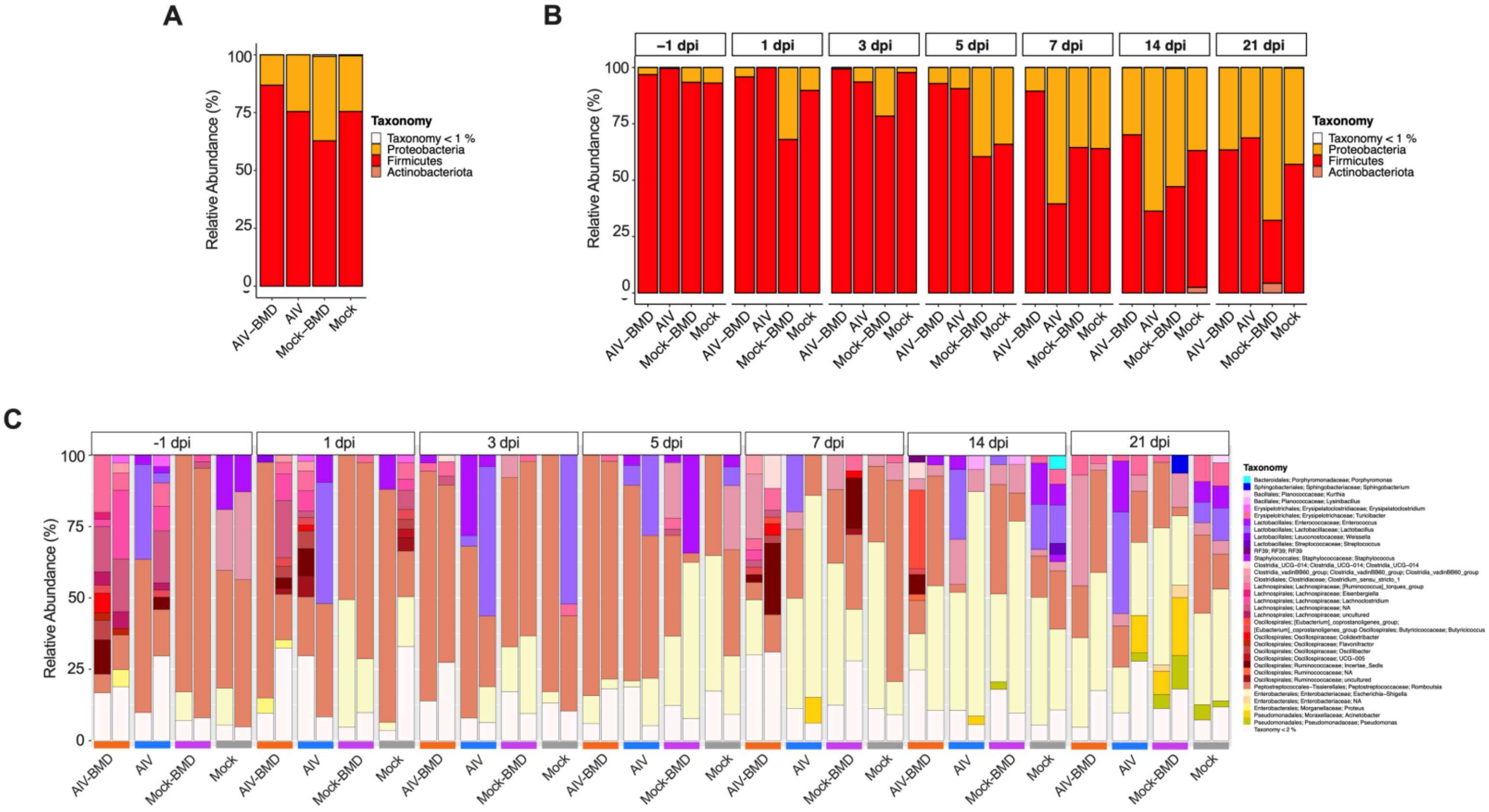

Figure 4.9. Relative abundance (%) of microbial communities of the feces at the phylum and lowest taxonomic classification. (A) Relative abundances agglomerated at the phylum level separated by group when all dpi were combined or (B) separated by dpi. (C) Relative abundances of each chicken at the lowest taxonomic rank identified separated by group and ordered by dpi.

Acknowledgements

We thank Brent Lovern and all the personnel from the Poultry Diagnostic and Research Center and the Animal Health Research Center at the University of Georgia. This study was supported by a subcontract from the Center for Research on Influenza Pathogenesis (CRIP) to DRP under contract HHSN272201400008C from the National Institute of Allergy and Infectious Diseases (NIAID) Centers for Influenza Research and Surveillance (CEIRS) and the Caswell S. Eidson endowment fund, University of Georgia.

CHAPTER 5

PATHOBIOLOGY AND DYSBIOSIS OF THE RESPIRATORY AND INTESTINAL MICROBIOTA IN 14 MONTHS OLD GOLDEN SYRIAN HAMSTERS INFECTED WITH SARS-COV-2

Brittany Seibert, C. Joaquin Caceres, Silvia Carnaccini, Stivalis Cardenas-Garcia, L. Claire Gay, Lucia Ortiz, Ginger Geiger, Daniela Rajao, Elizabeth Ottesen and Daniel R. Perez. (2022) (Plos Pathogens: 18(10)). Reprinted her with permission of the publisher.

Abstract

The pandemic of severe acute respiratory syndrome coronavirus 2 (SARS2) affected the geriatric population. Among research models, Golden Syrian hamsters (GSH) are one of the most representative to study SARS2 pathogenesis and host responses. However, animal studies that recapitulate the effects of SARS2 in the human geriatric population are lacking. To address this gap, we inoculated 14 months old GSH with a prototypic ancestral strain of SARS2 and studied the effects on virus pathogenesis, virus shedding, and respiratory and gastrointestinal microbiome changes. SARS2 infection led to high vRNA loads in the nasal turbinates (NT), lungs, and trachea as well as higher pulmonary lesions scores later in infection. Dysbiosis throughout SARS2 disease progression was observed in the pulmonary microbial dynamics with the enrichment of opportunistic pathogens (*Haemophilus*, *Fusobacterium, Streptococcus, Campylobacter*, and *Johnsonella)* and microbes associated with inflammation (*Prevotella*). Changes in the gut microbial community also reflected an increase in multiple genera previously associated with intestinal inflammation and disease (*Helicobacter, Mucispirillum*, *Streptococcus*, unclassified Erysipelotrichaceae, and Spirochaetaceae). Influenza A virus (FLUAV) pre-exposure resulted in slightly more pronounced pathology in the NT and lungs early on (3 dpc), and more notable changes in lungs compared to the gut microbiome dynamics. Similarities among aged GSH and the microbiome in critically ill COVID-19 patients, particularly in the lower respiratory tract, suggest that GSHs are a representative model to investigate microbial changes during SARS2 infection. The relationship between the residential microbiome and other confounding factors, such as SARS2 infection, in a widely used animal model,

contributes to a better understanding of the complexities associated with the host responses during viral infections.

Introduction

The severe acute respiratory syndrome coronavirus 2 (SARS2) is responsible for the ongoing coronavirus disease 2019 (COVID-19) pandemic. Clinical manifestations of infection are highly variable, ranging from asymptomatic or mild nonspecific flu-like symptoms to severe symptoms such as pneumonia, acute respiratory distress syndrome, multiple organ failure, and death (9, 287). Several risk factors have been identified for severe COVID-19 disease, including sex, age, obesity, cardiovascular conditions such as hypertension, smoking, among others (9, 287). Older individuals are at greater risk of developing acute respiratory distress amid SARS2 infection (288), leading to prolonged hospitalization and death (287). Animal models resembling human disease have been essential in understanding SARS2 pathogenesis. Golden Syrian hamsters (GSH) are naturally susceptible to SARS2 replication in the respiratory tract, inducing severe lung pathology (289, 290). Generally, GSH at 5-8 weeks of age have been used in experimental studies (291-296); however, multiple groups reported that 8-10-month-old GSHs develop more severe disease by exhibiting increased weight loss and slower lung recovery post-infection, emulating more severe disease presentation in older individuals (205, 297, 298). The vulnerability of enhanced illness in the elderly population has been hypothesized to encompass a combination of immunopathology from exacerbated immune response and immunosenescence (287). However, the mechanism and characteristics of age-related changes to the host such as the relationship between the immune response and host residential microbes during respiratory infections warrants further investigation.

While relatively established during adulthood, the residential host microbiota undergoes significant shifts in composition and diversity during the aging process, which can directly or indirectly affect the regulation of the immune system (299, 300). The deep respiratory microbiome is characterized by a diverse bacterial community in low abundances (301). In healthy individuals, the lung microbiota is generally dominated by commensal bacteria within the phyla Firmicutes such as *Veillonella spp* and Bacteroidetes such as *Prevotella spp* (301). Influenza A virus (FLUAV) and SARS2 infection affect the local bacterial community through abundance and composition changes (168, 195, 302, 303). Previous studies in humans reported that the lung microbiota of SARS2 infected patients consisted of opportunistic pathogens or enrichment of commensal bacteria such as *Pseudomonas*, Enterobacteriaceae, and *Acinetobacter* (195, 302).

Respiratory viral infections can also affect and induce changes in the gut microbiota through the gut-lung axis (207, 304). Further, gastrointestinal symptoms along with viral RNA (vRNA) in the feces have been observed occasionally during SARS2 infection (187, 305, 306). While the direct mechanism is unclear, intestinal dysbiosis in COVID-19 patients has been previously described in various human cohort studies (202, 307, 308). COVID-19 patients with severe symptoms presented dysbiosis of the gut microbiota characterized by commensal bacteria depletion and pathogenic bacteria enrichment (200, 202, 308, 309). Overall, fecal microbiome studies reported an association of opportunistic pathogens with COVID-19 infection, including *Streptococcus, Rothia, Veillonella, Erysipelatoclostridium, Actinomyces, Collinsella,* and *Morganella* (200, 308). While not fully understood, the intestinal microbiota affects various physiological functions, including metabolism, digestion, organ function, response to invading pathogens, and immune homeostasis (310). While human clinical samples are informative, there are also limitations, such as the environmental factors influenced by daily life (age, geographic location, diet, sex) or clinical management (antiviral or antibiotic treatment) that contribute to inter-individual variation. Human microbiome studies are limited since samples are mostly restricted to those from the nasopharynx or feces; lungs and intestinal tissues are more difficult to collect. However, it is well accepted that microbial communities vary in composition and abundance depending on different parts of the respiratory and intestinal tracts. Therefore, it is valuable to characterize the effect of SARS2 infection on the respiratory and intestinal microbiota in established animal models.

We recently analyzed the lung and cecum microbiota of K18-hACE2 mice after a low and high dose SARS2 infection (197). Within this animal model, we reported diversity and compositional changes in the respiratory and intestinal microbiota in a virus dose-dependent manner (197). However, the artificial expression of hACE2 does not mirror the natural susceptibility observed in humans. Therefore, we utilized an aged Syrian hamster model to analyze the pathobiology, host response and effects of SARS2 and pre-exposure of FLUAV H1N1 on the respiratory and intestinal microbiome in older patients. SARS2 challenged GSHs with and without prior FLUAV exposure had similar vRNA loads for respiratory and non-respiratory tissues except that FLUAV pre-exposure led to decreased SARS2 vRNA in the heart and nasal turbinates (NT). While SARS2 challenge led to overall higher pulmonary lesion scores later (6 days post challenge (dpc)) in infection than in the FLUAV pre-exposure group, FLUAV pre-exposed GSHs displayed slightly more pronounced pathology in the NT and lungs at 3 dpc. SARS2 challenge also impacted the microbial dynamics by enriching common opportunistic pathogens such as *Haemophilus, Fusobacterium, Streptococcus, Campylobacter,* and *Johnsonella*. Conjointly, SARS2 challenge led to dysbiosis in the small intestine (SI), cecum, and feces associated with more pronounced lesions in the cecum, notably in GSHs with FLUAV exposure. Several bacterial taxa were enriched in the SARS2 challenged GSH including *Helicobacter, Mucispirillum, Ileibacterium, Streptococcus,* unclassified Erysipelotrichaceae, Eubacteriaceae, and Spirochaetaceae while *Allobaculum* and unclassified Lachnospiraceae were depleted. Multiple taxa also correlated with vRNA load and pathological scores in respiratory and non-respiratory tissues. Altogether, SARS2 challenge with and without FLUAV exposure presented distinct disease pathology while both altered the respiratory and intestinal microbiota, suggesting that older GSH may be paramount in further investigating the effect of age on the host response to SARS2 infection.

Materials and Methods

Ethics Statement

Studies were approved by the Institutional Animal Care and Use Committee (IACUC) at the University of Georgia (Protocol A2019 03-032-Y2-A9). Studies were conducted under animal biosafety level (ABSL) 2 and ABSL3 for SARS2 inoculation. Animal studies and procedures were performed according to the Institutional Animal Care and Use Committee Guidebook of the Office of Laboratory Animal Welfare and Public Health Service Policy on Humane Care and Use of Laboratory Animals. Animal studies were carried out in compliance with the Animal Research: Reporting of *In Vivo* Experiments (ARRIVE) guidelines (https://arriveguidelines.org). Animals were humanely euthanized following guidelines approved by the American Veterinary Medical Association (AVMA).

Cells and Virus

Virus stocks of A/Puerto Rico/08/1934 (H1N1) were generated in 10-day old specific pathogen-free (SPF) embryonated chicken eggs. Madin-Darby canine kidney (MDCK) cells were a kind gift from Robert Webster (St Jude Children's Research Hospital, Memphis, TN, USA) and used for FLUAV titration. Virus stocks were titrated by tissue culture infectious dose 50 ($TCID_{50}$), and virus titers were established by the Reed and Muench method (227). Cells were maintained in Dulbecco's Modified Eagles Medium (DMEM, Sigma-Aldrich, St Louis, MO, USA) containing 10% fetal bovine serum (FBS), Sigma-Aldrich, St. Louis, MO, USA), 1% antibiotic/antimycotic (AB, Sigma-Aldrich, ST Louis, MO, USA) and 1% L-Glutamine (Sigma-Aldrich, St Louis, MO, USA). Cells were cultured at 37°C under 5% CO2.

Vero E6 Pasteur was kindly provided by Maria Pinto (Center for Virus research, University of Glasgow, Scotland, UK). Cells were maintained as previously described (237). SARS2 (Isolate USA-WA1/2020) was kindly provided by Dr. S. Mark Tompkins (Department of Infectious Diseases, University of Georgia). Viral stocks were prepared in Vero E6 Pasteur cells. Briefly, cells in a T75 flask were incubated for 1 h with 1 ml of viral inoculum. After incubation, the inoculum was removed, and cells were cultured with DMEM containing 2% FBS 1% AB. After 96 h, the supernatant was collected, centrifuged at 15,000 g for 15 min, aliquoted, and stored at -80ºC until use. Viral stocks were titrated by $TCID_{50}$ using the Reed and Muench method (227).

Hamster studies

4-months-old female golden Syrian hamsters (GSH) were purchased from Charles River Laboratories (Kingston, NY) and housed individually in ABSL2 facilities at the University of Georgia. At 13-months of age, GSH were randomly distributed into three groups (Fig 1A), anesthetized with isoflurane, and challenged intranasally (i.n.) with 100 µl of either phosphate buffer saline (PBS) or $1x10^5$ TCID50/GSH of Influenza (FLUAV) A/Puerto Rico/08/1934 (H1N1). GSH were monitored daily for clinical signs of disease throughout the entire course of the experiment. Fourteen days later, GSHs were boosted in the same way as previously described. Twelve days after the boost, a subset of GSHs were bled through the cranial vena cava to confirm the absence of antibodies against SARS2, which was performed using the SARS2 surrogate virus neutralization test (Genscript, Piscataway, NJ). Thirteen days after the boost, GSHs were transferred to ABSL3 containment and then challenged intranasally (i.n.) with 100 µl of either phosphate buffer saline (PBS) or $1x10^5$ TCID50/GSHs of SARS2 (Isolate USA-WA1/2020) the next day. At 3- and 6-days post-challenge (dpc), subsets of GSH were anesthetized with an intraperitoneal (i.p) injection (0.25-0.4 ml) of a ketamine/xylazine cocktail (150 mg/kg Ketamine, 10 mg/kg Xylazine), bled through the cranial vena cava, and then humanely euthanized with an intravenous injection of Euthasol (200mg/kg). Lungs, nasal turbinates (NT), trachea, heart, duodenum, ileum and cecum, and brain were collected from each GSH post-mortem. Tissues were stored at -80ºC until further analysis. Cages were changed the day before euthanasia for fecal collection. Feces from individual cages were collected and immediately stored at -80ºC until further processing.

Tissue sample preparations

Tissue homogenates for virus titration were generated using the TissueLyser II (Qiagen, Gaithersburg, MD). Briefly, 1ml of PBS-AB was added to each sample along with Tungsten carbide 3 mm beads (Qiagen). Samples were homogenized for 10 min and then centrifuged at 15,000 g for 10 min. Supernatants were collected, aliquoted, and stored at -80ºC until further analysis.

RNA extraction and RT-qPCR

RNAs were extracted from the tissue homogenates using the MagMax-96 AI/ND viral RNA isolation kit (ThermoFisher Scientific, Waltham, MA) following the manufacturer's protocol. A one-step real-time quantitative PCR (RT-qPCR) based on the Nucleoprotein gene segment was used as a surrogate of viral load, and it was employed using the primers 2019-nCov_N2-F (5'- TTACAAACATTGGCCGCAAA-3') and 2019-nCov_N2-R (5'- GCGCGACATTCCGAAGAA-3'). A probe with FAM as a reporter and TAMRA as a quencher was used (5'-FAM-ACAATTTGCCCCCAGCGCTTCAG-TAMRA-3'). The RT-qPCR was performed in a QuantStudio 3 Real-Time PCR System (ThermoFisher Scientific, Waltham, MA) using a Quantabio qScript XLT One-Step RT-qPCR ToughMix kit (Quantabio, Beverly, MA) in a 20 µl final reaction volume. Each reaction mixture contained a 1X master mix, 0.5 μM of each primer, 0.3 μM probe, and 5 μl of RNA. The qPCR cycling conditions were 50ºC, 20 min; 95 ºC, 1 min, 40 cycles at 95ºC, 1 min; 60ºC, 1 min; and 72ºC 1 s; with a final cooling step at 4ºC C. A standard curve was generated using 10-fold serial dilutions of a SARS2 virus stock of known titer to correlate RT-qPCR crossing point (Cp) values with the viral load from each tissue. Viral loads were calculated as Log_{10} TCID50 equivalents/per gram of tissue.

Histopathology and immunohistochemistry

Selected tissues included NT, trachea, lungs, heart, brain, and small and large intestines and were collected from each GSH in each group at 3- and 6-dpc for histopathological examination. Tissues were placed in 10% neutral-buffered formalin (NBF), fixed for at least 72 hours, paraffin-embedded, and processed for routine histopathology with hematoxylin and eosin staining (HE). A board-certified pathologist blinded to the study subjectively scored tissues based on percentage of the total parenchyma affected by lesions and inflammation as: none (0%), mild; <15% (1), mild to moderate; 16-30% (2), moderate; 31-50% (3), moderate to severe 51-75% (4) and severe; ≥75% (5). Features considered for the scoring were the following: presence and extent of necrosis, inflammation, endothelialitis, epithelial cell hypertrophy, hyperplasia, and regeneration (mitoses), mesothelial hyperplasia, and syncytia; presence and amount of intraluminal catarrhal/fibrino-necrotic/suppurative exudate, hemorrhage, edema, fibrin, and thrombi. Additionally, antibodies targeting the SARS-CoV-2 nucleocapsid (ThermoFisher Scientific, Waltham, MA; dilution 1/500), were also used to perform immunohistochemistry (IHC) on selected tissues.

DNA extraction, amplicon library preparation, and sequencing

DNA was extracted by using a MoBio Power Soil kit (Qiagen, Gaithersburg, MD) with minor changes according to the earth microbiome protocol as follows: additional incubation at 65 °C for 10 min after the addition of solution C1, beads were shaken at 20Hz for 20 min instead of 10 min, and samples were incubated at 4 °C for 10 min instead of 5 min and then stored at -80 °C until use. Following extraction, the V4 hypervariable region of the 16S rRNA gene was amplified using Phusion Hot Start 2 DNA polymerase (Thermo Fisher, Waltham, MA) using primers 515F (59-GTGCCAGCMGCCGCGGTAA-39) and 806R (59-GGACTACHVGGGTWTCTAAT-39) in 20 µl PCR reaction (8.9 µl of molecular-grade water, 4 µl of 5 HF buffer, 0.4 µl of 10mM deoxynucleoside triphosphates [dNTPs], 1.25 µl of 10 mM 515F, 1.25 µl of 10 mM 806R, 4 µl of DNA, and 0.2 µl of polymerase) under the following conditions: 98 °C (30 s), followed by 25 cycles of 98 °C (10 s), 52 °C (30 s), and 72 °C (30 s), a final elongation step at 72 °C (5 min), and held at 4 °C. The PCRs were performed in duplicates and then visualized on a 1% agarose gel. Duplicate PCR products of the same sample were pooled in equal volumes, cleaned by 0.45X of Agencourt AMPure XP magnetic beads (Beckman Coulter, Pasadena, CA) according to the manufacturer's protocol, and eluted in molecular biology grade water (Genesee Scientific, San Diego, CA). Amplicon concentration was measured using the Qubit dsDNA HS assay kit (Thermo Fisher) on a Qubit 3.0 fluorometer (Thermo Fisher). DNA concentrations were normalized to 1.0 ng/ml. Subsequently, amplified DNA was used in a secondary amplification/dual barcode annealing reaction. Forward and reverse dual barcode primers (primers and barcodes with different reference indexes) were designed based upon primers generated by Caporaso et al. (265). Secondary amplification reactions were performed using NEBNext high-fidelity 2 PCR master mix (NEB) in 50 µl reactions (26 µl of 2X mix, 20.5 µl of water, 2.5 µl of barcoded forward and reverse primers [10mM], 1 µl of DNA) under the following conditions: 98 °C (30 s), followed by four cycles of 98 °C (10 s), 52 °C (10 s), and 72 °C (10 s), followed by 6 cycles of 98 °C (10 s) and 72 °C (1 min), followed by a final extension of 72 °C (2 min) and then held at 4 °C. According to the manufacturer's protocol, samples were subsequently cleaned by 0.45X of Agencourt AMPure XP magnetic beads and eluted in molecular biology grade water. Fragment size distribution was analyzed on a subset of samples using the Agilent Bioanalyzer 2100 DNA-HS assay (Agilent, Santa Clara, CA, USA). Samples libraries were then normalized and pooled to a concentration of 2 nM based on a predicted total product size of 420 base pair (bp) using the Qubit dsDNA HS assay kit on the Qubit 3.0 fluorometer. The loading concentration of the pooled libraries was 8 pM. Libraries were sequenced using Illumina MiSeq V2 chemistry (Illumina, San Diego, CA), 2 by 250 paired-end. Negative controls, including an extraction blank and a PCR blank, were included in each sequencing run (2 runs total).

Data analysis

Primer removal and demultiplexing were performed using Illumina BaseSpace using default settings. Sequence analysis was performed in R (version 4.1.0) with open-source software package DADA2 (version 1.16.0) (266, 311). Each sequencing batch was processed separately until chimera removal. For each batch, the quality of the raw paired-end reads was visualized and used to determine the appropriate truncation of read 1 (R1) by 10 bp and read 2 (R2) by 50 bp. After truncation, reads were discarded if they contained more than 2 maxEE "expected errors" or a quality score of less than or equal to 2. Following, each quality-filtered and trimmed read was processed independently by applying the trained DADA2 algorithm. The reads were then merged with a minimum overlap of 20 bp. After merging, both sequencing batches were combined, and chimeras were removed using the consensus method with default settings. Taxonomy was assigned in DADA2 using the native implementation of the naive Bayesian classifier using the Silva v.38 database. A count table and taxonomy file were created and used for downstream analysis. Lungs and intestine / fecal samples were analyzed separately. In the lungs, a total of 843,402 reads with an average of 52,712 reads/sample were generated (S10A Fig). For the intestine/fecal samples, a total of 5,203,820 reads with an average of 58,469 reads/sample were generated (S10A Fig). Samples were then filtered to remove amplicon sequence variants (ASV) with non-classified phylum or classified as Chloroplast or Mitochondria using RStudio (version 2022.02.0) (269). Further, ASV found in less than 5% of samples and had a total abundance of fewer than 10 reads were removed to avoid potential contaminants in diversity estimates. Post-filtering, an average of 49,290 reads / sample were generated for lung samples, 60,329 reads / sample for duodenum samples, 68,703 reads / sample for ileum samples, 52,636 reads / sample for cecum samples, and 49,809 reads / sample for fecal samples. Negative controls, including an extraction blank and a PCR blank, resulted in an average of 2 reads/sample (Fig 5.1A).

Bioinformatic Analysis

Alpha diversity, examined by the observed number of ASV and Shannon diversity, was calculated using rarified counts using phyloseq (version 1.38.0) (271). Briefly, lung samples were rarified to 13,306 reads, and intestine/feces samples were rarified to 27,020 reads using command *rrarefy* in the vegan package (version 2.5.7) (272). Rarefaction plots were generated using phyloseq.extended package (version 0.1.1.6) and edited using ggplot2 package (version 3.3.5) (273). Rarefaction curves showed a similar number of observed species among the reads, suggesting adequate coverage (Fig 5.1B). The rarified counts were then imported into phyloseq, and diversity indexes were calculated using command *estimate richness*. Results were graphed using ggpubr package (version 0.4.0) (274). Statistical comparison across groups was performed using the Kruskal-Wallis, while the Wilcox rank test with Bonferroni correction was used for pair-wise comparisons.

Regarding beta diversity, a non-metric multidimensional scaling (NMDS) plot showing unweighted Jaccard and weighted Bray-Curtis dissimilarity metrics were calculated with 3 dimensions, a maximum of 500 random starts and 999 maximum iterations using the rarified count data. NMDS plots and ellipses based upon the standard deviation were illustrated using ‘ordiellipse’ from the vegan package. Beta diversity distances displayed in boxplots for comparison of within and across group distance metrics were created by calculating distances in vegan and then plotting using the ggplot2 package. Statistical pair-wise comparisons among groups were performed using the Wilcox rank test with Bonferroni correction. Multivariate statistics analysis, including permutational multivariate analysis of variance (PERMANOVA), were calculated using beta diversity distances with 1,000 permutations using vegan.

Relative abundances at the phylum and lowest classified level were generated using phyloseq. For the phylum taxonomic barplot, ASVs were agglomerated to the phylum level and then transformed into relative abundances using phyloseq. For the taxonomic barplot incorporating the lowest classification, relative abundances were calculated using phyloseq, and taxa with an overall prevalence of less than 1% were grouped. Differential analysis among groups of taxa at the genus level was performed using DeSeq2 (version 1.34.0), ALDEx2 (version 1.26.0), and linear discriminant analysis effect size (LEfSe) (275, 312-314). ASVs in less than 20% of samples with a total abundance of fewer than 10 reads were removed for all differential analyses. For Deseq2 analysis, counts with an added value of +1, used to account for 0, were inputted, and a p-value of < 0.01 from the Wald test with Benjamini-Hochberg correction was considered significant. For ALDEx2 analysis, counts with an added value of +1 were inputted, and a p-value of < 0.05 from Welch's t-test with Benjamini-Hochberg correction was considered significant. For LEfSE analysis, rarified counts were inputted, and a p-value < 0.05 was considered significant. The p-value threshold used to determine significance for results produced in Deseq2 was more strict because of the high standard error than ALDEx2 and LEfSE. Relative abundances were also visualized using a heatmap of the differential taxa using ggplot2. Correlation analysis was performed to understand better the relationship between taxa and different viral infection factors. Spearman correlation analysis was calculated by performing a log10 + 1 transformation on filtered count data and then calculated using the function 'associate' from the microbiome package. The final plots were combined using Prism (v 9.1.0). Scripts used for analysis can be found on github at https://github.com/brittanyaseibert/Seibertetal _SARS2FLUAV_AgedGSH.

Graphs/Statistical analyses

Data analyses and graphs were performed using GraphPad Prism software version 9.3 (GraphPad Software Inc., San Diego, CA). Graphs were edited using PDF Expert (Readdle Inc, Odesa, Ukraine) and Affinity Photo (Serif, West Bridgford, United Kingdom).

Data availability

The 16S sequencing data set was deposited under BioProject PRJNA848775.

Results

SARS2 infection in 14 months old GSH led to high viral loads, enhanced pathology, and consistent weight loss

GSHs were divided into 3 groups: SARS2 GSHs were challenged intranasally with 1 x 10^5 TCID50/hamster of SARS2 while FLUAV-SARS2 GSHs were pre-exposed to FLUAV (primed twice, 14 days apart at 1 x 10^5 TCID50/hamster) 13 days before SARS2 challenge (as above). FLUAV exposure was used to determine if such treatment would affect SARS2 infection, disease progression, and microbiome composition outcomes. The mock GSH group was challenged with 1XPBS. Clinical signs, including weight loss, SARS2 shedding and histopathological changes of different tissues were analyzed at 3 and 6 dpc (Fig 5.2A). Assessment of humoral responses against FLUAV obtained on 1 day prior to SARS2 challenge (27 days post 1st FLUAV dose) revealed antibody responses (hemagglutination inhibition (HAI) and enzyme-linked immunosorbent assay (ELISA)) below the limit of detection suggesting that inoculation of FLUAV in GSH led to restricted and/or abortive FLUAV replication. Therefore, the effects, if any, of prior-FLUAV exposure in GSH challenged with SARS2 would likely not be related to stimulation of antibody responses. After SARS2 challenge, the GSHs experienced clinical signs consistent with virus infection regardless of prior-FLUAV exposure starting at 2 dpc (SARS2: range 1.15 – 6.5% and FLUAV-SARS2: range 1.19 – 7.4%) and continued to deteriorate until 6 dpc when the study was terminated (SARS2: range 7.7 - 10.2% and FLUAV-SARS2: range 4.3 – 11.7%) (Fig 5.2B). Overall, a significant weight loss was observed upon SARS2 challenge regardless of previous FLUAV exposure.

In addition to weight loss, high SARS2 vRNA loads were detected from the NT, trachea, and lungs in both the SARS2 and FLUAV-SARS2 groups with no statistically significant differences at 3 and 6 dpc (Fig 5.2C and 1D). The exception was on vRNA load data from NT at 6 dpc, where statistically significant higher viral loads were detected in the SARS2 group (p = 0.0038; Two-way ANOVA). Further, 2 out of 3 trachea samples and 1 out of 3 lung samples had vRNA loads below limit of detection in the FLUAV-SARS group at 6 dpc. Notably at 3 dpc, vRNA loads were detected in the heart from the SARS2 group, but not from the FLUAV-SARS2 group (p = 0.0096; Two-

Way ANOVA). Low to undetectable vRNA loads were observed in the brain and intestine (duodenum, ileum, and cecum) at both 3 and 6 dpc in both the SARS2 and FLUAV-SARS2 challenged groups. Collectively, SARS2 challenge resulted in elevated vRNA loads in respiratory tissues and heart while FLUAV pre-exposure led to reduced SARS2 vRNA within the NT (at 6 dpc) and the heart (at 3 dpc). These observations suggest that prior FLUAV exposure led to a potential antiviral state that limited and/or delayed SARS2 replication in aged GSHs.

Histopathological analysis of GSH groups revealed that the organs most affected upon infection were the NT, lungs, tracheas, and large intestine. Overall, lesions appeared slightly more pronounced in the FLUAV-SARS2 GSH, with a few exceptions (Table 5.1). In both SARS2 challenged groups, lesions in the NT were more prominent at 3 dpc (Fig 5.3A-B) than at 6 dpc (Fig 5.3D-E). These ranged from mild-moderate to moderate-severe, multifocal, acute-subacute suppurative rhinitis with rare syncytia formation and abundant intraluminal catarrhal to fibrinosuppurative exudate deposition. Within both groups, variable amounts of intracytoplasmic virus antigen immunolabeling was present in epithelial cells (Fig 5.4A-F).

Tracheas presented minimal variations of findings between challenged groups at given time points. Scores were higher at 3 dpc (Fig 5.3G-H) versus at 6 dpc (Fig 5.3J-K), and lesions consisted of mild to moderate, multifocal, acute-subacute neutrophilic and histiocytic tracheitis with intraluminal muco-catarrhal exudate formation. No syncytia were found in any of these sections.

At 3 dpc, pulmonary lesions were overall milder in SARS2 GSH than in FLUAV-SARS2 GSH (Fig 5.3M-N and Table 5.1). In both SARS2 challenged groups, lesions were centered on the bronchi and bronchioles. They predominantly consisted of mild-moderate (Fig 5.3M) and moderate-severe (Fig 5.3N) multifocal, acute suppurative bronchitis/bronchiolitis with intraluminal exudate deposition. Syncytia were rarely observed in the bronchial respiratory epithelium at 3 dpc. At this time, peribronchial inflammation was mild, whereas perivascular cuffing and pulmonary vascular endothelialitis were accompanied by rare intravascular thrombi. Further, moderate amounts of virus antigen were present in bronchiolar epithelium and intraluminal necrotic cellular debris (Fig 5.4G-H). At 6 dpc more severe pulmonary lesion scores were observed in the SARS2 group than in FLUAV-SARS2 group. These consisted of moderate to severe, multifocal to diffuse, subacute interstitial pneumonia with marked alveolar proliferation of cuboidal epithelial cells (pneumocytes type II), replacing the necrotic pneumocytes type I (Fig 5.3P-Q). Pneumocytes type II often presented karyomegaly and multinucleation (syncytia). Alveoli were often collapsed or filled with hemorrhagic and suppurative exudate. Moderate multifocal, acute fibrinosuppurative pleuritis was observed mostly in the FLUAV-SARS2 group at 6 dpc. However, intracytoplasmic virus antigen staining was scarce at 6 dpc compared to 3 dpc (Fig 5.4J-K).

In the sections of small intestines, the inflammation was generally minimal and present in all groups, including the mock challenged, at both timepoints. Only in the SARS2 challenged groups, small numbers of eosinophils were migrating to the enterocyte lining (Fig 5.5A-E) and associated with mild non-specific lesions to the villi. Variable numbers of intraluminal protozoa and mixed bacteria appeared subjectively increased in the challenged GSHs. Protozoal morphologic features were mostly compatible with *Giardia muris (*Fig 5.5E – insert).

Typhlocolitis was more pronounced within the large intestine in the FLUAV-SARS2 GSH than in SARS2 GSH at both timepoints. Enterocytes were degenerating, sloughing into the lumen or within the glands, and were colonized by moderate numbers of mixed coccobacilli and filamentous bacteria. Especially in the challenged groups, there was a visible increase in *Entamoeba muris* and bacteria numbers (Fig 5.5G, I, and L – inserts).

Findings in the brain were inconsistent. Only 2 GSHs presented evidence of mild suppurative meningitis, one in SARS2 group and one in the FLUAV-SARS2 group at different time points (Table 5.2). No significant findings were observed in the heart sections in any group and timepoints. These results suggest that in the absence of FLUAV-pre-exposure, increased pulmonary lesions were seen in the later part of infection after SARS2 challenge. In contrast, FLUAV pre-exposure led to exacerbated pathological scores in the NT and lungs early after SARS2 challenge. FLUAV pre-exposure also led to more pronounced lesions in the cecum throughout infection after SARS2 challenge.

SARS2 challenge and FLUAV pre-exposure alters the composition of the lung microbiota in aged GSHs.

To characterize the lung microbiome, we sequenced the V4 region of 16S rRNA genes amplified from lung homogenates collected at 3 and 6 dpc. Alpha diversity (observed number of amplicon sequence variants (ASV's)) and Shannon diversity showed a trend towards an increased number of ASVs and diversity following SARS2 challenge, particularly in the FLUAV-SARS2 group; however, no significant differences were observed among the SARS2 challenged groups and mock when dpc were combined (Fig 5.6A). To determine changes in the lung microbial composition after SARS2 challenge, we analyzed beta diversity using unweighted Jaccard and weighted Bray-Curtis's dissimilarity metrics through non-metric multidimensional scaling (NMDS) ordination. Both ordinations showed clustering by group (R2= 0.22, p = 0.0030; PERMANOVA) and dpc (R2= 0.096, p = 0.025; PERMANOVA), though the interaction between the terms was not significant (Fig 5.6B and Fig 5.7A). The dissimilarity distance between the two SARS2 challenged groups and the mock was larger than the distance between the two challenged groups (FLUAV-SARS2: p < 0.0001 and SARS2: p = 0.00027; Wilcox) (Fig 5.6C). When analyzing the dispersion within the treatment groups using the unweighted and weighted distances, both groups challenged with SARS2 had lower intra-group variation than the mock (FLUAV-SARS2: p =0.015 and SARS2: p = 0.037; Wilcox); however, the difference in sample size could explain the results (Fig 5.6C and Fig 5.7B Fig). Overall, SARS2 challenge impacts the diversity within the lung microbial dynamics through changes in the relative abundance of different microbes, while prior FLUAV exposure amplified these changes.

At the phylum level, the lung microbiota was dominated by Bacteroidota (Bacteroidetes) (mean (x̄): 38.68%) and Firmicutes (x̄: 32.50%) in all three groups when both dpc were combined (Fig 5.6D). Prominently, the abundance of Fusobacteriota (x̄: SARS2: 6.57%, FLUAV-SARS2: 6.98%, mock: 0.60%) and Proteobacteria (x̄: SARS2:

25.79%, FLUAV-SARS2: 22.54%, mock: 2.6%) increased in the SARS2 challenged GSHs plausibly at the expense of Firmicutes (x̄: SARS2: 23.76%, FLUAV-SARS2: 28.87%, mock: 58.44%). A difference in relative abundance was also observed at lower taxonomic levels. Strikingly, a large increase in the relative abundance of *Haemophilus* was observed at 3 dpc (x̄: SARS2: 40.96%, FLUAV-SARS2: 24.74%, mock: 0%) and 6 dpc (x̄: SARS2: 15.49%, FLUAV-SARS2: 15.23%, mock: 0%) in both SARS2 challenged groups, consistent with overall increase of Proteobacteria (Fig 5.6E). While the cumulative *Haemophilus* relative abundance was similar at 6 dpc among the challenged groups, a higher prevalence of the genera was observed in FLUAV-SARS2 GSH (4/4) compared to SARS2 GSH (1/3). Increased relative abundances of *Prevotella 7* (x̄: SARS2: 5.93%, FLUAV-SARS2: 4.14%, mock: 0%), *Streptococcus* (x̄: SARS2: 5.85%, FLUAV-SARS2: 2.24%, mock: 0%), *Johnsonella* (x̄: SARS2: 1.45%, FLUAV-SARS2: 2.01%, mock: 0%), and *Fusobacterium* (x̄: SARS2: 8.54%, FLUAV-SARS2: 9.31%, mock: 0%) were also observed in both SARS2 challenged groups compared to the mock (Fig 5.6E).

We performed differential abundance testing at the genus level using three programs, DeSeq2, linear discriminant analysis effect size (LefSE), and ALDEx2. At the genus level, *Campylobacter, Fusobacterium, Haemophilus,* and *Moraxella* were identified as significantly enriched within the SARS2 group compared to the mock controls by 2 of 3 (Deseq2 and LefSE) differential analyses (Fig 5.8A and Table 5.3). *Prevotella 7, Johnsonella, Streptococcus, Fusobacterium,* and *Haemophilus* were identified as significantly enriched within the FLUAV-SARS2 GSHs in comparison with mock-challenge animals (Fig 5.8B and Table 5.3). Other taxa were considered significant in each group but were only identified in 1 of 3 differential analyses (Fig 5.9). In contrast, no genera were considered significantly different in at least 2/3 differential analysis when comparing SARS2 and FLUAV-SARS2 GSHs (Table 5.3 and Fig 5.9E-G). Collectively, SARS2 challenge with and without prior FLUAV exposure impacts the microbiota by enriching opportunistic pathogens; however, previous FLUAV exposure partially modulates this phenomenon with enrichment of *Haemophilus* later (6 dpc) in SARS2 infection.

Altered composition of the lung microbiota correlates with SARS2 vRNA loads and pathology.

We examined the association of multiple genera and unclassified families to SARS2 vRNA loads and pathology scores using Spearman correlation. *Prevotella 7, Fusobacterium,* and *Haemophilus* positively correlated with SARS2 challenge while *Prevotellaceae UCG-003* and *Anaerococcus* positively correlated with FLUAV pre-exposure (Fig 5.8C). *Escherichia-Shigella* negatively correlated with SARS2 challenge. We also observed a strong correlation between several bacterial taxa and SARS2 vRNA load in tissues, particularly within the respiratory tract (Fig 5.8C). For instance, *Rikenellaceae RC9 gut group, Johnsonella, Lachnoclostridium*, and *Dialister* positively correlated with increased vRNA in the NT while *Olsonella*, *Solobacterium*, and *Fenollaria* positively correlated with increased vRNA in the lungs. Within the trachea and the lungs, *Escherichia-Shigella* negatively correlated with vRNA loads. In non-respiratory tissues, *Moraxella* positively correlated with increased vRNA in the heart, and *Rikenellaceae RC9 gut group* and *Actinobacillus* positively correlated with increased vRNA in the cecum. On the other hand, *Anaerococcus* negatively correlated with vRNA in the ileum.

Strong correlations were also observed between several bacterial taxa and histopathological scores (Fig 5.8C, Table 5.1, and Table 5.2). *Prevotella 7* and *Haemophilus* positively correlated with more severe pathology scores in the NT and trachea. *Actinomyces*, *Bifidobacterium*, *Streptococcus*, and *UCG-005* positively correlated with more severe pathology scores in the NT, and *Actinomyces, Staphylococcus*, *Peptoniphilus*, and *Moraxella* in the trachea. Within the lungs, *Fusobacterium* positively correlated with more severe pathology while *Escherichia-Shigella* negatively correlated with increased severity in the trachea and the lungs. In non-respiratory tissues, unclassified Actinomycetaceae positively correlated with more severe pathology in the brain, while no genera were found to correlate with severity of the cecum. Correlations among the heart and SI pathology were not determined since the pathological score was the same for all GSH groups (Table 5.2).

SARS2 challenge and FLUAV pre-exposure alters the intestine and fecal microbiota composition in aged GSHs.

The V4 region of 16S rRNA genes amplified from the SI (duodenum and ileum), large intestine (cecum), and feces collected at 3 and 6 dpc was sequenced and analyzed. Fecal samples from 1 day before challenge (-1 dpc) were analyzed as a separate pre-challenge group (Fig 5.2A). Rarefaction curves of alpha diversity (observed number of ASV) and Shannon diversity showed adequate coverage and no significant differences among the groups when both dpc were combined; however, a difference in observed species among the sample sites was apparent (Fig 5.10A, B and Fig 5.11A). The cecum had the highest number of ASVs, followed by feces, ileum, and duodenum (Fig 5.10B). When analyzing the effect of FLUAV exposure on pre-challenge fecal samples, no significant alpha diversity differences were observed (Fig 5.11B). For downstream analysis, the duodenum and ileum samples were combined to encompass the SI. Beta diversity using NMDS ordination plots showed limited clustering of groups in unweighted (Jaccard) and weighted (Bray-Curtis) dissimilarity metrics (Fig 5.12); however, PERMANOVA analysis showed significant differences by group in the SI (R2 = 0.12, $p<0.001$) and feces (R2 = 0.14, $p<0.001$) but not within the cecum. There was also considerable overlap among the pre-exposed FLUAV GSH and mock GSH when analyzing the pre-challenge fecal samples (Fig 5.12G-H). When analyzing the inter-variation among the groups, the dissimilarity distance was similar within the SI and the cecum (Fig 5.13A-B). The SARS2 GSHs had lower intra-group variation than the mock challenged GSHs in the feces but not considered statistically significant (Fig 5.10C). Also in the feces, the dissimilarity distance comparing both SARS2 challenged groups to the mock was larger than the distance between the comparison of SARS2 versus FLUAV-SARS2 ($p < 0.001$; Wilcox) (Fig 5.10C). The distance between SARS2 challenged GSH and pre-challenge was not significantly different from the distance between SARS2 and FLUAV-SARS2 GSH ($p = 1$; Wilcox) but was significantly different from the comparisons with the mock (SARS2: $p = 0.0033$ and FLUAV-SARS2: $p =0.0024$; Wilcox). These findings suggest that the fecal microbiome composition of aged GSH challenged with SARS2 differs from the mock challenged GSH; however, the difference detected among the groups could be partially explained by intra-individual variations observed in the pre-challenge fecal samples.

At the phylum level, the intestinal and fecal microbiota were dominated by Bacteroidota (x̄: 44-74%) and Firmicutes (x̄: 20-40%) in all groups and sample sites (Fig 5.13C). However, relative abundance differences were observed at lower taxonomic levels among the different sample sites. The duodenum and ileum shared similar taxonomic profiles that were distinct from the cecum and fecal samples; however, unclassified Muribaculaceae (x̄: 56.69%) was the most prominent family among sample sites and groups when both dpc were combined (Fig 5.10D and Fig 5.13D). Markedly, decreased abundance of *Allobaculum* within both SARS2 groups was observed in the SI (x̄: SARS2: 6.72%, FLUAV-SARS2: 3.19%, mock: 12.88%), cecum (x̄: SARS2: 0.70%, FLUAV-SARS2: 0.61%, mock: 2.8%), and feces (x̄: SARS2: 4.50%, FLUAV-SARS2: 4.23%, mock: 7.36%). Within the SI, *Streptococcus* (x̄: SARS2: 2.42%, FLUAV-SARS2: 1.63%, mock: 0.0040%) and unclassified Erysipelotrichaceae, notably at 3 dpc, (x̄: SARS2 3 dpc: 9.704%, 6 dpc: 6.58%; FLUAV-SARS2 3 dpc: 8.04%, 6 dpc: 4.88%; mock 3 dpc: 3.20%, 6 dpc: 2.0%) were enriched while *Desulfovibrio* (x̄: SARS2: 1.39%, FLUAV-SARS2: 1.08%, mock: 3.30%) was reduced within both groups of SARS2 challenged GSH. Taxa enriched within the cecum in SARS2 challenged GSH included *Prevotellaceae UCG-003* (x: SARS2: 3.03%, FLUAV-SARS2: 2.67%, mock: 0.11%), *Helicobacter* (x̄: SARS2: 3.47%, FLUAV-SARS2: 4.03%, mock: 1.81%), *Mucispirillum* (x̄: SARS2: 2.46%, FLUAV-SARS2: 2.18%, mock: 0.55%) and unclassified Spirochaetaceae (x̄: SARS2: 6.42%, FLUAV-SARS2: 4.56%, mock: 0.02%) while *Treponema* (x̄: SARS2: 0.068%, FLUAV-SARS2: 0.065%, mock: 3.76%) was decreased in both challenged groups compared to the mock. Within the feces, *Ileibacterium* (x̄: SARS2: 7.55%, FLUAV-SARS2: 6.47%, mock: 3.02%, Pre-challenge: 2.46%), unclassified Erysipelotrichaceae (x̄: SARS2: 3.14%, FLUAV-SARS2: 1.92%, mock: 0.86%, Pre-challenge: 0.88%), and unclassified Eubacteriaceae (x̄: SARS2: 7.13%, FLUAV-SARS2: 4.64%, mock: 0.94%, Pre-challenge: 1.66%) were enriched while unclassified Lachnospiraceae (x̄: SARS2: 1.04%, FLUAV-SARS2: 0.75%, Pock: 3.53%, Pre-challenge: 1.89%) was reduced in both challenged groups compared to the mock.

Multiple taxa were identified as differentially enriched or reduced within the different groups in at least 2 out of 3 differential analyses when sample types were combined (Table 5.4 and Fig 5.14). Genera including *Prevotella*, *Fibrobacter,* and unclassified Spirochaetaceae within the SI and *UCG-005* and unclassified Spirochaetaceae within the cecum were differentially enriched in the FLUAV-SARS2 group versus mock challenge GSH (Table 5.5). No genera were considered differentially enriched in the SARS2 group when compared to the mock within the SI and cecum. On the other hand, *Allobaculum*, unclassified Prevotellaceae and *Mycoplasma* within the SI and unclassified Prevotellaceae and *Allobaculum* within the cecum were differentially enriched in the mock challenged GSH compared to both SARS2 challenged groups. While comparing SARS2 GSH and FLUAV-SARS2 GSH, *Fibrobacter,* unclassified [Eubacterium] coprostanoligenes group, and unclassified Spirochaetaceae within the SI and *Fibrobacter* and *UCG-005* within the cecum were differentially enriched in FLUAV-SARS2 GSH. Within the feces, *Elusimicrobium* and unclassified Spriochaetaceae were differentially enriched in the SARS2 group while *Parabacteroides*, *Elusimicrobium, Christensenellaceae R-7 group, NK4A214 group, UCG-005,* and unclassified

Spirochaetaceae were enriched in the FLUAV pre-exposed GSHs when compared to the mock. Unclassified Prevotellaceae, *Ligilactobacillus*, and unclassified Lachnospiraceae were differentially enriched in the mock. Compared to their respective pre-challenge feces, *Bifidobacterium, Allobaculum*, *Ileibacterium*, *Faecalibaculum,* and unclassified Eubacteriaceae were differentially enriched after SARS2 challenge, while an increase of *Prevotella* abundance was observed in the pre-challenge samples (Table 5.6). No significant taxa were observed when comparing the FLUAV-SARS2 feces and their respective pre-challenge samples in at least 2/3 differential analysis (Table 5.6). When comparing the two SARS2 challenge groups, *Anaerostipes* was enriched in the SARS2 GSHs while *Fibrobacter* and *UCG-005* were enriched in FLUAV-SARS2 GSHs. When analyzing the effect of FLUAV exposure prior to SARS2 challenge, *Anaerostipes* was enriched within the mock pre-exposed GSH (Table 5.6). Overall, SARS2 respiratory infection in aged GSH with and without prior FLUAV exposure led to enhanced gut dysbiosis.

We further examined the association of genera and unclassified families to vRNA loads and pathology scores. Correlations among the heart and SI pathology were removed since the pathological score was the same for all GSH. We initially observed strong correlations among several bacterial taxa and the sample site (Fig 5.15). However, when sample sites were analyzed separately, multiple genera, especially in the cecum and feces, had strong correlations among different infection factors, particularly with FLUAV pre-exposure and more severe pathology scores in the cecum (Fig 5.16). Taxa such as *Coxiella* in the SI, *UCG-005,* and *Fibrobacter* in the cecum and feces positively correlated with FLUAV exposure before SARS2 challenge, while *Peptococcus* in the cecum and *Lachnoclostridium* in the feces negatively correlated with FLUAV pre-exposure. Interestingly, *Bacteroidales RF16 group, Oscillibacter*, and multiple other genera within the SI, *Helicobacter* and *Christensenellaceae R-7* group within the cecum, and *NK4A214 group* within the feces positively correlated with more severe pathology in the cecum (Fig 5.16 and Table 5.2). Meanwhile, *Bifidobacterium* in the SI, *Fournierella* and unclassified Bifidobacteriaceae and Christensenellaceae in the cecum, and unclassified Bifidobacteriaceae and *Allobaculum* in the feces negatively correlated with more severe pathology in the cecum. Other taxa were also strongly associated with other infection factors such as vRNA loads and histopathology in the respiratory tissues, particularly bacteria identified in the cecum. Overall, several bacteria were enriched among the different groups and correlated with vRNA loads and pathology, suggesting that intestinal microbes may play a role in disease pathology such as severity of lesions within the cecum during respiratory viral infection.

Discussion

The present study uses an aged GSH model (14-months-old) to understand the pathobiology and respiratory/intestinal microbiota changes after SARS2 infection with and without previous FLUAV exposure. To our knowledge, there have been no previous studies that investigated the effect of SARS2 infection in 14-month aged GSH and how prior FLUAV exposure may affect the pathogenesis within this population subset. Investigating the interplay between FLUAV pre-exposure and SARS2 in the elderly population is imperative as FLUAV H1N1 was the most common detected co-infecting virus with SARS2, and patients with viral co-infection had more severe symptoms and required ICU admission in a recent study (315).

Aging has been shown to affect the immune response leading to increased susceptibility to infections (316). Understanding the effect of FLUAV pre-exposure to COVID-19 in the aging population is beneficial as seasonal influenza viruses are one of the most prevalent causes of morbidity and mortality in the elderly (317). In this old-age GSH model utilized within this study, SARS2 infection led to weight loss starting at 2 dpc and high vRNA loads in the NT, trachea, lungs, and heart at 3 and 6 dpc. This is consistent with previous studies using aged GSH at 7-9 months showing peak weight loss at 6 to 7 dpc (205, 297, 298). SARS2 and FLUAV-SARS2 GSHs had similar vRNA loads for respiratory and non-respiratory tissues except for significantly increased vRNA loads in the heart at 3 dpc and the NTs at 6 dpc in GSHs exposed to SARS2 only. Comparably, similar SARS2 vRNA loads within respiratory tissues between 6–8-weeks old GSHs infected with SARS2 and co-infected with FLUAV (PR8) H1N1 were observed at 4 dpc (293). While we observed a reduction of vRNA in the NT at 6 dpc, a recent report showed that prior IAV infection 14 days before SARS2 infection resulted in reduced SARS2 replication in the lung of male 6-8 weeks old GSH (298). High SARS2 viral loads in respiratory samples, including NT, trachea, and lungs, at early time points, were also observed in 8–10-month-old GSH, consistent with our findings (205, 297). Here, pulmonary lesions were overall milder in SARS2 GSH than FLUAV-SARS2 GSH at 3 dpc, with moderate numbers of inflammatory cells, like what was previously observed in GSH co-infected with FLUAV (293). However, more severe lesions were observed in SARS2 GSH compared to FLUAV-SARS2 GSH at 6 dpc. The dichotomy of these observations may be explained by faster disease progression and recovery in the FLUAV-SARS2 group compared to the SARS2 group or simply sample size effect.

Dysbiosis of the lung, intestine, and fecal microbiota composition was observed after SARS2 challenge with and without FLUAV pre-exposure. Numerous studies have reported that viral infections can affect the residential microbial composition and abundance within the respiratory tract (reviewed in (301)). In this study, beta diversity showed distinct clustering among both SARS2 challenged groups and the mock. Consistent with these observations, a previous study analyzing the oropharyngeal microbiota in humans showed beta diversity separations corresponding to COVID-19 severity (318). In contrast, no statistically significant differences in alpha diversity in the lower respiratory tract were detected among SARS2 challenged GSHs and the mock controls, consistent with observations in the upper and lower respiratory tract of COVID19 patients (302, 303, 318).

The aged GSH lung microbiota was observed to be dominated by Firmicutes and Bacteroidetes at the phylum level and *Prevotella spp.*, *Veillona spp.*, and *Streptococcus spp.*, at the genus level, which is consistent with previous studies of healthy human lungs (301). GSHs challenged with SARS2 exhibited an increased relative abundance of Proteobacteria at 3 and 6 dpc. The expansion of Proteobacteria members has previously been associated with FLUAV H1N1 infection and has been positively correlated with alveolar and systemic inflammation in patients with acute respiratory distress syndrome (301, 319). At the genus level, we observed enrichment of predominantly gram-negative bacteria within the genus *Prevotella 7, Campylobacter, Johnsonella, Fusobacterium, Haemophilus*, *Moraxella*, and gram-positive *Streptococcus* following SARS2 challenge.

We also observed a positive correlation between *Actinomyces*, *Bifidobacterium*, *Prevotella 7*, and *Haemophilus* with more severe NT histological scores, while *Fusobacterium* positively correlated with more severe lung scores. *Streptococcus pneumoniae*, *Klebsiella pneumoniae*, and *Haemophilus influenzae* are reported among the most common bacterial co-infections in COVID-19 patients (320). *Haemophilus* was also previously described as a hallmark of the oropharyngeal microbiome in critically ill COVID-19 patients (318). Further, *Prevotella* spp. have been associated with increased inflammation by stimulating epithelial cells to produce IL-6, IL-8, and CCL20, which can then prompt recruitment of neutrophils and mucosal Th17 immune responses (321). A recent study showed increased TGFβ, IL-17, and neutrophil recruitment within the respiratory tract of SARS2 infected aged GSH (40+ weeks) compared to young GSH (6-8 weeks) (298). Similarly, moderate to large numbers of neutrophils, notably at 6 dpc, were also observed within this study by histopathology in both SARS2 groups. Elevated levels of neutrophils within the lung are a hallmark of COVID-19 and has been hypothesized to contribute to the severe disease pathology observed in aged individuals (298, 322, 323). Increased serum levels of IL-6 and IL-8 have also been associated with disease severity in COVID-19 adult patients and enrichment of CCL20 has been observed in mechanically ventilated patients with COVID-19 (324-326). In contrast, other studies showed that bronchoalveolar lavage (BAL) samples of 50-77 years old COVID-19 positive patients were associated with *Acinetobacter*, *Chryseobacterium*, *Burkholderia*, and Enterobacteriaceae, while COVID-19 negative pneumonia patients were associated with *Prevotella*, *Campylobacter, Streptococcus*, and *Haemophilus* (194, 302). The SARS2 challenged GSHs within this study displayed more similar microbial signatures as observed in pneumonia patients as opposed to SARS2 patients, suggesting that bacteria within the genus *Prevotella*, *Campylobacter*, *Streptococcus*, and *Haemophilus* may be associated with a general respiratory disease pathology rather than a specific response to SARS2 infection.

Previous exposure to FLUAV in combination with SARS2 infection led to the enrichment of low abundance bacteria such as *Prevotella 7*, *Streptococcus, Johnsonella, Fusobacterium, Haemophilus,* and *Moraxella* within the lungs. *Haemophilus* was enriched in all GSHs at 3 and 6 dpc in the FLUAV-SARS2 group, while it was prevalent in only 1 out 3 GSHs at 6 dpc in the SARS2 group. These results suggest that previous innate immune response stimulation from FLUAV pre-exposure may influence the duration of opportunistic pathogen enrichment such as *Haemophilus* post-SARS2 infection. It has also been previously demonstrated that 6-8 week old GSH sustained heightened gene expression of interferon-stimulating genes 7 and 14 days post FLUAV infection (298). The innate immune response, including macrophages and neutrophils, is important for viral clearance but also plays a role in regulating commensal microbes (135). For instance, interferon-γ produced during T cell responses to FLUAV infection in mice correlated with suppression of phagocytosis by alveolar macrophages leading to the inhibition of initial bacterial clearance and the opportunity for secondary bacterial infections (327). Respiratory viral infections can also promote bacterial colonization in the lower respiratory tract by excessive mucus production, decreased cilia movement, and impairment of the innate immune response leading to inefficient bacterial clearance resulting in the enrichment of opportunistic pathogens (135).

We also examined the response of the gut microbiota to infection. While previous studies in humans have detected vRNA in the intestine and feces correlating with occasional reports of gastrointestinal symptoms, we observed very low to no vRNA in the small or large intestine of GSH's, consistent with previous reports (187, 188, 207). Numerous studies have also shown that acute and chronic lung diseases induce changes in gut microbiota through the gut-lung axis (208, 304). Due to the difficulty accessing intestinal samples, most human samples collected for microbiota analysis are fecal samples. Within human fecal samples, SARS2 infection has been associated with an increased relative abundance of opportunistic bacteria such as *Streptococcus*, *Rothia*, *Veillonella*, *Erysipelatoclostridium*, and *Actinomyces* while patients infected with FLUAV H1N1 was enriched in *Enterococcus, Prevotella, Finegoldia*, and *Peptoniphilus* (308). Meanwhile, fecal samples from young male GSHs infected with SARS2 displayed increased abundance of *Oscillospiraceae UCG-007, Helicobacter, Escherichia-Shigella*, and *Parasuturella* and decreased abundance of short-chain fatty acid (SCFA)-producing Firmicutes such as *Ruminoccocus, Lachnospiraceae NK4A136, and Lachnospiraceae UCG-001* (328). In accordance with previous studies, we observed enrichment of opportunistic bacteria including *Streptococcus* and *Helicobacter* in the SI and cecum while Lachnospiraceae was decreased in the feces of SARS2 challenged hamsters compared to the mock controls. Lachnospiraceae spp. have been previously described to produce SCFA, which plays a role in intestinal barrier integrity and modulation of pro-inflammatory factors, suggesting a beneficial role within a "healthy" gut microbiota (329). In addition, increased relative abundance of *Mucispirillum*, Erysipelotrichaceae, and Spirochaetaceae (spirochetosis) was observed within cecum and feces of SARS2 challenged GSH with and without FLUAV exposure, in which spp. from these genera have been associated with inflammatory gastrointestinal disorders or diarrhea (330-332). *Ruminococcaceae NK4A214 group, Helicobacter,* and *Chirstensenellaceae R-7* group within the cecum and feces also positively correlated with more severe pathology in the cecum and have been previously associated with chronic diseases such as chronic obstructive pulmonary disease, colorectal cancer, and ulcers (333-335).

Interestingly, multiple genera including *Bifidobacterium, Allobaculum, Ileibacterium, Faecalibaculum,* and unclassified Eubacteriaceae were enriched after SARS2 challenge compared to their respective pre-challenge fecal samples; however, no taxa were considered significantly enriched in the FLUAV exposed GSHs when compared to their pre-challenge counterpart. The results suggest that initial stimulation of the innate immune response may result in greater changes of the intestinal microbiota compared to subsequent immune activations, or differences previously observed among the mock and FLUAV-SARS2 GSH can be explained by individual variability. The interplay between the gut microbiome and respiratory viral infections is bidirectional (135). A respiratory virus infection can induce gut dysbiosis (135); for instance, FLUAV infection favors type I interferon immune response which then promotes the outgrowth of Proteobacteria (170). Contrastingly, the gut microbiome can also influence the immune response against the respiratory pathogen (135); for example, macrophages from mice treated with antibiotics to induce depletion of the commensal bacteria exhibit decreased responses to type 1 and II interferons and reduced capacity to regulate viral replication during FLUAV infection (251).

Several limitations of this study must be noted: Despite the collection of multiple tissues for analysis, the study contained a relatively small sample size. And while the immune response plays a crucial role during early viral infection and the host microbiota, the immune response was not evaluated in this study. Future studies, including the analysis of the immune response, are needed to understand the effect of previous respiratory virus exposure to SARS2 infection and how the adaptive and innate immune response modulates the microbiota at the site of infection or through the gut-lung axis. We did not detect antibodies post-FLUAV H1N1 inoculation, which is similar to what has been previously observed in 2-3 month old GSHs (336). While a recent study showed high viral titers of FLUAV H1N1 in GSHs, the study did not assess antibody titers for FLUAV (293).

In summary, we characterized the pathogenicity and identified respiratory and gut microbiota changes during SARS2 infection with and without FLUAV pre-exposure in an animal model, emulating in this case, the elderly population. Information on the characterization of the lower respiratory tract in the elderly population is limited because of the difficulty of accessing samples from patients (304). Because both SARS2 and FLUAV notably affect geriatric patients, understanding the disease pathology and the effect of the microbiota can potentially lead to the identification of differential host markers for disease severity within that demographic. While human BALF and fecal samples can be informative, human samples within elderly patients are more challenging to collect and tend to be highly variable and impacted by environmental conditions. As such, studying the effect of SARS2 infection on the microbiome in animal models in a controlled laboratory environment is a valuable alternative. In our work, specific microbial markers that have been previously reported in co-infections from opportunistic pathogens during COVID-19 were identified in the lungs of over aged GSHs challenged with SARS2 with and without FLUAV pre-exposure. Microbial changes within the different anatomical sections of the intestinal tract were also observed, warranting more in-depth studies investigating the complex relationship between the microbiota and pathogenicity in SARS2 in elderly patients.

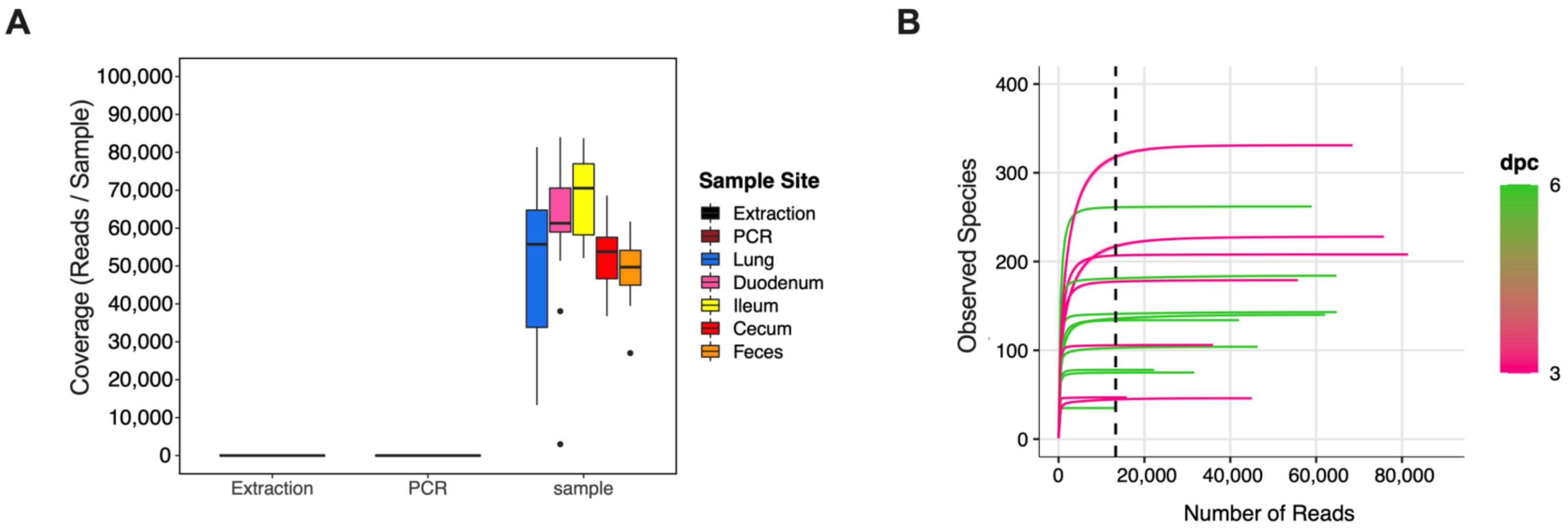

Figure 5.1 Sample coverage. (A) Sample coverage measured by the number of reads per sample separated by controls (DNA extraction and PCR blanks) and sample. The samples are color-coded by sample type (Lung: blue, Duodenum: pink, Ileum: yellow, Cecum: red, and Feces: orange). (B) Rarefaction curve of the lung samples colored by dpc (3 dpc: pink, 6 dpc: green). The dashed line (x = 13,306) represents the number of reads each sample was rarified for downstream diversity analyses.

Figure 5.2. Experimental design, body weight, and viral loads of aged GSHs post-SARS2 challenge. (A) 14-month female GSHs were randomly distributed into 3 groups: SARS2 GSHs were challenged with SARS2 (n = 6), FLUAV-SARS2 GSHs were pre-exposed to FLUAV twice and then challenged with SARS2 (n = 7), and mock GSH remained unchallenged (n = 3). A subset of GSH (n = 3 group/time point) were humanely euthanized at 3 and 6 dpc, and numerous tissues were collected. Feces was collected 1 day before challenge, and then 3 and 6 dpc for the remaining individuals. Illustration created with BioRender.com. (B) Weight change was calculated for all groups up to 6 dpc, including SARS2 (red triangles), FLUAV-SARS2 (blue triangles), and mock (white circles). Viral loads at (C) 3 dpc and (D) 6 dpc from the challenged groups were determined by RT-qPCR and conveyed as log10 TCID50 equivalent (TCID50eq) per gram of tissue. Error bars represent the mean ± SEM. Statistical analysis was performed by two-way ANOVA with a Dunnett's multiple comparisons test, * <0.05. NT- nasal turbinates, LI – large intestine.

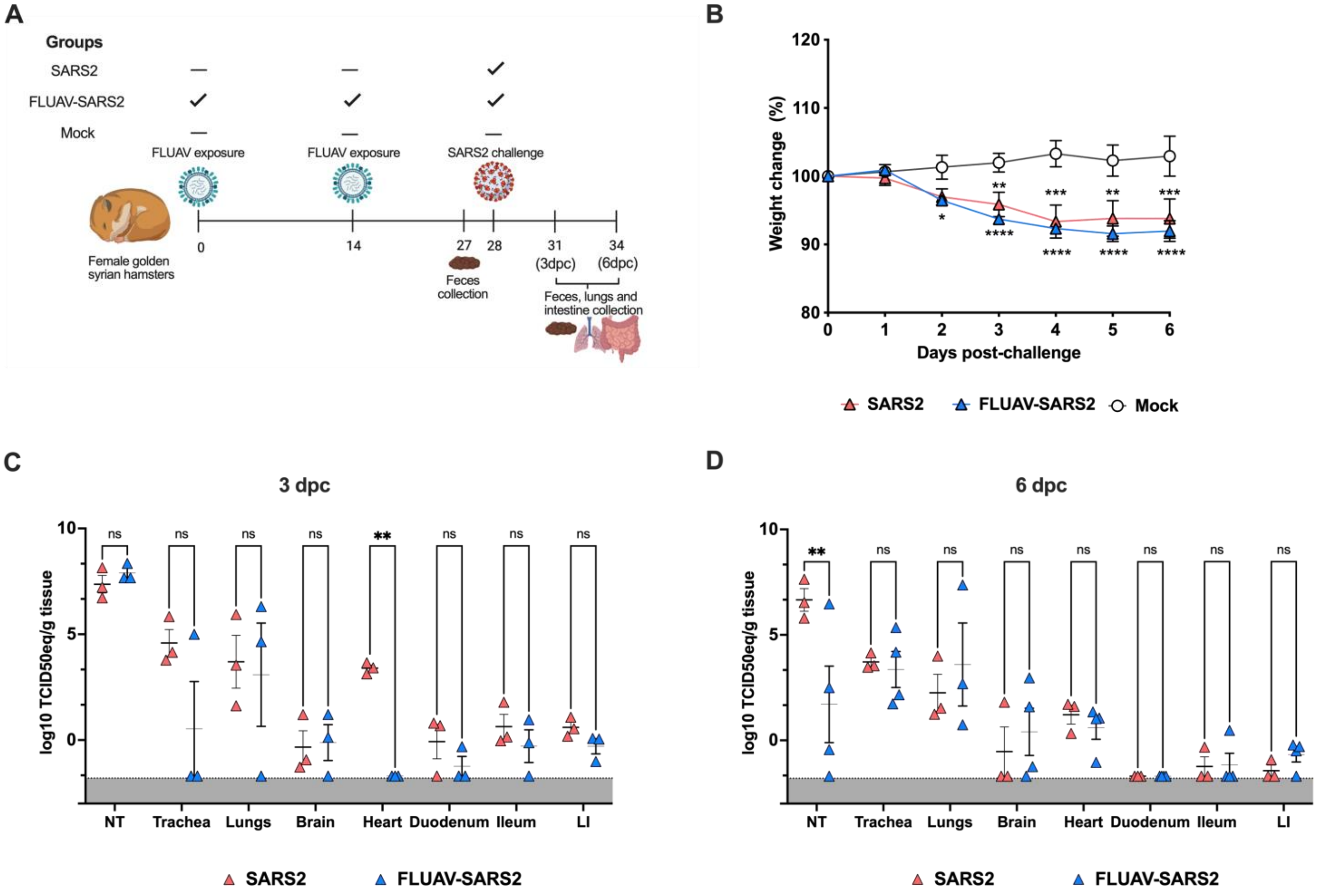
A
Groups
SARS2
FLUAV-SARS2
Mock
FLUAV exposure
FLUAV exposure
SARS2 challenge
Female golden syrian hamsters
0
14
27
28
31 (3dpc)
34 (6dpc)
Feces collection
Feces, lungs and intestine collection
B
Weight change (%)
120
110
100
90
80
Days post-challenge
0
1
2
3
4
5
6
*
**
****
***
****
**
****
***
****
SARS2
FLUAV-SARS2
Mock
C
3 dpc
log10 TCID50eq/g tissue
10
5
0
ns
ns
ns
ns
**
ns
ns
ns
NT
Trachea
Lungs
Brain
Heart
Duodenum
Ileum
LI
SARS2
FLUAV-SARS2
D
6 dpc
log10 TCID50eq/g tissue
10
5
0
**
ns
ns
ns
ns
ns
ns
ns
NT
Trachea
Lungs
Brain
Heart
Duodenum
Ileum
LI
SARS2
FLUAV-SARS2

Fig 5.3. Histopathologic findings in the different respiratory tissues of SARS2, FLUAV-SARS2, and mock-challenged hamsters at given timepoints. (A-F) Nasal turbinates. (G-L) Tracheas. (M-R) Lungs. (A-B) Moderate to severe necrotizing rhinitis in the infected hamsters at 3 dpc. The surface epithelium is necrotic, infiltrated by neutrophils and sloughing into the lumen (arrowhead). The lumen is filled with abundant intraluminal suppurative exudate (asterisk). (D-E) Rhinitis is still present in the infected hamsters at 6 dpc. The epithelium is irregular, with fewer necrotic cells sloughing into the lumen (arrowheads). The lumen is filled with abundant intraluminal suppurative exudate (asterisk). (C, F) No significant findings are observed in mock hamsters' nasal turbinates. (G-H) Clusters of neutrophils and lymphocytes are expanding the mucosal lamina propria (arrowheads) of infected hamsters' tracheas at 3 dpc. Occasionally, tracheal glands are dilated by intraluminal eosinophilic material (asterisk). (J-K) Similar small mix of neutrophils, macrophages, and lymphocytes (arrowheads) are observed in the tracheas of infected hamsters at 6 dpc. (I, L) No significant findings are observed in mock hamsters' tracheas. (M-N) At 3 dpc, the bronchiolar mucosa in infected hamsters is necrotic and sloughing into the lumen (asterisk). Small to moderate clusters of neutrophils and lymphocytes are infiltrating the peribronchiolar interstitium and bronchiolar mucosa (arrowheads). (P-Q) At 6-dpc, pneumonia is characterized by florid pneumocyte type II hyperplasia following the outline of the alveoli (arrows within insert: bottom right corner; HE, 40X), and syncytia. Moderate to large numbers of neutrophils, macrophages and lymphocytes are expanding the septa and pouring into the alveoli (arrowheads). (O, R) No significant findings are observed in the mock hamsters' lungs. All H&E images are pictured at 20X magnification.

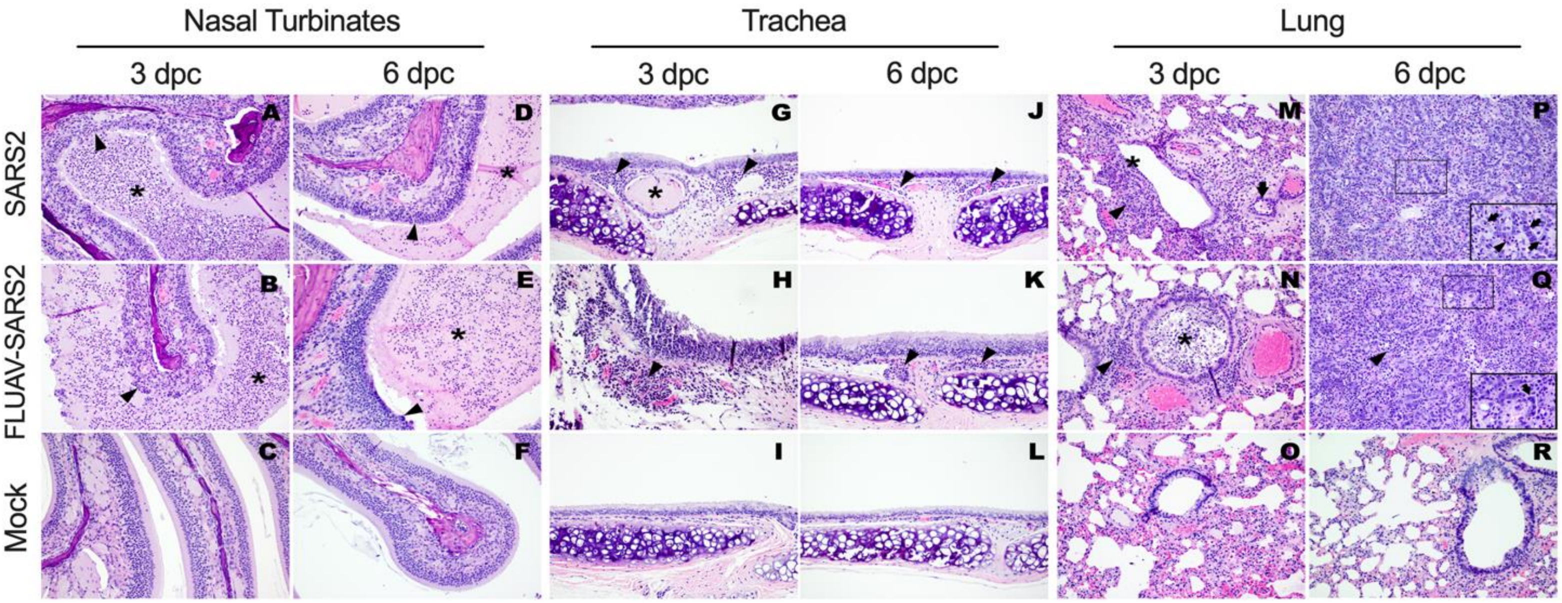
Nasal Turbinates
Trachea
Lung
3 dpc
6 dpc
3 dpc
6 dpc
3 dpc
6 dpc
SARS2
FLUAV-SARS2
Mock
A
D
G
J
M
P
B
E
H
K
N
Q
C
F
I
L
O
R

Fig 5.4. Immunohistochemistry staining in respiratory tissues of SARS2, FLUAV-SARS2, and mock-challenged hamsters at given timepoints. (A-F) Nasal turbinates. (G-L) Lungs. (A-B) Variable amounts of intracytoplasmic virus antigen (red) immunolabeling is present in epithelial cells in challenged GSH. (D-E) Low levels of virus antigen are present in the epithelial cells as evidenced by faint red immunostaining. (C, F) No significant virus antigens are observed in mock hamsters' nasal turbinates. (G-H) Moderate amounts of virus antigen (red) are present in bronchiolar epithelium and intraluminal necrotic cellular debris in challenged GSH. (J-K) The intracytoplasmic virus antigen (red) is scarce at this timepoint. (I, L) No significant amount of virus antigen (red) immunolabeling are observed in the mock hamsters' lungs. All immunohistochemistry images are at 40X magnification.

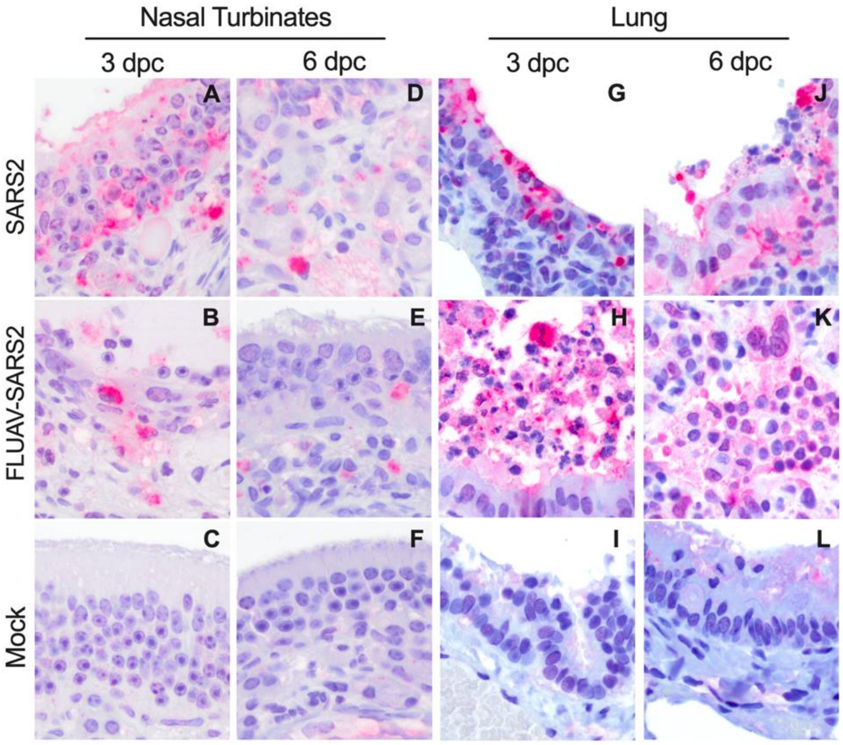

Figure 5.5. Histopathologic findings in intestinal tissues of SARS2, FLUAV-SARS2, and mock-challenged hamsters at given timepoints. (A-F) Small numbers of eosinophils, lymphocytes and macrophages are expanding the villi lamina propria (arrowheads) regardless of the timepoint and treatment groups. In the infected groups, the lacteals are dilated by small amounts of eosinophilic fluid (arrows). Increased numbers of protozoa compatible with Giardia spp. (insert) are populating the lumina in most sections. (G-H) At 3 dpc, moderate numbers of eosinophils, macrophages, and lymphocytes (arrowheads) are expanding the mucosa lamina propria in infected hamsters. The surface enterocytes are necrotic and sloughing into the lumen (arrow). The lumina contains mixed bacteria (insert) and protozoa. (I) In the mock infected hamsters, only small clusters of eosinophils are infiltrating the mucosa (arrowhead). Rare round protozoa (insert) are compatible with Entamoeba spp. (J and L) Small numbers of neutrophils infiltrate the mucosa lamina propria (arrowhead) in SARS2-only infected hamsters and mocks. Intestinal lumina contain mixed bacteria and a few round protozoa (insert) compatible with Entamoeba spp. (K) In FLUAV-SARS2 hamsters at 6 dpc, lesions recapitulate what is described at 3 dpc. The mucosa is infiltrated by mixed inflammatory cells (arrowheads), the glands lumen is dilated by increased bacteria (arrow), and enterocytes are sloughing into the lumen. All H&E images are pictured at 20X and inserts are at 40X magnification.

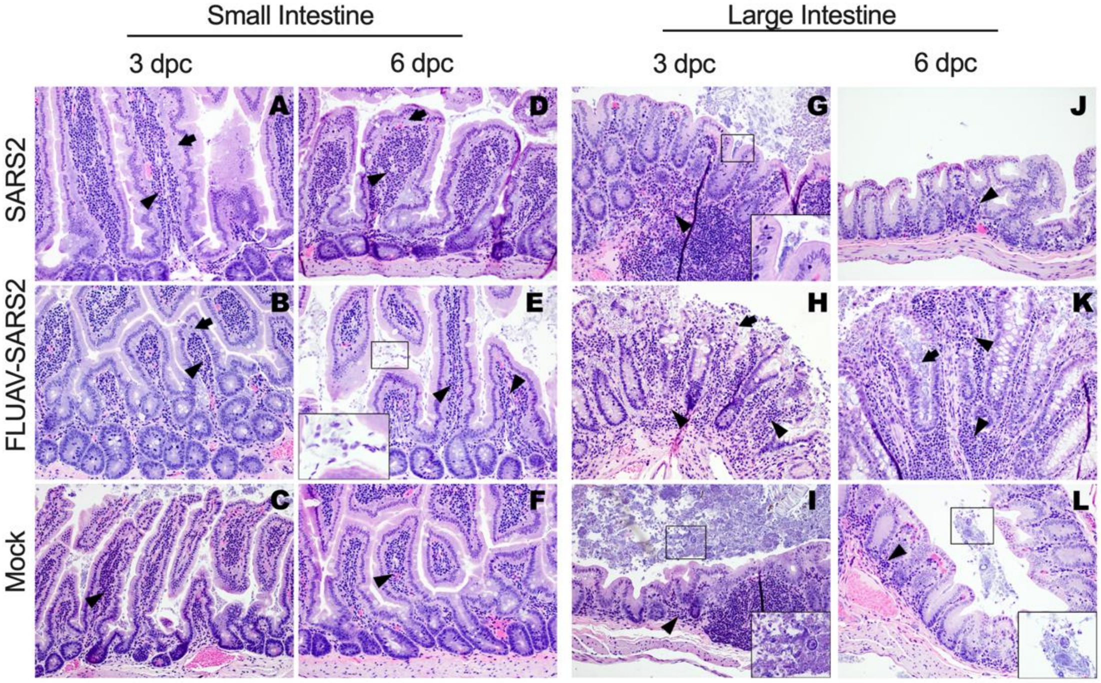
Small Intestine
Large Intestine
3 dpc
6 dpc
3 dpc
6 dpc
SARS2
FLUAV-SARS2
Mock
A
D
G
J
B
E
H
K
C
F
I
L

Figure 5.6. Diversity and taxonomic abundances of the lungs in SARS2, FLUAV-SARS2 and mock-challenged GSH. (A) Alpha diversity measure of the observed number of ASVs (left) and Shannon diversity (right) between SARS2 (red), FLUAV-SARS2 (blue), and mock (white) containing all dpc from the rarified ASV count table. Multiple group comparisons were performed using Kruskal-Wallis, while pair-wise comparisons were conducted using the Wilcox test with Bonferroni correction. (B) NMDS plot of unweighted Jaccard dissimilarity distance. The color designates groups (SARS2: red, FLUAV-SARS2: blue, and mock: black), and dpc is categorized by the shape (3 dpc: circle and 6 dpc: square). Ellipses were constructed using the standard deviation. (C) Comparison of unweighted Jaccard dissimilarity distance within each group and across multiple comparisons. Intra-group variation is marked with grey shading, while the inter-group comparisons are marked gold. Pair-wise comparisons were performed using the Wilcox test with Bonferroni correction. (D) Relative abundances agglomerated at the phylum level separated by group and dpc. Phyla in bold are those discussed within the results. (E) Relative abundances of each hamster at the lowest taxonomic rank identified separated by group and ordered by dpc. Taxa in bold are those discussed within the results. ns: non-significant ($p > 0.05$); * <0.05, ** < 0.005, *** < 0.0005, **** < 0.00005.

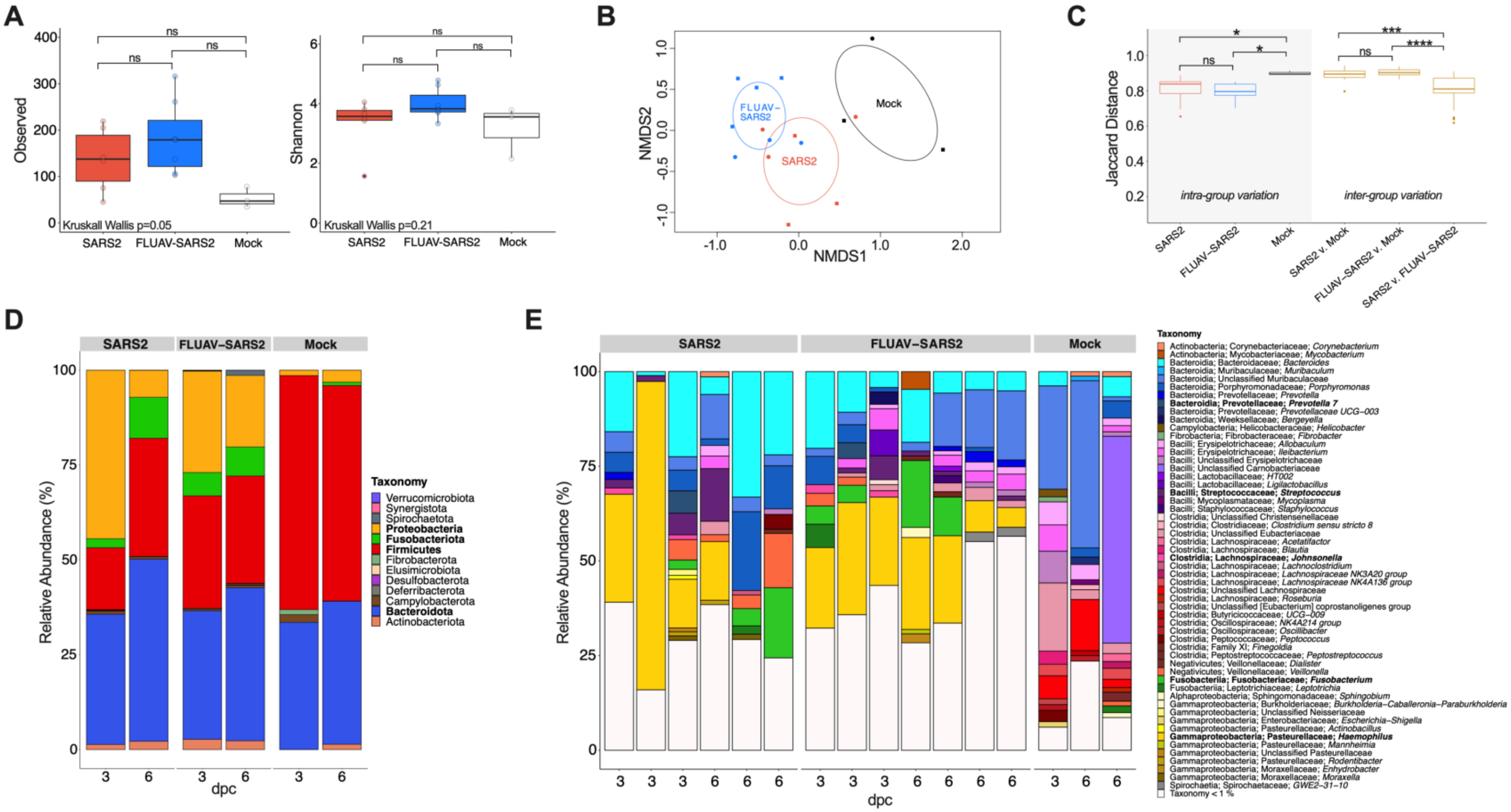
A
Observed
Kruskall Wallis p=0.05
ns
SARS2
FLUAV-SARS2
Mock
Shannon
Kruskall Wallis p=0.21
B
NMDS1
NMDS2
FLUAV-SARS2
SARS2
Mock
C
Jaccard Distance
intra-group variation
inter-group variation
SARS2 v. Mock
FLUAV-SARS2 v. Mock
SARS2 v. FLUAV-SARS2
*
***
****
D
Relative Abundance (%)
dpc
Taxonomy
Verrucomicrobiota
Synergistota
Spirochaetota
Proteobacteria
Fusobacteriota
Firmicutes
Fibrobacterota
Elusimicrobiota
Desulfobacterota
Deferribacterota
Campylobacterota
Bacteroidota
Actinobacteriota
E
Taxonomy
Actinobacteria; Corynebacteriaceae; Corynebacterium
Actinobacteria; Mycobacteriaceae; Mycobacterium
Bacteroidia; Bacteroidaceae; Bacteroides
Bacteroidia; Muribaculaceae; Muribaculum
Bacteroidia; Unclassified Muribaculaceae
Bacteroidia; Porphyromonadaceae; Porphyromonas
Bacteroidia; Prevotellaceae; Prevotella
Bacteroidia; Prevotellaceae; Prevotella 7
Bacteroidia; Prevotellaceae; Prevotellaceae UCG–003
Bacteroidia; Weeksellaceae; Bergeyella
Campylobacteria; Helicobacteraceae; Helicobacter
Fibrobacteria; Fibrobacteraceae; Fibrobacter
Bacilli; Erysipelotrichaceae; Allobaculum
Bacilli; Erysipelotrichaceae; Ileibacterium
Bacilli; Unclassified Erysipelotrichaceae
Bacilli; Unclassified Carnobacteriaceae
Bacilli; Lactobacillaceae; HT002
Bacilli; Lactobacillaceae; Ligilactobacillus
Bacilli; Streptococcaceae; Streptococcus
Bacilli; Mycoplasmataceae; Mycoplasma
Bacilli; Staphylococcaceae; Staphylococcus
Clostridia; Unclassified Christensenellaceae
Clostridia; Clostridiaceae; Clostridium sensu stricto 8
Clostridia; Unclassified Eubacteriaceae
Clostridia; Lachnospiraceae; Acetatifactor
Clostridia; Lachnospiraceae; Blautia
Clostridia; Lachnospiraceae; Johnsonella
Clostridia; Lachnospiraceae; Lachnoclostridium
Clostridia; Lachnospiraceae; Lachnospiraceae NK3A20 group
Clostridia; Lachnospiraceae; Lachnospiraceae NK4A136 group
Clostridia; Unclassified Lachnospiraceae
Clostridia; Lachnospiraceae; Roseburia
Clostridia; Unclassified [Eubacterium] coprostanoligenes group
Clostridia; Butyricicoccaceae; UCG–009
Clostridia; Oscillospiraceae; NK4A214 group
Clostridia; Oscillospiraceae; Oscillibacter
Clostridia; Peptococcaceae; Peptococcus
Clostridia; Family XI; Finegoldia
Clostridia; Peptostreptococcaceae; Peptostreptococcus
Negativicutes; Veillonellaceae; Dialister
Negativicutes; Veillonellaceae; Veillonella
Fusobacteriia; Fusobacteriaceae; Fusobacterium
Fusobacteriia; Leptotrichiaceae; Leptotrichia
Alphaproteobacteria; Sphingomonadaceae; Sphingobium
Gammaproteobacteria; Burkholderiaceae; Burkholderia–Caballeronia–Paraburkholderia
Gammaproteobacteria; Unclassified Neisseriaceae
Gammaproteobacteria; Enterobacteriaceae; Escherichia–Shigella
Gammaproteobacteria; Pasteurellaceae; Actinobacillus
Gammaproteobacteria; Pasteurellaceae; Haemophilus
Gammaproteobacteria; Pasteurellaceae; Mannheimia
Gammaproteobacteria; Unclassified Pasteurellaceae
Gammaproteobacteria; Pasteurellaceae; Rodentibacter
Gammaproteobacteria; Moraxellaceae; Enhydrobacter
Gammaproteobacteria; Moraxellaceae; Moraxella
Spirochaetia; Spirochaetaceae; GWE2–31–10
Taxonomy < 1 %

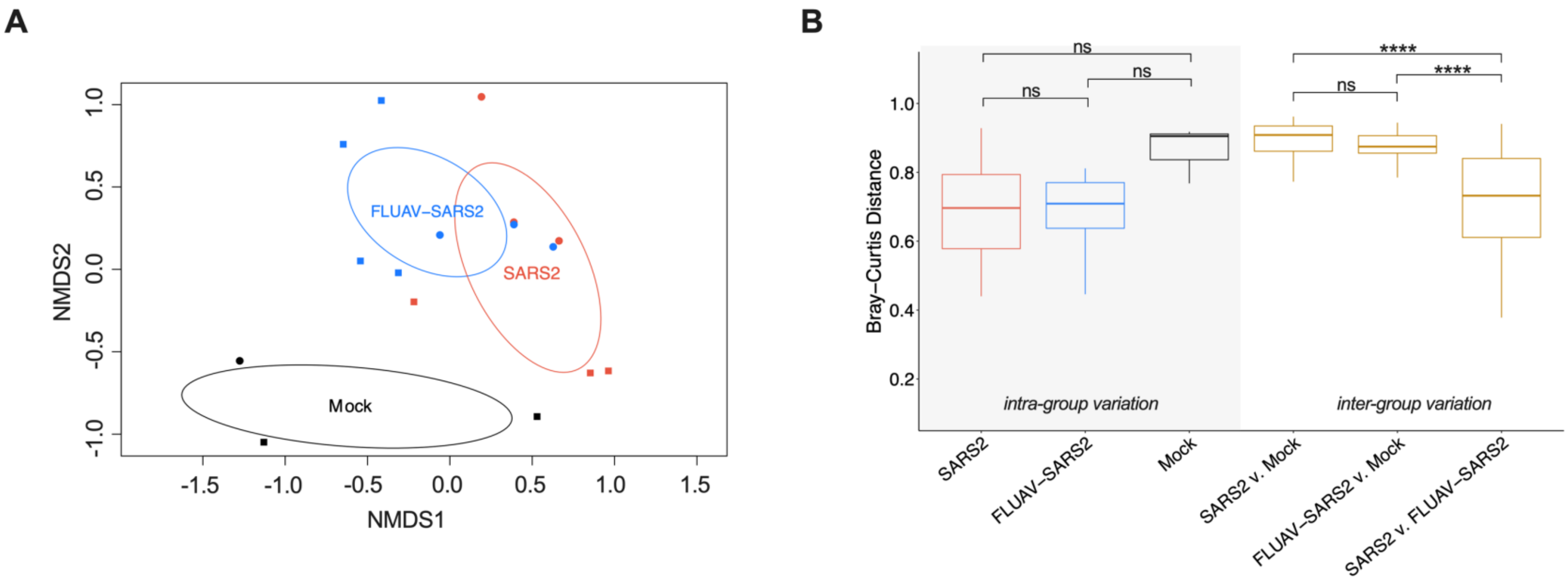

Fig 5.7. Beta diversity of the lungs in SARS2, FLUAV-SARS2 and mock-challenged GSH. (A) NMDS plot of weighted Bray-Curtis dissimilarity distance of the lung samples. The color designates groups (SARS2: red, FLUAV-SARS2: blue, and mock: white) and dpc by the shape (3 dpc: circle and 6 dpc: square). Ellipses were constructed to include all points within the group. (B) Comparison of weighted Bray-Curtis dissimilarity distance within each group and across multiple comparisons of the lung samples. Intra-group variation is marked grey shading, while the inter-group comparisons are marked gold. Pair-wise comparisons were performed using the Wilcox test with Bonferroni correction.

Fig 5.8. Differential taxonomic analysis of the lung microbiota in SARS2, FLUAV-SARS2 and mock-challenged GSH. (A-B) Cladogram of significantly ($p<0.05$) abundant taxa between (A) SARS2 (red) and mock (grey) or (B) FLUAV-SARS2 (blue) and mock (grey) using LEfSe analysis with default parameters. Taxa displayed in bold were significant in at least 2/3 differential analyses performed (Deseq2, ALDEx2, and LefSE). (C) A heatmap illustrating the spearman correlation among different infection factors and the relative abundance of bacterial taxa within the lungs. Correlations among pathology of the heart and SI were removed since the pathological score was the same for all GSH. Correlation labels and taxa displayed in bold have a spearman correlation value > 0.60 or < -0.60. SARS2 – challenged with SARS2, FLUAV – inoculated with FLUAV and then challenged with SARS2 (mock-challenged GSH were not included), NT- nasal turbinates, LI – large intestine.

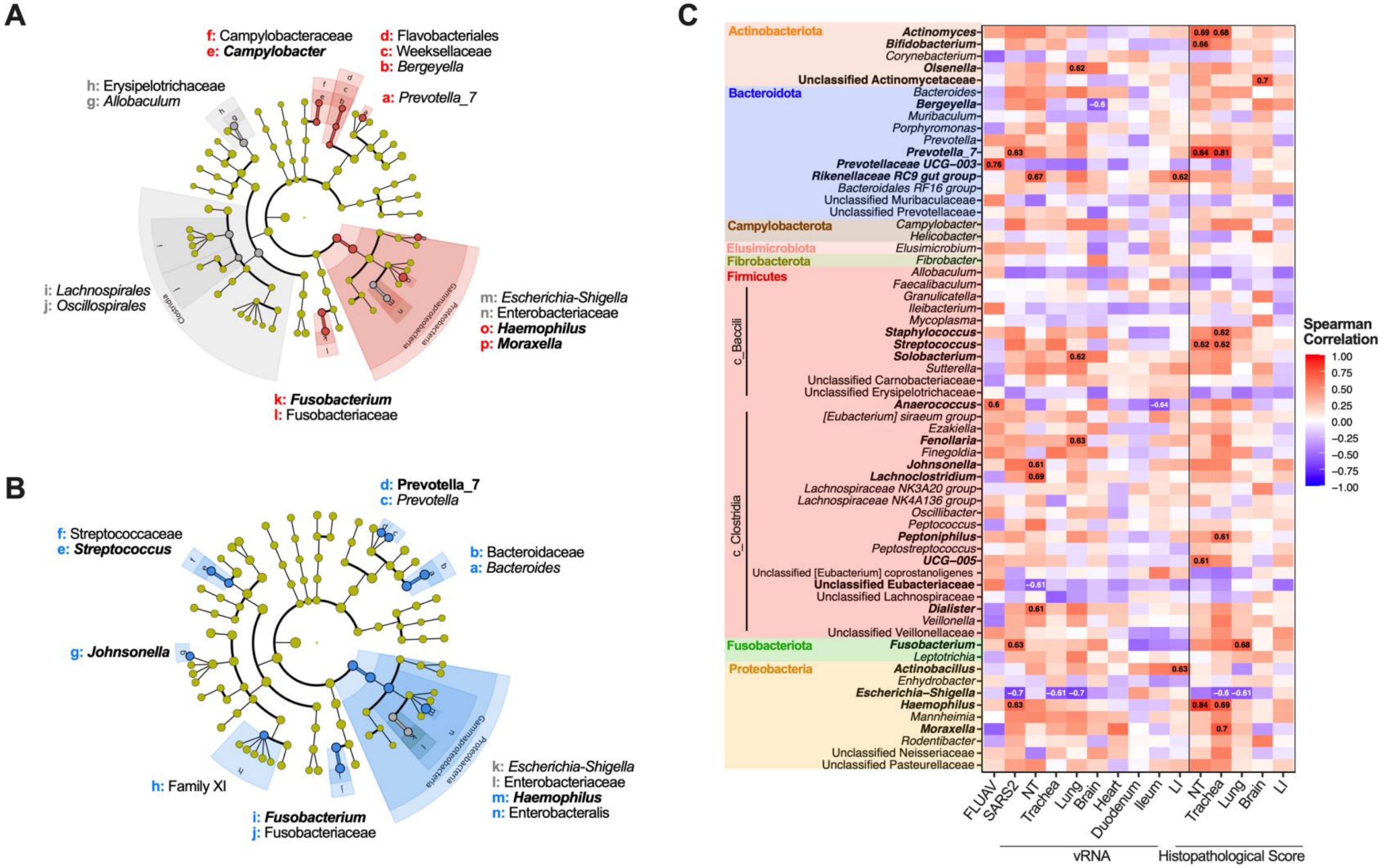
A
f: Campylobacteraceae
e: Campylobacter
d: Flavobacteriales
c: Weeksellaceae
b: Bergeyella
a: Prevotella_7
h: Erysipelotrichaceae
g: Allobaculum
i: Lachnospirales
j: Oscillospirales
Clostridia
m: Escherichia-Shigella
n: Enterobacteriaceae
o: Haemophilus
p: Moraxella
Gammaproteobacteria
Proteobacteria
k: Fusobacterium
l: Fusobacteriaceae
B
d: Prevotella_7
c: Prevotella
f: Streptococcaceae
e: Streptococcus
b: Bacteroidaceae
a: Bacteroides
g: Johnsonella
h: Family XI
i: Fusobacterium
j: Fusobacteriaceae
k: Escherichia-Shigella
l: Enterobacteriaceae
m: Haemophilus
n: Enterobacteralis
Gammaproteobacteria
Proteobacteria
C
Actinobacteriota
Actinomyces
Bifidobacterium
Corynebacterium
Olsenella
Unclassified Actinomycetaceae
Bacteroidota
Bacteroides
Bergeyella
Muribaculum
Porphyromonas
Prevotella
Prevotella_7
Prevotellaceae UCG–003
Rikenellaceae RC9 gut group
Bacteroidales RF16 group
Unclassified Muribaculaceae
Unclassified Prevotellaceae
Campylobacterota
Campylobacter
Helicobacter
Elusimicrobiota
Elusimicrobium
Fibrobacterota
Fibrobacter
Firmicutes
Allobaculum
Faecalibaculum
Granulicatella
Ileibacterium
Mycoplasma
c_Baccili
Staphylococcus
Streptococcus
Solobacterium
Sutterella
Unclassified Carnobacteriaceae
Unclassified Erysipelotrichaceae
Anaerococcus
c_Clostridia
[Eubacterium] siraeum group
Ezakiella
Fenollaria
Finegoldia
Johnsonella
Lachnoclostridium
Lachnospiraceae NK3A20 group
Lachnospiraceae NK4A136 group
Oscillibacter
Peptococcus
Peptoniphilus
Peptostreptococcus
UCG–005
Unclassified [Eubacterium] coprostanoligenes
Unclassified Eubacteriaceae
Unclassified Lachnospiraceae
Dialister
Veillonella
Unclassified Veillonellaceae
Fusobacteriota
Fusobacterium
Leptotrichia
Proteobacteria
Actinobacillus
Enhydrobacter
Escherichia–Shigella
Haemophilus
Mannheimia
Moraxella
Rodentibacter
Unclassified Neisseriaceae
Unclassified Pasteurellaceae
0.69 0.68
0.66
0.62
0.7
–0.6
0.63
0.84 0.81
0.76
0.67
0.62
0.62
0.62 0.62
0.62
0.6
–0.64
0.63
0.61
0.69
0.61
0.61
–0.61
0.61
0.63
0.68
0.63
–0.7
–0.61 –0.7
–0.6 –0.61
0.63
0.84 0.69
0.7
FLUAV
SARS2
NT
Trachea
Lung
Brain
Heart
Duodenum
Ileum
LI
NT
Trachea
Lung
Brain
LI
vRNA
Histopathological Score
Spearman Correlation
1.00
0.75
0.50
0.25
0.00
–0.25
–0.50
–0.75
–1.00

Fig 5.9. Differential taxonomic analysis of the lung microbiota using Deseq2, ALDEx2, and LefSE. (A, C, E) Bacterial taxa identified at different relative abundances between (A) SARS2 (red), and mock (grey) or (C) FLUAV-SARS2 (blue), and mock (grey) or (E) SARS2 (red) and FLUAV-SARS2 (blue) groups using DeSeq2. Significantly enriched taxa were plotted with log2 fold change and the corresponding standard error estimate. (B, D, F) Effect size plot showing the median log2 fold difference (difference between) by the median log2 dispersion (difference within) when comparing (B) SARS2 and mock or (D) FLUAV-SARS2 and mock or (F) SARS2 and FLUAV-SARS2. Taxa considered significant by the Wilcox test are shown in green, taxa with BH corrected p-values are shown in red, while taxa with an effect size greater than 1.5 are outlined in blue. (G) Cladogram showing significantly ($p<0.05$) abundant taxa between SARS2 (red) and FLUAV-SARS2 (blue) using linear discriminant analysis effect size (LEfSe) analysis with default parameters. Taxa are color-coded by phylum, and bold taxa are considered significant in at least 2 of the 3 differential analyses performed (Deseq2, ALDEx2, and LefSE). Significant taxa using Deseq2 were determined by having a p-value < 0.01, while significant taxa using ALDEx2 and LEfSE were determined by having a p-value < 0.05.

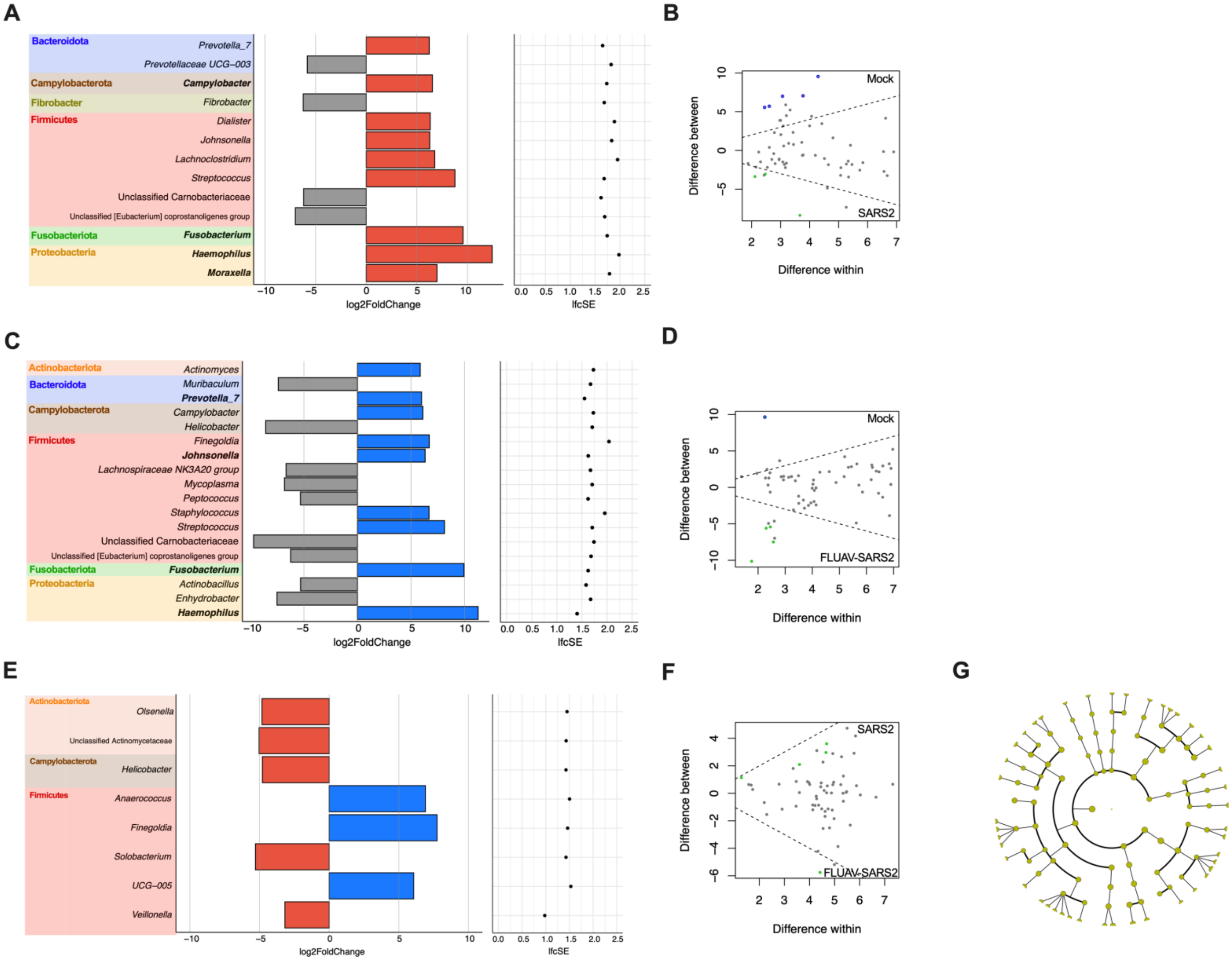
A
Bacteroidota
Prevotella_7
Prevotellaceae UCG−003
Campylobacterota
Campylobacter
Fibrobacter
Fibrobacter
Firmicutes
Dialister
Johnsonella
Lachnoclostridium
Streptococcus
Unclassified Carnobacteriaceae
Unclassified [Eubacterium] coprostanoligenes group
Fusobacteriota
Fusobacterium
Proteobacteria
Haemophilus
Moraxella
−10 −5 0 5 10
log2FoldChange
0.0 0.5 1.0 1.5 2.0 2.5
lfcSE
B
Mock
SARS2
Difference between
Difference within
C
Actinobacteriota
Actinomyces
Bacteroidota
Muribaculum
Prevotella_7
Campylobacterota
Campylobacter
Helicobacter
Firmicutes
Finegoldia
Johnsonella
Lachnospiraceae NK3A20 group
Mycoplasma
Peptococcus
Staphylococcus
Streptococcus
Unclassified Carnobacteriaceae
Unclassified [Eubacterium] coprostanoligenes group
Fusobacteriota
Fusobacterium
Proteobacteria
Actinobacillus
Enhydrobacter
Haemophilus
log2FoldChange
lfcSE
D
Mock
FLUAV-SARS2
Difference between
Difference within
E
Actinobacteriota
Olsenella
Unclassified Actinomycetaceae
Campylobacterota
Helicobacter
Firmicutes
Anaerococcus
Finegoldia
Solobacterium
UCG−005
Veillonella
log2FoldChange
lfcSE
F
SARS2
FLUAV-SARS2
Difference between
Difference within
G

Fig 5.10. Diversity and taxonomic abundances of the intestine and feces in SARS2, FLUAV-SARS2 and mock-challenged hamsters. (A) Rarefaction curve of the intestine and fecal samples colored by sample type. The dashed line (x = 27,020) represents the number of reads each sample was rarified for downstream diversity analyses. (B) The observed number of ASVs between FLUAV-SARS2 (red), SARS2 (blue), mock (white), and pre-challenge (grey) containing all dpc of different sample types from the rarified ASV count table. Statistical analysis comparing the different groups within each sample type was performed using Kruskal-Wallis. (C) Comparison of unweighted Jaccard dissimilarity distance within each group and across multiple comparisons in feces. Intra-group variation is marked with grey shading, while the inter-group comparisons are colored gold. Pair-wise comparisons were performed using the Wilcox test with Bonferroni correction. Comparisons that are not indicated by an asterisk were considered non-significant ($p > 0.05$). (D) Heatmap of the relative abundances of taxa with a relative abundance > 1%. Relative abundances greater than 10% are shown in green. Taxa are color-coded by phylum. Taxa in bold are those discussed within the results. * <0.05, ** < 0.005, *** < 0.0005, **** < 0.00005.

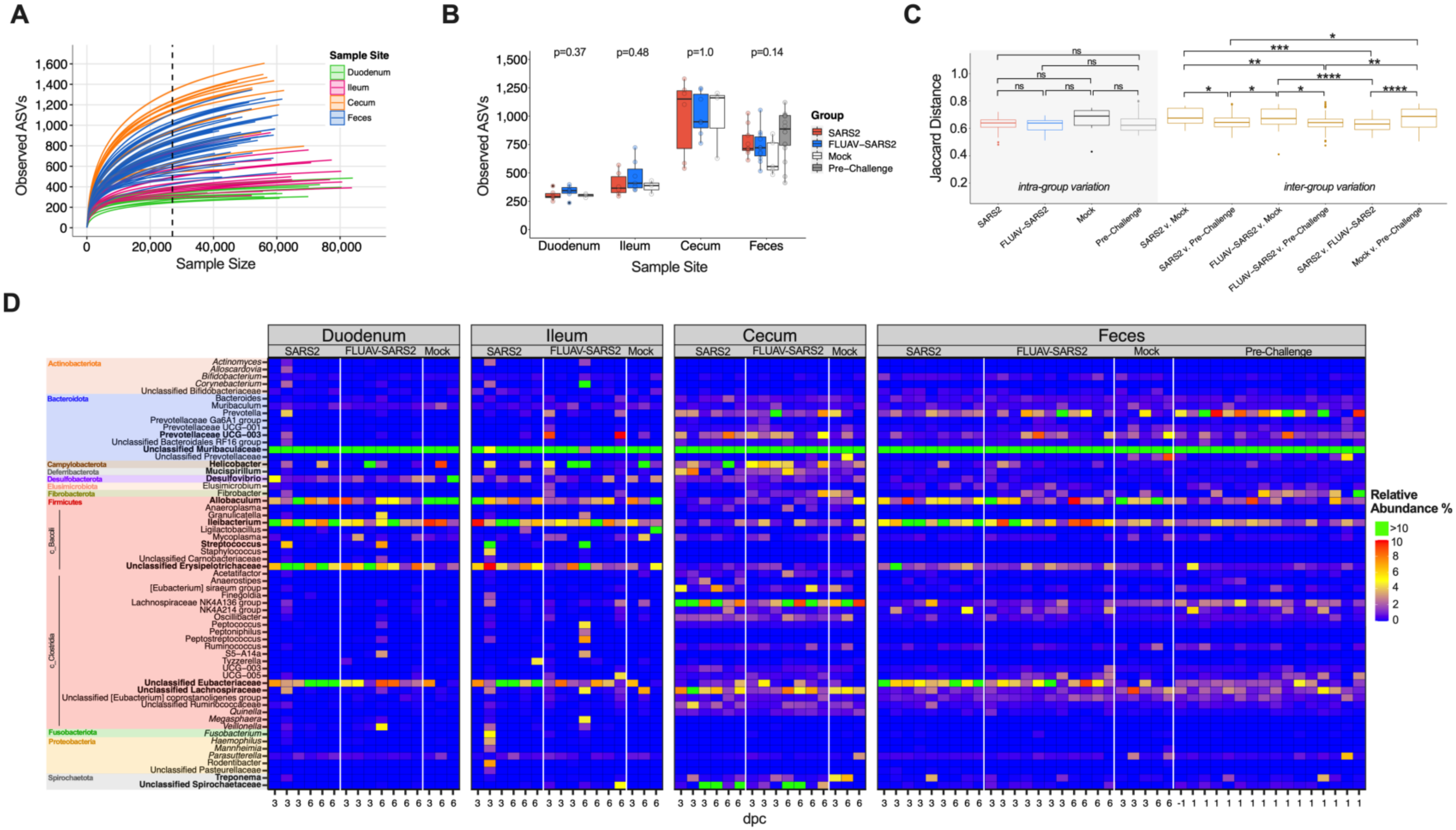
A
Observed ASVs
1,600
1,400
1,200
1,000
800
600
400
200
0
20,000
40,000
60,000
80,000
Sample Size
Sample Site
Duodenum
Ileum
Cecum
Feces
B
p=0.37
p=0.48
p=1.0
p=0.14
Observed ASVs
1,500
1,250
1,000
750
500
250
0
Duodenum
Ileum
Cecum
Feces
Sample Site
Group
SARS2
FLUAV–SARS2
Mock
Pre–Challenge
C
Jaccard Distance
1.0
0.8
0.6
0.4
0.2
ns
*
***
**
****
intra-group variation
inter-group variation
SARS2
FLUAV–SARS2
Mock
Pre–Challenge
SARS2 v. Mock
SARS2 v. Pre–Challenge
FLUAV–SARS2 v. Mock
FLUAV–SARS2 v. Pre–Challenge
SARS2 v. FLUAV–SARS2
Mock v. Pre–Challenge
D
Duodenum
Ileum
Cecum
Feces
SARS2
FLUAV–SARS2
Mock
Pre–Challenge
Actinobacteriota
Actinomyces
Alloscardovia
Bifidobacterium
Corynebacterium
Unclassified Bifidobacteriaceae
Bacteroidota
Bacteroides
Muribaculum
Prevotella
Prevotellaceae Ga6A1 group
Prevotellaceae UCG–001
Prevotellaceae UCG–003
Unclassified Bacteroidales RF16 group
Unclassified Muribaculaceae
Unclassified Prevotellaceae
Campylobacterota
Helicobacter
Deferribacterota
Mucispirillum
Desulfobacterota
Desulfovibrio
Elusimicrobiota
Elusimicrobium
Fibrobacterota
Fibrobacter
Firmicutes
Allobaculum
Anaeroplasma
Granulicatella
Ileibacterium
Ligilactobacillus
Mycoplasma
Streptococcus
Staphylococcus
Unclassified Carnobacteriaceae
Unclassified Erysipelotrichaceae
c_Bacilli
Acetatifactor
Anaerostipes
[Eubacterium] siraeum group
Finegoldia
Lachnospiraceae NK4A136 group
NK4A214 group
Oscillibacter
Peptococcus
Peptoniphilus
Peptostreptococcus
Ruminococcus
S5–A14a
Tyzzerella
UCG–003
UCG–005
Unclassified Eubacteriaceae
Unclassified Lachnospiraceae
Unclassified [Eubacterium] coprostanoligenes group
Unclassified Ruminococcaceae
Quinella
Megasphaera
Veillonella
c_Clostridia
Fusobacteriota
Fusobacterium
Proteobacteria
Haemophilus
Mannheimia
Parasutterella
Rodentibacter
Unclassified Pasteurellaceae
Spirochaetota
Treponema
Unclassified Spirochaetaceae
3 3 3 6 6 6 3 3 3 6 6 6 6 3 6 6
3 3 3 6 6 6 3 3 3 6 6 6 6 3 6 6
3 3 3 6 6 6 3 3 3 6 6 6 6 3 6 6
3 3 3 3 3 6 6 6 3 3 3 3 3 3 6 6 6 6 3 3 3 6 6 -1 1 1 1 1 1 1 1 1 1 1 1 1 1 1 1 1
dpc
Relative Abundance %
>10
10
8
6
4
2
0

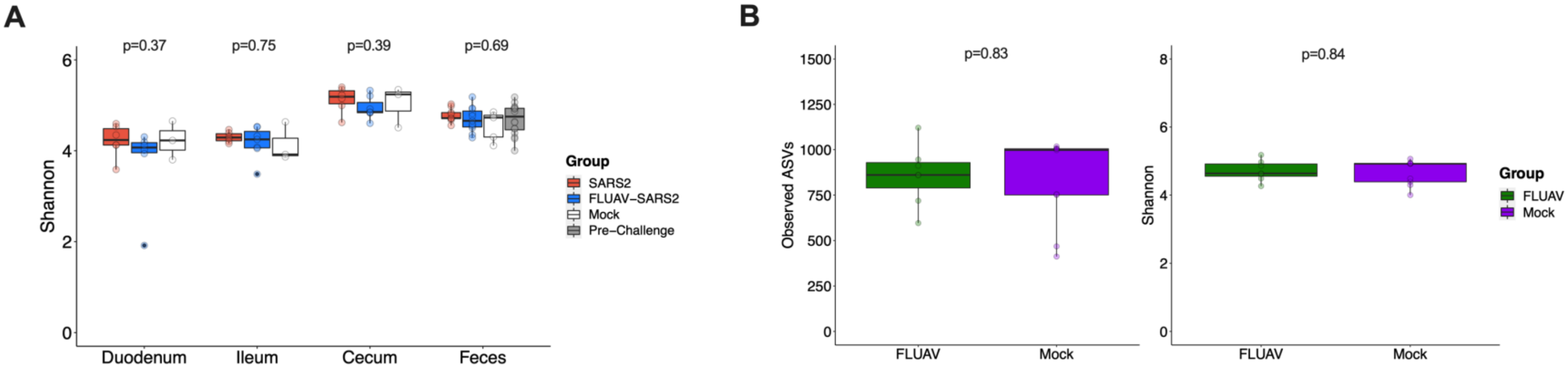

Fig 5.11. Diversity analysis of the intestine and feces in SARS2, FLUAV-SARS2 and mock-challenged GSH. (A) Shannon diversity of the intestinal/fecal samples between FLUAV-SARS2 (red), SARS2 (blue), mock (white), and pre-challenge (grey) containing all dpc from the rarified ASV count table. Multiple group comparisons were performed using Kruskal-Wallis, while pair-wise comparisons were conducted using the Wilcox test with Bonferroni correction. (B) Alpha diversity measure of the observed number of ASVs (left) and Shannon diversity (right) between FLUAV exposed (green) and mock (purple) pre-challenge fecal samples from the rarified ASV count table. Pair-wise comparisons were conducted using the Wilcox test with Bonferroni correction.

Fig 5.12. NMDS plots of the intestine and feces in SARS2, FLUAV-SARS2 and mock-challenged GSH. NMDS plot of unweighted Jaccard distance (A, C, E, G) and weighted Bray-Curtis (B, C, F, H) dissimilarity distance of the small intestine, including the duodenum and ileum (A and B), cecum (C and D) and the feces (E and F). Groups are designated by the color (FLUAV-SARS2: red, SARS2: blue, mock: white, pre-challenge: grey) and sample type by the shape (duodenum: circle and ileum: square) or dpc by the shape (3 dpc: circle and 6 dpc: square). Ellipses were constructed using the standard deviation. Comparison between FLUAV exposure and mock controls when analyzing pre-challenge fecal samples were also compared (G and H).

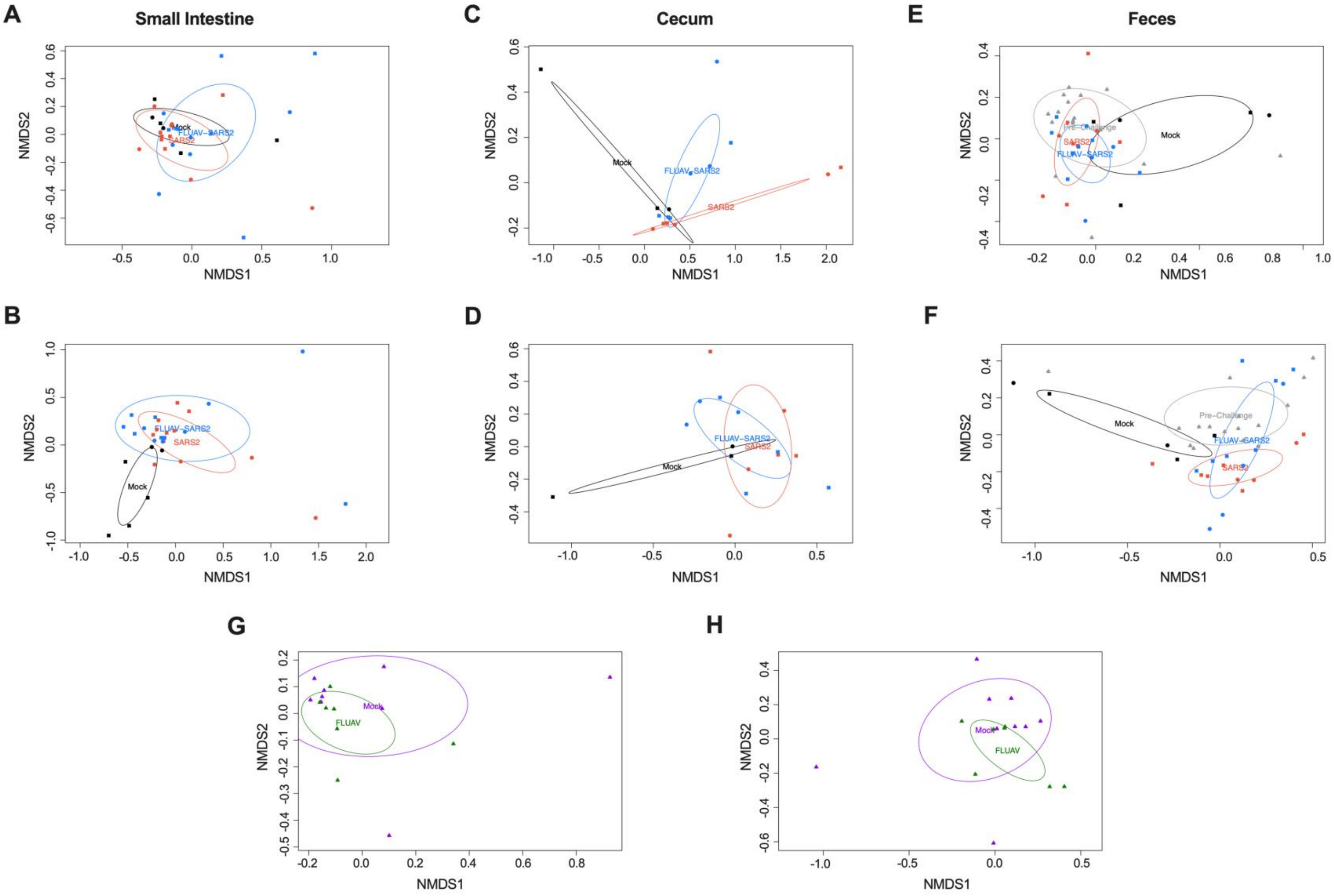

A
Small Intestine
C
Cecum
E
Feces
B
D
F
G
H
NMDS1
NMDS2
Mock
FLUAV–SARS2
SARS2
Pre-Challenge
FLUAV

Fig 5.13. Beta diversity and taxonomic abundances of the intestine and feces in SARS2, FLUAV-SARS2 and mock-challenged GSH. Comparison of unweighted Jaccard dissimilarity distance within each group and across multiple comparisons in the small intestine, including the duodenum and ileum (A) and the cecum (B). Intra-group variation is marked with grey shading, while the inter-group comparisons are colored gold. Pair-wise comparisons were performed using the Wilcox test with Bonferroni correction. (C) Relative abundances agglomerated at the phylum level separated by sample type and group. (D) Relative abundances of each hamster at the lowest taxonomic rank identified separated by sample type, group, and ordered by dpc.

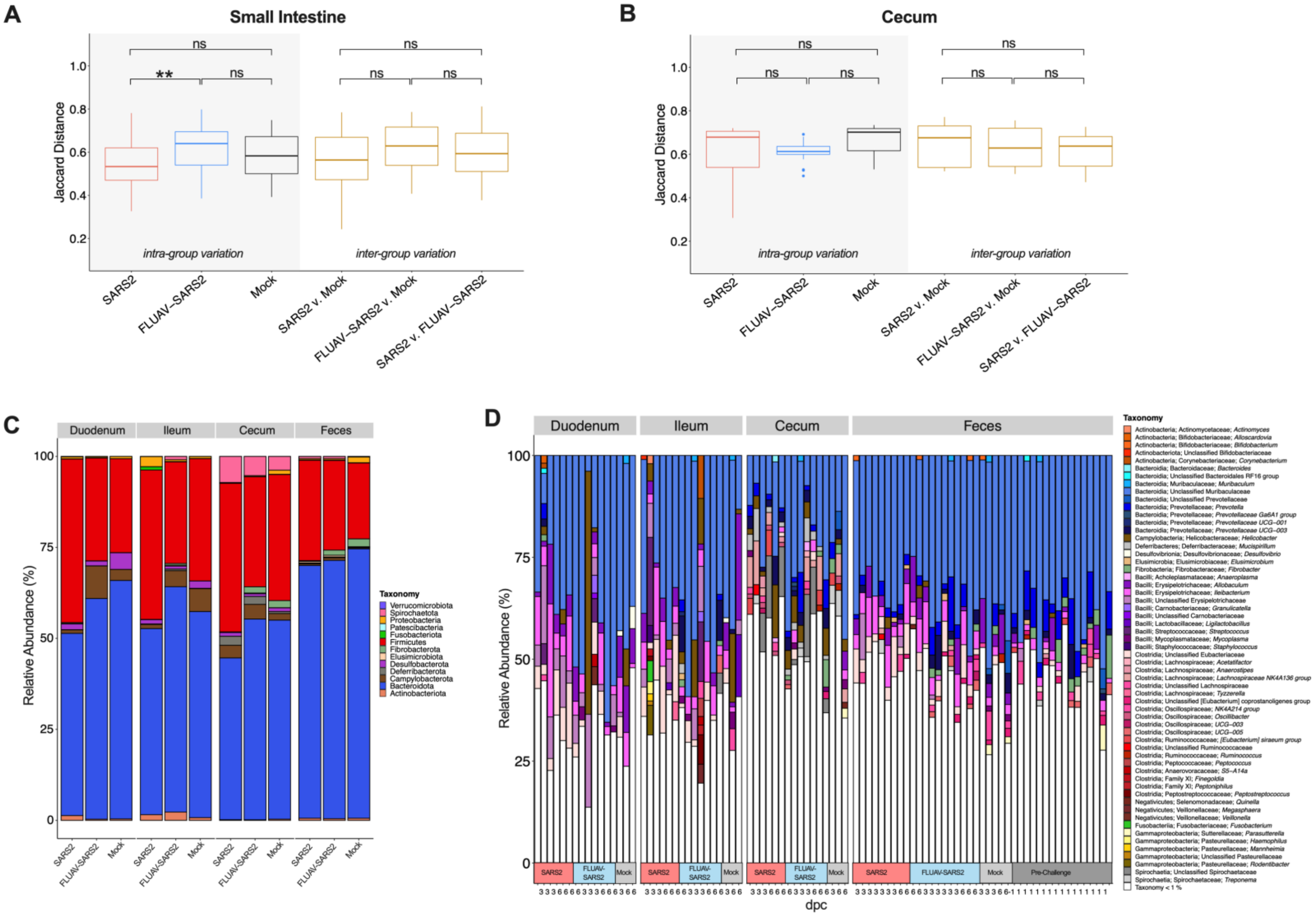
A
Small Intestine
Jaccard Distance
1.0
0.8
0.6
0.4
0.2
ns
**
ns
ns
ns
ns
intra-group variation
inter-group variation
SARS2
FLUAV–SARS2
Mock
SARS2 v. Mock
FLUAV–SARS2 v. Mock
SARS2 v. FLUAV–SARS2
B
Cecum
Jaccard Distance
ns
ns
ns
ns
ns
ns
intra-group variation
inter-group variation
SARS2
FLUAV–SARS2
Mock
SARS2 v. Mock
FLUAV–SARS2 v. Mock
SARS2 v. FLUAV–SARS2
C
Duodenum
Ileum
Cecum
Feces
Relative Abundance (%)
100
75
50
25
0
SARS2
FLUAV-SARS2
Mock
Taxonomy
Verrucomicrobiota
Spirochaetota
Proteobacteria
Patescibacteria
Fusobacteriota
Firmicutes
Fibrobacterota
Elusimicrobiota
Desulfobacterota
Deferribacterota
Campylobacterota
Bacteroidota
Actinobacteriota
D
Duodenum
Ileum
Cecum
Feces
Relative Abundance (%)
SARS2
FLUAV-SARS2
Mock
Pre-Challenge
dpc
Taxonomy
Actinobacteria; Actinomycetaceae; *Actinomyces*
Actinobacteria; Bifidobacteriaceae; *Alloscardovia*
Actinobacteria; Bifidobacteriaceae; *Bifidobacterium*
Actinobacteriota; Unclassified Bifidobacteriaceae
Actinobacteria; Corynebacteriaceae; *Corynebacterium*
Bacteroidia; Bacteroidaceae; *Bacteroides*
Bacteroidia; Unclassified Bacteroidales RF16 group
Bacteroidia; Muribaculaceae; *Muribaculum*
Bacteroidia; Unclassified Muribaculaceae
Bacteroidia; Unclassified Prevotellaceae
Bacteroidia; Prevotellaceae; *Prevotella*
Bacteroidia; Prevotellaceae; *Prevotellaceae Ga6A1 group*
Bacteroidia; Prevotellaceae; *Prevotellaceae UCG–001*
Bacteroidia; Prevotellaceae; *Prevotellaceae UCG–003*
Campylobacteria; Helicobacteraceae; *Helicobacter*
Deferribacteres; Deferribacteraceae; *Mucispirillum*
Desulfovibrionia; Desulfovibrionaceae; *Desulfovibrio*
Elusimicrobia; Elusimicrobiaceae; *Elusimicrobium*
Fibrobacteria; Fibrobacteraceae; *Fibrobacter*
Bacilli; Acholeplasmataceae; *Anaeroplasma*
Bacilli; Erysipelotrichaceae; *Allobaculum*
Bacilli; Erysipelotrichaceae; *Ileibacterium*
Bacilli; Unclassified Erysipelotrichaceae
Bacilli; Carnobacteriaceae; *Granulicatella*
Bacilli; Unclassified Carnobacteriaceae
Bacilli; Lactobacillaceae; *Ligilactobacillus*
Bacilli; Streptococcaceae; *Streptococcus*
Bacilli; Mycoplasmataceae; *Mycoplasma*
Bacilli; Staphylococcaceae; *Staphylococcus*
Clostridia; Unclassified Eubacteriaceae
Clostridia; Lachnospiraceae; *Acetatifactor*
Clostridia; Lachnospiraceae; *Anaerostipes*
Clostridia; Lachnospiraceae; *Lachnospiraceae NK4A136 group*
Clostridia; Unclassified Lachnospiraceae
Clostridia; Lachnospiraceae; *Tyzzerella*
Clostridia; Unclassified [Eubacterium] coprostanoligenes group
Clostridia; Oscillospiraceae; *NK4A214 group*
Clostridia; Oscillospiraceae; *Oscillibacter*
Clostridia; Oscillospiraceae; *UCG–003*
Clostridia; Oscillospiraceae; *UCG–005*
Clostridia; Ruminococcaceae; *[Eubacterium] siraeum group*
Clostridia; Unclassified Ruminococcaceae
Clostridia; Ruminococcaceae; *Ruminococcus*
Clostridia; Peptococcaceae; *Peptococcus*
Clostridia; Anaerovoracaceae; *S5–A14a*
Clostridia; Family XI; *Finegoldia*
Clostridia; Family XI; *Peptoniphilus*
Clostridia; Peptostreptococcaceae; *Peptostreptococcus*
Negativicutes; Selenomonadaceae; *Quinella*
Negativicutes; Veillonellaceae; *Megasphaera*
Negativicutes; Veillonellaceae; *Veillonella*
Fusobacteriia; Fusobacteriaceae; *Fusobacterium*
Gammaproteobacteria; Sutterellaceae; *Parasutterella*
Gammaproteobacteria; Pasteurellaceae; *Haemophilus*
Gammaproteobacteria; Pasteurellaceae; *Mannheimia*
Gammaproteobacteria; Unclassified Pasteurellaceae
Gammaproteobacteria; Pasteurellaceae; *Rodentibacter*
Spirochaetia; Unclassified Spirochaetaceae
Spirochaetia; Spirochaetaceae; *Treponema*
Taxonomy < 1 %

Fig 5.14. Differential taxonomic analysis of the intestine and feces microbiota using Deseq2, ALDEx2, and LefSE. Bacterial taxa identified at different relative abundances between (A left) FLUAV-SARS2 (red), and mock (grey) or (B left) SARS2 (blue), and mock (grey) or (C left) FLUAV-SARS2 (red) and SARS2 (blue) groups using DeSeq2 when all sample types (duodenum, ileum, cecum, and feces) were combined. Significantly enriched taxa were plotted with log2 fold change and the corresponding standard error estimate. Taxa in bold were those considered significant in at least 2 of the 3 differential analyses performed. Effect size plot showing the median log2 fold difference (difference between) by the median log2 dispersion (difference within) when comparing (A middle) SARS2, and mock or (B middle) FLUAV-SARS2, and mock or (C middle) SARS2 and FLUAV-SARS2 when all sample types (duodenum, ileum, cecum, and feces) were combined. Taxa considered significant by the Wilcox test are shown in green, taxa considered significant by BH corrected p-values are shown in red, while taxa with an effect size greater than 1.5 are outlined in blue. Cladogram showing significantly ($p<0.05$) abundant taxa between (A right) SARS2 (red) and mock (grey) or (B right) FLUAV-SARS2 (blue), and mock (grey) or (C right) SARS2 (red) and FLUAV-SARS2 (blue) using linear discriminant analysis effect size (LEfSe) analysis with default parameters when all sample types (duodenum, ileum, cecum, and feces) were combined. Taxa are color-coded by phylum, and bold taxa are considered significant in at least 2 of the 3 differential analyses performed. Significant taxa using Deseq2 were determined by having a $p\text{-value} < 0.01$, while significant taxa using ALDEx2 and LEfSE were determined by having a $p\text{-value} < 0.05$.

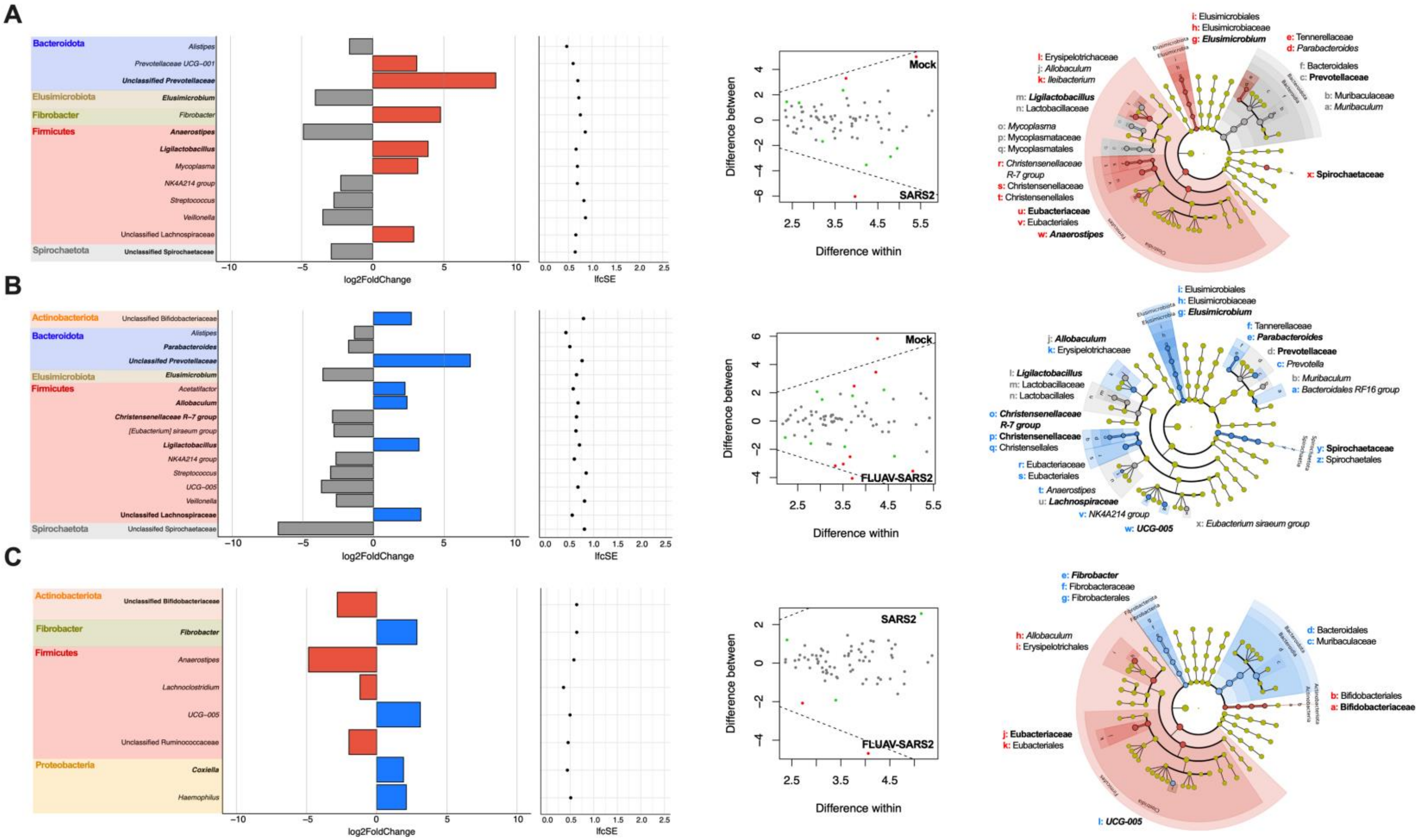
A
Bacteroidota
Alistipes
Prevotellaceae UCG−001
Unclassified Prevotellaceae
Elusimicrobiota
Elusimicrobium
Fibrobacter
Fibrobacter
Firmicutes
Anaerostipes
Ligilactobacillus
Mycoplasma
NK4A214 group
Streptococcus
Veillonella
Unclassified Lachnospiraceae
Spirochaetota
Unclassified Spirochaetaceae
−10
−5
0
5
10
log2FoldChange
0.0
0.5
1.0
1.5
2.0
2.5
lfcSE
Difference between
Difference within
Mock
SARS2
4
2
0
−2
−4
−6
2.5
3.5
4.5
5.5
i: Elusimicrobiales
h: Elusimicrobiaceae
g: Elusimicrobium
e: Tennerellaceae
d: Parabacteroides
f: Bacteroidales
c: Prevotellaceae
b: Muribaculaceae
a: Muribaculum
l: Erysipelotrichaceae
j: Allobaculum
k: Ileibacterium
m: Ligilactobacillus
n: Lactobacillaceae
o: Mycoplasma
p: Mycoplasmataceae
q: Mycoplasmatales
r: Christensenellaceae R-7 group
s: Christensenellaceae
t: Christensenellales
u: Eubacteriaceae
v: Eubacteriales
w: Anaerostipes
x: Spirochaetaceae
Elusimicrobiota
Elusimicrobia
Bacteroidota
Bacteroidia
Firmicutes
Clostridia
B
Actinobacteriota
Unclassified Bifidobacteriaceae
Bacteroidota
Alistipes
Parabacteroides
Unclassifed Prevotellaceae
Elusimicrobiota
Elusimicrobium
Firmicutes
Acetatifactor
Allobaculum
Christensenellaceae R−7 group
[Eubacterium] siraeum group
Ligilactobacillus
NK4A214 group
Streptococcus
UCG−005
Veillonella
Unclassifed Lachnospiraceae
Spirochaetota
Unclassifed Spirochaetaceae
−10
−5
0
5
10
log2FoldChange
0.0
0.5
1.0
1.5
2.0
2.5
lfcSE
Difference between
Difference within
Mock
FLUAV-SARS2
6
4
2
0
−2
−4
2.5
3.5
4.5
5.5
i: Elusimicrobiales
h: Elusimicrobiaceae
g: Elusimicrobium
f: Tannerellaceae
e: Parabacteroides
d: Prevotellaceae
c: Prevotella
b: Muribaculum
a: Bacteroidales RF16 group
j: Allobaculum
k: Erysipelotrichaceae
l: Ligilactobacillus
m: Lactobacillaceae
n: Lactobacillales
o: Christensenellaceae R-7 group
p: Christensenellaceae
q: Christensellales
r: Eubacteriaceae
s: Eubacteriales
t: Anaerostipes
u: Lachnospiraceae
v: NK4A214 group
w: UCG-005
x: Eubacterium siraeum group
y: Spirochaetaceae
z: Spirochaetales
Elusimicrobiota
Elusimicrobia
Spirochaetota
Spirochaetia
C
Actinobacteriota
Unclassified Bifidobacteriaceae
Fibrobacter
Fibrobacter
Firmicutes
Anaerostipes
Lachnoclostridium
UCG−005
Unclassified Ruminococcaceae
Proteobacteria
Coxiella
Haemophilus
−10
−5
0
5
10
log2FoldChange
0.0
0.5
1.0
1.5
2.0
2.5
lfcSE
Difference between
Difference within
SARS2
FLUAV-SARS2
2
0
−2
−4
2.5
3.5
4.5
e: Fibrobacter
f: Fibrobacteraceae
g: Fibrobacterales
h: Allobaculum
i: Erysipelotrichales
d: Bacteroidales
c: Muribaculaceae
b: Bifidobacteriales
a: Bifidobacteriaceae
j: Eubacteriaceae
k: Eubacteriales
l: UCG-005
Fibrobacterota
Fibrobacteria
Bacteroidota
Bacteroidia
Actinobacteriota
Actinobacteria
Firmicutes
Clostridia

Fig 5.15. Associations between taxa within the intestine/fecal microbiota and infection factors A heatmap illustrating the Spearman correlation among different infection factors and the relative abundance of bacterial taxa when all sample types (duodenum, ileum, cecum, and feces) were combined. Correlations with histopathological score in the heart and small intestine were not included. Pre-challenge feces were also not included in this analysis. Taxa are color-coded by phylum. Correlation labels have a spearman correlation value > 0.60 or < -0.60. FLUAV – inoculated with FLUAV and then challenged with SARS-CoV-2 (mock-challenge GSH were not included), SARSCoV2 – challenged with SARS-CoV-2, NT- nasal turbinates, LI – large intestine.

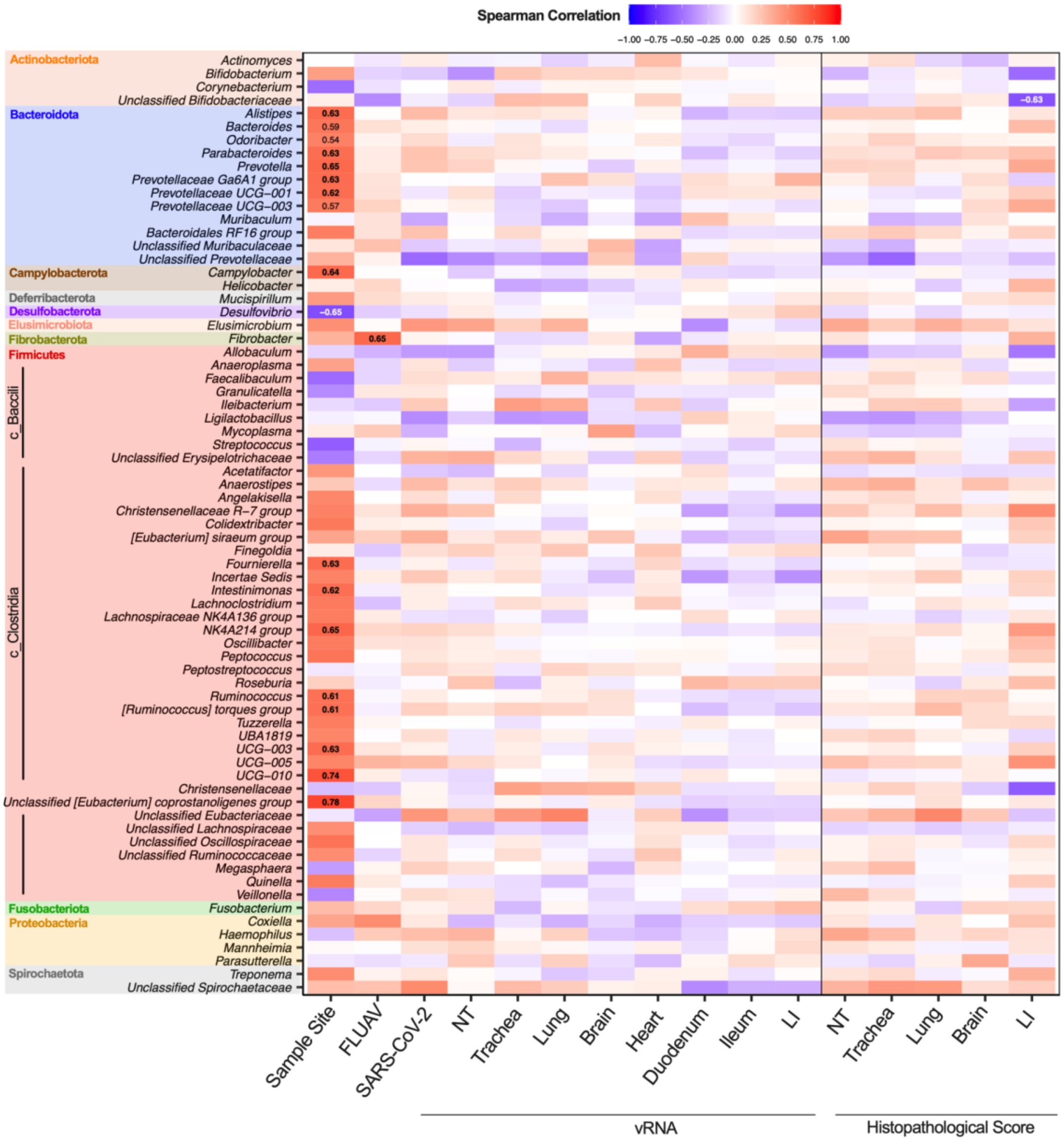

Spearman Correlation
−1.00 −0.75 −0.50 −0.25 0.00 0.25 0.50 0.75 1.00
Actinobacteriota
Actinomyces
Bifidobacterium
Corynebacterium
Unclassified Bifidobacteriaceae
−0.63
Bacteroidota
Alistipes
0.63
Bacteroides
0.59
Odoribacter
0.54
Parabacteroides
0.63
Prevotella
0.65
Prevotellaceae Ga6A1 group
0.63
Prevotellaceae UCG−001
0.62
Prevotellaceae UCG−003
0.57
Muribaculum
Bacteroidales RF16 group
Unclassified Muribaculaceae
Unclassified Prevotellaceae
Campylobacterota
Campylobacter
0.64
Helicobacter
Deferribacterota
Mucispirillum
Desulfobacterota
Desulfovibrio
−0.65
Elusimicrobiota
Elusimicrobium
Fibrobacterota
Fibrobacter
0.65
Firmicutes
Allobaculum
Anaeroplasma
Faecalibaculum
Granulicatella
Ileibacterium
Ligilactobacillus
Mycoplasma
Streptococcus
Unclassified Erysipelotrichaceae
c_Baccili
Acetatifactor
Anaerostipes
Angelakisella
Christensenellaceae R−7 group
Colidextribacter
[Eubacterium] siraeum group
Finegoldia
Fournierella
0.63
Incertae Sedis
Intestinimonas
0.62
Lachnoclostridium
Lachnospiraceae NK4A136 group
NK4A214 group
0.65
Oscillibacter
Peptococcus
Peptostreptococcus
Roseburia
Ruminococcus
0.61
[Ruminococcus] torques group
0.61
Tuzzerella
UBA1819
UCG−003
0.63
UCG−005
UCG−010
0.74
Christensenellaceae
Unclassified [Eubacterium] coprostanoligenes group
0.78
Unclassified Eubacteriaceae
Unclassified Lachnospiraceae
Unclassified Oscillospiraceae
Unclassified Ruminococcaceae
Megasphaera
Quinella
Veillonella
c_Clostridia
Fusobacteriota
Fusobacterium
Proteobacteria
Coxiella
Haemophilus
Mannheimia
Parasutterella
Spirochaetota
Treponema
Unclassified Spirochaetaceae
Sample Site
FLUAV
SARS-CoV-2
NT
Trachea
Lung
Brain
Heart
Duodenum
Ileum
LI
NT
Trachea
Lung
Brain
LI
vRNA
Histopathological Score

Fig 5.16. Associations between taxa within the intestine and fecal microbiota and infection factors. A heatmap illustrating the Spearman correlation among different infection factors and the relative abundance of bacterial taxa within the small intestine (duodenum and ileum), cecum and feces. Correlations among pathology of the heart and small intestine were removed since the pathological score was the same for all GSH. Taxa are color-coded by phylum. Correlation labels and taxa displayed in bold have a spearman correlation value > 0.60 or < -0.60. FLUAV – inoculated with FLUAV and then challenged with SARS-CoV-2 (mock-challenged GSH were not included), SARSCoV2 – challenged with SARS-CoV-2, NT- nasal turbinates.

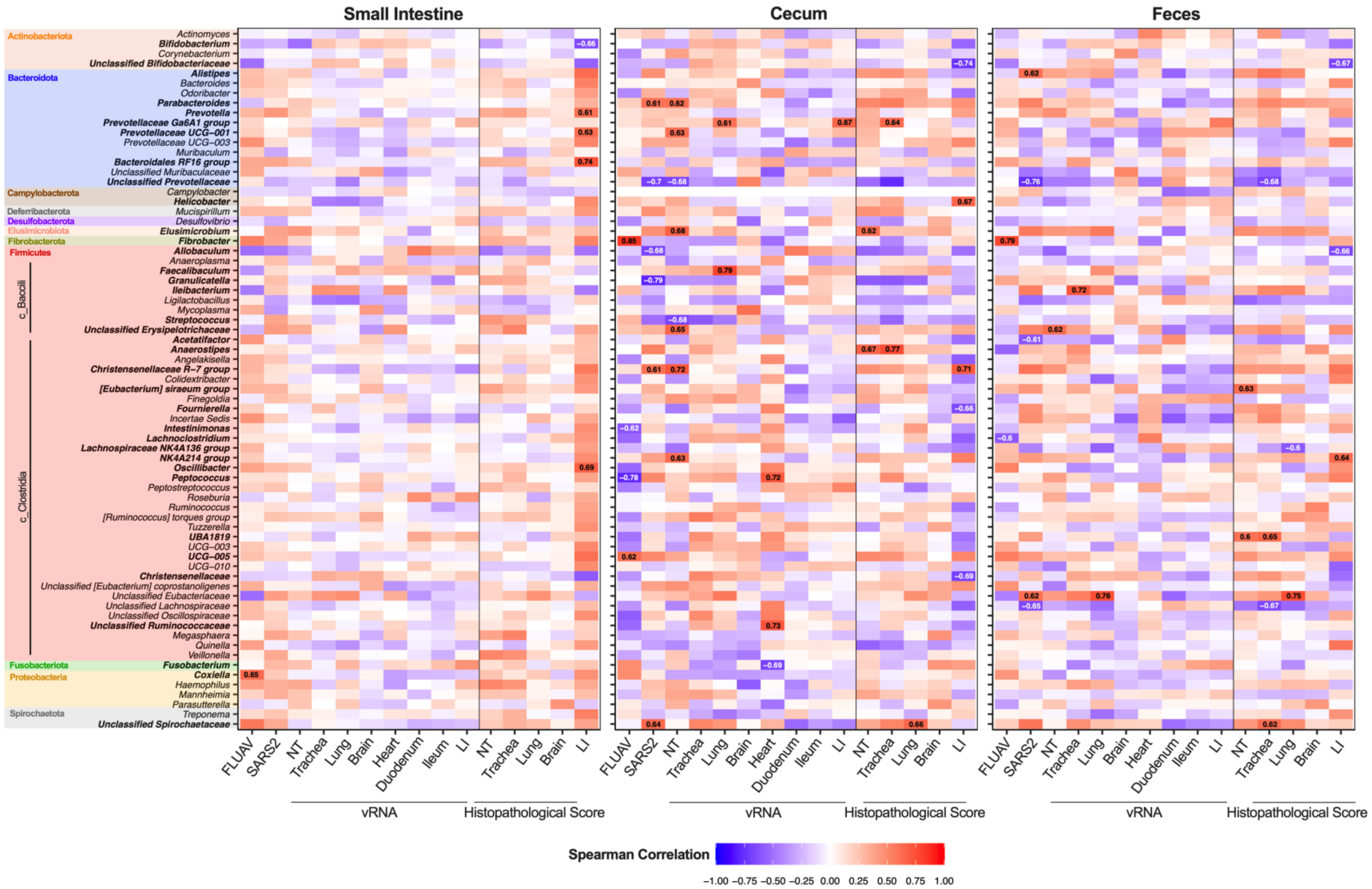
Small Intestine
Cecum
Feces
Actinobacteriota
Bacteroidota
Campylobacterota
Deferribacterota
Desulfobacterota
Elusimicrobiota
Fibrobacterota
Firmicutes
c_Baccili
c_Clostridia
Fusobacteriota
Proteobacteria
Spirochaetota
Actinomyces
Bifidobacterium
Corynebacterium
Unclassified Bifidobacteriaceae
Alistipes
Bacteroides
Odoribacter
Parabacteroides
Prevotella
Prevotellaceae Ga6A1 group
Prevotellaceae UCG−001
Prevotellaceae UCG−003
Muribaculum
Bacteroidales RF16 group
Unclassified Muribaculaceae
Unclassified Prevotellaceae
Campylobacter
Helicobacter
Mucispirillum
Desulfovibrio
Elusimicrobium
Fibrobacter
Allobaculum
Anaeroplasma
Faecalibaculum
Granulicatella
Ileibacterium
Ligilactobacillus
Mycoplasma
Streptococcus
Unclassified Erysipelotrichaceae
Acetatifactor
Anaerostipes
Angelakisella
Christensenellaceae R−7 group
Colidextribacter
[Eubacterium] siraeum group
Finegoldia
Fournierella
Incertae Sedis
Intestinimonas
Lachnoclostridium
Lachnospiraceae NK4A136 group
NK4A214 group
Oscillibacter
Peptococcus
Peptostreptococcus
Roseburia
Ruminococcus
[Ruminococcus] torques group
Tuzzerella
UBA1819
UCG−003
UCG−005
UCG−010
Christensenellaceae
Unclassified [Eubacterium] coprostanoligenes
Unclassified Eubacteriaceae
Unclassified Lachnospiraceae
Unclassified Oscillospiraceae
Unclassified Ruminococcaceae
Megasphaera
Quinella
Veillonella
Fusobacterium
Coxiella
Haemophilus
Mannheimia
Parasutterella
Treponema
Unclassified Spirochaetaceae
FLUAV
SARS2
NT
Trachea
Lung
Brain
Heart
Duodenum
Ileum
LI
NT
Trachea
Lung
Brain
LI
vRNA
Histopathological Score
Spearman Correlation
−1.00
−0.75
−0.50
−0.25
0.00
0.25
0.50
0.75
1.00

Table 5.1. H&E pathology scores of respiratory tissues. Subjectively scored tissues (blind) based on percentage of the total parenchyma affected by lesions and inflammation as: none (0%), mild; <15% (1), mild to moderate; 16-30% (2), moderate; 31-50% (3), moderate to severe 51-75% (4) and severe; ≥75% (5). A dash is used to separate the score evaluated for each individual hamster separated by group and days post-challenge (dpc).

Group	**dpc**	**Nasal Turbinates**	**Trachea**	**Lung**
SARS2	3	3 / 3 / 3	1 / 2 / 3	2 / 2 / 2
	6	3 / 2 / 3	1 / NA / 1	5 / 4 / 5
FLUAV-SARS2	3	3 / 4 / 4	1 / 3 / 1	3 / 4 / 3
	6	3 / 2 / 3 / 3	2 / 1 / NA / NA	3 / 4 / 5 / 4
Mock	3	0	0	0
	6	0 / 0	0 / 0	0 / 0

Table 5.2. H&E pathology scores of different tissues. Subjectively scored tissues (blind) based on percentage of the total parenchyma affected by lesions and inflammation as: none (0%), mild; <15% (1), mild to moderate; 16-30% (2), moderate; 31-50% (3), moderate to severe 51-75% (4) and severe; ≥75% (5). A dash is used to separate the score evaluated for each individual hamster separated by group and days post challenge (dpc).

Group	dpc	Brain	Heart	Small Intestine	Cecum
SARS2	3	0 / 0 / 0	0 / 0 / 0	1 / 1 / 1	1 / 2 / 1
	6	0 / 0 / 1	0 / 0 / 0	1 / 1 / 1	1 / 2 / 1
FLUAV-SARS2	3	1 / 0 / 0	0 / 0 / 0	1 / 1 / 1	3 / 1 / 2
	6	0 / 0 / 0 / 0	0 / 0 / 0 / 0	1 / 1 / 1 /1	1 / 1 / 1 / 3
Mock	3	0	0	1	1
	6	0 / 0	0 / 0	1 / 1	1 / 1

Table 5.3. Taxa considered significant among multiple differential analyses within the lungs. Shown in bold are enriched groups that were considered significant in at least 2 of the 3 differential analyses performed. Adjusted p-values are reported: Deseq2 (Benjamini-Hochberg adjusted p-value) and ALDEx2 (Benjamini-Hochberg adjusted p-value using Wilcox t-test). $p < 0.05$ was considered significant for ALDEx2 and LefSE analysis and $p < 0.01$ was considered significant for Deseq2 analysis.

	SARS2 v. Mock				FLUAV-SARS2 v. Mock				SARS2 v. FLUAV-SARS2			
Genus	*Deseq2*	*ALDEx2*	*LefSE*	*Enriched*	*Deseq2*	*ALDEx2*	*LefSE*	*Enriched*	*Deseq2*	*ALDEx2*	*LefSE*	*Enriched*
Prevotella_7	0.00096	0.50	> 0.05	SARS2	0.00063	0.33	0.015	**FLUAV-SARS2**	0.97	0.99	> 0.05	NA
Campylobacter	0.00096	0.51	0.043	**SARS2**	0.0019	0.48	> 0.05	FLUAV-SARS2	0.91	0.93	> 0.05	NA
Streptococcus	2.98E-06	0.97	> 0.05	SARS2	2.34E-05	0.97	0.034	**FLUAV-SARS2**	0.79	0.97	> 0.05	NA
Johnsonella	0.0026	0.67	> 0.05	SARS2	0.0063	0.37	0.015	**FLUAV-SARS2**	0.91	0.99	> 0.05	NA
Fusobacterium	9.76E-07	0.49	0.043	**SARS2**	2.81E-08	0.3	0.015	**FLUAV-SARS2**	0.84	0.98	> 0.05	NA
Haemophilus	1.58E-08	0.50	0.043	**SARS2**	6.23E-14	0.30	0.015	**FLUAV-SARS2**	0.61	0.89	> 0.05	NA
Moraxella	0.00088	0.51	0.043	**SARS2**	0.78	0.95	> 0.05	NA	0.098	0.60	> 0.05	NA

Table 5.4. Taxa considered significant among multiple differential analyses of SARS-CoV-2 challenged aged Golden Syrian hamsters when samples from the intestine and feces were combined. Pre-Challenge group was not included within these analyses. Shown in bold are enriched groups that were considered significant in at least 2 of the 3 differential analyses performed. Adjusted p-values are reported: Deseq2 (Benjamini-Hochberg adjusted p-value) and ALDEx2 (Benjamini-Hochberg adjusted p-value using Wilcox t-test). $p < 0.05$ was considered significant for ALDEx2 and LefSE analysis and $p < 0.01$ was considered significant for Deseq2 analysis.

	SARS2 v. Mock				FLUAV-SARS2 v. Mock				SARS2 v. FLUAV-SARS2			
Taxa	*Deseq2*	*ALDEx2*	*LefSE*	*Enriched*	*Deseq2*	*ALDEx2*	*LefSE*	*Enriched*	*Deseq2*	*ALDEx2*	*LefSE*	*Enriched*
Unclassified Bifidobacteriaceae	0.95	0.88	> 0.05	NA	0.0034	0.34	> 0.05	NA	1.7E-04	0.16	0.0058	**SARS2**
Parabacteroides	0.021	0.20	0.036	SARS2	0.0026	0.11	0.0084	**FLUAV-SARS2**	0.76	0.86	> 0.05	NA
Unclassified Prevotellaceae	3.8E-33	8.4E-04	4.2E-05	**Mock**	1.1E-17	4.7E-04	1.8E-04	**Mock**	0.52	0.81	> 0.05	NA
Elusimicrobium	3.0E-07	0.037	0.0028	**SARS2**	4.7E-07	0.0060	2.4E-04	**FLUAV-SARS2**	0.68	0.92	> 0.05	NA
Fibrobacter	9.1E-09	0.21	> 0.05	Mock	0.75	0.28	> 0.05	NA	1.7E-04	3.7E-05	5.1E-06	**FLUAV-SARS2**
Allobaculum	0.33	0.34	0.036	NA	0.0025	0.034	7.2E-04	**Mock**	0.067	0.60	0.033	NA
Anaerostipes	2.2E-07	0.34	0.017	**SARS2**	0.69	0.86	0.027	FLUAV-SARS2	3.4E-15	0.36	> 0.05	SARS2
Christensenellaceae R-7 group	0.044	0.38	0.045	SARS2	6.4E-05	0.94	0.0060	**FLUAV-SARS2**	0.85	0.77	> 0.05	NA
Ligilactobacillus	1.0E-07	0.14	0.0048	**Mock**	5.9E-05	0.023	7.6E-04	**Mock**	0.92	0.75	> 0.05	NA
Mycoplasma	4.5E-05	0.07	0.0059	Mock	0.46	0.17	> 0.05	NA	0.25	0.67	> 0.05	NA
UCG-005	0.44	0.29	> 0.05	NA	6.3E-07	0.034	0.0065	**FLUAV-SARS2**	1.4E-08	0.25	0.024	**FLUAV-SARS2**
Unclassified Eubacteriaceae	0.064	0.029	1.3E-04	**SARS2**	0.85	0.040	> 0.05	NA	0.029	0.59	0.0068	SARS2
Unclassified Lachnospiraceae	9.1E-05	0.34	> 0.05	Mock	3.5E-08	0.19	0.041	**Mock**	0.26	0.84	> 0.05	NA
Coxiella	0.21	0.35	> 0.05	NA	0.040	0.26	> 0.05	FLUAV-SARS2	1.7E-04	0.0088	> 0.05	**FLUAV-SARS2**
Unclassified Spirochaetaceae	5.2E-05	0.038	0.0015	**SARS2**	2.1E-15	9.4E-04	5.5E-06	**FLUAV-SARS2**	0.75	0.62	> 0.05	NA

Table 5.5. Taxa considered significant among multiple differential analyses within the different anatomical sites in the intestine and feces. Shown in bold are enriched groups that were considered significant in at least 2 of the 3 differential analyses performed. Adjusted p-values are reported: Deseq2 (Benjamini-Hochberg adjusted p-value) and ALDEx2 (Benjamini-Hochberg adjusted p-value using Wilcox t-test). $p < 0.05$ was considered significant for ALDEx2 and LefSE analysis and $p < 0.01$ was considered significant for Deseq2 analysis.

	SARS2 v. Mock				FLUAV-SARS2 v. Mock				SARS2 v. FLUAV-SARS2			
Taxa	*Deseq2*	*ALDEx2*	*LefSE*	*Enriched*	*Deseq2*	*ALDEx2*	*LefSE*	*Enriched*	*Deseq2*	*ALDEx2*	*LefSE*	*Enriched*
Small Intestine (Duodenum and Ileum)												
Unclassified Bifidobacteriaceae	0.96	0.95	> 0.05	NA	0.035	0.57	> 0.05	Mock	0.0099	0.31	0.027	**SARS2**
Prevotella	0.034	0.64	> 0.05	SARS2	0.0022	0.11	0.005	**FLUAV-SARS2**	0.44	0.67	> 0.05	NA
Unclassified Prevotellaceae	9.47E-06	0.63	0.040	**Mock**	8.22E-08	0.44	> 0.05	Mock	NA	0.82	> 0.05	NA
Fibrobacter	NA	0.85	> 0.05	NA	0.0072	0.45	0.019	**FLUAV-SARS2**	0.0099	0.47	0.037	**FLUAV-SARS2**
Allobaculum	0.24	0.50	> 0.05	NA	0.0040	0.1	0.0050	**Mock**	0.033	0.30	0.011	SARS2
Mycoplasma	0.008	0.18	0.0065	**Mock**	0.45	0.45	> 0.05	NA	0.037	0.72	> 0.05	FLUAV-SARS2
Unclassified [Eubacterium] coprostanoligenes group	0.035	0.85	> 0.05	SARS2	0.93	0.94	> 0.05	NA	0.0099	0.46	0.0075	**FLUAV-SARS2**
Unclassified Spirochaetaceae	0.45	0.89	> 0.05	NA	0.004	0.27	0.0026	**FLUAV-SARS2**	0.0099	0.22	0.0097	**FLUAV-SARS2**
Cecum												
Unclassified Prevotellaceae	1.4E-10	0.52	0.011	**Mock**	7.2E-05	0.45	0.039	**Mock**	0.74	0.94	> 0.05	NA
Fibrobacter	0.0077	0.66	> 0.05	NA	0.98	0.97	> 0.05	NA	1.8E-05	0.11	0.0033	**FLUAV-SARS2**
Allobaculum	0.0077	0.53	0.02	**Mock**	0.0089	0.28	0.017	**Mock**	0.98	0.99	> 0.05	NA
UCG-005	0.45	0.85	> 0.05	NA	0.010	0.27	0.030	**FLUAV-SARS2**	0.036	0.61	> 0.05	**FLUAV-SARS2**
Unclassified Spirochaetaceae	1.5E-09	0.59	> 0.05	SARS2	1.2E-09	0.29	0.016	**FLUAV-SARS2**	0.98	1	> 0.05	NA
Feces												
Parabacteroides	0.036	0.2	> 0.05	SARS2	2.6E-04	0.038	0.0078	**FLUAV-SARS2**	0.75	0.81	> 0.05	NA
Unclassified Prevotellaceae	4.8E-24	0.034	0.0018	**Mock**	5.7E-12	0.014	8.7E-04	**Mock**	0.61	0.86	> 0.05	NA
Elusimicrobium	4.5E-04	0.17	0.027	**SARS2**	6.5E-05	0.047	0.0077	**FLUAV-SARS2**	0.96	0.98	> 0.05	NA
Fibrobracter	2.38E-04	0.21	> 0.05	NA	0.83	0.89	> 0.05	NA	1.85E-07	0.049	4.6E-04	**FLUAV-SARS2**
Ligilactobacillus	0.0053	0.28	0.027	**Mock**	7.8E-07	0.16	0.016	**Mock**	0.25	0.78	> 0.05	NA
Anaerostipes	2.4E-04	0.44	> 0.05	SARS2	0.97	0.73	> 0.05	NA	3.5E-08	0.4	0.047	**SARS2**
Christensenellaceae R-7 group	0.019	0.17	0.022	SARS2	0.0013	0.22	0.015	**FLUAV-SARS2**	0.37	0.92	> 0.05	NA
NK4A214 group	0.026	0.59	> 0.05	SARS2	1.70E-05	0.094	0.011	**FLUAV-SARS2**	0.89	0.73	> 0.05	NA
UCG-005	0.95	0.44	> 0.05	NA	0.0019	0.17	0.02	**FLUAV-SARS2**	4.3E-09	0.36	0.02	**FLUAV-SARS2**
Unclassified Lachnospiraceae	2.3E-04	0.12	0.0063	**Mock**	1.4E-06	0.015	0.0018	**Mock**	0.59	0.79	> 0.05	NA
Unclassified Spirochaetaceae	3.7E-04	0.062	0.0078	**SARS2**	1.36E-06	0.14	0.0097	**FLUAV-SARS2**	0.26	0.79	> 0.05	NA

Table 5.6. Taxa considered significant among multiple differential analyses comparing FLUAV pre-exposure to the mock pre-challenge and post-challenged fecal samples. Shown in bold are enriched groups that were considered significant in at least 2 of the 3 differential analyses performed. Adjusted p-values are reported: Deseq2 (Benjamini-Hochberg adjusted p-value) and ALDEx2 (Benjamini-Hochberg adjusted p-value using Wilcox t-test). $p < 0.05$ was considered significant for ALDEx2 and LefSE analysis and $p < 0.01$ was considered significant for Deseq2 analysis.

	FLUAV Pre-challenge v. Mock Pre-challenge				SARS2 v. Pre-challenge				FLUAV-SARS2 v. Pre-challenge			
Genus	*Deseq2*	*ALDEx2*	*LefSE*	*Enriched*	*Deseq2*	*ALDEx2*	*LefSE*	*Enriched*	*Deseq2*	*ALDEx2*	*LefSE*	*Enriched*
Bifidobacterium	0.92	0.96	> 0.05	NA	2.7E-04	0.09	0.0095	**SARS2**	0.035	0.45	0.033	NA
Prevotella	0.75	0.96	> 0.05	NA	0.0080	0.15	0.045	**Pre-Challenged**	0.92	0.55	> 0.05	NA
Allobaculum	0.99	0.96	> 0.05	NA	0.0028	0.11	0.025	**SARS2**	0.55	0.63	> 0.05	NA
Ileibacterium	0.92	0.99	> 0.05	NA	4.9E-05	0.055	0.0032	**SARS2**	0.026	0.21	0.0057	FLUAV-SARS2
Faecalibacterium	0.99	NA	> 0.05	NA	3.8E-05	0.022	0.0015	**SARS2**	0.026	0.19	0.0043	FLUAV-SARS2
Anaerostipes	5.3E-09	0.18	0.0015	**Mock**	0.80	0.65	>0.05	NA	0.0047	0.82	> 0.05	Pre-challenge
Unclassified Eubacteriaceae	0.71	0.98	>0.05	NA	2.3E-07	0.017	>0.05	**SARS2**	0.28	0.53	0.021	FLUAV-SARS2

Acknowledgements

We thank Kristine R. Wilcox and all the personnel from the Life Sciences vivarium and the Animal Health Research Center at the University of Georgia. We thank the personnel from the Animal Health Research Center, University of Georgia. We are also grateful to the Histology laboratory personnel, College of Veterinary Medicine, University of Georgia. This study was supported by a subcontract from the Center for Research on Influenza Pathogenesis (CRIP) to DRP under contract HHSN272201400008C from the National Institute of Allergy and Infectious Diseases (NIAID) Centers for Influenza Research and Surveillance (CEIRS). This research was also supported by the University of Georgia College of Veterinary Medicine Office of Research and Faculty and Graduate Affairs (ORFGA) Competitive Research Grant for Graduate Students. DRP receives funds from the Georgia Research Alliance and the Caswell S. Edison endowment fund, University of Georgia. Sponsors.

CHAPTER 6

SUMMARY AND CONCLUSSIONS

Human respiratory viral infections contribute to yearly morbidity, mortality, and economic losses worldwide. These include a broad range of viruses belonging to diverse families with unique viral and genomic structures, disease severity, seasonality of circulation, mode and efficiency of transmission, and risk factors associated with susceptible populations to infection (38). Furthermore, intermittent pandemics can lead to millions of deaths and disruption of everyday life and economies worldwide, as illustrated in the 2009 influenza pandemic and, more recently, the COVID-19 pandemic (38). The main objective of my dissertation was to investigate environmental and host factors that impact respiratory virus pathogenesis and transmission *in vitro* and *in vivo.* I explored these effects using two primary respiratory pathogens: influenza A virus (FLUAV) and severe acute respiratory syndrome coronavirus 2 (SARS-CoV-2).

Transmission of FLUAV occurs through two main mechanisms, contact or airborne transmission. Previous studies reported differences in pathogenesis and virus deposition when inoculating animal models via aerosol versus intranasal inoculation (34-36, 210, 212, 241). Therefore, aerosol inoculation of *in vitro* cell culture can be valuable in studying molecular markers that influence the transmission efficiency of FLUAV and virus-cell interactions resembling natural infection in the human respiratory tract. In chapter 3, I developed a simple *in vitro* model system to infect multiple different cell types via aerosol inoculation. I determined the relative aerosol infectious dose 50 for three FLUAV subtypes, including a pandemic H1N1, seasonal swine H3N2, and avian H9N2. Utilizing the *in vitro* aerosol exposure design, I show that all three viruses could infect a commonly used cell line, Madin-Darby canine kidney (MDCK) cells, and a recently developed immortalized differentiated human airway epithelial cell line (BCi-NS1.1) (226). Among the different viruses, I observed higher aerosol infection efficiency in the pH1N1 strain compared to the seasonal swine H3N2 and avian H9N2 in MDCK cells and differentiated human cells. The results from this study demonstrated differences among three FLUAVs in two cell lines, suggesting that understanding aerosol infectivity *in vitro* in conjunction with *in vivo* studies can be used for pandemic risk assessment of influenza viruses and the importance of molecular markers involved in transmission efficiency.

Human FLUAV infections exhibit a broad range of clinical disease severity ranging from asymptomatic infection to death (9). Multiple risk factors for severe disease contribute to enhanced disease pathogenesis. Regarding FLUAV, children, the elderly, pregnant women, and individuals with immunosuppression or chronic medical conditions are at higher risk of developing more severe disease (9). The complex relationship between host and viral factors influences the pathogenesis severity, notably the host immune response. In recent years, the respiratory and intestinal microbiota has been shown to directly impact host cells or indirectly impact the immune system during viral infections (45, 46). However, various biological and environmental factors such as sex, age, diet, and disease status can affect the diversity and abundance of bacteria associated with good health leading to dysbiosis (48, 51, 52). In chapter 4, I explored the effect of antibiotic growth promoter (AGP) administration post avian influenza virus (AIV) H9N2 infection on growth performance, virus shedding, and the respiratory and intestinal microbiome composition. Previous reports showed that numerous AGPs alter the composition and diversity of the microbiota in different parts of the avian intestinal tract and are associated with protection against enteric pathogens (211, 253-260). Although AGP-induced changes in the intestinal microbiome have been previously associated with growth and protection against enteric pathogens, it is currently unknown if these changes could affect the susceptibility to a respiratory pathogen, such as AIV. Results from this study suggest that AIV infection does not lead to weight reduction when BMD is administered as an AGP. When analyzing virus shedding, similar OP shedding was observed for broilers fed a standard diet and those supplemented with BMD; however, OP infectious virus shedding was prolonged compared to those fed a standard diet. Further, one chicken fed a supplemented BMD diet shed virus via the cloaca compared to those fed a standard diet. Concurrently, changes, specifically a decrease of "beneficial" bacteria, within the oropharyngeal, cloacal, and fecal microbiota were observed notably during AIV infection. Investigating the relationship between AGP-induced microbiota changes and AIV infection will further increase our comprehension of the microbiota's impact on AIV infection in poultry and the effect of AGP administration on the physiology of broiler chickens during respiratory virus infection.

While FLUAV requires annual changes to the vaccine to protect against current circulating strains, the severe acute respiratory syndrome coronavirus 2 (SARS2) is responsible for the recent coronavirus disease 2019 (COVID-19) pandemic. Similar to FLUAV, clinical manifestations of infection are highly variable, and several risk factors for severe disease have been identified (9). In particular, the COVID-19 pandemic notably affected the geriatric population, who are at greater risk of developing acute respiratory distress infection leading to prolonged hospitalization and death (9). However, the mechanism of age-related pathogenicity is not fully understood. Here, I utilized an aged Syrian hamster model resembling ~60-year-old humans to analyze the pathobiology, host response, and effects of SARS2 on the respiratory and intestinal microbiome. I identified specific microbial markers observed in severe COVID-19 patients within the lungs of aged hamsters infected with SARS-CoV-2. Prior influenza A virus (H1N1) exposure amplified these changes. Similarities among aged GSH and critically ill COVID-19 patients suggest that GSHs are a valuable model for investigating microbial changes during SARS2 infection. The relationship between age, residential microbiome, and viral pathogens contribute to a better understanding of the complexities associated with the host responses during viral infection while limiting potential environmental factors that may contribute to inter-individual variation.

Taking into account the studies and results observed within these studies, the future directions of the work should aim at the following:

1. Regarding the aerosol exposure chamber (Chapter 3), my thesis analyzed aerosol infection efficiency *in vitro*. It would be beneficial to pair the *in vitro* results with experiments *in vivo* utilizing animal models such as mice, guinea pigs, and ferrets.
2. To further expand this aerosol exposure system (Chapter 3), the system can be utilized to analyze molecular markers associated with the modulation of aerosol transmission efficiency, assessing the evolution-driven selection of variants involved in aerosol transmission and analyzing the difference of FLUAV recombination through direct inoculation or via aerosol inoculation. Additional

testing of FLUAV strains of various subtypes and influenza B virus (FLUBV) can also contribute to the greater understanding of dissecting mechanisms underlying aerosol transmission difference among FLUAV subtypes and FLUBV.

3. Concerning analyzing the effect of AGPs on AIV infection (Chapter 4), it would be interesting to analyze different antibiotic growth promoters, such as virginiamycin, which has been previously demonstrated to have a different effect on the microbiome compared to BMD. This may provide knowledge of various microbiome changes before infection influences AIV shedding.
4. In addition to analyzing different antibiotic growth promoters (Chapter 4), future studies are needed to understand if AGP supplementation and its effect on the microbiome alters the host immune response during respiratory virus infection. Numerous studies showed that the immune response is closely connected to the host microbiota, in which both components play an essential role during early viral infection and the host microbiota; however, I did not evaluate the immune response when analyzing the BMD effect on AIV infection.
5. Regarding the analysis of FLUAV pre-exposure and SARS-CoV-2 infection on the respiratory and intestinal microbiome, I did not detect antibodies post-FLUAV H1N1 inoculation; however, infectious virus titers of FLUAV were not analyzed before SARS-CoV-2 infection. Therefore, it would be beneficial to understand the microbiome changes during SARS-CoV-2 after confirmed infectious FLUAV virus infection or during the co-infection of both viruses.
6. Furthermore, studies analyzing the direct effect of the microbiota on SARS-CoV-2 by depleting the intestinal microbiome before infection could provide greater

insight into the direct impact of the microbiome immune modulation during SARS-CoV-2 infection.

REFERENCES

1. Harper A, Vijayakumar V, Ouwehand AC, Ter Haar J, Obis D, Espadaler J, Binda S, Desiraju S, Day R. 2020. Viral Infections, the Microbiome, and Probiotics. Front Cell Infect Microbiol 10:596166.
2. Chen R, Holmes EC. 2008. The evolutionary dynamics of human influenza B virus. J Mol Evol 66:655-63.
3. Rajao DS, Perez DR. 2018. Universal Vaccines and Vaccine Platforms to Protect against Influenza Viruses in Humans and Agriculture. Front Microbiol 9:123.
4. Perez DR, Angel M, Gonzalez-Reiche AS, Santos J, Obadan A, Martinez-Sobrido L. 2017. Plasmid-Based Reverse Genetics of Influenza A Virus. *In* Perez DR (ed), Reverse Genetics of RNA Viruses. Humana Press, New York.
5. Perez DR, Seibert B, Ferreri L, Lee CW, Rajao D. 2020. Plasmid-Based Reverse Genetics of Influenza A Virus. Methods Mol Biol 2123:37-59.
6. Seibert B, Cardenas-Garcia S, Rajao D, Perez DR. 2022. Reverse Genetics for Influenza A and B Viruses Driven by Swine Polymerase I Promoter. Methods Mol Biol 2465:257-281.
7. Tong S, Li Y, Rivailler P, Conrardy C, Castillo DA, Chen LM, Recuenco S, Ellison JA, Davis CT, York IA, Turmelle AS, Moran D, Rogers S, Shi M, Tao Y, Weil MR, Tang K, Rowe LA, Sammons S, Xu X, Frace M, Lindblade KA, Cox NJ, Anderson LJ, Rupprecht CE, Donis RO. 2012. A distinct lineage of influenza A virus from bats. Proc Natl Acad Sci U S A 109:4269-74.
8. Tong S, Zhu X, Li Y, Shi M, Zhang J, Bourgeois M, Yang H, Chen X, Recuenco S, Gomez J, Chen LM, Johnson A, Tao Y, Dreyfus C, Yu W, McBride R, Carney PJ, Gilbert AT, Chang J, Guo Z, Davis CT, Paulson JC, Stevens J, Rupprecht CE, Holmes EC, Wilson IA, Donis RO. 2013. New world bats harbor diverse influenza A viruses. PLoS Pathog 9:e1003657.
9. Flerlage T, Boyd DF, Meliopoulos V, Thomas PG, Schultz-Cherry S. 2021. Influenza virus and SARS-CoV-2: pathogenesis and host responses in the respiratory tract. Nat Rev Microbiol 19:425-441.
10. Caceres CJ, Rajao DS, Perez DR. 2021. Airborne Transmission of Avian Origin H9N2 Influenza A Viruses in Mammals. Viruses 13.
11. Peacock THP, James J, Sealy JE, Iqbal M. 2019. A Global Perspective on H9N2 Avian Influenza Virus. Viruses 11.
12. Alexander DJ. 2003. Should we change the definition of avian influenza for eradication purposes? Avian Dis 47:976-81.
13. Carnaccini S, Perez DR. 2020. H9 Influenza Viruses: An Emerging Challenge. Cold Spring Harb Perspect Med 10.
14. Butt KM, Smith GJ, Chen H, Zhang LJ, Leung YH, Xu KM, Lim W, Webster RG, Yuen KY, Peiris JS, Guan Y. 2005. Human infection with an avian H9N2 influenza A virus in Hong Kong in 2003. J Clin Microbiol 43:5760-7.

15. Cong YL, Wang CF, Yan CM, Peng JS, Jiang ZL, Liu JH. 2008. Swine infection with H9N2 influenza viruses in China in 2004. Virus Genes 36:461-9.
16. Guan Y, Shortridge KF, Krauss S, Webster RG. 1999. Molecular characterization of H9N2 influenza viruses: were they the donors of the "internal" genes of H5N1 viruses in Hong Kong? Proc Natl Acad Sci U S A 96:9363-7.
17. Lam TT, Wang J, Shen Y, Zhou B, Duan L, Cheung CL, Ma C, Lycett SJ, Leung CY, Chen X, Li L, Hong W, Chai Y, Zhou L, Liang H, Ou Z, Liu Y, Farooqui A, Kelvin DJ, Poon LL, Smith DK, Pybus OG, Leung GM, Shu Y, Webster RG, Webby RJ, Peiris JS, Rambaut A, Zhu H, Guan Y. 2013. The genesis and source of the H7N9 influenza viruses causing human infections in China. Nature 502:241-4.
18. Pu J, Yin Y, Liu J, Wang X, Zhou Y, Wang Z, Sun Y, Sun H, Li F, Song J, Qu R, Gao W, Wang D, Wang Z, Yan S, Chen M, Zeng J, Jiang Z, Sun H, Zong Y, Wang C, Tong Q, Bi Y, Huang Y, Du X, Chang KC, Liu J. 2021. Reassortment with dominant chicken H9N2 influenza virus contributed to the fifth H7N9 virus human epidemic. J Virol doi:10.1128/JVI.01578-20.
19. Sun H, Li F, Liu Q, Du J, Liu L, Sun H, Li C, Liu J, Zhang X, Yang J, Duan Y, Bi Y, Pu J, Sun Y, Tong Q, Wang Y, Du X, Shu Y, Chang KC, Liu J. 2021. Mink is a highly susceptible host species to circulating human and avian influenza viruses. Emerg Microbes Infect 10:472-480.
20. Um S, Siegers JY, Sar B, Chin S, Patel S, Bunnary S, Hak M, Sor S, Sokhen O, Heng S, Chau D, Sothyra T, Khalakdina A, Mott JA, Olsen SJ, Claes F, Sovann L, Karlsson EA. 2021. Human Infection with Avian Influenza A(H9N2) Virus, Cambodia, February 2021. Emerg Infect Dis 27:2742-2745.
21. Wang Y, Niu S, Zhang B, Yang C, Zhou Z. 2021. The whole genome analysis for the first human infection with H10N3 influenza virus in China. J Infect doi:10.1016/j.jinf.2021.06.021.
22. Berhane Y, Hisanaga T, Kehler H, Neufeld J, Manning L, Argue C, Handel K, Hooper-McGrevy K, Jonas M, Robinson J, Webster RG, Pasick J. 2009. Highly pathogenic avian influenza virus A (H7N3) in domestic poultry, Saskatchewan, Canada, 2007. Emerg Infect Dis 15:1492-5.
23. Choi YK, Ozaki H, Webby RJ, Webster RG, Peiris JS, Poon L, Butt C, Leung YH, Guan Y. 2004. Continuing evolution of H9N2 influenza viruses in Southeastern China. J Virol 78:8609-14.
24. Monne I, Hussein HA, Fusaro A, Valastro V, Hamoud MM, Khalefa RA, Dardir SN, Radwan MI, Capua I, Cattoli G. 2013. H9N2 influenza A virus circulates in H5N1 endemically infected poultry population in Egypt. Influenza Other Respir Viruses 7:240-3.
25. Treanor J. 2004. Influenza vaccine--outmaneuvering antigenic shift and drift. N Engl J Med 350:218-20.
26. Cowling BJ, Ip DK, Fang VJ, Suntarattiwong P, Olsen SJ, Levy J, Uyeki TM, Leung GM, Malik Peiris JS, Chotpitayasunondh T, Nishiura H, Mark Simmerman J. 2013. Aerosol transmission is an important mode of influenza A virus spread. Nat Commun 4:1935.
27. Turgeon N, Hamelin ME, Verreault D, Levesque A, Rheaume C, Carbonneau J, Checkmahomed L, Girard M, Boivin G, Duchaine C. 2019. Design and

Validation with Influenza A Virus of an Aerosol Transmission Chamber for Ferrets. Int J Environ Res Public Health 16.

28. Lv J, Gao J, Wu B, Yao M, Yang Y, Chai T, Li N. 2021. Aerosol Transmission of Coronavirus and Influenza Virus of Animal Origin. Front Vet Sci 8:572012.

29. Richard M, Fouchier RA. 2016. Influenza A virus transmission via respiratory aerosols or droplets as it relates to pandemic potential. FEMS Microbiol Rev 40:68-85.

30. Blachere FM, Lindsley WG, Pearce TA, Anderson SE, Fisher M, Khakoo R, Meade BJ, Lander O, Davis S, Thewlis RE, Celik I, Chen BT, Beezhold DH. 2009. Measurement of airborne influenza virus in a hospital emergency department. Clin Infect Dis 48:438-40.

31. Fabian P, McDevitt JJ, DeHaan WH, Fung RO, Cowling BJ, Chan KH, Leung GM, Milton DK. 2008. Influenza virus in human exhaled breath: an observational study. PLoS One 3:e2691.

32. Lindsley WG, Blachere FM, Thewlis RE, Vishnu A, Davis KA, Cao G, Palmer JE, Clark KE, Fisher MA, Khakoo R, Beezhold DH. 2010. Measurements of airborne influenza virus in aerosol particles from human coughs. PLoS One 5:e15100.

33. Milton DK, Fabian MP, Cowling BJ, Grantham ML, McDevitt JJ. 2013. Influenza virus aerosols in human exhaled breath: particle size, culturability, and effect of surgical masks. PLoS Pathog 9:e1003205.

34. Belser JA, Gustin KM, Katz JM, Maines TR, Tumpey TM. 2015. Comparison of traditional intranasal and aerosol inhalation inoculation of mice with influenza A viruses. Virology 481:107-12.

35. Jegede A, Fu Q, Lin M, Kumar A, Guan J. 2019. Aerosol exposure enhanced infection of low pathogenic avian influenza viruses in chickens. Transbound Emerg Dis 66:435-444.

36. Mooij P, Stammes MA, Mortier D, Fagrouch Z, van Driel N, Verschoor EJ, Kondova I, Bogers W, Koopman G. 2021. Aerosolized Exposure to H5N1 Influenza Virus Causes Less Severe Disease Than Infection via Combined Intrabronchial, Oral, and Nasal Inoculation in Cynomolgus Macaques. Viruses 13.

37. Yi Zhanga, Zhendong Guoa, Zhongyi Wanga, Yingying Fub, Zongzheng Zhaoa, Linna Liua, Qiana J. 2017. Comparison of traditional intranasal and aerosol inhalation inoculation of guinea pigs with visualizing influenza virus. Journal of Aerosol Science 110:43-52.

38. Leung NHL. 2021. Transmissibility and transmission of respiratory viruses. Nat Rev Microbiol 19:528-545.

39. V'Kovski P, Kratzel A, Steiner S, Stalder H, Thiel V. 2021. Coronavirus biology and replication: implications for SARS-CoV-2. Nat Rev Microbiol 19:155-170.

40. Oude Munnink BB, Sikkema RS, Nieuwenhuijse DF, Molenaar RJ, Munger E, Molenkamp R, van der Spek A, Tolsma P, Rietveld A, Brouwer M, Bouwmeester-Vincken N, Harders F, Hakze-van der Honing R, Wegdam-Blans MCA, Bouwstra RJ, GeurtsvanKessel C, van der Eijk AA, Velkers FC, Smit LAM, Stegeman A, van der Poel WHM, Koopmans MPG. 2021. Transmission of SARS-CoV-2 on mink farms between humans and mink and back to humans. Science 371:172-177.

41. Harrison AG, Lin T, Wang P. 2020. Mechanisms of SARS-CoV-2 Transmission and Pathogenesis. Trends Immunol 41:1100-1115.
42. Bartleson JM, Radenkovic D, Covarrubias AJ, Furman D, Winer DA, Verdin E. 2021. SARS-CoV-2, COVID-19 and the Ageing Immune System. Nat Aging 1:769-782.
43. Chen N, Zhou M, Dong X, Qu J, Gong F, Han Y, Qiu Y, Wang J, Liu Y, Wei Y, Xia J, Yu T, Zhang X, Zhang L. 2020. Epidemiological and clinical characteristics of 99 cases of 2019 novel coronavirus pneumonia in Wuhan, China: a descriptive study. Lancet 395:507-513.
44. Wang D, Hu B, Hu C, Zhu F, Liu X, Zhang J, Wang B, Xiang H, Cheng Z, Xiong Y, Zhao Y, Li Y, Wang X, Peng Z. 2020. Clinical Characteristics of 138 Hospitalized Patients With 2019 Novel Coronavirus-Infected Pneumonia in Wuhan, China. JAMA 323:1061-1069.
45. Chen CJ, Wu GH, Kuo RL, Shih SR. 2017. Role of the intestinal microbiota in the immunomodulation of influenza virus infection. Microbes Infect 19:570-579.
46. Pichon M, Lina B, Josset L. 2017. Impact of the Respiratory Microbiome on Host Responses to Respiratory Viral Infection. Vaccines (Basel) 5.
47. de Oliveira GLV, Oliveira CNS, Pinzan CF, de Salis LVV, Cardoso CRB. 2021. Microbiota Modulation of the Gut-Lung Axis in COVID-19. Front Immunol 12:635471.
48. Woodall CA, McGeoch LJ, Hay AD, Hammond A. 2022. Respiratory tract infections and gut microbiome modifications: A systematic review. PLoS One 17:e0262057.
49. Enaud R, Prevel R, Ciarlo E, Beaufils F, Wieers G, Guery B, Delhaes L. 2020. The Gut-Lung Axis in Health and Respiratory Diseases: A Place for Inter-Organ and Inter-Kingdom Crosstalks. Front Cell Infect Microbiol 10:9.
50. He Y, Wen Q, Yao F, Xu D, Huang Y, Wang J. 2017. Gut-lung axis: The microbial contributions and clinical implications. Crit Rev Microbiol 43:81-95.
51. Gierse LC, Meene A, Schultz D, Schwaiger T, Schroder C, Mucke P, Zuhlke D, Hinzke T, Wang H, Methling K, Kreikemeyer B, Bernhardt J, Becher D, Mettenleiter TC, Lalk M, Urich T, Riedel K. 2021. Influenza A H1N1 Induced Disturbance of the Respiratory and Fecal Microbiome of German Landrace Pigs - a Multi-Omics Characterization. Microbiol Spectr 9:e0018221.
52. Groves HT, Cuthbertson L, James P, Moffatt MF, Cox MJ, Tregoning JS. 2018. Respiratory Disease following Viral Lung Infection Alters the Murine Gut Microbiota. Front Immunol 9:182.
53. Kuss SK, Best GT, Etheredge CA, Pruijssers AJ, Frierson JM, Hooper LV, Dermody TS, Pfeiffer JK. 2011. Intestinal microbiota promote enteric virus replication and systemic pathogenesis. Science 334:249-52.
54. Robinson CM. 2019. Enteric viruses exploit the microbiota to promote infection. Curr Opin Virol 37:58-62.
55. Robinson CM, Jesudhasan PR, Pfeiffer JK. 2014. Bacterial lipopolysaccharide binding enhances virion stability and promotes environmental fitness of an enteric virus. Cell Host Microbe 15:36-46.
56. (ICTV) ICoToV. https://ictv.global/taxonomy/. Accessed

57. Anonymous. 2017. Chapter 21 - Orthomyxoviridae, p Pages 389-410. *In* N. James MacLachlan, Edward J. Dubovi (ed), Fenner's Veterinary Virology (Fifth Edition). Academic Press.
58. Bouvier NM, Palese P. 2008. The biology of influenza viruses. Vaccine 26 Suppl 4:D49-53.
59. Paules C, Subbarao K. 2017. Influenza. Lancet 390:697-708.
60. Mosley VM, Wyckoff RW. 1946. Electron micrography of the virus of influenza. Nature 157:263.
61. Seladi-Schulman J, Steel J, Lowen AC. 2013. Spherical influenza viruses have a fitness advantage in embryonated eggs, while filament-producing strains are selected in vivo. J Virol 87:13343-53.
62. Palese P, Shaw M. 2007. Orthomyxoviridae: the viruses and their replication. Lippincott Williams & Wilkins, Philadelphia.
63. Fodor E, Te Velthuis AJW. 2020. Structure and Function of the Influenza Virus Transcription and Replication Machinery. Cold Spring Harb Perspect Med 10.
64. Dou D, Revol R, Ostbye H, Wang H, Daniels R. 2018. Influenza A Virus Cell Entry, Replication, Virion Assembly and Movement. Front Immunol 9:1581.
65. Wright P, Nuemann G, Kawaoka Y. 2007. Orthomyxoviruses., Fields virology, 5th edn ed. Lippincott Williams & Wilkins, Philadelphia.
66. Yamayoshi S, Watanabe M, Goto H, Kawaoka Y. 2016. Identification of a Novel Viral Protein Expressed from the PB2 Segment of Influenza A Virus. J Virol 90:444-56.
67. Zamarin D, Ortigoza MB, Palese P. 2006. Influenza A virus PB1-F2 protein contributes to viral pathogenesis in mice. J Virol 80:7976-83.
68. Hayashi T, MacDonald LA, Takimoto T. 2015. Influenza A Virus Protein PA-X Contributes to Viral Growth and Suppression of the Host Antiviral and Immune Responses. J Virol 89:6442-52.
69. Obadan AO, Santos J, Ferreri L, Thompson AJ, Carnaccini S, Geiger G, Gonzalez Reiche AS, Rajao DS, Paulson JC, Perez DR. 2019. Flexibility In Vitro of Amino Acid 226 in the Receptor-Binding Site of an H9 Subtype Influenza A Virus and Its Effect In Vivo on Virus Replication, Tropism, and Transmission. J Virol 93.
70. Ji ZX, Wang XQ, Liu XF. 2021. NS1: A Key Protein in the "Game" Between Influenza A Virus and Host in Innate Immunity. Front Cell Infect Microbiol 11:670177.
71. Garten W, Bosch FX, Linder D, Rott R, Klenk HD. 1981. Proteolytic activation of the influenza virus hemagglutinin: The structure of the cleavage site and the enzymes involved in cleavage. Virology 115:361-74.
72. Rajao DS, Vincent AL, Perez DR. 2018. Adaptation of Human Influenza Viruses to Swine. Front Vet Sci 5:347.
73. Connor RJ, Kawaoka Y, Webster RG, Paulson JC. 1994. Receptor specificity in human, avian, and equine H2 and H3 influenza virus isolates. Virology 205:17-23.
74. Rogers GN, Paulson JC. 1983. Receptor determinants of human and animal influenza virus isolates: differences in receptor specificity of the H3 hemagglutinin based on species of origin. Virology 127:361-73.

75. Rust MJ, Lakadamyali M, Zhang F, Zhuang X. 2004. Assembly of endocytic machinery around individual influenza viruses during viral entry. Nat Struct Mol Biol 11:567-73.
76. Bui M, Whittaker G, Helenius A. 1996. Effect of M1 protein and low pH on nuclear transport of influenza virus ribonucleoproteins. J Virol 70:8391-401.
77. Dou D, Hernandez-Neuta I, Wang H, Ostbye H, Qian X, Thiele S, Resa-Infante P, Kouassi NM, Sender V, Hentrich K, Mellroth P, Henriques-Normark B, Gabriel G, Nilsson M, Daniels R. 2017. Analysis of IAV Replication and Co-infection Dynamics by a Versatile RNA Viral Genome Labeling Method. Cell Rep 20:251-263.
78. Amorim MJ, Bruce EA, Read EK, Foeglein A, Mahen R, Stuart AD, Digard P. 2011. A Rab11- and microtubule-dependent mechanism for cytoplasmic transport of influenza A virus viral RNA. J Virol 85:4143-56.
79. Fujii Y, Goto H, Watanabe T, Yoshida T, Kawaoka Y. 2003. Selective incorporation of influenza virus RNA segments into virions. Proc Natl Acad Sci U S A 100:2002-7.
80. Wang CC, Prather KA, Sznitman J, Jimenez JL, Lakdawala SS, Tufekci Z, Marr LC. 2021. Airborne transmission of respiratory viruses. Science 373.
81. Lindsley WG, Pearce TA, Hudnall JB, Davis KA, Davis SM, Fisher MA, Khakoo R, Palmer JE, Clark KE, Celik I, Coffey CC, Blachere FM, Beezhold DH. 2012. Quantity and size distribution of cough-generated aerosol particles produced by influenza patients during and after illness. J Occup Environ Hyg 9:443-9.
82. Johnson D, Lynch R, Marshall C, Mead K, Hirst D. 2013. Aerosol Generation by Modern Flush Toilets. Aerosol Sci Technol 47:1047-1057.
83. Abkarian M, Mendez S, Xue N, Yang F, Stone HA. 2020. Speech can produce jet-like transport relevant to asymptomatic spreading of virus. Proc Natl Acad Sci U S A 117:25237-25245.
84. Fernandez Tena A, Casan Clara P. 2012. Deposition of inhaled particles in the lungs. Arch Bronconeumol 48:240-6.
85. Thomas RJ. 2013. Particle size and pathogenicity in the respiratory tract. Virulence 4:847-58.
86. Wallace LE, Liu M, van Kuppeveld FJM, de Vries E, de Haan CAM. 2021. Respiratory mucus as a virus-host range determinant. Trends Microbiol 29:983-992.
87. Vahey MD, Fletcher DA. 2019. Influenza A virus surface proteins are organized to help penetrate host mucus. Elife 8.
88. Cohen M, Zhang XQ, Senaati HP, Chen HW, Varki NM, Schooley RT, Gagneux P. 2013. Influenza A penetrates host mucus by cleaving sialic acids with neuraminidase. Virol J 10:321.
89. Guo H, Rabouw H, Slomp A, Dai M, van der Vegt F, van Lent JWM, McBride R, Paulson JC, de Groot RJ, van Kuppeveld FJM, de Vries E, de Haan CAM. 2018. Kinetic analysis of the influenza A virus HA/NA balance reveals contribution of NA to virus-receptor binding and NA-dependent rolling on receptor-containing surfaces. PLoS Pathog 14:e1007233.
90. Sakai T, Nishimura SI, Naito T, Saito M. 2017. Influenza A virus hemagglutinin and neuraminidase act as novel motile machinery. Sci Rep 7:45043.

91. Cheng YS. 2014. Mechanisms of pharmaceutical aerosol deposition in the respiratory tract. AAPS PharmSciTech 15:630-40.
92. Yan J, Grantham M, Pantelic J, Bueno de Mesquita PJ, Albert B, Liu F, Ehrman S, Milton DK, Consortium E. 2018. Infectious virus in exhaled breath of symptomatic seasonal influenza cases from a college community. Proc Natl Acad Sci U S A 115:1081-1086.
93. Gralton J, Tovey ER, McLaws ML, Rawlinson WD. 2013. Respiratory virus RNA is detectable in airborne and droplet particles. J Med Virol 85:2151-9.
94. Yang W, Elankumaran S, Marr LC. 2011. Concentrations and size distributions of airborne influenza A viruses measured indoors at a health centre, a day-care centre and on aeroplanes. J R Soc Interface 8:1176-84.
95. Leung NHL, Chu DKW, Shiu EYC, Chan KH, McDevitt JJ, Hau BJP, Yen HL, Li Y, Ip DKM, Peiris JSM, Seto WH, Leung GM, Milton DK, Cowling BJ. 2020. Respiratory virus shedding in exhaled breath and efficacy of face masks. Nat Med 26:676-680.
96. Lindsley WG, Blachere FM, Beezhold DH, Thewlis RE, Noorbakhsh B, Othumpangat S, Goldsmith WT, McMillen CM, Andrew ME, Burrell CN, Noti JD. 2016. Viable influenza A virus in airborne particles expelled during coughs versus exhalations. Influenza Other Respir Viruses 10:404-13.
97. Lindsley WG, Noti JD, Blachere FM, Thewlis RE, Martin SB, Othumpangat S, Noorbakhsh B, Goldsmith WT, Vishnu A, Palmer JE, Clark KE, Beezhold DH. 2015. Viable influenza A virus in airborne particles from human coughs. J Occup Environ Hyg 12:107-13.
98. Poon LL, Song T, Rosenfeld R, Lin X, Rogers MB, Zhou B, Sebra R, Halpin RA, Guan Y, Twaddle A, DePasse JV, Stockwell TB, Wentworth DE, Holmes EC, Greenbaum B, Peiris JS, Cowling BJ, Ghedin E. 2016. Quantifying influenza virus diversity and transmission in humans. Nat Genet 48:195-200.
99. Yen HL, Liang CH, Wu CY, Forrest HL, Ferguson A, Choy KT, Jones J, Wong DD, Cheung PP, Hsu CH, Li OT, Yuen KM, Chan RW, Poon LL, Chan MC, Nicholls JM, Krauss S, Wong CH, Guan Y, Webster RG, Webby RJ, Peiris M. 2011. Hemagglutinin-neuraminidase balance confers respiratory-droplet transmissibility of the pandemic H1N1 influenza virus in ferrets. Proc Natl Acad Sci U S A 108:14264-9.
100. Gao Y, Zhang Y, Shinya K, Deng G, Jiang Y, Li Z, Guan Y, Tian G, Li Y, Shi J, Liu L, Zeng X, Bu Z, Xia X, Kawaoka Y, Chen H. 2009. Identification of amino acids in HA and PB2 critical for the transmission of H5N1 avian influenza viruses in a mammalian host. PLoS Pathog 5:e1000709.
101. Brown EG, Liu H, Kit LC, Baird S, Nesrallah M. 2001. Pattern of mutation in the genome of influenza A virus on adaptation to increased virulence in the mouse lung: identification of functional themes. Proc Natl Acad Sci U S A 98:6883-8.
102. Steel J, Lowen AC, Mubareka S, Palese P. 2009. Transmission of influenza virus in a mammalian host is increased by PB2 amino acids 627K or 627E/701N. PLoS Pathog 5:e1000252.
103. Van Hoeven N, Pappas C, Belser JA, Maines TR, Zeng H, Garcia-Sastre A, Sasisekharan R, Katz JM, Tumpey TM. 2009. Human HA and polymerase

subunit PB2 proteins confer transmission of an avian influenza virus through the air. Proc Natl Acad Sci U S A 106:3366-71.

104. Chou YY, Albrecht RA, Pica N, Lowen AC, Richt JA, Garcia-Sastre A, Palese P, Hai R. 2011. The M segment of the 2009 new pandemic H1N1 influenza virus is critical for its high transmission efficiency in the guinea pig model. J Virol 85:11235-41.
105. Tumpey TM, Maines TR, Van Hoeven N, Glaser L, Solorzano A, Pappas C, Cox NJ, Swayne DE, Palese P, Katz JM, Garcia-Sastre A. 2007. A two-amino acid change in the hemagglutinin of the 1918 influenza virus abolishes transmission. Science 315:655-9.
106. Roberts KL, Shelton H, Scull M, Pickles R, Barclay WS. 2011. Lack of transmission of a human influenza virus with avian receptor specificity between ferrets is not due to decreased virus shedding but rather a lower infectivity in vivo. J Gen Virol 92:1822-1831.
107. Xie C, Su W, Sia SF, Choy KT, Morrell S, Zhou J, Peiris M, Bloom JD, Yen HL. 2022. A(H1N1)pdm09 Influenza Viruses Replicating in Ferret Upper or Lower Respiratory Tract Differed in Onward Transmission Potential by Air. J Infect Dis 225:65-74.
108. Krammer F, Smith GJD, Fouchier RAM, Peiris M, Kedzierska K, Doherty PC, Palese P, Shaw ML, Treanor J, Webster RG, Garcia-Sastre A. 2018. Influenza. Nat Rev Dis Primers 4:3.
109. Lowen AC, Mubareka S, Steel J, Palese P. 2007. Influenza virus transmission is dependent on relative humidity and temperature. PLoS Pathog 3:1470-6.
110. Lowen AC, Steel J, Mubareka S, Palese P. 2008. High temperature (30 degrees C) blocks aerosol but not contact transmission of influenza virus. J Virol 82:5650-2.
111. Schaffer FL, Soergel ME, Straube DC. 1976. Survival of airborne influenza virus: effects of propagating host, relative humidity, and composition of spray fluids. Arch Virol 51:263-73.
112. Noti JD, Blachere FM, McMillen CM, Lindsley WG, Kashon ML, Slaughter DR, Beezhold DH. 2013. High humidity leads to loss of infectious influenza virus from simulated coughs. PLoS One 8:e57485.
113. Kormuth KA, Lin K, Prussin AJ, 2nd, Vejerano EP, Tiwari AJ, Cox SS, Myerburg MM, Lakdawala SS, Marr LC. 2018. Influenza Virus Infectivity Is Retained in Aerosols and Droplets Independent of Relative Humidity. J Infect Dis 218:739-747.
114. Ye Y, Chang PH, Hartert J, Wigginton KR. 2018. Reactivity of Enveloped Virus Genome, Proteins, and Lipids with Free Chlorine and UV254. Environ Sci Technol 52:7698-7708.
115. Schuit M, Gardner S, Wood S, Bower K, Williams G, Freeburger D, Dabisch P. 2020. The Influence of Simulated Sunlight on the Inactivation of Influenza Virus in Aerosols. J Infect Dis 221:372-378.
116. Dhakal S, Klein SL. 2019. Host Factors Impact Vaccine Efficacy: Implications for Seasonal and Universal Influenza Vaccine Programs. J Virol 93.
117. Klein SL. 2012. Sex differences in prophylaxis and therapeutic treatments for viral diseases. Handb Exp Pharmacol doi:10.1007/978-3-642-30726-3_22:499-522.

118. Caceres CJ, Seibert B, Cargnin Faccin F, Cardenas-Garcia S, Rajao DS, Perez DR. 2022. Influenza antivirals and animal models. FEBS Open Bio 12:1142-1165.
119. Honce R, Wohlgemuth N, Meliopoulos VA, Short KR, Schultz-Cherry S. 2020. Influenza in High-Risk Hosts-Lessons Learned from Animal Models. Cold Spring Harb Perspect Med 10.
120. Milner JJ, Beck MA. 2012. The impact of obesity on the immune response to infection. Proc Nutr Soc 71:298-306.
121. Penkert RR, Jones BG, Hacker H, Partridge JF, Hurwitz JL. 2017. Vitamin A differentially regulates cytokine expression in respiratory epithelial and macrophage cell lines. Cytokine 91:1-5.
122. Taylor AK, Cao W, Vora KP, De La Cruz J, Shieh WJ, Zaki SR, Katz JM, Sambhara S, Gangappa S. 2013. Protein energy malnutrition decreases immunity and increases susceptibility to influenza infection in mice. J Infect Dis 207:501-10.
123. Chan KH, Zhang AJ, To KK, Chan CC, Poon VK, Guo K, Ng F, Zhang QW, Leung VH, Cheung AN, Lau CC, Woo PC, Tse H, Wu W, Chen H, Zheng BJ, Yuen KY. 2010. Wild type and mutant 2009 pandemic influenza A (H1N1) viruses cause more severe disease and higher mortality in pregnant BALB/c mice. PLoS One 5:e13757.
124. Engels G, Hierweger AM, Hoffmann J, Thieme R, Thiele S, Bertram S, Dreier C, Resa-Infante P, Jacobsen H, Thiele K, Alawi M, Indenbirken D, Grundhoff A, Siebels S, Fischer N, Stojanovska V, Muzzio D, Jensen F, Karimi K, Mittrucker HW, Arck PC, Gabriel G. 2017. Pregnancy-Related Immune Adaptation Promotes the Emergence of Highly Virulent H1N1 Influenza Virus Strains in Allogenically Pregnant Mice. Cell Host Microbe 21:321-333.
125. Marcelin G, Aldridge JR, Duan S, Ghoneim HE, Rehg J, Marjuki H, Boon AC, McCullers JA, Webby RJ. 2011. Fatal outcome of pandemic H1N1 2009 influenza virus infection is associated with immunopathology and impaired lung repair, not enhanced viral burden, in pregnant mice. J Virol 85:11208-19.
126. Vom Steeg LG, Klein SL. 2019. Sex and sex steroids impact influenza pathogenesis across the life course. Semin Immunopathol 41:189-194.
127. Talbot HK. 2017. Influenza in Older Adults. Infect Dis Clin North Am 31:757-766.
128. Hilty M, Burke C, Pedro H, Cardenas P, Bush A, Bossley C, Davies J, Ervine A, Poulter L, Pachter L, Moffatt MF, Cookson WO. 2010. Disordered microbial communities in asthmatic airways. PLoS One 5:e8578.
129. Segal LN, Clemente JC, Tsay JC, Koralov SB, Keller BC, Wu BG, Li Y, Shen N, Ghedin E, Morris A, Diaz P, Huang L, Wikoff WR, Ubeda C, Artacho A, Rom WN, Sterman DH, Collman RG, Blaser MJ, Weiden MD. 2016. Enrichment of the lung microbiome with oral taxa is associated with lung inflammation of a Th17 phenotype. Nat Microbiol 1:16031.
130. Dickson RP, Erb-Downward JR, Freeman CM, McCloskey L, Falkowski NR, Huffnagle GB, Curtis JL. 2017. Bacterial Topography of the Healthy Human Lower Respiratory Tract. mBio 8.

131. Pattaroni C, Watzenboeck ML, Schneidegger S, Kieser S, Wong NC, Bernasconi E, Pernot J, Mercier L, Knapp S, Nicod LP, Marsland CP, Roth-Kleiner M, Marsland BJ. 2018. Early-Life Formation of the Microbial and Immunological Environment of the Human Airways. Cell Host Microbe 24:857-865 e4.
132. Sender R, Fuchs S, Milo R. 2016. Revised Estimates for the Number of Human and Bacteria Cells in the Body. PLoS Biol 14:e1002533.
133. Remot A, Descamps D, Noordine ML, Boukadiri A, Mathieu E, Robert V, Riffault S, Lambrecht B, Langella P, Hammad H, Thomas M. 2017. Bacteria isolated from lung modulate asthma susceptibility in mice. ISME J 11:1061-1074.
134. Wu H, Kuzmenko A, Wan S, Schaffer L, Weiss A, Fisher JH, Kim KS, McCormack FX. 2003. Surfactant proteins A and D inhibit the growth of Gram-negative bacteria by increasing membrane permeability. J Clin Invest 111:1589-602.
135. Hanada S, Pirzadeh M, Carver KY, Deng JC. 2018. Respiratory Viral Infection-Induced Microbiome Alterations and Secondary Bacterial Pneumonia. Front Immunol 9:2640.
136. Huxley EJ, Viroslav J, Gray WR, Pierce AK. 1978. Pharyngeal aspiration in normal adults and patients with depressed consciousness. Am J Med 64:564-8.
137. Bassis CM, Erb-Downward JR, Dickson RP, Freeman CM, Schmidt TM, Young VB, Beck JM, Curtis JL, Huffnagle GB. 2015. Analysis of the upper respiratory tract microbiotas as the source of the lung and gastric microbiotas in healthy individuals. mBio 6:e00037.
138. Marsh RL, Kaestli M, Chang AB, Binks MJ, Pope CE, Hoffman LR, Smith-Vaughan HC. 2016. The microbiota in bronchoalveolar lavage from young children with chronic lung disease includes taxa present in both the oropharynx and nasopharynx. Microbiome 4:37.
139. Venkataraman A, Bassis CM, Beck JM, Young VB, Curtis JL, Huffnagle GB, Schmidt TM. 2015. Application of a neutral community model to assess structuring of the human lung microbiome. mBio 6.
140. Dickson RP, Erb-Downward JR, Freeman CM, McCloskey L, Beck JM, Huffnagle GB, Curtis JL. 2015. Spatial Variation in the Healthy Human Lung Microbiome and the Adapted Island Model of Lung Biogeography. Ann Am Thorac Soc 12:821-30.
141. Gollwitzer ES, Saglani S, Trompette A, Yadava K, Sherburn R, McCoy KD, Nicod LP, Lloyd CM, Marsland BJ. 2014. Lung microbiota promotes tolerance to allergens in neonates via PD-L1. Nat Med 20:642-7.
142. Yun Y, Srinivas G, Kuenzel S, Linnenbrink M, Alnahas S, Bruce KD, Steinhoff U, Baines JF, Schaible UE. 2014. Environmentally determined differences in the murine lung microbiota and their relation to alveolar architecture. PLoS One 9:e113466.
143. Yu G, Gail MH, Consonni D, Carugno M, Humphrys M, Pesatori AC, Caporaso NE, Goedert JJ, Ravel J, Landi MT. 2016. Characterizing human lung tissue microbiota and its relationship to epidemiological and clinical features. Genome Biol 17:163.

144. Dubourg G, Edouard S, Raoult D. 2019. Relationship between nasopharyngeal microbiota and patient's susceptibility to viral infection. Expert Rev Anti Infect Ther 17:437-447.
145. Zhou Q, Xie G, Liu Y, Wang H, Yang Y, Shen K, Dai W, Li S, Zheng Y. 2020. Different nasopharynx and oropharynx microbiota imbalance in children with Mycoplasma pneumoniae or influenza virus infection. Microb Pathog 144:104189.
146. Wen Z, Xie G, Zhou Q, Qiu C, Li J, Hu Q, Dai W, Li D, Zheng Y, Wen F. 2018. Distinct Nasopharyngeal and Oropharyngeal Microbiota of Children with Influenza A Virus Compared with Healthy Children. Biomed Res Int 2018:6362716.
147. Langevin S, Pichon M, Smith E, Morrison J, Bent Z, Green R, Barker K, Solberg O, Gillet Y, Javouhey E, Lina B, Katze MG, Josset L. 2017. Early nasopharyngeal microbial signature associated with severe influenza in children: a retrospective pilot study. J Gen Virol 98:2425-2437.
148. Ding T, Song T, Zhou B, Geber A, Ma Y, Zhang L, Volk M, Kapadia SN, Jenkins SG, Salvatore M, Ghedin E. 2019. Microbial Composition of the Human Nasopharynx Varies According to Influenza Virus Type and Vaccination Status. mBio 10.
149. Tarabichi Y, Li K, Hu S, Nguyen C, Wang X, Elashoff D, Saira K, Frank B, Bihan M, Ghedin E, Methe BA, Deng JC. 2015. The administration of intranasal live attenuated influenza vaccine induces changes in the nasal microbiota and nasal epithelium gene expression profiles. Microbiome 3:74.
150. Ramos-Sevillano E, Wade WG, Mann A, Gilbert A, Lambkin-Williams R, Killingley B, Nguyen-Van-Tam JS, Tang CM. 2019. The Effect of Influenza Virus on the Human Oropharyngeal Microbiome. Clin Infect Dis 68:1993-2002.
151. Tsang TK, Lee KH, Foxman B, Balmaseda A, Gresh L, Sanchez N, Ojeda S, Lopez R, Yang Y, Kuan G, Gordon A. 2020. Association Between the Respiratory Microbiome and Susceptibility to Influenza Virus Infection. Clin Infect Dis 71:1195-1203.
152. Lee KH, Foxman B, Kuan G, Lopez R, Shedden K, Ng S, Balmaseda A, Gordon A. 2019. The respiratory microbiota: associations with influenza symptomatology and viral shedding. Ann Epidemiol 37:51-56 e6.
153. Kolde R, Franzosa EA, Rahnavard G, Hall AB, Vlamakis H, Stevens C, Daly MJ, Xavier RJ, Huttenhower C. 2018. Host genetic variation and its microbiome interactions within the Human Microbiome Project. Genome Med 10:6.
154. Gu L, Deng H, Ren Z, Zhao Y, Yu S, Guo Y, Dai J, Chen X, Li K, Li R, Wang G. 2019. Dynamic Changes in the Microbiome and Mucosal Immune Microenvironment of the Lower Respiratory Tract by Influenza Virus Infection. Front Microbiol 10:2491.
155. Kaul D, Rathnasinghe R, Ferres M, Tan GS, Barrera A, Pickett BE, Methe BA, Das SR, Budnik I, Halpin RA, Wentworth D, Schmolke M, Mena I, Albrecht RA, Singh I, Nelson KE, Garcia-Sastre A, Dupont CL, Medina RA. 2020. Microbiome disturbance and resilience dynamics of the upper respiratory tract during influenza A virus infection. Nat Commun 11:2537.

156. Chrun T, Leng J, La Ragione RM, Graham SP, Tchilian E. 2021. Changes in the Nasal Microbiota of Pigs Following Single or Co-Infection with Porcine Reproductive and Respiratory Syndrome and Swine Influenza A Viruses. Pathogens 10.
157. Chen HW, Liu PF, Liu YT, Kuo S, Zhang XQ, Schooley RT, Rohde H, Gallo RL, Huang CM. 2016. Nasal commensal Staphylococcus epidermidis counteracts influenza virus. Sci Rep 6:27870.
158. Jo A, Won J, Gil CH, Kim SK, Lee KM, Yoon SS, Kim HJ. 2022. Nasal symbiont Staphylococcus epidermidis restricts the cellular entry of influenza virus into the nasal epithelium. NPJ Biofilms Microbiomes 8:26.
159. Wang J, Li F, Sun R, Gao X, Wei H, Li LJ, Tian Z. 2013. Bacterial colonization dampens influenza-mediated acute lung injury via induction of M2 alveolar macrophages. Nat Commun 4:2106.
160. Planet PJ, Parker D, Cohen TS, Smith H, Leon JD, Ryan C, Hammer TJ, Fierer N, Chen EI, Prince AS. 2016. Lambda Interferon Restructures the Nasal Microbiome and Increases Susceptibility to Staphylococcus aureus Superinfection. mBio 7:e01939-15.
161. Sender R, Fuchs S, Milo R. 2016. Are We Really Vastly Outnumbered? Revisiting the Ratio of Bacterial to Host Cells in Humans. Cell 164:337-40.
162. Donaldson GP, Lee SM, Mazmanian SK. 2016. Gut biogeography of the bacterial microbiota. Nat Rev Microbiol 14:20-32.
163. Tunney MM, Einarsson GG, Wei L, Drain M, Klem ER, Cardwell C, Ennis M, Boucher RC, Wolfgang MC, Elborn JS. 2013. Lung microbiota and bacterial abundance in patients with bronchiectasis when clinically stable and during exacerbation. Am J Respir Crit Care Med 187:1118-26.
164. Friedman ES, Bittinger K, Esipova TV, Hou L, Chau L, Jiang J, Mesaros C, Lund PJ, Liang X, FitzGerald GA, Goulian M, Lee D, Garcia BA, Blair IA, Vinogradov SA, Wu GD. 2018. Microbes vs. chemistry in the origin of the anaerobic gut lumen. Proc Natl Acad Sci U S A 115:4170-4175.
165. Costea PI, Hildebrand F, Arumugam M, Backhed F, Blaser MJ, Bushman FD, de Vos WM, Ehrlich SD, Fraser CM, Hattori M, Huttenhower C, Jeffery IB, Knights D, Lewis JD, Ley RE, Ochman H, O'Toole PW, Quince C, Relman DA, Shanahan F, Sunagawa S, Wang J, Weinstock GM, Wu GD, Zeller G, Zhao L, Raes J, Knight R, Bork P. 2018. Enterotypes in the landscape of gut microbial community composition. Nat Microbiol 3:8-16.
166. Rinninella E, Raoul P, Cintoni M, Franceschi F, Miggiano GAD, Gasbarrini A, Mele MC. 2019. What is the Healthy Gut Microbiota Composition? A Changing Ecosystem across Age, Environment, Diet, and Diseases. Microorganisms 7.
167. Bradley KC, Finsterbusch K, Schnepf D, Crotta S, Llorian M, Davidson S, Fuchs SY, Staeheli P, Wack A. 2019. Microbiota-Driven Tonic Interferon Signals in Lung Stromal Cells Protect from Influenza Virus Infection. Cell Rep 28:245-256 e4.
168. Gu S, Chen Y, Wu Z, Chen Y, Gao H, Lv L, Guo F, Zhang X, Luo R, Huang C, Lu H, Zheng B, Zhang J, Yan R, Zhang H, Jiang H, Xu Q, Guo J, Gong Y, Tang L, Li L. 2020. Alterations of the Gut Microbiota in Patients With Coronavirus Disease 2019 or H1N1 Influenza. Clin Infect Dis 71:2669-2678.

169. Al Khatib HA, Mathew S, Smatti MK, Eltai NO, Pathan SA, Al Thani AA, Coyle PV, Al Maslamani MA, Yassine HM. 2021. Profiling of Intestinal Microbiota in Patients Infected with Respiratory Influenza A and B Viruses. Pathogens 10.
170. Deriu E, Boxx GM, He X, Pan C, Benavidez SD, Cen L, Rozengurt N, Shi W, Cheng G. 2016. Influenza Virus Affects Intestinal Microbiota and Secondary Salmonella Infection in the Gut through Type I Interferons. PLoS Pathog 12:e1005572.
171. Wang J, Li F, Wei H, Lian ZX, Sun R, Tian Z. 2014. Respiratory influenza virus infection induces intestinal immune injury via microbiota-mediated Th17 cell-dependent inflammation. J Exp Med 211:2397-410.
172. Yildiz S, Mazel-Sanchez B, Kandasamy M, Manicassamy B, Schmolke M. 2018. Influenza A virus infection impacts systemic microbiota dynamics and causes quantitative enteric dysbiosis. Microbiome 6:9.
173. Sencio V, Barthelemy A, Tavares LP, Machado MG, Soulard D, Cuinat C, Queiroz-Junior CM, Noordine ML, Salome-Desnoulez S, Deryuter L, Foligne B, Wahl C, Frisch B, Vieira AT, Paget C, Milligan G, Ulven T, Wolowczuk I, Faveeuw C, Le Goffic R, Thomas M, Ferreira S, Teixeira MM, Trottein F. 2020. Gut Dysbiosis during Influenza Contributes to Pulmonary Pneumococcal Superinfection through Altered Short-Chain Fatty Acid Production. Cell Rep 30:2934-2947 e6.
174. Ichinohe T, Pang IK, Kumamoto Y, Peaper DR, Ho JH, Murray TS, Iwasaki A. 2011. Microbiota regulates immune defense against respiratory tract influenza A virus infection. Proc Natl Acad Sci U S A 108:5354-9.
175. Sencio V, Gallerand A, Gomes Machado M, Deruyter L, Heumel S, Soulard D, Barthelemy J, Cuinat C, Vieira AT, Barthelemy A, Tavares LP, Guinamard R, Ivanov S, Grangette C, Teixeira MM, Foligne B, Wolowczuk I, Le Goffic R, Thomas M, Trottein F. 2021. Influenza Virus Infection Impairs the Gut's Barrier Properties and Favors Secondary Enteric Bacterial Infection through Reduced Production of Short-Chain Fatty Acids. Infect Immun 89:e0073420.
176. Hu X, Zhao Y, Yang Y, Gong W, Sun X, Yang L, Zhang Q, Jin M. 2020. Akkermansia muciniphila Improves Host Defense Against Influenza Virus Infection. Front Microbiol 11:586476.
177. Oh JZ, Ravindran R, Chassaing B, Carvalho FA, Maddur MS, Bower M, Hakimpour P, Gill KP, Nakaya HI, Yarovinsky F, Sartor RB, Gewirtz AT, Pulendran B. 2014. TLR5-mediated sensing of gut microbiota is necessary for antibody responses to seasonal influenza vaccination. Immunity 41:478-492.
178. Stefan KL, Kim MV, Iwasaki A, Kasper DL. 2020. Commensal Microbiota Modulation of Natural Resistance to Virus Infection. Cell 183:1312-1324 e10.
179. Li H, Liu X, Chen F, Zuo K, Wu C, Yan Y, Chen W, Lin W, Xie Q. 2018. Avian Influenza Virus Subtype H9N2 Affects Intestinal Microbiota, Barrier Structure Injury, and Inflammatory Intestinal Disease in the Chicken Ileum. Viruses 10.
180. Yitbarek A, Weese JS, Alkie TN, Parkinson J, Sharif S. 2018. Influenza A virus subtype H9N2 infection disrupts the composition of intestinal microbiota of chickens. FEMS Microbiol Ecol 94.
181. Yitbarek A, Taha-Abdelaziz K, Hodgins DC, Read L, Nagy E, Weese JS, Caswell JL, Parkinson J, Sharif S. 2018. Gut microbiota-mediated protection against

influenza virus subtype H9N2 in chickens is associated with modulation of the innate responses. Sci Rep 8:13189.

182. Yitbarek A, Astill J, Hodgins DC, Parkinson J, Nagy E, Sharif S. 2019. Commensal gut microbiota can modulate adaptive immune responses in chickens vaccinated with whole inactivated avian influenza virus subtype H9N2. Vaccine 37:6640-6647.

183. Cui J, Li F, Shi ZL. 2019. Origin and evolution of pathogenic coronaviruses. Nat Rev Microbiol 17:181-192.

184. Wang MY, Zhao R, Gao LJ, Gao XF, Wang DP, Cao JM. 2020. SARS-CoV-2: Structure, Biology, and Structure-Based Therapeutics Development. Front Cell Infect Microbiol 10:587269.

185. Hu B, Guo H, Zhou P, Shi ZL. 2021. Characteristics of SARS-CoV-2 and COVID-19. Nat Rev Microbiol 19:141-154.

186. Vahidy FS, Pan AP, Ahnstedt H, Munshi Y, Choi HA, Tiruneh Y, Nasir K, Kash BA, Andrieni JD, McCullough LD. 2021. Sex differences in susceptibility, severity, and outcomes of coronavirus disease 2019: Cross-sectional analysis from a diverse US metropolitan area. PLoS One 16:e0245556.

187. Chen Y, Chen L, Deng Q, Zhang G, Wu K, Ni L, Yang Y, Liu B, Wang W, Wei C, Yang J, Ye G, Cheng Z. 2020. The presence of SARS-CoV-2 RNA in the feces of COVID-19 patients. J Med Virol 92:833-840.

188. Cheung KS, Hung IFN, Chan PPY, Lung KC, Tso E, Liu R, Ng YY, Chu MY, Chung TWH, Tam AR, Yip CCY, Leung KH, Fung AY, Zhang RR, Lin Y, Cheng HM, Zhang AJX, To KKW, Chan KH, Yuen KY, Leung WK. 2020. Gastrointestinal Manifestations of SARS-CoV-2 Infection and Virus Load in Fecal Samples From a Hong Kong Cohort: Systematic Review and Meta-analysis. Gastroenterology 159:81-95.

189. Wang H, Wang H, Sun Y, Ren Z, Zhu W, Li A, Cui G. 2021. Potential Associations Between Microbiome and COVID-19. Front Med (Lausanne) 8:785496.

190. Yang T, Chakraborty S, Saha P, Mell B, Cheng X, Yeo JY, Mei X, Zhou G, Mandal J, Golonka R, Yeoh BS, Putluri V, Piyarathna DWB, Putluri N, McCarthy CG, Wenceslau CF, Sreekumar A, Gewirtz AT, Vijay-Kumar M, Joe B. 2020. Gnotobiotic Rats Reveal That Gut Microbiota Regulates Colonic mRNA of Ace2, the Receptor for SARS-CoV-2 Infectivity. Hypertension 76:e1-e3.

191. Edwinson A, Yang L, Chen J, Grover M. 2021. Colonic expression of Ace2, the SARS-CoV-2 entry receptor, is suppressed by commensal human microbiota. Gut Microbes 13:1984105.

192. De Maio F, Posteraro B, Ponziani FR, Cattani P, Gasbarrini A, Sanguinetti M. 2020. Nasopharyngeal Microbiota Profiling of SARS-CoV-2 Infected Patients. Biol Proced Online 22:18.

193. A.E. Budding, E. Sieswerda, B.B. Wintermans, Bos MP. 2022. An age dependent pharyngeal microbiota signature associated with SARS-CoV-2 infection. Preprint (The Lancet).

194. Fan J, Li X, Gao Y, Zhou J, Wang S, Huang B, Wu J, Cao Q, Chen Y, Wang Z, Luo D, Zhou T, Li R, Shang Y, Nie X. 2020. The lung tissue microbiota features of 20 deceased patients with COVID-19. J Infect 81:e64-e67.

195. Shen Z, Xiao Y, Kang L, Ma W, Shi L, Zhang L, Zhou Z, Yang J, Zhong J, Yang D, Guo L, Zhang G, Li H, Xu Y, Chen M, Gao Z, Wang J, Ren L, Li M. 2020. Genomic Diversity of Severe Acute Respiratory Syndrome-Coronavirus 2 in Patients With Coronavirus Disease 2019. Clin Infect Dis 71:713-720.
196. Hoque MN, Akter S, Mishu ID, Islam MR, Rahman MS, Akhter M, Islam I, Hasan MM, Rahaman MM, Sultana M, Islam T, Hossain MA. 2021. Microbial co-infections in COVID-19: Associated microbiota and underlying mechanisms of pathogenesis. Microb Pathog 156:104941.
197. Seibert B, Caceres CJ, Cardenas-Garcia S, Carnaccini S, Geiger G, Rajao DS, Ottesen E, Perez DR. 2021. Mild and Severe SARS-CoV-2 Infection Induces Respiratory and Intestinal Microbiome Changes in the K18-hACE2 Transgenic Mouse Model. Microbiol Spectr 9:e0053621.
198. Liu T, Wu J, Han C, Gong Z, Regina G, Chen J, Dou F, Silvestri R, Chen C, Yu Z. 2021. RS-5645 attenuates inflammatory cytokine storm induced by SARS-CoV-2 spike protein and LPS by modulating pulmonary microbiota. Int J Biol Sci 17:3305-3319.
199. Nagai M, Moriyama M, Ichinohe T. 2021. Oral Bacteria Combined with an Intranasal Vaccine Protect from Influenza A Virus and SARS-CoV-2 Infection. mBio 12:e0159821.
200. Zuo T, Zhang F, Lui GCY, Yeoh YK, Li AYL, Zhan H, Wan Y, Chung ACK, Cheung CP, Chen N, Lai CKC, Chen Z, Tso EYK, Fung KSC, Chan V, Ling L, Joynt G, Hui DSC, Chan FKL, Chan PKS, Ng SC. 2020. Alterations in Gut Microbiota of Patients With COVID-19 During Time of Hospitalization. Gastroenterology 159:944-955 e8.
201. Zuo T, Liu Q, Zhang F, Lui GC, Tso EY, Yeoh YK, Chen Z, Boon SS, Chan FK, Chan PK, Ng SC. 2021. Depicting SARS-CoV-2 faecal viral activity in association with gut microbiota composition in patients with COVID-19. Gut 70:276-284.
202. Cao J, Wang C, Zhang Y, Lei G, Xu K, Zhao N, Lu J, Meng F, Yu L, Yan J, Bai C, Zhang S, Zhang N, Gong Y, Bi Y, Shi Y, Chen Z, Dai L, Wang J, Yang P. 2021. Integrated gut virome and bacteriome dynamics in COVID-19 patients. Gut Microbes 13:1-21.
203. Reinold J, Farahpour F, Fehring C, Dolff S, Konik M, Korth J, van Baal L, Hoffmann D, Buer J, Witzke O, Westendorf AM, Kehrmann J. 2021. A Pro-Inflammatory Gut Microbiome Characterizes SARS-CoV-2 Infected Patients and a Reduction in the Connectivity of an Anti-Inflammatory Bacterial Network Associates With Severe COVID-19. Front Cell Infect Microbiol 11:747816.
204. Koester ST, Li N, Lachance DM, Morella NM, Dey N. 2021. Variability in digestive and respiratory tract Ace2 expression is associated with the microbiome. PLoS One 16:e0248730.
205. Imai M, Iwatsuki-Horimoto K, Hatta M, Loeber S, Halfmann PJ, Nakajima N, Watanabe T, Ujie M, Takahashi K, Ito M, Yamada S, Fan S, Chiba S, Kuroda M, Guan L, Takada K, Armbrust T, Balogh A, Furusawa Y, Okuda M, Ueki H, Yasuhara A, Sakai-Tagawa Y, Lopes TJS, Kiso M, Yamayoshi S, Kinoshita N, Ohmagari N, Hattori SI, Takeda M, Mitsuya H, Krammer F, Suzuki T, Kawaoka

Y. 2020. Syrian hamsters as a small animal model for SARS-CoV-2 infection and countermeasure development. Proc Natl Acad Sci U S A 117:16587-16595.
206. Sencio V, Machelart A, Robil C, Benech N, Hoffmann E, Galbert C, Deryuter L, Heumel S, Hantute-Ghesquier A, Flourens A, Brodin P, Infanti F, Richard V, Dubuisson J, Grangette C, Sulpice T, Wolowczuk I, Pinet F, Prevot V, Belouzard S, Briand F, Duterque-Coquillaud M, Sokol H, Trottein F. 2022. Alteration of the gut microbiota following SARS-CoV-2 infection correlates with disease severity in hamsters. Gut Microbes 14:2018900.
207. Sencio V, Benech N, Robil C, Deruyter L, Heumel S, Machelart A, Sulpice T, Lamaziere A, Grangette C, Briand F, Sokol H, Trottein F. 2022. Alteration of the gut microbiota's composition and metabolic output correlates with COVID-19-like severity in obese NASH hamsters. Gut Microbes 14:2100200.
208. Sokol H, Contreras V, Maisonnasse P, Desmons A, Delache B, Sencio V, Machelart A, Brisebarre A, Humbert L, Deryuter L, Gauliard E, Heumel S, Rainteau D, Dereuddre-Bosquet N, Menu E, Ho Tsong Fang R, Lamaziere A, Brot L, Wahl C, Oeuvray C, Rolhion N, Van Der Werf S, Ferreira S, Le Grand R, Trottein F. 2021. SARS-CoV-2 infection in nonhuman primates alters the composition and functional activity of the gut microbiota. Gut Microbes 13:1-19.
209. Belser JA, Maines TR, Tumpey TM, Katz JM. 2010. Influenza A virus transmission: contributing factors and clinical implications. Expert Rev Mol Med 12:e39.
210. Gustin KM, Belser JA, Wadford DA, Pearce MB, Katz JM, Tumpey TM, Maines TR. 2011. Influenza virus aerosol exposure and analytical system for ferrets. Proc Natl Acad Sci U S A 108:8432-7.
211. Hao H, Cheng G, Iqbal Z, Ai X, Hussain HI, Huang L, Dai M, Wang Y, Liu Z, Yuan Z. 2014. Benefits and risks of antimicrobial use in food-producing animals. Front Microbiol 5:288.
212. Watanabe T, Iwatsuki-Horimoto K, Kiso M, Nakajima N, Takahashi K, Jose da Silva Lopes T, Ito M, Fukuyama S, Hasegawa H, Kawaoka Y. 2018. Experimental infection of Cynomolgus Macaques with highly pathogenic H5N1 influenza virus through the aerosol route. Sci Rep 8:4801.
213. Marriott AC, Dennis M, Kane JA, Gooch KE, Hatch G, Sharpe S, Prevosto C, Leeming G, Zekeng EG, Staples KJ, Hall G, Ryan KA, Bate S, Moyo N, Whittaker CJ, Hallis B, Silman NJ, Lalvani A, Wilkinson TM, Hiscox JA, Stewart JP, Carroll MW. 2016. Influenza A Virus Challenge Models in Cynomolgus Macaques Using the Authentic Inhaled Aerosol and Intra-Nasal Routes of Infection. PLoS One 11:e0157887.
214. MacInnes H, Zhou Y, Gouveia K, Cromwell J, Lowery K, Layton RC, Zubelewicz M, Sampath R, Hofstadler S, Liu Y, Cheng YS, Koster F. 2011. Transmission of aerosolized seasonal H1N1 influenza A to ferrets. PLoS One 6:e24448.
215. Frise R, Bradley K, van Doremalen N, Galiano M, Elderfield RA, Stilwell P, Ashcroft JW, Fernandez-Alonso M, Miah S, Lackenby A, Roberts KL, Donnelly CA, Barclay WS. 2016. Contact transmission of influenza virus between ferrets imposes a looser bottleneck than respiratory droplet transmission allowing propagation of antiviral resistance. Sci Rep 6:29793.

216. Belser JA, Sun X, Brock N, Pappas C, Pulit-Penaloza JA, Zeng H, Jang Y, Jones J, Carney PJ, Chang J, Long NV, Diep NT, Thor S, Di H, Yang G, Cook PW, Creager HM, Wang D, McFarland J, Dong PV, Wentworth DE, Tumpey TM, Barnes JR, Stevens J, Davis CT, Maines TR. 2020. Genetically and Antigenically Divergent Influenza A(H9N2) Viruses Exhibit Differential Replication and Transmission Phenotypes in Mammalian Models. J Virol 94.
217. Richard M, van den Brand JMA, Bestebroer TM, Lexmond P, de Meulder D, Fouchier RAM, Lowen AC, Herfst S. 2020. Influenza A viruses are transmitted via the air from the nasal respiratory epithelium of ferrets. Nat Commun 11:766.
218. Horwood PF, Fabrizio T, Horm SV, Metlin A, Ros S, Tok S, Jeevan T, Seiler P, Y P, Rith S, Suttie A, Buchy P, Karlsson EA, Webby R, Dussart P. 2020. Transmission experiments support clade-level differences in the transmission and pathogenicity of Cambodian influenza A/H5N1 viruses. Emerg Microbes Infect 9:1702-1711.
219. Guan M, Hall JS, Zhang X, Dusek RJ, Olivier AK, Liu L, Li L, Krauss S, Danner A, Li T, Rutvisuttinunt W, Lin X, Hallgrimsson GT, Ragnarsdottir SB, Vignisson SR, TeSlaa J, Nashold SW, Jarman R, Wan XF. 2019. Aerosol Transmission of Gull-Origin Iceland Subtype H10N7 Influenza A Virus in Ferrets. J Virol 93.
220. Kimble JB, Angel M, Wan H, Sutton TC, Finch C, Perez DR. 2014. Alternative reassortment events leading to transmissible H9N1 influenza viruses in the ferret model. J Virol 88:66-71.
221. Lednicky JA, Hamilton SB, Tuttle RS, Sosna WA, Daniels DE, Swayne DE. 2010. Ferrets develop fatal influenza after inhaling small particle aerosols of highly pathogenic avian influenza virus A/Vietnam/1203/2004 (H5N1). Virol J 7:231.
222. Sorrell EM, Wan H, Araya Y, Song H, Perez DR. 2009. Minimal molecular constraints for respiratory droplet transmission of an avian-human H9N2 influenza A virus. Proc Natl Acad Sci U S A 106:7565-70.
223. Bolyen E, Rideout JR, Dillon MR, Bokulich NA, Abnet CC, Al-Ghalith GA, Alexander H, Alm EJ, Arumugam M, Asnicar F, Bai Y, Bisanz JE, Bittinger K, Brejnrod A, Brislawn CJ, Brown CT, Callahan BJ, Caraballo-Rodriguez AM, Chase J, Cope EK, Da Silva R, Diener C, Dorrestein PC, Douglas GM, Durall DM, Duvallet C, Edwardson CF, Ernst M, Estaki M, Fouquier J, Gauglitz JM, Gibbons SM, Gibson DL, Gonzalez A, Gorlick K, Guo J, Hillmann B, Holmes S, Holste H, Huttenhower C, Huttley GA, Janssen S, Jarmusch AK, Jiang L, Kaehler BD, Kang KB, Keefe CR, Keim P, Kelley ST, Knights D, et al. 2019. Reproducible, interactive, scalable and extensible microbiome data science using QIIME 2. Nat Biotechnol 37:852-857.
224. Lowen AC, Bouvier NM, Steel J. 2014. Transmission in the guinea pig model. Curr Top Microbiol Immunol 385:157-83.
225. Creager HM, Zeng H, Pulit-Penaloza JA, Maines TR, Tumpey TM, Belser JA. 2017. In vitro exposure system for study of aerosolized influenza virus. Virology 500:62-70.
226. Walters MS, Gomi K, Ashbridge B, Moore MA, Arbelaez V, Heldrich J, Ding BS, Rafii S, Staudt MR, Crystal RG. 2013. Generation of a human airway

epithelium derived basal cell line with multipotent differentiation capacity. Respir Res 14:135.

227. Reed LJ, Muench H. 1938. A SIMPLE METHOD OF ESTIMATING FIFTY PER CENT ENDPOINTS. American Journal of Epidemiology 27:493-497.
228. Cao G, Noti JD, Blachere FM, Lindsley WG, Beezhold DH. 2011. Development of an improved methodology to detect infectious airborne influenza virus using the NIOSH bioaerosol sampler. J Environ Monit 13:3321-8.
229. Fischer WA, 2nd, King LS, Lane AP, Pekosz A. 2015. Restricted replication of the live attenuated influenza A virus vaccine during infection of primary differentiated human nasal epithelial cells. Vaccine 33:4495-504.
230. Zaqout S, Becker LL, Kaindl AM. 2020. Immunofluorescence Staining of Paraffin Sections Step by Step. Front Neuroanat 14:582218.
231. Maines TR, Jayaraman A, Belser JA, Wadford DA, Pappas C, Zeng H, Gustin KM, Pearce MB, Viswanathan K, Shriver ZH, Raman R, Cox NJ, Sasisekharan R, Katz JM, Tumpey TM. 2009. Transmission and pathogenesis of swine-origin 2009 A(H1N1) influenza viruses in ferrets and mice. Science 325:484-7.
232. Ye J, Sorrell EM, Cai Y, Shao H, Xu K, Pena L, Hickman D, Song H, Angel M, Medina RA, Manicassamy B, Garcia-Sastre A, Perez DR. 2010. Variations in the hemagglutinin of the 2009 H1N1 pandemic virus: potential for strains with altered virulence phenotype? PLoS Pathog 6:e1001145.
233. Tang Y, Lee CW, Zhang Y, Senne DA, Dearth R, Byrum B, Perez DR, Suarez DL, Saif YM. 2005. Isolation and characterization of H3N2 influenza A virus from turkeys. Avian Dis 49:207-13.
234. Pena L, Vincent AL, Loving CL, Henningson JN, Lager KM, Li W, Perez DR. 2012. Strain-dependent effects of PB1-F2 of triple-reassortant H3N2 influenza viruses in swine. J Gen Virol 93:2204-2214.
235. Ma W. 2020. Swine influenza virus: Current status and challenge. Virus Res 288:198118.
236. Yassine HM, Al-Natour MQ, Lee CW, Saif YM. 2007. Interspecies and intraspecies transmission of triple reassortant H3N2 influenza A viruses. Virol J 4:129.
237. Caceres CJ, Cardenas-Garcia S, Carnaccini S, Seibert B, Rajao DS, Wang J, Perez DR. 2021. Efficacy of GC-376 against SARS-CoV-2 virus infection in the K18 hACE2 transgenic mouse model. Sci Rep 11:9609.
238. Pu J, Wang S, Yin Y, Zhang G, Carter RA, Wang J, Xu G, Sun H, Wang M, Wen C, Wei Y, Wang D, Zhu B, Lemmon G, Jiao Y, Duan S, Wang Q, Du Q, Sun M, Bao J, Sun Y, Zhao J, Zhang H, Wu G, Liu J, Webster RG. 2015. Evolution of the H9N2 influenza genotype that facilitated the genesis of the novel H7N9 virus. Proc Natl Acad Sci U S A 112:548-53.
239. Kimble JB, Sorrell E, Shao H, Martin PL, Perez DR. 2011. Compatibility of H9N2 avian influenza surface genes and 2009 pandemic H1N1 internal genes for transmission in the ferret model. Proc Natl Acad Sci U S A 108:12084-8.
240. Bekking C, Yip L, Groulx N, Doggett N, Finn M, Mubareka S. 2019. Evaluation of bioaerosol samplers for the detection and quantification of influenza virus from artificial aerosols and influenza virus-infected ferrets. Influenza Other Respir Viruses 13:564-573.

241. Hao XY, Li FD, Lv Q, Xu YF, Han YL, Gao H. 2019. Establishment of BALB/C mouse models of influenza A H1N1 aerosol inhalation. J Med Virol 91:1918-1929.
242. Jackwood MW, Stallknecht DE. 2007. Molecular epidemiologic studies on North American H9 avian influenza virus isolates from waterfowl and shorebirds. Avian Dis 51:448-50.
243. Bonfante F, Mazzetto E, Zanardello C, Fortin A, Gobbo F, Maniero S, Bigolaro M, Davidson I, Haddas R, Cattoli G, Terregino C. 2018. A G1-lineage H9N2 virus with oviduct tropism causes chronic pathological changes in the infundibulum and a long-lasting drop in egg production. Vet Res 49:83.
244. Qi X, Tan D, Wu C, Tang C, Li T, Han X, Wang J, Liu C, Li R, Wang J. 2016. Deterioration of eggshell quality in laying hens experimentally infected with H9N2 avian influenza virus. Vet Res 47:35.
245. Arafat N, Abd El Rahman S, Naguib D, El-Shafei RA, Abdo W, Eladl AH. 2020. Co-infection of Salmonella enteritidis with H9N2 avian influenza virus in chickens. Avian Pathol 49:496-506.
246. Chu J, Zhang Q, Zuo Z, El-Ashram S, Guo Y, Zhao P, Huang S, He C, Khan A. 2017. Co-infection of Chlamydia psittaci with H9N2, ORT and Aspergillus fumigatus contributes to severe pneumonia and high mortality in SPF chickens. Sci Rep 7:13997.
247. Dalby AR, Iqbal M. 2014. A global phylogenetic analysis in order to determine the host species and geography dependent features present in the evolution of avian H9N2 influenza hemagglutinin. PeerJ 2:e655.
248. Fusaro A, Monne I, Salviato A, Valastro V, Schivo A, Amarin NM, Gonzalez C, Ismail MM, Al-Ankari AR, Al-Blowi MH, Khan OA, Maken Ali AS, Hedayati A, Garcia Garcia J, Ziay GM, Shoushtari A, Al Qahtani KN, Capua I, Holmes EC, Cattoli G. 2011. Phylogeography and evolutionary history of reassortant H9N2 viruses with potential human health implications. J Virol 85:8413-21.
249. Peiris M, Yuen KY, Leung CW, Chan KH, Ip PL, Lai RW, Orr WK, Shortridge KF. 1999. Human infection with influenza H9N2. Lancet 354:916-7.
250. Zhang G, Xu L, Zhang J, Fang Q, Zeng J, Liu Y, Ke C. 2022. A H9N2 Human Case and Surveillance of Avian Influenza Viruses in Live Poultry Markets - Huizhou City, Guangdong Province, China, 2021. China CDC Wkly 4:8-10.
251. Abt MC, Osborne LC, Monticelli LA, Doering TA, Alenghat T, Sonnenberg GF, Paley MA, Antenus M, Williams KL, Erikson J, Wherry EJ, Artis D. 2012. Commensal bacteria calibrate the activation threshold of innate antiviral immunity. Immunity 37:158-70.
252. Yitbarek A, Alkie T, Taha-Abdelaziz K, Astill J, Rodriguez-Lecompte JC, Parkinson J, Nagy E, Sharif S. 2018. Gut microbiota modulates type I interferon and antibody-mediated immune responses in chickens infected with influenza virus subtype H9N2. Benef Microbes 9:417-427.
253. Costa MC, Bessegatto JA, Alfieri AA, Weese JS, Filho JA, Oba A. 2017. Different antibiotic growth promoters induce specific changes in the cecal microbiota membership of broiler chicken. PLoS One 12:e0171642.

254. Proctor A, Phillips GJ. 2019. Differential Effects of Bacitracin Methylene Disalicylate (BMD) on the Distal Colon and Cecal Microbiota of Young Broiler Chickens. Front Vet Sci 6:114.
255. Liu YL, Yan T, Li XY, Duan YL, Yang X, Yang XJ. 2020. Effects of Bacillus subtilis and antibiotic growth promoters on the growth performance, intestinal function and gut microbiota of pullets from 0 to 6 weeks. Animal doi:10.1017/S1751731120000191:1-10.
256. Dumonceaux TJ, Hill JE, Hemmingsen SM, Van Kessel AG. 2006. Characterization of intestinal microbiota and response to dietary virginiamycin supplementation in the broiler chicken. Appl Environ Microbiol 72:2815-23.
257. Crisol-Martinez E, Stanley D, Geier MS, Hughes RJ, Moore RJ. 2017. Understanding the mechanisms of zinc bacitracin and avilamycin on animal production: linking gut microbiota and growth performance in chickens. Appl Microbiol Biotechnol 101:4547-4559.
258. Adewole D, Akinyemi F. 2021. Gut Microbiota Dynamics, Growth Performance, and Gut Morphology in Broiler Chickens Fed Diets Varying in Energy Density with or without Bacitracin Methylene Disalicylate (BMD). Microorganisms 9.
259. Mysara M, Berkell M, Xavier BB, De Backer S, Lammens C, Hautekiet V, Petkov S, Goossens H, Kumar-Singh S, Malhotra-Kumar S. 2021. Assessing the Impact of Flavophospholipol and Virginiamycin Supplementation on the Broiler Microbiota: a Prospective Controlled Intervention Study. mSystems doi:10.1128/mSystems.00381-21:e0038121.
260. Danzeisen JL, Kim HB, Isaacson RE, Tu ZJ, Johnson TJ. 2011. Modulations of the chicken cecal microbiome and metagenome in response to anticoccidial and growth promoter treatment. PLoS One 6:e27949.
261. Broom LJ. 2018. Gut barrier function: Effects of (antibiotic) growth promoters on key barrier components and associations with growth performance. Poult Sci 97:1572-1578.
262. Administration FaD. 2013. https://www.fda.gov/downloads/animalveterinary/guidancecomplianceenforcement/guidanceforindustry/ucm299624.pdf. Accessed
263. Seibert B, Caceres CJ, Carnaccini S, Cardenas-Garcia S, Gay LC, Ortiz L, Geiger G, Rajao DS, Ottesen E, Perez DR. 2022. Pathobiology and dysbiosis of the respiratory and intestinal microbiota in 14 months old Golden Syrian hamsters infected with SARS-CoV-2. PLoS Pathog 18:e1010734.
264. Cardenas-Garcia S, Ferreri L, Wan Z, Carnaccini S, Geiger G, Obadan AO, Hofacre CL, Rajao D, Perez DR. 2019. Maternally-Derived Antibodies Protect against Challenge with Highly Pathogenic Avian Influenza Virus of the H7N3 Subtype. Vaccines (Basel) 7.
265. Caporaso JG, Lauber CL, Walters WA, Berg-Lyons D, Huntley J, Fierer N, Owens SM, Betley J, Fraser L, Bauer M, Gormley N, Gilbert JA, Smith G, Knight R. 2012. Ultra-high-throughput microbial community analysis on the Illumina HiSeq and MiSeq platforms. ISME J 6:1621-4.
266. Callahan BJ, McMurdie PJ, Rosen MJ, Han AW, Johnson AJ, Holmes SP. 2016. DADA2: High-resolution sample inference from Illumina amplicon data. Nat Methods 13:581-3.

267. Bokulich NA, Kaehler BD, Rideout JR, Dillon M, Bolyen E, Knight R, Huttley GA, Gregory Caporaso J. 2018. Optimizing taxonomic classification of marker-gene amplicon sequences with QIIME 2's q2-feature-classifier plugin. Microbiome 6:90.
268. Bokulich N, Robeson M, Dillon M, Ziemski M, Kaehler B, O'Rourke D. 2021. bokulich-lab/RESCRIPt: 2021.11.0 doi:https://doi.org/10.5281/zenodo.5722925, Zenodo.
269. Team R. 2020. RStudio: Integrated Development for R, PBC, Boston, MA. http://www.rstudio.com/.
270. Bisanz JE. 2018. qiime2R: Importing QIIME2 artifacts and associated data into R sessions, https://github.com/jbisanz/qiime2R.
271. McMurdie PJ, Holmes S. 2013. phyloseq: an R package for reproducible interactive analysis and graphics of microbiome census data. PLoS One 8:e61217.
272. Jari Oksanen, F. Guillaume Blanchet, Michael Friendly, Roeland Kindt, Pierre Legendre, Dan McGlinn, Peter R. Minchin, R. B. O'Hara, Gavin L. Simpson, Peter Solymos, M. Henry H. Stevens, Eduard Szoecs, Wagner H. 2020. vegan: Community Ecology Package, vR package version 2.5-7. https://CRAN.R-project.org/package=vegan.
273. Wickham H. 2016. ggplot2: Elegant Graphics for Data, Springer-Verlag, New York. https://ggplot2.tidyverse.org.
274. Kassambara A. 2020. ggpubr: 'ggplot2' Based Publication Ready Plots, vR package version 0.4.0. https://CRAN.R-project.org/package=ggpubr.
275. Segata N, Izard J, Waldron L, Gevers D, Miropolsky L, Garrett WS, Huttenhower C. 2011. Metagenomic biomarker discovery and explanation. Genome Biol 12:R60.
276. Zou A, Nadeau K, Xiong X, Wang PW, Copeland JK, Lee JY, Pierre JS, Ty M, Taj B, Brumell JH, Guttman DS, Sharif S, Korver D, Parkinson J. 2022. Systematic profiling of the chicken gut microbiome reveals dietary supplementation with antibiotics alters expression of multiple microbial pathways with minimal impact on community structure. Microbiome 10:127.
277. Yan W, Sun C, Zheng J, Wen C, Ji C, Zhang D, Chen Y, Hou Z, Yang N. 2019. Efficacy of Fecal Sampling as a Gut Proxy in the Study of Chicken Gut Microbiota. Front Microbiol 10:2126.
278. Prescott JF, Sivendra R, Barnum DA. 1978. The use of bacitracin in the prevention and treatment of experimentally-induced necrotic enteritis in the chicken. Can Vet J 19:181-3.
279. Butaye P, Devriese LA, Haesebrouck F. 2003. Antimicrobial growth promoters used in animal feed: effects of less well known antibiotics on gram-positive bacteria. Clin Microbiol Rev 16:175-88.
280. Li J, Xiao Y, Fan Q, Yang H, Yang C, Zhang G, Chen S. 2022. Dietary Bacitracin Methylene Disalicylate Improves Growth Performance by Mediating the Gut Microbiota in Broilers. Antibiotics (Basel) 11.
281. Lee SJ, Cho S, La TM, Lee HJ, Lee JB, Park SY, Song CS, Choi IS, Lee SW. 2020. Comparison of microbiota in the cloaca, colon, and magnum of layer chicken. PLoS One 15:e0237108.

282. Soares BD, de Brito KCT, Grassotti TT, Filho HCK, de Camargo TCL, Carvalho D, Dorneles IC, Otutumi LK, Cavalli LS, de Brito BG. 2021. Respiratory microbiota of healthy broilers can act as reservoirs for multidrug-resistant Escherichia coli. Comp Immunol Microbiol Infect Dis 79:101700.
283. Glendinning L, McLachlan G, Vervelde L. 2017. Age-related differences in the respiratory microbiota of chickens. PLoS One 12:e0188455.
284. Ganz HH, Doroud L, Firl AJ, Hird SM, Eisen JA, Boyce WM. 2017. Community-Level Differences in the Microbiome of Healthy Wild Mallards and Those Infected by Influenza A Viruses. mSystems 2.
285. Ngunjiri JM, Taylor KJM, Ji H, Abundo MC, Ghorbani A, Kc M, Lee CW. 2021. Influenza A virus infection in turkeys induces respiratory and enteric bacterial dysbiosis correlating with cytokine gene expression. PeerJ 9:e11806.
286. Lin J, Hunkapiller AA, Layton AC, Chang YJ, Robbins KR. 2013. Response of intestinal microbiota to antibiotic growth promoters in chickens. Foodborne Pathog Dis 10:331-7.
287. Chen Y, Klein SL, Garibaldi BT, Li H, Wu C, Osevala NM, Li T, Margolick JB, Pawelec G, Leng SX. 2021. Aging in COVID-19: Vulnerability, immunity and intervention. Ageing Res Rev 65:101205.
288. Wu C, Chen X, Cai Y, Xia J, Zhou X, Xu S, Huang H, Zhang L, Zhou X, Du C, Zhang Y, Song J, Wang S, Chao Y, Yang Z, Xu J, Zhou X, Chen D, Xiong W, Xu L, Zhou F, Jiang J, Bai C, Zheng J, Song Y. 2020. Risk Factors Associated With Acute Respiratory Distress Syndrome and Death in Patients With Coronavirus Disease 2019 Pneumonia in Wuhan, China. JAMA Intern Med 180:934-943.
289. Cleary SJ, Pitchford SC, Amison RT, Carrington R, Robaina Cabrera CL, Magnen M, Looney MR, Gray E, Page CP. 2020. Animal models of mechanisms of SARS-CoV-2 infection and COVID-19 pathology. Br J Pharmacol 177:4851-4865.
290. Selvaraj P, Lien CZ, Liu S, Stauft CB, Nunez IA, Hernandez M, Nimako E, Ortega MA, Starost MF, Dennis JU, Wang TT. 2021. SARS-CoV-2 infection induces protective immunity and limits transmission in Syrian hamsters. Life Sci Alliance 4.
291. Dhakal S, Ruiz-Bedoya CA, Zhou R, Creisher PS, Villano JS, Littlefield K, Ruelas Castillo J, Marinho P, Jedlicka AE, Ordonez AA, Bahr M, Majewska N, Betenbaugh MJ, Flavahan K, Mueller ARL, Looney MM, Quijada D, Mota F, Beck SE, Brockhurst J, Braxton AM, Castell N, Stover M, D'Alessio FR, Metcalf Pate KA, Karakousis PC, Mankowski JL, Pekosz A, Jain SK, Klein SL, Johns Hopkins C-HSG. 2021. Sex Differences in Lung Imaging and SARS-CoV-2 Antibody Responses in a COVID-19 Golden Syrian Hamster Model. mBio 12:e0097421.
292. Choudhary S, Kanevsky I, Yildiz S, Sellers RS, Swanson KA, Franks T, Rathnasinghe R, Munoz-Moreno R, Jangra S, Gonzalez O, Meade P, Coskran T, Qian J, Lanz TA, Johnson JG, Tierney CA, Smith JD, Tompkins K, Illenberger A, Corts P, Ciolino T, Dormitzer PR, Dick EJ, Jr., Shivanna V, Hall-Ursone S, Cole J, Kaushal D, Fontenot JA, Martinez-Romero C, McMahon M, Krammer F, Schotsaert M, Garcia-Sastre A. 2022. Modeling SARS-CoV-2: Comparative

Pathology in Rhesus Macaque and Golden Syrian Hamster Models. Toxicol Pathol doi:10.1177/01926233211072767:1926233211072767.

293. Kinoshita T, Watanabe K, Sakurai Y, Nishi K, Yoshikawa R, Yasuda J. 2021. Co-infection of SARS-CoV-2 and influenza virus causes more severe and prolonged pneumonia in hamsters. Sci Rep 11:21259.

294. O'Donnell KL, Pinski AN, Clancy CS, Gourdine T, Shifflett K, Fletcher P, Messaoudi I, Marzi A. 2021. Pathogenic and transcriptomic differences of emerging SARS-CoV-2 variants in the Syrian golden hamster model. EBioMedicine 73:103675.

295. Rizvi ZA, Dalal R, Sadhu S, Binayke A, Dandotiya J, Kumar Y, Shrivastava T, Gupta SK, Aggarwal S, Tripathy MR, Rathore DK, Yadav AK, Medigeshi GR, Pandey AK, Samal S, Asthana S, Awasthi A. 2022. Golden Syrian hamster as a model to study cardiovascular complications associated with SARS-CoV-2 infection. Elife 11.

296. Sia SF, Yan LM, Chin AWH, Fung K, Choy KT, Wong AYL, Kaewpreedee P, Perera R, Poon LLM, Nicholls JM, Peiris M, Yen HL. 2020. Pathogenesis and transmission of SARS-CoV-2 in golden hamsters. Nature 583:834-838.

297. Osterrieder N, Bertzbach LD, Dietert K, Abdelgawad A, Vladimirova D, Kunec D, Hoffmann D, Beer M, Gruber AD, Trimpert J. 2020. Age-Dependent Progression of SARS-CoV-2 Infection in Syrian Hamsters. Viruses 12.

298. Oishi K, Horiuchi S, Minkoff JM, tenOever BR. 2022. The Host Response to Influenza A Virus Interferes with SARS-CoV-2 Replication during Coinfection. J Virol 96:e0076522.

299. Bosco N, Noti M. 2021. The aging gut microbiome and its impact on host immunity. Genes Immun 22:289-303.

300. Zheng D, Liwinski T, Elinav E. 2020. Interaction between microbiota and immunity in health and disease. Cell Res 30:492-506.

301. Man WH, de Steenhuijsen Piters WA, Bogaert D. 2017. The microbiota of the respiratory tract: gatekeeper to respiratory health. Nat Rev Microbiol 15:259-270.

302. Gaibani P, Viciani E, Bartoletti M, Lewis RE, Tonetti T, Lombardo D, Castagnetti A, Bovo F, Horna CS, Ranieri M, Viale P, Re MC, Ambretti S. 2021. The lower respiratory tract microbiome of critically ill patients with COVID-19. Sci Rep 11:10103.

303. Sulaiman I, Chung M, Angel L, Tsay JJ, Wu BG, Yeung ST, Krolikowski K, Li Y, Duerr R, Schluger R, Thannickal SA, Koide A, Rafeq S, Barnett C, Postelnicu R, Wang C, Banakis S, Perez-Perez L, Shen G, Jour G, Meyn P, Carpenito J, Liu X, Ji K, Collazo D, Labarbiera A, Amoroso N, Brosnahan S, Mukherjee V, Kaufman D, Bakker J, Lubinsky A, Pradhan D, Sterman DH, Weiden M, Heguy A, Evans L, Uyeki TM, Clemente JC, de Wit E, Schmidt AM, Shopsin B, Desvignes L, Wang C, Li H, Zhang B, Forst CV, Koide S, Stapleford KA, Khanna KM, et al. 2021. Microbial signatures in the lower airways of mechanically ventilated COVID-19 patients associated with poor clinical outcome. Nat Microbiol 6:1245-1258.

304. Saint-Criq V, Lugo-Villarino G, Thomas M. 2021. Dysbiosis, malnutrition and enhanced gut-lung axis contribute to age-related respiratory diseases. Ageing Res Rev 66:101235.

305. Du M, Cai G, Chen F, Christiani DC, Zhang Z, Wang M. 2020. Multiomics Evaluation of Gastrointestinal and Other Clinical Characteristics of COVID-19. Gastroenterology 158:2298-2301 e7.

306. Qian Q, Fan L, Liu W, Li J, Yue J, Wang M, Ke X, Yin Y, Chen Q, Jiang C. 2021. Direct Evidence of Active SARS-CoV-2 Replication in the Intestine. Clin Infect Dis 73:361-366.

307. Yeoh YK, Zuo T, Lui GC, Zhang F, Liu Q, Li AY, Chung AC, Cheung CP, Tso EY, Fung KS, Chan V, Ling L, Joynt G, Hui DS, Chow KM, Ng SSS, Li TC, Ng RW, Yip TC, Wong GL, Chan FK, Wong CK, Chan PK, Ng SC. 2021. Gut microbiota composition reflects disease severity and dysfunctional immune responses in patients with COVID-19. Gut 70:698-706.

308. Gu S, Chen Y, Wu Z, Chen Y, Gao H, Lv L, Guo F, Zhang X, Luo R, Huang C, Lu H, Zheng B, Zhang J, Yan R, Zhang H, Jiang H, Xu Q, Guo J, Gong Y, Tang L, Li L. 2020. Alterations of the Gut Microbiota in Patients with COVID-19 or H1N1 Influenza. Clin Infect Dis doi:10.1093/cid/ciaa709.

309. Tao W, Zhang G, Wang X, Guo M, Zeng W, Xu Z, Cao D, Pan A, Wang Y, Zhang K, Ma X, Chen Z, Jin T, Liu L, Weng J, Zhu S. 2020. Analysis of the intestinal microbiota in COVID-19 patients and its correlation with the inflammatory factor IL-18. Med Microecol 5:100023.

310. Thaiss CA, Zmora N, Levy M, Elinav E. 2016. The microbiome and innate immunity. Nature 535:65-74.

311. Team RC. 2014. R: A language and environment for statistical computing, R Foundation for Statistical Computing, http://www.R-project.org/.

312. Nearing JT, Douglas GM, Hayes MG, MacDonald J, Desai DK, Allward N, Jones CMA, Wright RJ, Dhanani AS, Comeau AM, Langille MGI. 2022. Microbiome differential abundance methods produce different results across 38 datasets. Nat Commun 13:342.

313. Love MI, Huber W, Anders S. 2014. Moderated estimation of fold change and dispersion for RNA-seq data with DESeq2. Genome Biol 15:550.

314. Fernandes AD, Reid JN, Macklaim JM, McMurrough TA, Edgell DR, Gloor GB. 2014. Unifying the analysis of high-throughput sequencing datasets: characterizing RNA-seq, 16S rRNA gene sequencing and selective growth experiments by compositional data analysis. Microbiome 2:15.

315. Alosaimi B, Naeem A, Hamed ME, Alkadi HS, Alanazi T, Al Rehily SS, Almutairi AZ, Zafar A. 2021. Influenza co-infection associated with severity and mortality in COVID-19 patients. Virol J 18:127.

316. Bartley JM, Zhou X, Kuchel GA, Weinstock GM, Haynes L. 2017. Impact of Age, Caloric Restriction, and Influenza Infection on Mouse Gut Microbiome: An Exploratory Study of the Role of Age-Related Microbiome Changes on Influenza Responses. Front Immunol 8:1164.

317. Dugan HL, Henry C, Wilson PC. 2020. Aging and influenza vaccine-induced immunity. Cell Immunol 348:103998.

318. de Castilhos J, Zamir E, Hippchen T, Rohrbach R, Schmidt S, Hengler S, Schumacher H, Neubauer M, Kunz S, Muller-Esch T, Hiergeist A, Gessner A, Khalid D, Gaiser R, Cullin N, Papagiannarou SM, Beuthien-Baumann B, Kramer A, Bartenschlager R, Jager D, Muller M, Herth F, Duerschmied D, Schneider J,

Schmid RM, Eberhardt JF, Khodamoradi Y, Vehreschild M, Teufel A, Ebert MP, Hau P, Salzberger B, Schnitzler P, Poeck H, Elinav E, Merle U, Stein-Thoeringer CK. 2021. Severe dysbiosis and specific Haemophilus and Neisseria signatures as hallmarks of the oropharyngeal microbiome in critically ill COVID-19 patients. Clin Infect Dis doi:10.1093/cid/ciab902.

319. Chaban B, Albert A, Links MG, Gardy J, Tang P, Hill JE. 2013. Characterization of the upper respiratory tract microbiomes of patients with pandemic H1N1 influenza. PLoS One 8:e69559.
320. Zhu X, Ge Y, Wu T, Zhao K, Chen Y, Wu B, Zhu F, Zhu B, Cui L. 2020. Co-infection with respiratory pathogens among COVID-2019 cases. Virus Res 285:198005.
321. Larsen JM. 2017. The immune response to Prevotella bacteria in chronic inflammatory disease. Immunology 151:363-374.
322. Blanco-Melo D, Nilsson-Payant BE, Liu WC, Uhl S, Hoagland D, Moller R, Jordan TX, Oishi K, Panis M, Sachs D, Wang TT, Schwartz RE, Lim JK, Albrecht RA, tenOever BR. 2020. Imbalanced Host Response to SARS-CoV-2 Drives Development of COVID-19. Cell 181:1036-1045 e9.
323. Kulkarni U, Zemans RL, Smith CA, Wood SC, Deng JC, Goldstein DR. 2019. Excessive neutrophil levels in the lung underlie the age-associated increase in influenza mortality. Mucosal Immunol 12:545-554.
324. Luporini RL, Rodolpho JMA, Kubota LT, Martin A, Cominetti MR, Anibal FF, Pott-Junior H. 2021. IL-6 and IL-10 are associated with disease severity and higher comorbidity in adults with COVID-19. Cytokine 143:155507.
325. Li J, Rong L, Cui R, Feng J, Jin Y, Chen X, Xu R. 2021. Dynamic changes in serum IL-6, IL-8, and IL-10 predict the outcome of ICU patients with severe COVID-19. Ann Palliat Med 10:3706-3714.
326. Saris A, Reijnders TDY, Reijm M, Hollander JC, de Buck K, Schuurman AR, Duitman J, Heunks L, Aman J, Bogaard HJ, Nossent EJ, van der Poll T, Bontkes HJ, Amsterdam UMCCsg. 2021. Enrichment of CCR6(+) CD8(+) T cells and CCL20 in the lungs of mechanically ventilated patients with COVID-19. Eur J Immunol 51:1535-1538.
327. Sun K, Metzger DW. 2008. Inhibition of pulmonary antibacterial defense by interferon-gamma during recovery from influenza infection. Nat Med 14:558-64.
328. Sencio V, Machado MG, Trottein F. 2021. The lung-gut axis during viral respiratory infections: the impact of gut dysbiosis on secondary disease outcomes. Mucosal Immunol 14:296-304.
329. Chen Y, Liu Y, Wang Y, Chen X, Wang C, Chen X, Yuan X, Liu L, Yang J, Zhou X. 2022. Prevotellaceae produces butyrate to alleviate PD-1/PD-L1 inhibitor-related cardiotoxicity via PPARalpha-CYP4X1 axis in colonic macrophages. J Exp Clin Cancer Res 41:1.
330. Herp S, Durai Raj AC, Salvado Silva M, Woelfel S, Stecher B. 2021. The human symbiont Mucispirillum schaedleri: causality in health and disease. Med Microbiol Immunol 210:173-179.
331. Tsinganou E, Gebbers JO. 2010. Human intestinal spirochetosis--a review. Ger Med Sci 8:Doc01.

332. Kaakoush NO. 2015. Insights into the Role of Erysipelotrichaceae in the Human Host. Front Cell Infect Microbiol 5:84.
333. Mancabelli L, Milani C, Lugli GA, Turroni F, Cocconi D, van Sinderen D, Ventura M. 2017. Identification of universal gut microbial biomarkers of common human intestinal diseases by meta-analysis. FEMS Microbiol Ecol 93.
334. Chiu YC, Lee SW, Liu CW, Lin RC, Huang YC, Lan TY, Wu LS. 2021. Comprehensive profiling of the gut microbiota in patients with chronic obstructive pulmonary disease of varying severity. PLoS One 16:e0249944.
335. Martin ME, Solnick JV. 2014. The gastric microbial community, Helicobacter pylori colonization, and disease. Gut Microbes 5:345-50.
336. Jennings R, Brand CM, McLaren C, Shepherd L, Potter C. 1974. The immune response of hamsters to purified haemagglutinins and whole influenza virus vaccines following live influenza virus infection. Med Microbiol Immunol 160:295-309.

APPENDIX

LIST OF REAGENTS/SUPPLIES

The following table contains a comprehensive list of reagents and supplies used to perform the different laboratory assays of this research.

Table A.1. List of reagents/supplies used for this research work

Reagent/supply	**Brand**	**Catalog**	**Procedure**
Mass Dosing Chamber (Large)	DSI	601-2036-001	Aerosol Exposure
Buxco Mass Dosing Controller	DSI	---	Aerosol Exposure
Aeroneb Lab Control Module	Kent Scientific	NEB-7000	Aerosol Exposure
HEPA-CAP 75, inlet 3/8 to 1/2" stepped barb, outlet 3/8 to 1/2" stepped barb	VWR	28137-886	Aerosol Exposure
Labconco™ Liquid Traps	Fisher Scientific	16-317-33	Aerosol Exposure
BioLite+ High-volume Sample Pump	SKC	228-9615	Aerosol Exposure
PTFE Filters for SARS, 0.3 µm, 37 mm	SKC	225-1722	Aerosol Exposure
6 well Tissue culture plates	VWR	82050-842	Cell Culture
Falcon® Filter Cap Cell Culture Flasks, T25 Flask	VWR	82051-074	Cell Culture
CellStar Filter Cap Cell Culture Flasks, T75 Flask	VWR	82050-856 (CS)	Cell Culture
Dulbecco's Modified Eagle's Medium (DMEM)	Sigma-Aldrich	D6429-6X500ML	Cell Culture
Gibco Opti-MEM | Reduced Serum Medium	Fisher Scientific	31985088	Cell Culture
Gibco™ PBS, pH 7.4	ThermoFisher	10010049	Cell Culture
Antibiotic/antimycotic solution, Corning	VWR	45000-616	Cell Culture
L-Glutamine	Sigma-Aldrich	G7513-100ML	Cell Culture
Fetal Bovine Serum	Sigma-Aldrich	F4135-6X500ML	Cell Culture

PneumaCult™-Ex Plus Medium	StemCell	5040	HAE cells
PneumaCult™-ALI Medium	StemCell	5001	HAE cells
Heparin Solution	StemCell	7980	HAE cells
Hydrocortisone Stock Solution	StemCell	7925	HAE cells
Gibco Penicillin-Streptomycin	Fisher Scientific	15-070-063	HAE cells
Gibco™ Amphotericin B	Fisher Scientific	15-290-018	HAE cells
Gentamicin solution (10mL)	Millipore Sigma	G1397-10ML	HAE cells
HEPES Buffered Saline Solution, 500 mL	Lonza	CC-5024	HAE cells
Trypsin-EDTA	Sigma-Aldrich	T3924-500ML	HAE cells
Collagen from human placenta	Sigma-Aldrich	C7521-50MG	HAE cells
Acetic Acid	---	---	HAE cells
Water, HyClone™ HyPure, Cell Culture Grade	VWR	16750-114	HAE cells
Corning® Transwell® polyester membrane cell culture inserts	Millipore Sigma	CLS3460-48EA	HAE cells
0.22um filter unit with pores	VWR	97066-214	HAE cells
9-day-old SPF eggs	---	---	Viral stocks
96 well Tissue culture plate	VWR	82050-771	Virus Titration
Trypsin, TPCK Treated (500mg)	Worthington Biochemical Corporation	LS003741	Virus Titration
96 well V-bottom plates	VWR	29442-402	Virus Titration
Isopropanol (molecular grade)	Sigma-Aldrich	9516-500mL	RNA extraction
MagMAX AI/ND Viral RNA extraction Kit	ThermoFisher	AM1835	RNA extraction
M+25 primer (STD purification)	IDT	---	RT-qPCR
M-124 primer (STD purification)	IDT	---	RT-qPCR
M-124_Ca/04_CJC primer (STD purification)	IDT	---	RT-qPCR
M-124_Ty/04_CJC primer (STD purification)	IDT	---	RT-qPCR
M+64 FAM labeled probe (HPLC purification)	IDT	---	RT-qPCR

2019-nCov_N2-F primer (STD purification)	IDT	---	RT-qPCR
2019-nCov_N2-R (STD purification)	IDT	---	RT-qPCR
FAM labeled probe (HPLC purification)	IDT	---	RT-qPCR
Quantabio qScript XLT One-Step RT-qPCR ToughMix kit	VWR	89236-668	RT-qPCR
Paraformaldehyde, 4% in PBS 250ml	ThermoFisher	C872C77	Immunofluorescence of HAE cells
Formalin solution, neutral buffered, 10%	Sigma-Aldrich	HT501128-4L	Immunofluorescence of HAE cells
Fisherbrand Histoplast PE Paraffin	Fisher Scientific	22900700	Immunofluorescence of HAE cells
Harris Hematoxylin	Anatech LTD	842	Immunofluorescence of HAE cells
Eosin-Y, Alcoholic	Anatech LTD	832	Immunofluorescence of HAE cells
Xylenes	Fisher Scientific	X5-20	Immunofluorescence of HAE cells
Sodium citrate tribasic dihydrate	Sigma-Aldrich	S4641-500G	Immunofluorescence of HAE cells
Triton X-100 Detergent	Sigma-Aldrich	9002-93-1 (500ml)	Immunofluorescence of HAE cells
Bovine Serum Albumin	Sigma-Aldrich	A2153-100G	Immunofluorescence of HAE cells
Anti-KRT5 antibody produced in rabbit	Millipore Sigma	HPA059479-25UL	Immunofluorescence of HAE cells
Monoclonal Anti-Acetylated Tubulin antibody, 100 uL	Thomas Scientific	T7451-100UL	Immunofluorescence of HAE cells
Club Cell Protein (CC16) Human, Rabbit Polyclonal Antibody	BioVendor	RD181022220-01	Immunofluorescence of HAE cells
MUC5AC Monoclonal Antibody	ThermoFisher	MA5-12178	Immunofluorescence of HAE cells
Anti-TFF3 antibody produced in rabbit	Millipore Sigma	HPA035464-25UL	Immunofluorescence of HAE cells
Anti-Hemagglutinin Rabbit Monoclonal Antibody [clone: 10]	VWR	103644-176	Immunofluorescence of HAE cells
anti-hemagglutinin H9 antibody	---	---	Immunofluorescence of HAE cells
Donkey anti-Rabbit IgG (H+L) Highly Cross-Adsorbed Secondary Antibody, Alexa Fluor 488	ThermoFisher	A-21206	Immunofluorescence of HAE cells

Goat anti-Mouse IgG (H+L) Highly Cross-Adsorbed Secondary Antibody, Alexa Fluor 594	ThermoFisher	A-11032	Immunofluorescence of HAE cells
Plain Microscope slides	Fisher Scientific	12-550-A3	Immunofluorescence of HAE cells
Corning Square and Rectangular Cover Glasses	Fisher Scientific	12-553-450	Immunofluorescence of HAE cells
VECTASHIELD® PLUS Antifade Mounting Medium (10ml)	Vector Laboratories	H-1900-10	Immunofluorescence of HAE cells
ActinGreen™ 488 ReadyProbes™ Reagent (AlexaFluor™ 488 phalloidin)	ThermoFisher	R37110	Immunofluorescence of HAE cells
Maackia Amurensis Lectin II (MAL II), Biotinylated	Vector Laboratories	B-1265-1	Immunofluorescence of HAE cells
Sambucus Nigra Lectin	Vector Laboratories	F13012	Immunofluorescence of HAE cells
Streptavidin, Alexa Fluor™ 594 Conjugate	ThermoFisher	S32356	Immunofluorescence of HAE cells
Bacitracin Methylene Disalicylate	Animal Health International	13737945	Antibiotic Growth Promoter
IDEXX AI MultiS-Screen Ab Test	IDEXX	99-12119	ELISA
Syringes (1mL)	ThermoFisher	14-826-88	Viral isolation
Puritan® Swab, Rayon Tipped Swabs, Polystyrene Handle	VWR	10808-146	OP and CL Swabs
Brain Heart Infusion Broth	Sigma-Aldrich	53286-500G	OP and CL Swabs
DNeasy PowerSoil HTP 96 Kit	Qiagen	12955-4	DNA Extractions
TissueLyser II	Qiagen	85300	Tissue homogenates
Tungsten Carbide Beads, 3 mm (200)	Qiagen	69997	Tissue homogenates
Phusion Hot Start II DNA Polymerase (2 U/μL)	ThermoFisher	F549L	Sequencing
dNTP Mix (10 mM each)	ThermoFisher	R0192	Sequencing
NEBNext High-fidelity 2X master mix for 250 rxns	Fisher Scientific	M0541L	Sequencing
515F primer (STD purification)	IDT	---	Sequencing
806R primer (STD purification)	IDT	---	Sequencing

SYBR Safe	ThermoFisher	S33102	Sequencing
GeneRuler 1kb Plus ladder	ThermoFisher	SM0311	Sequencing
TBE Buffer 10X (molecular biology grade)	Calbiochem	US1574795-1L	Sequencing
Agarose (analytical grade)	Promega	V3125	Sequencing
Buffer EB (elution buffer)	Qiagen	19086	Sequencing
Magnetic stand for tubes	ThermoFisher	12321D	Sequencing
Bioanalyzer high sensitivity DNA Analysis	Agilent	5067-4626	Sequencing
Sodium hydroxide solution	Sigma-Aldrich	72068-100ML	Sequencing
Agencourt AMPure XP beads	Agencourt	A63880	Sequencing
EDTA	Sigma-Aldrich	E6635-500G	Sequencing
MiSeq Reagent Kit v2 (500-cycles)	Illumina	MS-102-2003	Sequencing
MiSeq Reagent Nano Kit v2 (500-cycles)	Illumina	MS-103-1003	Sequencing
Qubit dsDNA HS assay Kit	ThermoFisher	Q32854	Sequencing
Qubi assay tubes	ThermoFisher	Q32856	Sequencing
Trizma hydrochloride	Sigma-Aldrich	T1535	Sequencing
Tween 20	J. T. Baker	X251-07	Sequencing
Gloves	MidSci	78886	General
Ethanol (for 70% ethanol solution)	ThermoFisher	22032601	General
Distilled water	---	---	General
Bleach	---	---	General
Cryogenic vial storage boxes	ThermoFisher	07-200-615	General
10uL filter tips	USA Scientific	1180-3810	General
200 uL filter tips	USA Scientific	1180-8810	General
1000 uL filter tips	USA Scientific	1182-1830	General
20 uL filter tips	USA Scientific	1183-1810	General
100 uL filter tips	USA Scientific	1183-1840	General
0.2mL strip tubes	USA Scientific	1402-4708	General
Microcentrifuge tubes (2mL)	USA Scientific	1420-2799	General
Microcentrifuge tubes (1.5mL)	USA Scientific	1615-5599	General
Screw cap tubes (1.5mL)	Genesee	21-256	General
15mL conical tubes	Fisher Scientific	0553859B	General
50ml conical tubes	Thomas Scientific	1159M36	General

Biohazard Autoclave bags (mini)	Genesee	30-162R	General
Bleach	Grainger	41H893	General
Storage boxes and dividers	VWR	82007-154	General
5mL serological pipettes	VWR	82050-478	General
10mL serological pipettes	VWR	82050-482	General
25 ml serological pipettes	VWR	82051-182	General
50 ml serological pipettes	VWR	82051-212	General
Large label for laser printers	USA Scientific	9187-2016	General
RNaseZAP	Sigma-Aldrich	R2020-250ML	General
Water (molecular biology grade)	VWR	82007-332	General